Presented to the Higher Degree of Research, Macquarie University in fulfilment of the requirements for the degree of Doctor of Philosophy

The microchemical and microstructural evolution of fluid and melt transfer in deep crustal shear zones

PhD Thesis

Department of Earth and Planetary Sciences

Macquarie University

David Silva

Sydney, June 2019

Contents

Abstract

Fluids and melt are increasingly recognised as key agents of weakening, promoting crustal deformation in mountain building systems. Zones of deformation within these systems, tens of kilometres deep in the crust, are considered principal conduits for melt or aqueous fluid flow (i.e. mass transfer) and are sites of melt-rock or fluid-rock reaction. In the high-temperature middle and lower crust, melt-present deformation and melt-rock interaction in high-strain zones enhances orogenesis due to (1) hydration reaction softening and (2) the intrinsic weak competence of melt-present deformation. Consequently, melt-present and hydrous high-strain zones act as powerful strain accommodators, facilitating the exhumation of deep crustal basement rocks. This combination of geological processes is interpreted as essential for having enabled the Palaeozoic Alice Springs Orogeny, an intracontinental orogenic event that formed compressional mountain belts within the interior of the Australian plate. As aqueous fluids have classically been invoked for fluid-driven reaction weakening in the middle- and upper-crust, the role of melt in rheological weakening during orogenesis has somewhat been overlooked, particularly in intracontinental orogens.

The aim of this thesis is to fill that knowledge gap by recognizing high-strain zones of intense melt-rock interaction and studying the microstructural and microchemical characteristics of the melt pathways. The overarching theme of the thesis is an attempt to determine what role weak rheological zones played in the deformation of the Australian plate during the intracontinental Alice Springs Orogeny. The study presents tectonic-scale geodynamic modelling in addition to a detailed analysis of exhumed ancient metamorphic rocks that are interpreted to have formed during melt-present deformation in the Gough Dam shear zone (GDSZ), Central Australia.

During compressive tectonic periods, primary features such as the geometry of the orogenic system, pre-existing crustal structures and transmitted stresses are highly relevant in the accommodation and concentration of differential stress within continental plates, with enhancement of intracontinental orogenesis if principal transmitted stresses are oriented at a low angle to the weak intraplate zone. Secondary stresses to the principal N-S tectonic activity on the Australian continent, contributed to marked periodicity during the Alice Springs Orogeny, as indicated by a strong temporal link between tectonic activity in Eastern and Central Australia. Deep-seated, km-scale shear zones comprising low to high vol% of biotite-rich glimmerite schist and felsic components are exposed in the core of the Alice Spring Orogeny, crosscutting ancient granulite protoliths. The glimmerite schist components are interpreted to have replaced the precursor granulites during melt-rock interaction, increasing the temperature and the proportion of biotite in the high-strain zones with calculated increase of time-integrated melt flux. Within the GDSZ, (1) Granite dykes, (2) granite lenses and (3) faceted K-feldspar phenocrysts hosted in K-feldspar-quartz-rich glimmerite schist all contain undeformed K-feldspar and quartz components, implying channelized melt

flux within the high-strain zone and posterior collapse and entrapment of crystalline phases from the fluxing melt. These relationships are consistent with melt-present high-strain deformation combined with melt-induced reaction softening. The episodic nature of tectonic activity may be controlled by melt-production at depth, periods of melt pressure and/or stress build-up and release enhanced by periods of plate tectonic reconfigurations changing the nature of far-field stresses.Author’s declaration of originality

Acknowledgements

I would like to sincerely thank my supervisors Nathan Daczko and Sandra Piazolo for the opportunity to participate in this project and for guiding me through this journey of geological discovery. Without your support, the completion of this thesis wouldn't have been possible and for that I am truly grateful.

A big thank you to the staff at Macquarie Geoanalytical labs for the time spent with me, mainly Olivier Alard, Yoann Gréau, Tim Murphy, Yi-Jen Lai, Manal Bebbington, Peter Wieland and Nigel Wilson. Your knowledge was paramount to improve the quality of my data, which contributed to the successful completion of this thesis.

Without friends, these last three years at Macquarie and, in a broader sense, in Australia wouldn't have been half as wonderful as they were. A special thanks to my friends with whom I "wasted" so much precious time, "ze French" Romain Thilhac, Bruno Colas, Olivier "Grand chef" Alard, Hadrien Henry and Yohan Greau, and the not so French Beñat Oliveira and Cait Stuart.

Last but not least, thank you to Sandra and Nathan's students, including Hindol Gathak, Robyn Gardner, Kim Jessop, Jonathan Munnikhuis and Uvana Meek, for all the help and fun talks at the department.

Catia Dias, my partner, thank you for your constant support and for all these wonderful years by my side.

Mãe, pai e Julieta, esta obra é tanto minha como vossa porque sem o vosso apoio, este sonho nunca se teria realizado. Obrigado.

I, David Silva, declare that all the material presented in this thesis is, to the best of my knowledge, my own original research, except where otherwise acknowledged. No part of this thesis has been submitted to any other university or institution.

_____ 01/06/2019

David Silva Date

Department of Earth and Planetary Sciences,

Macquarie University,

North Ryde, Australia

david.barbosa-da-silva@hdr.mq.edu.au

Chapter 1. Introduction: aims and thesis structure

Structural and compositional differentiation of the crust by orogenesis has traditionally been associated with convergent plate margins (e.g. see definition of an orogenic belt in Kearey et al., 2009). In contrast to orogens formed proximal to plate boundaries, intracontinental orogenesis occurs distant from the plate margins (Cunningham, 2005; Aitken et al., 2013; Raimondo et al., 2014). The documentation of intracontinental orogens is sparse when compared to their plate-margin equivalents (Molnar & Tapponnier, 1975; Tommasi et al., 1995; Raimondo et al., 2014 and reference therein). Fundamentally, orogenesis requires localisation of deformation, i.e. focussed into a weak zone. To achieve crustal thickening far from the tectonic stresses commonly focused at the plate margins, intracontinental orogens require either gravitational instabilities (e.g. upper mantle Rayleigh-Taylor instabilities; Neil & Houseman, 1999; Housemann & Molnar, 2001; Gorczyk et al., 2013) or lithospheric transmission of far-field stresses into plate interiors (Shaw et al., 1991; Roberts & Houseman, 2001; Handy & Brun, 2004). Thus, a prerequisite for intracontinental orogenesis is the combination of intraplate regions of rheologically weak lithosphere and either gravitational instabilities or transmission of far-field stress. Zones of mechanical weakness facilitate localisation of deformation and accommodate the relatively lower stresses present at plate interiors (e.g. Coblentz et al., 1995, 1998). Initiation and maintenance of orogenesis is dependent on the stress field orientation relative to the structure of the weakened crust (e.g. Tikoff & Teyssier, 1994). Therefore, knowledge of intraplate weak zones, their origin, orientation and structure, and the interplay between strain localization and far-field stresses, is fundamental to understand the formation of intracontinental orogenies.

Orogenesis in many geodynamic settings involves the significant migration and transfer of melt through the lower and middle crust (Hollister & Crawford, 1986; Hutton, 1988; Brown, 1994; Keay et al., 1997; Rapp et al., 2003; Weinberg et al, 2004; Daczko et al., 2016). This melt migration is essential in the segregation of highly silicic melt from lower to upper crustal levels, contributing to the observed vertical differentiation of the crust (Brun et al., 1990; D'Lemos et al., 1992; Petford et al., 1995; Vigneresse, 1995). The melt ascent can be performed by various mechanisms, in which dyking is the most commonly detected in the crust (Brown, 1994; Petford, 1995, 1996; Weinberg, 1996). An alternative to dyking is self-propagating hydrofractures (Bons & van Milligen, 2001; Bons et al., 2009), increasingly recognised in the crust (Hall & Klisters, 2016). High-strain zones also play an important role in the ascent of melt (Rosenberg, 2004; Stuart et al., 2018), creating open channels for the ascending melt, due to fluid pressure gradients created by reduced mean stress in the weaker high-strain rocks (Rosenberg, 2004; Hobbs & Ord, 2010), coupled with buoyancy forces (Sibson, 1994; Fusseis et al., 2009; Kohlstedt & Holtzman, 2009). The recognition of high-strain zones as melt pathways is easier following crystallisation of a macroscopic proportion of the fluxing

melt to form a high-strain zone will abundant leucocratic seams, pockets or dykes. An interpretation of melt-present deformation is much more difficult in cases where high-strain zones present with very low proportions of crystallised melt, usually much less than 7 to 10% (Rosenberg & Handy, 2005; Brown & Solar, 1998; Weinberg et al, 2013; Stuart et al, 2018a). Below this threshold, microstructure studies are necessary to infer the former presence of melt in high-strain zones. Such high-strain zones present microstructures in the form of pseudomorphed melt pockets within grains or at grain boundary triple points, and pseudomorphed interstitial melt forming elongated minerals along grain boundaries and minerals with low apparent dihedral angles (<60°); melt-fluxed high-strain zones commonly lack microstructures indicative of sub-solidus crystal-plastic deformation (von Bargen & Waff, 1986; Závada et al., 2007; Holness et al., 2011; Cesare et al., 2015; Stuart et al., 2017, 2018a; Lee et al., 2018).

In the crust, metasomatism in high-strain zones has been associated with flux of low silica, water-rich fluids during retrograde metamorphic conditions (White & Knipe, 1978; Etheridge et al., 1983; McCraig et al., 1990; Ferry, 1994; Gonçalves et al., 2012). These fluxed rocks contain abundant hydrous minerals, high variance assemblages and considerable changes in bulk chemistry. The identification of hydrous crystallization reactions involving high-silica melts in magmatic systems by Beard et al. (2004), lead to the interpretation of hydration during melt flux and melt-rock interaction involving migration of hydrous melts through high-strain zones (Daczko et al., 2016; Stuart et al., 2018b). These metasomatic reactions typically involve dissolution of minerals in precursor rocks and precipitation of hydrous minerals (Meek et al., 2019). The crystallization of hydrous phases can have a considerable effect in weakening previously competent rocks and even in pre-existing high strain zones (Wintsch et al., 1995; Stünitz & Tullis, 2001; Yardley, 2009; Geydan et al., 2014). The melt-assisted softening reactions coupled with the exponential weakening effect of small melt volumes in the high-strain zone forms extremely weakened rocks with a high predisposition to strain accommodation compared to the surrounding rock (Rosenberg & Handy, 2005; Searle, 2013; Lee et al., 2018). This type of extremely weak high-strain zone may play an important role in the initiation and perpetuation of exhumation of lower crust in intracontinental settings (e.g. Závada et al., 2018). The overarching goal of this thesis is therefore to explore the role of melt-present high-strain zones in intracontinental orogenesis using the natural laboratory of the Alice Springs Orogen, central Australia.

To achieve the proposed goals of the thesis, various instruments such as Scanning Electron Microscope (SEM) combined with Energy X-ray Dispersive Spectroscopy (EDS), Electron Backscatter Diffraction (EBSD) and Cathodoluminescence, Synchrotron X-ray, Electron Microprobe (EMP) and Laser Ablation Inductively Coupled Mass Spectrometry (La–ICP–MS) were used for both petrographic imagery and mineral chemical analysis of the collected samples. Numerical rheological models using the thin viscous sheet approximation were used to recreate the deformation of the Australian lithosphere during the Alice Springs Orogeny.

1-1. Aims

The aims of the thesis are:

1 - Assess the continental-scale geodynamic effect of lithospheric weak zones in central Australia, coupled with changing far-field stresses, on the observed spatial strain intensity, localization and kinematics of deformation in an intracontinental setting, i.e. the Alice Springs Orogeny;

2 - Identify the changes resulting from high-strain melt flux on the chemical, mineralogical and rheological evolution of a mid-crustal high-strain zone, i.e. the Gough Dam shear zone;

3 - Identify macroscopic and microstructural attributes of former melt ascent through sub-solidus rocks during melt-present deformation in a high-strain zone and assess the role that melt-present deformation plays in enabling intracontinental orogenesis.

1-2. Thesis structure

This thesis comprises 6 chapters: this introductory chapter (Chapter 1), four related studies, and a synthesis chapter (Chapter 6). Chapter 2 introduces the key macroscopic and microscale features of a high-strain zone that is interpreted to have experienced migration or flux of an externally-derived and reactive melt. The chapter explores the role that melt-present deformation may have played in driving extreme rheological weakening and thus facilitating intracontinental orogenesis. Chapter 3 describes a rheological numerical model of the Australian plate that investigates variations in regional stresses and the geometry and shape of weak zones in central Australia. The paper explores which combination of parameters and therefore model outcomes best match the key characteristics of deformation periods within the Alice Springs Orogeny. Chapter 4 details the key characteristics of biotite-rich glimmerite rocks within the Gough Dam shear zone. Reaction replacement relationships form the basis of an interpretation involving melt-rock interaction driving dissolution-precipitation and replacement of quartzite mylonite by glimmerite. Detailed glimmerite and modified quartzite host rock microstructure, allied with thorough mineral chemical characterisation and monazite geochronology support a model of melt flux of an externally-derived melt in a high-strain zone driving extreme metasomatism (sensu lato) and formation of glimmerite. Chapter 5 details field and microstructural evidence indicative of former melt-present deformation and identifies collapse structures where expulsion of melt from the melt pathways resulted in the entrapment of undeformed K-feldspar ± quartz phenocrysts in a high-strain zone. Trapped phenocrysts are proposed as a new microstructure indicative of the former presence of melt. The synthesis and conclusions (Chapter 6) brings together the findings from the previous chapters and contextualizes them within the framework of the thesis aims. The key outcomes of the

thesis are summarized as: melt migration and ascent along mid-crustal high-strain zones during the Alice Springs Orogeny resulted in: (1) reaction softening by melt-rock metasomatism forming glimmerite rock types, and (2) extreme rheological weakening due to the physical presence of melt during high-strain deformation. The combination of these two outcomes enhanced intracontinental orogenesis, creating the impressive scale of orogenesis documented in central Australia.

1-3. Published parts

Chapter 3, Intracontinental Orogeny Enhanced by Far-field Extension and Local Weak Crust, was published in Tectonics 37(12), 4421–4443 in November 2018, and was co-authored by Sandra Piazolo, Nathan Daczko, Gregory Houseman, Tom Raimondo and Lynn Evans.

Chapters are formatted according to manuscript preparation requirements as set forward by journals, resulting in slight style changes between chapters. Each chapter includes an introduction tailored to the specific material presented, which includes a degree of similar background information as a matter of necessity. The adaptation of these manuscripts into thesis chapters results in unavoidable repetition of background material. Two of the three unpublished chapters of the thesis have recently been submitted for publication (Chapter 2 and 4) and the final chapter will be submitted in the very near future (Chapter 5).

1-4. Author contribution

The direction for each of the manuscripts was determined by the candidate in discussion with Nathan Daczko (ND) and Sandra Piazolo (SP). Initial directions were developed further by the candidate, ND, and SP during discussions of results and preparation of the manuscripts. Field work, data acquisition, analysis, interpretation, and manuscript preparation were undertaken by the candidate under supervision and reviews of ND and SP, unless explicitly stated otherwise below.

Certain parts of this thesis were developed in conjunction with or with contributions by other authors. The manuscripts, except for Chapter 2, were written by the candidate with reviews by ND, SP, other co-authors, reviewers and journal editors. The candidate was involved in idea development and preparation of Chapter 2, which was written by SP and ND, and 10% of this paper can be credited towards this thesis. Field work and sampling was conducted with assistance from SP and ND. ND and Kim Jessop performed the Synchrotron trace element mapping of H–Qtz sample used in Chapter 4.

1-5. References

Aitken, A. R. A., Raimondo, T., Capitanio, F. A., 2013. The intraplate character of supercontinent tectonics. Gondwana Research, 24: 807–814.

Beard, J. S., Ragland, P. C., Rushmer, T., 2004. Hydration crystallization reactions between anhydrous minerals and hydrous melt to yield amphibole and biotite in igneous rocks: description and implications. The Journal of Geology, 112(5): 617–621.

Bons, P. D., & van Milligen, B. P., 2001. New experiment to model self-organized critical transport and accumulation of melt and hydrocarbons from their source rocks. Geology, 29(10): 919–922.

Bons, P. D., Becker, J. K., Elburg, M. A., Urtson, K., 2009. Granite formation: stepwise accumulation of melt or connected networks? Earth and Environmental Science Transactions of the Royal Society of Edinburgh, 100(1–2): 105–115.

Brown, M., 1994. The generation, segregation, ascent and emplacement of granite magma: the migmatite-to-crustally-derived granite connection in thickened orogens. Earth-Science Reviews 36: 83–130.

Brown, M. & Solar, G. S., 1998. Shear-zone systems and melts: feedback relations and self-organization in orogenic belts. Journal of Structural Geology, 20: 211–227.

Brun, J.P., Gapais, D., Cogne, J.P., Ledru, P., Vigneresse, J.L., 1990. The Flamanville granite (northwestern France): an unequivocal example of a syntectonically expanding pluton. Geological Journal, 25(3–4): 271–286.

Cesare, B., Acosta-Vigil, A., Bartoli, O., Ferrero, S., 2015. What can we learn from melt inclusions in migmatites and granulites? Lithos, 239: 186–216.

Coblentz, D. D., Sandiford, M., Richardson, R. M., Zhou, S., Hillis, R., 1995. The origins of the intraplate stress field in continental Australia. Earth and Planetary Science Letters, 133(3-4): 299–309.

Coblentz, D. D., Zhou, S., Hillis, R. R., Richardson, R. M., Sandiford, M., 1998. Topography, boundary forces, and the Indo-Australian intraplate stress field. Journal of Geophysical Research: Solid Earth, 103(B1): 919–931.

Cunningham, D., 2005. Active intracontinental transpressional mountain building in the mongolian Altai: Defining a new class of orogen. Earth and Planetary Science Letters 240(2): 436–444.

Daczko, N.R., Piazolo, S., Meek, U., Stuart, C. A., Elliot, V., 2016. Hornblendite delineates zones of mass transfer through the lower crust. Scientific Reports, 6: 31369.

Etheridge, M. A., Wall, V. J., Vernon, R. H., 1983. The role of the fluid phase during regional metamorphism and deformation. Journal of Metamorphic Geology, 1(3): 205–226.

Ferry, J. M., 1994. A historical review of metamorphic fluid flow. Journal of Geophysical Research, 99: 15487–98.

Fusseis, F., Regenauer-Lieb, K., Liu, J., Hough, R. M., De Carlo, F., 2009. Creep cavitation can establish a dynamic granular fluid pump in ductile shear zones. Nature, 459(7249): 974.

Goncalves, P., Oliot, E., Marquer, D., Connolly, J. A. D., 2012. Role of chemical processes on shear zone formation: an example from the Grimsel metagranodiorite (Aar massif, Central Alps). Journal of Metamorphic Geology, 30(7): 703–722.

Gorczyk, W., Hobbs, B., Gessner, K., Gerya, T., 2013. Intracratonic geodynamics. Gondwana Research, 24(3-4): 838–848.

Gueydan, F., Précigout, J., Montesi, L. G., 2014. Strain weakening enables continental plate tectonics. Tectonophysics, 631: 189–196.

Hall, D., & Kisters, A., 2016. Episodic granite accumulation and extraction from the mid-crust. Journal of Metamorphic Geology, 34(5): 483–500.

Handy, M. R., & Brun, J. P., 2004. Seismicity, structure and strength of the continental lithosphere. Earth and Planetary Science Letters, 223(3-4): 427–441.

Hobbs, B. E., & Ord, A., 2010. The mechanics of granitoid systems and maximum entropy production rates. Philosophical Transactions of the Royal Society A: Mathematical, Physical and Engineering Sciences, 368(1910): 53–93.

Hollister, L. S., Crawford, M. L., 1986. Melt-enhanced deformation: a major tectonic process. Geology, 14: 558–561.

Holness, M. B., Cesare, B., Sawyer, E. W., 2011. Melted rocks under the microscope: microstructures and their interpretation. Elements, 7(4): 247–252.

Houseman, G., & Molnar, P., 2001. Mechanisms of lithospheric rejuvenation associated with continental orogeny. Geological Society, London, Special Publications, 184(1): 13–38.

Hutton, D. H., 1988. Granite emplacement mechanisms and tectonic controls: Inferences from deformation studies. Earth and Environmental Science Transactions of the Royal Society of Edinburgh, 79(2-3): 245–255.

Kearey, P., Klepeis, K. A., Vine, F. J., 2009. Global tectonics, 3rd ed. John Wiley & Sons, UK.

Keay, S., Collins, W. J., McCulloch, M. T., 1997. A three-component Sr-Nd isotopic mixing model for granitoid genesis, Lachlan fold belt, eastern Australia. Geology 25: 307–310.

Kohlstedt, D. L., & Holtzman, B. K., 2009. Shearing melt out of the Earth: an experimentalist's perspective on the influence of deformation on melt extraction. Annual Review of Earth Planetary Sciences 37: 1–33.

Lee, A. L., Torvela, T., Lloyd, G. E., Walker, A. M., 2018. Melt organisation and strain partitioning in the lower crust. Journal of Structural Geology, 113: 188-199

Levine, J.S.F., Mosher, S., Siddoway, C.S., 2013. Relationship between syndeformational partial melting and crustal-scale magmatism and tectonism across the Wet Mountains, central Colorado. Lithosphere 5(5): 456–476.

McCaig, A. M., & Knipe, R. J., 1990. Mass-transport mechanisms in deforming rocks: Recognition, using microstructural and microchemical criteria. Geology, 18(9): 824–827.

Meek, U., Piazolo, S., Daczko, N. R., 2019 The field and microstructural signatures of deformation-assisted melt transfer: Insights from magmatic arc lower crust, New Zealand. Journal of Metamorphic Geology.

Molnar, P., & Dayem, K. E., 2010. Major intracontinental strike-slip faults and contrasts in lithospheric strength. Geosphere, 6(4): 444–467.

Neil, E. A. & Houseman, G. A., 1999. Rayleigh–Taylor instability of the upper mantle and its role in intraplate orogeny. Geophysical Journal International, 138(1): 89–107.

Petford, N., 1996. Dykes or diapirs? Earth and Environmental Science Transactions of the Royal Society of Edinburgh 87: 105–114.

Petford, N., Lister, J. R., Kerr, R. C., 1994. The ascent of felsic magmas in dykes. Lithos, 32(1–2): 161–168.

Raimondo, T., Hand, M., Collins, W. J., 2014. Compressional intracontinental orogens: Ancient and modern perspectives. Earth–Science Reviews, 130: 128–153.

Rapp, R. P., Shimizu, N., Norman, M. D., 2003. Growth of early continental crust by partial melting of eclogite. Nature 425: 605–609.

Roberts, E. A. & Houseman, G. A., 2001. Geodynamics of central Australia during the intraplate Alice Springs orogeny: Thin viscous sheet models. Geological Society, London, Special Publications, 184(1): 139–164.

Rosenberg, C. L., 2004. Shear zones and magma ascent: a model based on a review of the Tertiary magmatism in the Alps. Tectonics, 23(3).

Rosenberg, C. L., & Handy, M. R., 2005. Experimental deformation of partially melted granite revisited: implications for the continental crust. Journal of Metamorphic Geology, 23(1): 19-28.

Searle, M., 2013. Crustal melting, ductile flow, and deformation in mountain belts: cause and effect relationships. Lithosphere 5(6): 547–554.

Shaw, R., Etheridge, M., Lambeck, K., 1991. Development of the late–Proterozoic to mid-Paleozoic intracratonic Amadeus basin in central Australia: A key to understanding tectonic forces in plate interiors. Tectonics, 10(4): 688–721.

Sibson, R. H., 1994. Crustal stress, faulting and fluid flow. Geological Society, London, Special Publications, 78(1): 69–84.

Stuart, C. A., Daczko, N. R., Piazolo, S., 2017. Local partial melting of the lower crust triggered by hydration through melt–rock interaction: an example from Fiordland, New Zealand. Journal of Metamorphic Geology, 35(2): 213–230.

Stuart, C. A., Meek, U., Daczko, N. R., Piazolo, S., Huang, J. X., 2018b. Chemical signatures of melt–rock interaction in the root of a magmatic arc. Journal of Petrology, 59(2): 321–340.

Stuart, C. A., Piazolo, S., Daczko, N. R., 2018a. The recognition of former melt flux through high-strain zones. Journal of Metamorphic Geology, 36(8): 1049–1069.

Stünitz, H., & Tullis, J., 2001. Weakening and strain localization produced by syn-deformational reaction of plagioclase. International Journal of Earth Sciences, 90(1): 136–148.

Tikoff, B., & Teyssier, C., 1994. Strain modeling of displacement-field partitioning in transpressional orogens. Journal of Structural Geology, 16(11): 1575–1588.

Tommasi, A., Vauchez, A., Daudré, B., 1995. Initiation and propagation of shear zones in a heterogeneous continental lithosphere. Journal of Geophysical Research: Solid Earth, 100(B11): 22083–22101.

von Bargen, N., & Waff, H. S., 1986. Permeabilities, interfacial areas and curvatures of partially molten systems: results of numerical computations of equilibrium microstructures. Journal of Geophysical Research: Solid Earth, 91(B9): 9261–9276.

Weinberg, R. F., 1996. Ascent mechanism of felsic magmas: news and views. Earth and Environmental Science Transactions of the Royal Society of Edinburgh 87: 95–103.

Weinberg, R. F., Hasalová, P., Ward, L., Fanning, C. M., 2013. Interaction between deformation and magma extraction in migmatites: Examples from Kangaroo Island. South Australia Bulletin, 125(7-8): 1282–1300.

Weinberg, R. F., Sial, A. N., Mariano, G., 2004. Close spatial relationship between plutons and shear zones. Geology, 32(5): 377–380.

White, S. T., & Knipe, R. J., 1978. Transformation-and reaction-enhanced ductility in rocks. Journal of the Geological Society, 135(5): 513–516.

Wintsch, R. P., Christoffersen, R., Kronenberg, A. K., 1995. Fluid-rock reaction weakening of fault zones. Journal of Geophysical Research: Solid Earth, 100(B7): 13021–13032.

Yardley, B. W., 2009. The role of water in the evolution of the continental crust. Journal of the Geological Society, 166(4): 585–600.

Závada, P., Schulmann, K., Konopásek, J., Ulrich, S., Lexa, O., 2007. Extreme ductility of feldspar aggregates—Melt-enhanced grain boundary sliding and creep failure: Rheological implications for felsic lower crust. Journal of Geophysical Research: Solid Earth, 112(B10).

Závada, P., Schulmann, K., Racek, M., Hasalová, P., Jeřábek, P., Weinberg, R. F., Štípská, P., Roberts, A., 2018. Role of strain localization and melt flow on exhumation of deeply subducted continental crust. Lithosphere, 10(2): 217–238.

Chapter 2. Melt-present shear zones enable intracontinental orogenesis

Sandra Piazolo[1,2*], Nathan R. Daczko[2], David Silva[2] and Tom Raimondo[3]

[1]Earth & Environment, University of Leeds, UK

[2]Earth & Environmental Sciences, Macquarie University, Australia

[3]Natural & Built Environments and Future Industries Institute, University of South Australia, Australia

*E-mail address: S.Piazolo@leeds.ac.uk

Keywords: intracontinental orogeny, Alice Springs Orogeny, melt-present deformation, rheological weakening, far-field stresses, geochronology, glimmerite

Abstract

Localized rheological weakening is required to initiate and sustain intracontinental orogenesis, but the reasons for weakening remain debated. The intracontinental Alice Springs Orogen (ASO) dominates the lithospheric architecture of central Australia and involved prolonged (450–300 Ma) but episodic mountain building. The mid-crustal core of the ASO is exposed at its eastern margin, where field relationships and microstructures demonstrate that deformation was accommodated in biotite-rich shear zones. Rheological weakening was caused by localized melt-present deformation coupled with melt-induced reaction softening. This interpretation is supported by the coeval and episodic nature of melt-present deformation, igneous activity and sediment shed from the developing orogen. Our study identifies localized melt availability as an important ingredient enabling intracontinental orogenesis.

2-1. Introduction

Collisional mountain belts distal to plate boundaries are commonly referred to as intracontinental orogens (Cunningham, 2005; Aitken, 2011, 2013; Raimondo et al., 2014). Continental plates exhibit prolonged periods of tectonic quiescence at plate interiors, consistent with the scarcity and low magnitude of seismicity, and low maximum horizontal stresses compared to plate boundaries (e.g. Coblentz et al., 1998; Quigley et al., 2010; Aitken et al., 2013; Mueller et al., 2012, 2015; Heidbach et al., 2016). This contrasts with strain localization at the 10–100 km scale observed in intracontinental orogens. While lithospheric weakening is essential to enable such strain localization, its root causes remain largely unexplored besides suggestions of gravitational and

thermal instabilities (e.g. Houseman & Molnar, 2001; Holford et al., 2011).

Central Asia (Tien Shan and Altai) and central Australia (Alice Springs and Petermann Orogens) feature the best known modern and ancient examples of intracontinental orogens, respectively. The Alice Springs Orogen (ASO; Fig. 1) lies within a >1 Ga stable tectonic plate and involved shortening of up to 100 km and deposition of multiple synorogenic sedimentary sequences, each up to 4 km thick, implying a scale of mountain building and convergence typical of collisional orogens developed at plate boundaries (e.g. Teyssier, 1985; Haines et al., 2001; Klootwijk, 2013; Raimondo et al., 2014). Differential exhumation has resulted in a tilted crustal section exposing the mid-crustal orogenic core; from NW to SE, metamorphic grade progressively increases, shear zones widen and their deformation behavior becomes more ductile (Raimondo et al., 2011; 2014).

Whereas upper-crustal processes can be studied in active orogens (e.g. Tien Shan), the eastern Alice Springs Orogen offers the opportunity to investigate the deep-seated mechanics of intracontinental orogenesis and is the focus of this study. We link field and microstructural observations from a representative high-grade crustal-scale shear zone to episodic orogen-wide igneous activity, localized deformation and metamorphism, and synorogenic sedimentation to evaluate the role of melt availability in enabling intracontinental orogenesis.

2-2. Shear zone characteristic

2-2.1. Regional structure

The Paleozoic Alice Springs Orogen is exposed in central Australia (Fig. 1). It is characterized by a pervasive network of NW–SE-trending shear zones with hydrous mineral assemblages that truncate Paleoproterozoic granulite facies metamorphic fabrics (e.g. Collins & Teyssier, 1989; Cartwright & Buick, 1999). In the NW, the orogen is ~300 km wide and involves thrusts tens to hundreds of meters wide with < 2 km spacing (Fig. 1c; Collins & Teyssier, 1989). Deformation was accommodated by low-pressure (< 5 kbar) greenschist to lower amphibolite facies schists and quartzo-feldspathic mylonites characterized by solid-state deformation (e.g., Cartwright & Buick, 1999; Raimondo et al., 2011, 2017). In contrast, the deeper orogenic section to the SE is ~80 km wide, of higher metamorphic grade (6.5–7.0 kbar; 650–700 °C; Mawby et al., 1999; Raimondo et al., 2014) and has a bivergent structure. Deformation is localized into 5–8 crustal-scale steep reverse shear zones of 1–4 km width, spaced at 8–12 km intervals. These zones are dominated by biotite-bearing rocks ± muscovite, garnet, sillimanite, staurolite, kyanite and K-feldspar.

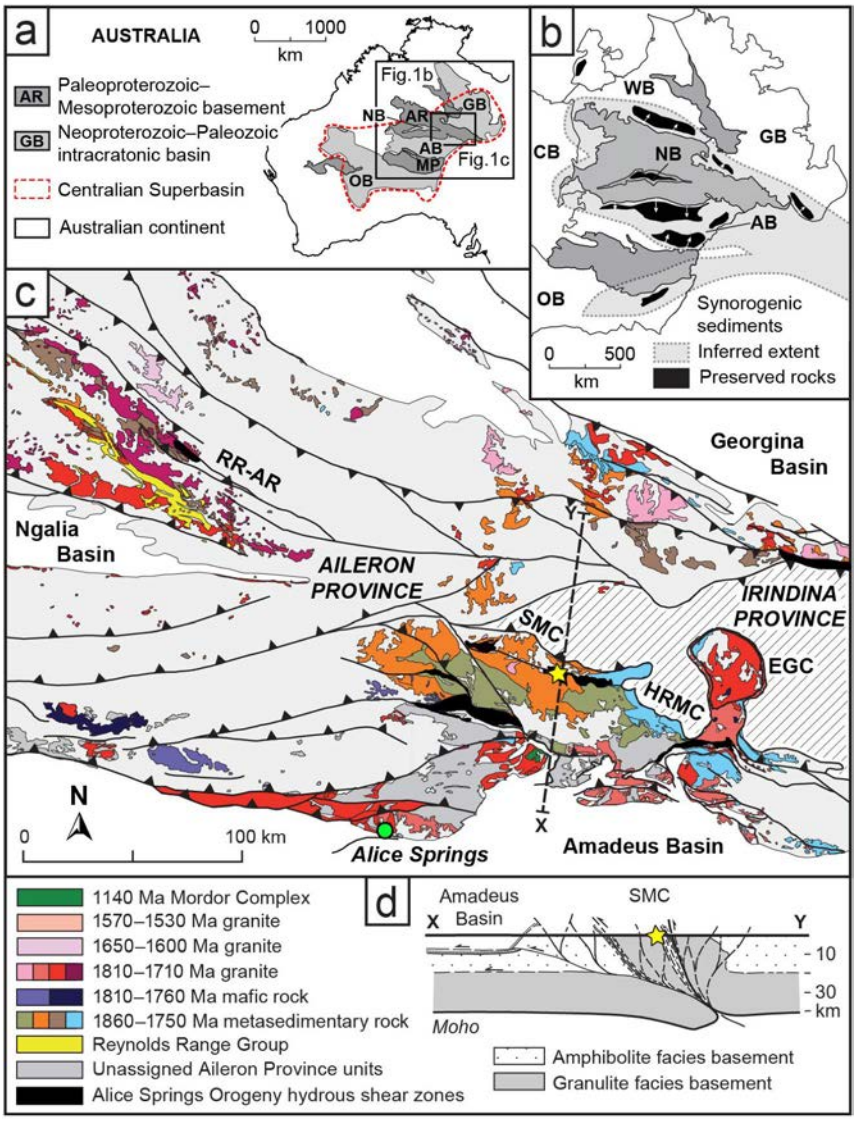

Figure 1. Geological context of the Alice Springs Orogen (ASO). (a,b) Lateral extent and position of the orogen within the Paleozoic Australian continent (white outline with major terranes shown); note the ASO was approximately 1000 km inland from the W, N and S continental margins and 200–300 km from the E. The intracratonic sedimentary basins of central Australia indicate the footprint of the former Centralian Superbasin and key ASO synorogenic depocenters; (c) Generalised geological map of the eastern Arunta Region; note the Gough Dam shear zone field site indicated with a gold star (23.147 °S, 134.565 °E); (d) Cross-section along profile X–Y indicated in (c), showing a bivergent crustal-scale pop-up structure. Figure modified from Collins & Teyssier (1989), Raimondo et al. (2011) and Scrimgeour (2013). AB–Amadeus Basin, AR–Arunta Region, CB–Canning Basin, EGC–Entia Gneiss Complex, GB–Georgina Basin, GDSZ–Gough Dam shear zone, HRMC–Harts Range Metaigneous Complex, MP–Musgrave Province, NB–Ngalia Basin, OB–Officer Basin, RR-AR–Reynolds-Anmatjira Ranges, SMC–Strangways Metamorphic Complex, SR–Strangways Range, WB–Wiso Basin.

2-2.2. Features of a representative mid-crustal shear zone

The Gough Dam shear zone (GDSZ) is 1–2 km in thickness, steeply north-dipping (60–80°) with reverse kinematics, E–SE striking (090–150°) over 55 km and juxtaposes two different Proterozoic basement packages (Collins & Shaw, 1995; Figure 1). Adjacent to the shear zone boundaries, anhydrous granulite facies basement rocks exhibit an irregularly spaced foliation and cm to dm folding with little strain localization along lithological boundaries. In contrast, biotite alignment defines the pervasive

shear foliation which is consistent over hundreds of meters across and along strike. Centimeter- to dm-scale compositional banding is foliation-parallel, continuous and varies in biotite mode (Figure 2a–d); three components can be distinguished.

Biotite-poor felsic Component 1 (C1; <5 vol.% biotite) includes lenses and layers of varying thickness (0.5–10 cm); some are seen as rootless folds and others as continuous trains resembling apparent pinch-and-swell structures (Figure 2a–d). C1 is K-feldspar- and quartz-rich, has a small range of grain sizes (1–3 mm) and is bordered by biotite-rich selvedges (Figure 2d–e). Feldspar grains are rectangular, interlocking and without clear crystallographic or shape preferred orientation (Figure 2). They occur with interstitial quartz and less commonly plagioclase or K-feldspar. Interstitial grains exhibit connectivity in three dimensions (i.e. interstitial grains that are spatially separate in 2D sections exhibit the same crystallographic orientation), high aspect ratios and low dihedral angles (Figure 2e).

Finer-grained (~1 mm) granitic Component 2 (C2; 5–25 vol.% biotite) constitutes most of the shear zone (Figure 2a–d) and displays the same microstructures observed in C1 but also “string of beads” textures (Figure 2e & 2f).

Biotite-rich Component 3 (C3, >50 vol.% biotite) is seen as selvedges around C1 and as mm-thick seams and continuous cm- to m-thick glimmerite bands in C2 (Figure 2a–d). Biotite is medium grained (~1 mm), aligned foliation-parallel, rarely kinked and commonly lacks undulose extinction (Figure 2g). The glimmerite assemblage contains 1–3 additional minerals in minor proportions (muscovite, quartz, K-feldspar, sillimanite, garnet, magnetite, kyanite ± staurolite). Quartz is interstitial, with aspect ratios >8 and occurs between biotite grains (Figure 2g).

2-3. Temporal pattern of orogenic activity

A compilation of orogen-wide geochronological datasets shown in Figure 3 and Table S1 demonstrates an episodic temporal evolution of the ASO. The data exhibit overlap of igneous activity (Ig), derived from peraluminous granitic pegmatite dykes (Buick et al., 2008) and small granitic plugs (Buick et al., 2001), with metamorphic and deformation ages of shear zones (D). Some shear zones show repeated reactivation during separate episodes of orogenic activity (e.g. Raimondo et al., 2014; Table S1). The timing of peaks in synorogenic sedimentation (S) at c. 450–435 Ma, c. 385–365 Ma and c. 340–315 Ma coincides with three of the igneous and tectonometamorphic episodes.

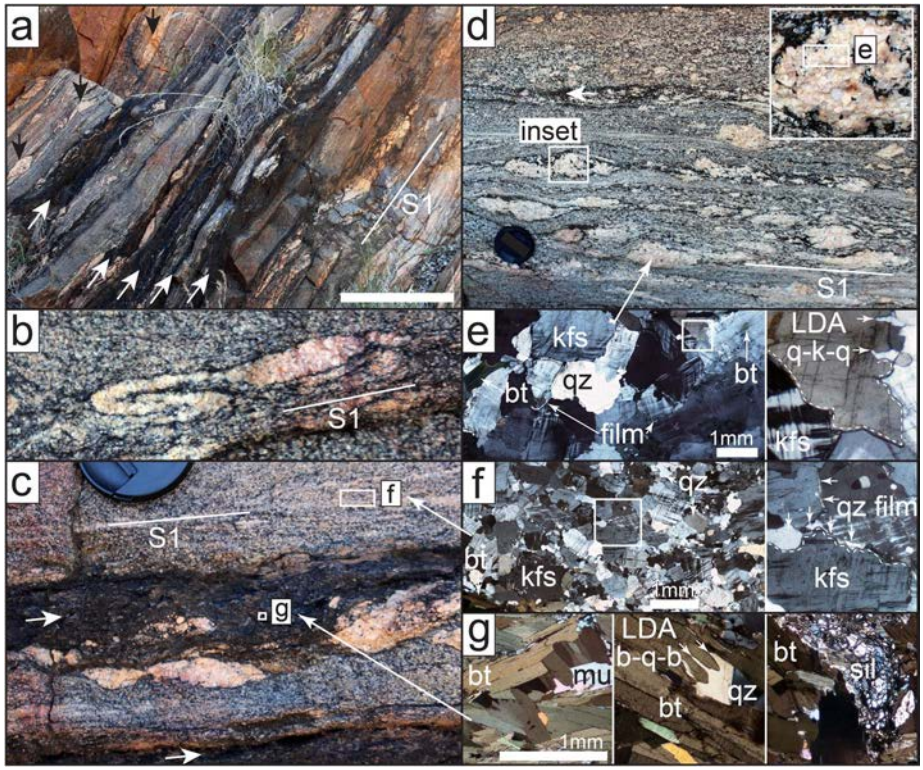

Figure 2. Field and microstructural relationships of the Gough Dam shear zone; S1 represents the shear foliation. (a) Outcrop-scale features showing fine-grained, well-foliated granitic bands with biotite-rich glimmerite (white arrows) and trains of biotite-poor components (black arrows); (b,c) Fine-grained and well-foliated granitic component with elongate lens-shaped biotite-poor component (rare rootless folds) and biotite-rich glimmerite components (white arrows). (d) Outcrop-scale and detailed views of the granitic component with a high abundance of lens-shaped biotite-poor felsic components with pronounced biotite-rich selvedges; (e–f) Photomicrographs and detailed views featuring K-feldspar–quartz-rich lens (e) and granitic component (f) showing interlocking rectangular K-feldspar grains with quartz grain boundary films and very small, equidimensional quartz grains decorating grain boundaries forming “string of beads” textures. Inset to right shows interstitial K-feldspar with low apparent dihedral angles (LDA) between fingers of a single quartz grain (LDA q-k-q); all minerals display limited evidence of crystal-plastic deformation (i.e. undulose extinction, subgrain boundaries, core-mantle structures, shape and crystallographic preferred orientation etc.) and have irregular disequilibrium boundaries (dashed lines). (g) Photomicrographs of biotite-rich glimmerite components showing assemblages including biotite, muscovite, quartz and sillimanite; quartz and biotite are intergrown such that quartz displays low apparent dihedral angles between two biotite grains (LDA b-q-b); all minerals display limited evidence of crystal-plastic deformation (i.e. grains lack undulose extinction, kinking, etc.).

2-4. Discussion

2-4.1. Melt-present deformation

The GDSZ accommodated a thrust-parallel displacement of ~40 km based on the number of shear zones across the orogen in the SE, its steep dip angle and the amount of total orogenic shortening. Hence, shear strain is in the order of 20–40 as the GDSZ thickness is 1–2 km. The GDSZ lacks microstructural evidence of dynamic recrystallization/solid-state crystal-plastic deformation, e.g. mantled porphyroclasts, bimodal grain size distribution, undulose extinction or kinking (Passchier and Trouw 2005). Instead, microstructures indicative of the former presence of melt are commonly preserved. These include disequilibrium grain boundaries (dashed lines; Figure 2e–f),

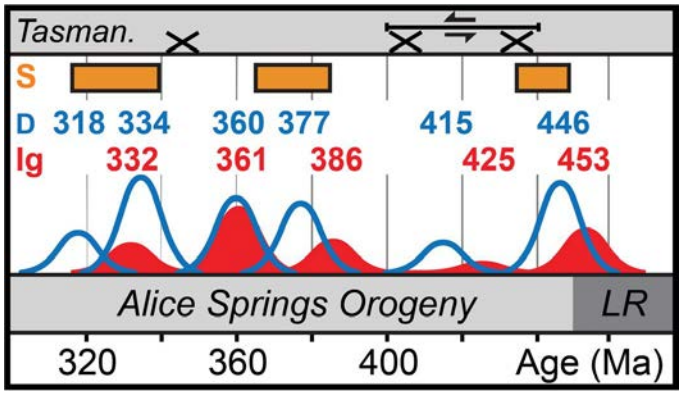

Figure 3. Gaussian-summation probability density distribution plots of orogen-wide age data for synorogenic sedimentation (S, orange), deformation/metamorphism (D, blue) and igneous activity (Ig, red) (see GSA Repository for methods and tabulated data; Table DR1). Synorogenic sedimentation intervals are based on biostratigraphic evidence in orogenic deposits (Haines et al., 2001; Shaw et al., 1992), metamorphic and deformation ages are established by syntectonic monazite, garnet and mica geochronology (Table DR1 and related references), and igneous activity is derived from peraluminous granitic pegmatite dykes (Buick et al., 2008) and minor plutons (Buick et al., 2001). North-south extensional activity formed the deep epicratonic Larapinta Rift (LR; 460–480 Ma) and immediately preceded the compressional Alice Springs Orogeny. The timing of orogenic activity along the eastern margin of Australia in the Tasmanides (Tasman.) is dominantly extensional, with periods of compression (marked as "x") or significant strike slip movement (double arrows) shown (Raimondo et al., 2014; Silva et al., 2018).

interstitial minerals with apparent low dihedral angles (<60°) and grains with aspect ratio > 8 representing grain boundary films (Fig. 2e–g; Vernon, 2011). Furthermore, component C1 exhibits typical igneous features including unimodal grain size and near-randomly-oriented, interlocking, rectangular feldspar crystals with interstitial quartz (inset Figure 2d).

Recent work has shown that during melt-present deformation, microstructures indicative of the former presence of melt are formed and can be preserved. In such shear zones, strain is dominantly accommodated by viscous melt flow, resulting in a viscosity drop of at least one order of magnitude relative to solid-state deformation (Stuart et al., 2018a,b; Lee et al., 2018; Pakrash et al., 2018; Meek et al., 2019). If annealing had been an important process, delicate microstructures such as high aspect ratio interstitial grains with low dihedral angles and "string of beads" microstructures would have been erased (e.g. Piazolo et al. 2005).

The ubiquitous evidence of former melt presence within the GDSZ focuses attention on the origin of the melt. The anhydrous and infertile nature of the granulite facies basement rocks that host the shear zone is inconsistent with local derivation of melt (Buick et al., 2008), and markedly contrasts with the hydrous character of the deformed rocks. Abundant biotite growth during shearing and a lack of partial melting textures (e.g. peritectic minerals surrounded by leucosome and reaction consumption of hydrous phases) further argues against in-situ melting of the host rocks during the ASO. These relationships suggest that melt was externally derived, implying melt flux through the shear zone during deformation.

2-4.2. Melt-present shearing and melt–rock interaction facilitate enhanced rheological weakening

Whereas the spatial relationship between biotite-rich selvedges and felsic igneous lenses is most notable in the GDSZ, similar features also occur adjacent to other biotite-poor igneous components. Biotite selvedges are commonly connected by biotite seams, and cm- to dm-thick biotite-rich glimmerite bands invariably contain some igneous features (Fig. 2a–d). This spatial association suggests a causal relationship, whereby biotite formed due to interaction between a hydrous melt and the host rock. Like a dynamic version of the hydration crystallization reactions of Beard et al. (2004), disequilibrium during melt-rock interaction drives the dissolution of precursor granulite and the precipitation of a biotite-rich assemblage in equilibrium with the fluxing melt (Stuart et al., 2016, 2017; Meek et al., 2019). This results in melt-mediated replacement reactions (Daczko et al., 2016), analogous to lower temperature aqueous fluid-mediated replacement reactions (Putnis, 2009).

Accordingly, in the biotite-rich glimmerite bands, melt flux drove widespread melt–rock interaction and metasomatism, producing a locally hydrated rock through biotite crystallization. Experimental data shows that ascending peraluminous melts become increasingly reactive (Clemens, 2003), explaining widespread melt-induced reactions during melt flux. Exothermic biotite growth (Haack & Zimmerman, 1996) and melt flux-related heating maintained sufficiently high temperature to limit melt crystallization during reaction and ascent through the exposed structural level. Deformation is commonly dilatant at the grain scale due to deformation inconsistencies between adjacent grains, causing increased porosity and permeability and enhanced melt migration. Additionally, deformation enhances melt expulsion by synkinematic filter pressing (e.g. Park & Means, 1996), explaining the observed low abundance of preserved quartzo-feldspathic igneous material in the glimmerite bands.

Development of the biotite-rich glimmerite bands represents a form of reaction softening (Watts & Williams, 1983), commonly attributed to aqueous fluid–rock interaction (e.g., Teall, 1885; Brodie & Rutter, 1985). As we argue above, melt–rock interaction is the root cause of mica growth and drives concomitant rheological weakening. Any fluid (including melt) cannot support shear stresses; hence, melt-bearing rocks are intrinsically weak (e.g., van der Molen & Paterson, 1979; Rutter & Neumann, 1995). Rosenberg & Handy (2005) show that >7 vol.% melt weakens rocks by at least one order of magnitude. This observation has been extended to shear zones to infer rheological weakening of 1–2 orders of magnitude at the km-scale (Brown & Solar, 1998; Marchildon & Brown, 2003; Weinberg & Mark, 2008; Jamieson et al., 2011) and orogen-scale (Hollister & Crawford, 1986; Harris, 2007 and references therein). In addition, fluid overpressure (Hubbert & Rubey, 1959) and melt-induced heating enhances weakening within a deforming rock (Tommasi et al., 1994). We therefore interpret that ASO mid-crustal shear zones were weak during episodes of melt flux due to melt-present deformation and melt-induced reaction softening.

2-4.3. Orogenic episodicity: dynamic feedback between far-field stresses, melt availability and rheological weakening

The intracontinental setting of the ASO suggests that orogenesis involved a localized weak zone within otherwise strong lithosphere. Recent work shows that the failed Larapinta Rift (LR; Figure 3), together with its thick sedimentary fill, represents the required weak zone and, additionally, global-scale plate reorganization drove rift-inversion and strain localization (Silva et al., 2018 and references therein). While the importance of fault reactivation in controlling deformation patterns has been widely recognized (e.g. De Graciansky et al. 2010, Kober et al. 2013), the episodic nature of the ASO (Figure 3) suggests another factor must play a role. If orogenesis was enabled solely by reactivation of pre-existing faults, strain localization at rheological interfaces or the presence of weak rift fill sediments, then continuous deformation may be expected. In contrast, magmatic systems are inherently episodic due to the link between melt pressure build-up, release and melt extraction (e.g. Schmeling, 2006).

Episodic melt-present deformation requires a fertile source, a mechanism to cause melting, and alternating melt-present weakening/deformation and subsequent fault strengthening. For the ASO, a fertile source has been contentious, as hydrous shear zones cut anhydrous granulite (Buick et al., 2008); proposed candidates include unmetamorphosed sedimentary rocks of the neighboring intracratonic Neoproterozoic–Paleozoic Amadeus and Georgina Basins (Figure 1), or the Cambrian–Ordovician Harts Range Group deposited in the epicratonic Larapinta rift basin (Irindina Province in Fig. 1; Maidment et al., 2013). These sources require either tectonic underthrusting (Buick et al., 2008) or deep burial (Tucker et al., 2015) to deliver fertile crust to deeper structural levels and facilitate melt production.

We argue that in the deep crust, recently deposited sediments underwent prograde metamorphism to produce melt over a sustained period, but that melt migration and associated deformation was only facilitated when (a) an external force was applied due to plate reorganization and associated continuous external stresses; and (b) melt pressure was sufficiently high to overcome yield stresses. During melt release, deformation was highly localized and melt-present, facilitating fault reactivation through rheological weakening (see analogue experimental results from Zanella et al., 2015). Upon melt source drainage (Schmeling, 2006), steep shear zones became strong and deformation ceased, allowing melt pressure to gradually build up again; conceptually this is similar to the fluid-deformation cycles envisaged by the fault valve concept (Sibson, 1990). Once melt pressure was sufficiently high, shear zones became active again, initiating another episode of simultaneous igneous and tectonic activity. By this mechanism, repeated episodes of melt-present deformation and melt-induced reaction softening drove substantial weakening, and thus melt availability played a critical role in enabling intracontinental orogenesis.

2-5. Acknowledgments

This research was supported by ARC Discovery Grant DP160103449. A. Putnis (Curtin University) is thanked for discussions. This is contribution 1379 from the ARC Centre of Excellence for Core to Crust Fluid Systems (http://www.CCFS.mq.edu.au) and GEMOC (http://www.GEMOC.mq.edu.au). We thank L. Ratschbacher, G. Solar, and C. Teyssier for constructive reviews and D. Brown for editorial handling.

2-6. References

Aitken, A. R. A., 2011, Did the growth of Tibetan topography control the locus and evolution of Tien Shan mountain building? Geology, v. 39, p. 459–462.

Aitken, A. R. A., Raimondo, T., & Capitanio, F. A. 2013, The intraplate character of supercontinent tectonics: Gondwana Research, v. 24, p. 807–814.

Beard, J. S., Ragland, P. C., & Rushmer, T., 2004, Hydration crystallization reactions between anhydrous minerals and hydrous melt to yield amphibole and biotite in igneous rocks: description and implications: The Journal of Geology, v. 112, p. 617–621.

Brodie, K. H., & Rutter E. H., 1985, On the relationship between deformation and metamorphism, with special reference to the behaviour of basic rocks. In: Metamorphic Reactions: Kinetics, Textures and Deformation (eds Thompson, A. B. and Rubie, D. C.): Advances in Physical Geochemistry, v. 4, p. 138–179.

Brown, M., & Solar, G. S., 1998, Shear-zone systems and melts: feedback relations and self-organization in orogenic belts: Journal of Structural Geology, v. 20, p. 211-227.

Buick, I. S., Hand, M., Williams, I. S., Mawby, J., Miller, J. A., & Nicoll, R. S., 2005, Detrital zircon provenance constraints on the evolution of the Harts Range Metamorphic Complex (central Australia): links to the Centralian Superbasin: Journal of the Geological Society, v. 162, p. 777–787.

Buick, I. S., Miller, J. A., Williams, I. S., & Cartwright, I., 2001, Ordovician high-grade metamorphism of a newly recognised late Neoproterozoic terrane in the northern Harts Range, central Australia. Journal of Metamorphic Geology, v. 19, p. 373–394.

Buick, I. S., Storkey, A., & Williams, I. S., 2008, Timing relationships between pegmatite emplacement, metamorphism and deformation during the intra-plate Alice Springs Orogeny, central Australia: Journal of Metamorphic Geology, v. 26, p. 915–936.

Cartwright, I., & Buick, I. S., 1999, Meteoric fluid flow within Alice Springs age shear zones, Reynolds Range, central Australia: Journal of Metamorphic Geology, v. 17, p. 397–414.

Clemens, J. D., 2003, S-type granitic magmas—petrogenetic issues, models and evidence: Earth-Science Reviews, v. 61, p. 1-18.

Coblentz, D. D., Zhou, S., Hillis, R. R., Richardson, R. M., Sandiford, M., 1998, Topography, boundary forces, and the Indo-Australian intraplate stress field. Journal of Geophysical Research: Solid Earth, v. 103, p. 919-931.

Collins, W. & Shaw, R., 1995, Geochronological constraints on orogenic events in the Arunta inlier: A review. Precambrian Research, v. 71, p.315–346.

Collins, W. & Teyssier, C., 1989. Crustal scale ductile fault systems in the Arunta inlier, central Australia. Tectonophysics, 158(1): 49–66. Collins, W. J., & Teyssier, C., 1989, Crustal scale ductile fault systems in the Arunta Inlier, central Australia: Tectonophysics, v. 158, p. 49-66.

Cunningham, D., 2005, Active intracontinental transpressional mountain building in the Mongolian Altai: Defining a new class of orogen: Earth and Planetary Science Letters, v. 240, p. 436–444.

Daczko, N. R., Piazolo, S., Meek, U., Stuart, C. A., & Elliott, V., 2016, Hornblendite delineates zones of mass transfer through the lower crust: Scientific reports, 6.

De Graciansky, P. C., Roberts, D. G., & Tricart, P., 2010. The late Cretaceous phase and Onset of Alpine shortening. In: “The Western Alps, from rift to passive margin to orogenic belt: an integrated geoscience overview”. (Developments in Surface processes, Elsevier), v. 14, p. 169-182.

Dyksterhuis, S., & Müller, R. D., 2008, Cause and evolution of intraplate orogeny in Australia: Geology, v. 36, p. 495–498.

Haack, U. K., & Zimmermann, H. D., 1996, Retrograde mineral reactions: a heat source in the continental crust?: Geologische Rundschau, v. 85, p. 130–137.

Haines, P. W., Hand, M., & Sandiford, M., 2001, Palaeozoic synorogenic sedimentation in central and northern Australia; a review of distribution and timing with implications for the evolution of intracontinental orogens: Australian Journal of Earth Sciences, v. 48, p. 911–928.

Harris, N., 2007, Channel flow and the Himalayan-Tibetan orogen: A critical review: Journal of the Geological Society, v. 164, p. 511–523.

Heidbach, O., Rajabi, M., Reiter, K., & Ziegler, M., 2016, World stress map 2016. Science, v. 277, p. 956-1.

Hollister, L. S., & Crawford, M. L., 1986, Melt-enhanced deformation: A major tectonic process: Geology, v. 14, p. 558–561.

Holford, S. P., Hillis, R. R., Hand, M. & Sandiford, M., 2011. Thermal weakening localizes intraplate deformation along the southern Australian continental margin. Earth and Planetary Science Letters, v. 305, p. 207-214.

Houseman, G., & Molnar, P., 2001, Mechanisms of lithospheric rejuvenation associated with continental orogeny: Geological Society, London, Special Publications, v. 184, p. 13–38.

Hubbert, M. K., & Rubey, W. W., 1959, Role of pore fluid pressure in the mechanics of overthrust faulting, in Mechanics of fluid-filled porous solids and its application to overthrust faulting: Geological Society of America Bulletin, v. 70, p. 115–205.

Jamieson, R.A., Unsworth, M.J., Harris, N.B., Rosenberg, C.L. & Schulmann, K., 2011, Crustal melting and the flow of mountains. Elements, v. 7, p. 253–260.

Klootwijk, C., 2013, Middle–Late Paleozoic Australia–Asia convergence and tectonic extrusion of Australia: Gondwana Research, v. 24, p. 5–54.

Kober, M., Seib, N., Kley, J., & Voigt, T., 2013. Thick-skinned thrusting in the northern Tien Shan foreland, Kazakhstan: structural inheritance and polyphase deformation. Geological Society, London, Special Publications, v. 377, p. 19-42

Lee, A. L., Torvela, T., Lloyd, G. E., & Walker, A. M. (2018). Melt organisation and strain partitioning in the lower crust. Journal of Structural Geology, v. 113, p. 188-199.

Maidment, D. W., Hand, M. & Williams, I. S., 2013. High grade metamorphism of sedimentary rocks during Palaeozoic rift basin formation in central Australia. Gondwana Research, 24(3–4), 865-885.

Marchildon, N., & Brown, M., 2003, Spatial distribution of melt-bearing structures in anatectic rocks from Southern Brittany, France: implications for melt transfer at grain-to orogen-scale: Tectonophysics, v. 364, p. 215–235.

Mawby, J., Hand, M. & Foden, J. 1999. Sm–Nd evidence for high-grade Ordovician metamorphism in the Arunta Block, central Australia. Journal of Metamorphic Geology, 17, 653-668, doi: 10.1046/j.1525-1314.1999.00224.x.

Meek, U., Piazolo, S., & Daczko, N. R., in press, The field and microstructural signatures of deformation-assisted melt transfer: insights from magmatic arc lower crust, New Zealand. Journal of Metamorphic Geology.

Mueller, R., Dyksterhuis, S., Rey, P., 2012, Australian paleo-stress fields and tectonic reactivation over the past 100 Ma. Australian Journal of Earth Sciences, v. 59, p. 13-28.

Mueller, R., Yatheesh, V., Shuhail, M., 2015, The tectonic stress field of India since the Oligocene. Gondwana Research, v. 28, p. 612-624.

Park, Y., & Means, W. D., 1996, Direct observation of deformation processes in crystal mushes. Journal of Structural Geology, v. 18, p. 847–858.

Passchier, C. W., & Trouw, R. A., 2005. Microtectonics. Springer Science & Business Media.

Piazolo, S., Bestmann, M., Prior, D.J. and Spiers, C.J., 2006. Temperature dependent grain boundary migration in deformed-then-annealed material: observations from experimentally deformed synthetic rocksalt. Tectonophysics, v. 427, p.55-71.

Prakash, A., Piazolo, S., Saha, L., Bhattacharya, A., Pal, D. K., & Sarkar, S., 2018, Deformation behavior of migmatites: insights from microstructural analysis of a garnet–

sillimanite–mullite–quartz–feldspar-bearing anatectic migmatite at Rampura–Agucha, Aravalli–Delhi Fold Belt, NW India. International Journal of Earth Sciences, v. 107, p. 2265-2292.

Putnis, A., 2009, Mineral replacement reactions: Reviews in mineralogy and geochemistry, v. 70, p. 87–124.

Quigley, M.C., Clark, D., Sandiford, M., 2010. Tectonic geomorphology of Australia. Geol. Soc. Lond. Spec. Publ. v. 346, p. 243–265

Raimondo, T., Clark, C., Hand, M., & Faure, K., 2011, Assessing the geochemical and tectonic impacts of fluid–rock interaction in mid-crustal shear zones: a case study from the intracontinental Alice Springs Orogen, central Australia: Journal of Metamorphic Geology, v. 29, p. 821–850.

Raimondo, T., Hand, M., & Collins, W. J., 2014, Compressional intracontinental orogens: Ancient and modern perspectives: Earth-Science Reviews, v. 130, p. 128–153.

Raimondo, T., Payne, J., Wade, B., Lanari, P., Clark, C., & Hand, M., 2017, Trace element mapping by LA-ICP-MS: assessing geochemical mobility in garnet: Contributions to Mineralogy and Petrology, v. 172, p. 17-38.

Rosenberg, C. L., & Handy, M. R., 2005, Experimental deformation of partially melted granite revisited: implications for the continental crust: Journal of Metamorphic Geology, v. 23, p. 19–28.

Rutter, E. H., & Neumann, D. H. K., 1995, Experimental deformation of partially molten Westerly granite under fluid-absent conditions, with implications for the extraction of granitic magmas: Journal of Geophysical Research: Solid Earth, v. 100, p. 15697-15715.

Shaw, R. D., Zeitler, P. K., McDougall, I., & Tingate, P. R., 1992, The Palaeozoic history of an unusual intracratonic thrust belt in central Australia based on 40Ar-39Ar, K-Ar and fission track dating. Journal of the Geological Society, v. 149, p. 937-954.

Sibson, R. H., 1990. Conditions for fault-valve behaviour. Geological Society, London, Special Publications, v. 54, p. 15-28.

Silva, D., Piazolo, S., Daczko, N. R., Houseman, G., Raimondo, T., & Evans, L., 2018, Intracontinental Orogeny Enhanced by Far-Field Extension and Local Weak Crust: Tectonics, v. 37, p. 4421-4443.

Stuart, C. A., Piazolo, S., & Daczko, N. R., 2016, Mass transfer in the lower crust: Evidence for incipient melt assisted flow along grain boundaries in the deep arc granulites of Fiordland, New Zealand. Geochemistry, Geophysics, Geosystems, v. 17, p. 3733–3753.

Stuart, C. A., Daczko, N. R., & Piazolo, S., 2017, Local partial melting of the lower crust triggered by hydration through melt–rock interaction: an example from Fiordland, New Zealand. Journal of Metamorphic Geology, v. 35, p. 213–230.

Stuart, C. A., Meek, U., Daczko, N. R., Piazolo, S., & Huang, J. X., 2018a, Chemical signatures of melt–rock interaction in the root of a magmatic arc. Journal of Petrology, v. 59, p. 321–340.

Stuart, C. A., Piazolo, S., & Daczko, N. R., 2018b, The recognition of former melt flux through high-strain zones. Journal of Metamorphic Geology, v. 36, p. 1049-1069.

Teall, J. J. H., 1885, The metamorphism of dolerite into hornblende schist: Quart. J. Geol. Soc. London, v. 41, p. 133–145.

Teyssier, C., 1985. A crustal thrust system in an intracratonic tectonic environment. Journal of Structural Geology, v. 7, p. 689–700.

Tommasi, A., Vauchez, A., Femandes, L. A., & Porcher, C. C., 1994, Magma-assisted strain localization in an orogen-parallel transcurrent shear zone of southern Brazil. Tectonics, v. 13, p. 421-437.

Tucker, N. M., Hand, M., & Payne, J. L., 2015, A rift-related origin for regional medium-pressure, high-temperature metamorphism: Earth and Planetary Science Letters, v. 421, p. 75–88.

Van der Molen, I., & Paterson, M. S., 1979, Experimental deformation of partially-melted granite: Contributions to Mineralogy and Petrology, v. 70, p. 299–318.

Vernon, R. H., 2011, Microstructures of melt-bearing regional metamorphic rocks: Geological Society of America Memoirs, v. 207, p. 1–11.

Watts, M.J., & Williams, G.D., 1983, Strain geometry, micro- structure and mineral chemistry in metagabbro shear zones: a study of softening mechanisms during progressive mylonitization: Journal of Structural Geology, v. 5, p. 507–517.

Weinberg, R. F., & Mark, G., 2008, Magma migration, folding, and disaggregation of migmatites in the Karakoram Shear Zone, Ladakh, NW India: Geological Society of America Bulletin, v. 120, p. 994-1009.

Zanella, A., Cobbold, P. R., & de Veslud, C. L. C., 2014. Physical modelling of chemical compaction, overpressure development, hydraulic fracturing and thrust detachments in organic-rich source rock. Marine and Petroleum Geology, v. 55, p.262-274.

Chapter 3. Intracontinental Orogeny Enhanced by Far-field Extension and Local Weak crust

David Silva[1*], Sandra Piazolo[1,2], Nathan R. Daczko[1], Gregory Houseman[2], Tom Raimondo[3,4] and Lynn Evans[5]

[1]ARC Centre of Excellence for Core to Crust Fluid Systems and GEMOC, Department of Earth and Planetary Sciences, Macquarie University, NSW 2109, Australia

[2]School of Earth and Environment, Institute of Geophysics and Tectonics, University of Leeds, Leeds, UK

[3]School of Natural and Built Environments, University of South Australia, GPO Box 2471, Adelaide, SA 5001, Australia

[4]Future Industries Institute, University of South Australia, Adelaide, South Australia, Australia

[5]School of Earth, Atmosphere and Environmental Sciences, Monash University, Clayton, Victoria, Australia

*E-mail address: david.barbosa-da-silva@hdr.mq.edu.au

Keywords: Intracontinental orogeny; numerical modelling; thin viscous sheet; stress transmission; stress accommodation

Abstract

The accommodation of intraplate stresses in preexisting weak regions of plate interiors is here investigated using thin viscous sheet numerical models. The intraplate stresses are governed by multicomponent and multidirectional stresses originating at plate boundaries. The modeled scenarios mimic plate boundary conditions during the intraplate Alice Springs Orogeny (ASO), central Australia, and include (1) a northwest-southeast zone of weak lithosphere within strong continental blocks to the north and south and (2) a principal south directed stress condition at the northern boundary that causes minor clockwise rotation of the northern block. Alternative tectonic environments are investigated in additional models that include (1) secondary compressional or extensional stresses acting at the eastern boundary, representing the temporally variable stress conditions during the Tasmanides Orogeny, and (2) an eastern wedge-shaped zone of rheologically weak lithosphere, mirroring rift fill of the Irindina sub-basin. Our results highlight that a low angle between major crustal features (e.g., orogenic elongation and preexisting regional structures) and the principal transmitted stresses is highly relevant in the concentration of elevated levels of differential stress

and subsequent localization of deformation in plate interiors. Secondary stresses orthogonal to the principal acting stresses may introduce effects that explain the episodic orogenic activity in the case of the ASO. The combination of secondary extensional stresses at the eastern boundary of Australia and weak lithosphere of the preexisting Irindina sub-basin strongly influences the observed spatial strain intensity, localization, and kinematics of deformation during the ASO.

3-1. Introduction

The theory of plate tectonics has, since its emergence in the 1960s, provided a remarkably coherent framework to explain the majority of large-scale geological features observable at the Earth's surface, including mountain belts, rift valleys, and volcanic chains. One of the cornerstones of the plate tectonics theory is the assumption that plate boundaries are the main loci of tectonic stresses that drive the formation of large-scale geological features. Accordingly, it predicts that mountain belts are formed at plate boundaries. Intracontinental compressional orogens, however, which are distinct from conventional compressional orogens by their location within plate interiors, do not follow this fundamental rule (Cunningham, 2005; Raimondo et al., 2014). In contrast, they represent major zones of strain localization associated with crustal thickening and deep exhumation of basement rocks distal from active plate boundaries (Cunningham, 2005; Hand & Sandiford, 1999; Raimondo et al., 2010; Sandiford et al., 2001). As such, understanding the underlying causes and processes enabling intracontinental orogeny is one of the remaining gaps in our knowledge of the fundamental workings of the Earth.

The Neoproterozoic Petermann and Paleozoic Alice Springs Orogens of central Australia are primary examples of ancient intracontinental orogenesis that have been extensively studied in recent years (e.g., Aitken et al., 2009; Camacho & McDougall, 2000; Hand & Sandiford, 1999; McLaren et al., 2009; Raimondo et al., 2014, and references therein). Currently, intracontinental orogenesis is recognized in several parts of the world, such as central Asia (Tien Shan and Altai Orogens; Cunningham, 2005; Molnar & Tapponnier, 1975), South America (Borborema Province; Neves, 2003; Tommasi et al., 1995), North America (Sevier-Laramide Orogen and Kapuskasing uplift; Livaccari, 1991; Marshak et al., 2000; Perry et al., 2006), Iberia (Spanish Central System; Andeweg et al., 1999), and Africa (Atlas Mountains and Damara Belt; Kröner, 1977; Ramdani, 1998; Teixell et al., 2003). Just like their plate boundary counterparts, these orogens involve crustal thickening coupled with topographic highs, exhumation of high-grade metamorphic rocks, localized melting and magmatism, and enhanced erosion feeding sediments into deep basins at the orogenic front(s).

Details of the underlying causes of intracontinental orogenesis are a matter of ongoing debate. In contrast to mountain belts developed at plate boundaries,

intracontinental orogens require a stress component locally derived in the intraplate region by deep lithospheric instabilities (e.g., upper mantle gravitational [Rayleigh-Taylor] instabilities; Gorczyk et al., 2013; Gorczyk & Vogt, 2015; Neil & Houseman, 1999; Pysklywec & Beaumont, 2004) or by transmission of horizontal forces by strong lithosphere into plate interiors (Handy & Brun, 2004; Roberts & Houseman, 2001; Shaw et al., 1991). As an example, the loci of stress production that caused orogenesis in central Australia (e.g., Peterman and Alice Springs Orogens) are debated as being driven by either proximal intraplate stress or distal plate boundary stresses (see Raimondo et al., 2014, for a comprehensive review). In the case of the Alice Springs Orogeny (ASO), the argument for transmission of plate boundary stresses is evidenced by the complementary tectonic evolution of the accretionary Tasman Orogenic System (Champion et al., 2009; Collins, 2002; Glen, 2013; Gray & Foster, 2004; Raimondo et al., 2014). While geophysical and geological data show that many intraplate regions are under compressional stress regimes originating from far-field stresses (Coblentz et al., 1998; Hurd & Zoback, 2012; Zoback et al., 1989), intracontinental orogens are surprisingly rare when compared to their peri-plate located orogen counterparts; hence, the presence of zones of mechanical weakness in plate interiors must be one of the principal requirements to allow intraplate orogenesis. The seismological impact of active intracontinental orogens is closely related to stress transmission and stress accommodation in the lithosphere (Thomas & Powell, 2017); consequently, in-depth studies of this special class of orogen are needed to better understand the relevance of plate boundary stress conditions to intracontinental orogenic activity.

In summary, one class of intracontinental orogeny requires (1) far-field stresses transmitted through relatively strong plate margins and (2) a rheologically weak plate interior. The magnitude and direction of far-field stresses are directly related to the plate boundary configuration and the efficiency of lithospheric stress transfer (e.g., Roberts & Houseman, 2001). Previous numerical models focused their simulations on some or all of the aforementioned requirements, using inherited crustal structures of contrasting competence (e.g., Braun & Shaw, 2001; Heron & Pysklywec, 2016), lithospheric buckling instabilities (e.g., Regenauer-Lieb et al., 2015), or upper mantle gravitational Rayleigh-Taylor instabilities (e.g., Gorczyk et al., 2013; Gorczyk & Vogt, 2015; Neil & Houseman, 1999) to explain the observed spatio-temporal tectonic evolution of the central Australian region. The current debate therefore focuses on the nature of the far-field stresses (orientation and magnitude through time), the transmission of these stresses from plate boundaries to plate interiors, and the localization, orientation, structural architecture, and kinematics of orogenic activity.

Klootwijk (2013) highlights that both primary collisional forces at plate boundaries (i.e., forces acting near perpendicular to orogen strike) and secondary plate boundary forces (i.e., forces contributing to the shear and normal traction acting at a low angle relative to the orogen strike) govern the character of intracontinental orogens. Proposed zones of weakness present in plate interiors include (1) old regional sutures

(Braun & Shaw, 2001; Heron et al., 2016; Sandiford & Hand, 1998); (2) thermally weakened areas due to either sedimentary blanketing of high heat-producing crust or the upwelling of hot uppermost lithospheric mantle into the lower crust (Cunningham, 2013; Sandiford & Hand, 1998; Shaw et al., 1991; Walter et al., 1995), a variant of the latter being Rayleigh-Taylor gravitational instabilities (Gorczyk et al., 2013; Gorczyk & Vogt, 2015; Neil & Houseman, 1999); (3) a preexisting network of metasomatized midcrustal shear zones (Cartwright & Buick, 1999; Raimondo et al., 2011, 2013); and (4) deep sedimentary basins (Haines et al., 2001; Klootwijk, 2013). Depending on the rheological model of the lithosphere and geothermal gradient used (Burov & Watts, 2006), increased crustal thickness may decrease the strength of the lithosphere, owing to greater resistance of mantle rocks to deformation compared to the quartzo-feldspatic crust (Kusznir & Park, 1987; Ranalli & Murphy, 1987); although, decreasing lithospheric thickness during extension can increase or decrease its strength depending on the strain rate (i.e., fast strain rate = strain softening; slow strain rate = strain hardening; Kusznir & Park, 1987).

In order to investigate the underlying causes of intracontinental orogeny, we utilize simple first-order rheological models to understand the importance of (1) the geometry of intracontinental weak zones and (2) secondary plate boundary stresses. To constrain our model setup and compare model results to a real geological scenario, we utilize data from the long-lived (450–300 Ma) ASO in central Australia (Buick et al., 2008; Haines et al., 2001; Mawby et al., 1999), situated at the center of the Australian plate. The ASO is an ideal case study because it is one of the few intracontinental orogens that is now deeply exhumed, with midcrustal to lower crustal rocks exposed over several hundred kilometers of outcrop (Figure 1). Furthermore, the ASO has a strongly episodic pattern of orogenic activity that is difficult to reconcile with current models of its formation (Raimondo et al., 2014).

We present results from numerical modeling extending the previous model of Roberts & Houseman (2001) that implemented far-field compressional stresses transmitted from the northern plate boundary to induce crustal thickening in a broad preexisting weak zone at the plate center. In contrast to this existing model that allowed a free secondary boundary to the east, our model adds another layer of complexity with either (1) compressional or (2) extensional stresses along the eastern boundary. Furthermore, we explore not only the effect of a pronounced preexisting weak zone oriented NW-SE that follows the pre-ASO Larapinta Rift (Klootwijk, 2013; Maidment, 2005) but also the existence of an eastern weak wedge. The latter is inspired by the recent recognition of an asymmetric bivergent sub-basin rift represented by the ~35-km deep Harts Range Group (HRG) of the Irindina Province (Maidment, 2005; Tucker et al., 2015).

In the following, we first present a summary of the geological characteristics of the ASO, including the configuration of the Australian plate during the Paleozoic and the timing of plate movement, magmatism, metamorphism, deformation, and synorogenic

sedimentation. This is followed by the general model setup, description of the models tested, and model analysis where numerical results are presented and discussed in the light of features specific to the ASO and to intracontinental orogenesis in general.

3-2. The paleozoic ASO: a deeply exhumed example of intracontinental mountain building

3-2.1. General geological background and structural architecture

The ASO was a long-lived intracontinental mountain building event during the Ordovician to Carboniferous (450–300 Ma; Collins & Teyssier, 1989; Hand & Sandiford, 1999; Mawby et al., 1999). It is expressed in the Arunta Region of central Australia as a roughly E-W trending, ~700-km-long orogenic belt (Figure 1) characterized by an extensive regional network of anastomosing shear zones and thrust faults (Ballèvre et al., 2000; Cartwright et al., 1999; Raimondo et al., 2011, 2014). The width of the orogen varies from ~300 km in the west to ~80 km in the east. The eastern Alice Springs Orogen is characterized by crustal thickening and deep exhumation of ensialic granulitic basement rocks (Figure 1b), which from W to E are roughly constituted by the midcrustal Reynolds-Anmatjira Ranges, the midcrustal to deep-crustal Strangways Range and the deep-crustal Harts Range. The grade of metamorphism and pervasiveness of fluid hydration/retrogression of the granulitic basement increases from 5–6 kbar and 500–600 °C in northwest (Reynolds-Anmatjira Ranges; Raimondo et al., 2011) to 10.5 kbar and 880 °C in the southeast (Harts Range; Mawby et al., 1999; Tucker et al., 2015).

The Reynolds-Anmatjira Ranges represent part of a tilted crustal-scale pop-up structure with the axial zone exhuming midcrustal granulites (Collins & Teyssier, 1989; Figures 1b and 1c). Discrete ASO-aged shear zones, up to 300 m wide, trend NW-SE and truncate Proterozoic folds and metamorphic fabrics (Cartwright & Buick, 1999; Collins & Teyssier, 1989; Raimondo et al., 2011). They exhibit north and south dipping foliations with dip-slip stretching lineations and a reverse sense of motion.

The Strangways Range represents a broad belt of granulite-facies basement up to ~125 km wide, formed as a consequence of the approximately 1,730-Ma Strangways Orogeny (Figures 1b and 1c). Multiple kilometer-scale shear zones dissect the terrane; these were reactivated during the ASO and include the West Bore and Gough Dam shear zones along its northern boundary and the Harry Creek Shear Zone at its southern boundary (Figure 1b). Together, the shear zones form a network of steeply dipping amphibolite- to greenschist-facies schist belts with south directed thrusting (Bendall, 2000; Ballèvre et al., 2000; Collins & Teyssier, 1989). The increase in shear zone width from the Reynolds-Anmatjira Ranges to the Strangways Range reflects a progressively deeper level of denudation (Raimondo et al., 2014).

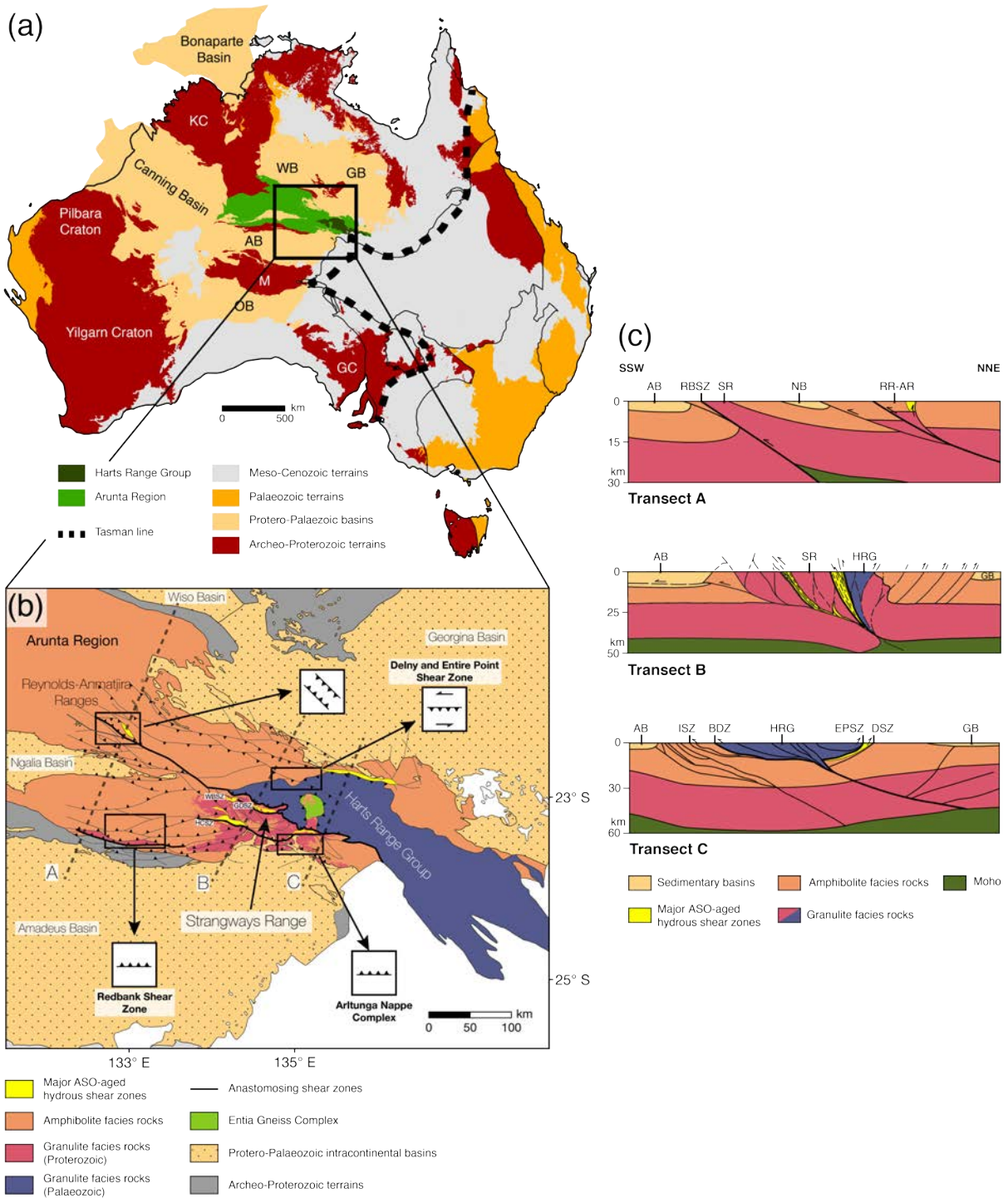

Figure 1. Geologic characteristics of the Alice Springs Orogeny and its regional context. (a): Generalized geologic map of the Australian continent, showing the major tectonic subdivisions, the location of the Arunta Region, and position of Transects A–C (modified after Raimondo et al., 2014). (b): Regional geologic map of the SE Arunta Region, emphasizing the distribution of granulite and amphibolite facies basement rocks and the location of the Reynolds-Anmatjira Ranges, Strangways Range, and the Harts Range in relation to major faults and hydrous shear zones (modified after Ballèvre et al., 2000; Collins & Teyssier, 1989; Maidment, 2005; Raimondo et al., 2011; Scrimgeour, 2013). (c): Simplified structural cross sections from Transect A (modified after Raimondo et al., 2014), Transect B (modified after Ballèvre et al., 2000; Collins & Teyssier, 1989), and Transect C (modified after Maidment et al., 2013), showing the differential exhumation patterns and structural architecture along strike of the Alice Springs Orogen. Abbreviations: AB, Amadeus Basin; AR, Anmatjira Range; BDZ, Bruna Detachment Zone; DSZ, Delny Shear Zone; EPSZ, Entire Point Shear Zone; GB, Georgina Basin; GC, Gawler Craton; GDSZ, Gough Dam Shear Zone; HCSZ, Harry Creek Shear Zone; HRG, Harts Range Group; ISZ, Illogwa Shear Zone; KC, Kimberley Craton; M, Musgrave Province; NB, Ngalia Basin; OB, Officer Basin; RBSZ, Redbank Shear Zone; RR, Reynolds Range; SR, Strangways Range; WBSZ, West Bore Shear Zone; WB, Wiso Basin.

The Harts Range is dominated by exposures of the HRG, a thick package of metabasic and amphibolite to granulite facies metasedimentary rocks contained in a roughly wedge-shaped area with a maximum width of ~150 km (Buick et al., 2005; Hand et al., 1999; Mawby et al., 1999; Figures 1b and 1c). Protoliths to the HRG were deposited in the Irindina sub-basin, an asymmetrical bivergent rift formed toward the eastern plate margin during the approximately 520-Ma Stanovos Event. This rift is situated at the SE extremity of the Late Ordovician Larapinta seaway, an extensional corridor that cut diagonally across the Australian continent. The seaway connected the depositional system of central Australia with the Canning Basin at the NW continental margin (Hand et al., 1999; Webby, 1978). It coincides with a continental-scale magnetic lineament suggesting a deep-seated structural discontinuity (Maidment, 2005; Myers et al., 1996; Shaw et al., 1995). The HRG was metamorphosed to granulite facies during the extensional Larapinta Event (480–460 Ma), as a consequence of high heat flow, mafic magmatism, and extremely deep burial to maximum depths of 30–35 km (Buick et al., 2001, 2005; Maidment, 2005; Maidment et al., 2013; Tucker et al., 2015). The western sector of the HRG is mostly constituted by the Irindina Gneiss, exhumed from 20- to 25-km depth during the ASO, and mafic Meta-Igneous Complex intrusive rocks (emplacement at approximately 520 Ma; Maidment et al., 2013; Tucker et al., 2015).

From detailed structural mapping, Teyssier (1985) estimated that compression during the ASO resulted in shortening of up to 100 km in the eastern Arunta Region. The northern Arunta Region is characterized by dominantly coaxial deformation with upright and symmetrical reverse faults (Figures 1b and 1c). This coaxial movement is most pronounced in the NW sector, while a change to a noncoaxial sinistral kinematic regime is seen in the NE sector (Collins & Teyssier, 1989; Weisheit et al., 2016). Two of the most significant tectonic discontinuities are the Redbank Shear Zone and the Arltunga Nappe Complex. The Redbank Shear Zone consists of an ~400-km-long E-W trending zone of up to 10-km width. Thrust reactivation of this preexisting structure occurred at 450–420 Ma, displacing the Moho by up to 25 km (Biermeier et al., 2003; Wright et al., 1990). The Arltunga Nappe Complex separates the HRG from the underlying granulite facies rocks of the Strangways Range (Collins & Shaw, 1995; Figures 1b and 1c). The nappes extend E-W for ~100 km and probably involved piggyback imbrication on a regional scale, with significant crustal thickening of ~10 km constrained by K- feldspar, mica, and amphibole thermochronology (Dunlap et al., 1995).

3-2.2. Timing of tectonic evolution: ASO and surrounding tectonic regions

In the following section, we summarize the main tectonic activity during the ASO (450–300 Ma; Figure 2) and place this activity in the context of coeval events within or at the margin of the Australian plate.

During the Ordovician-Carboniferous, the Australian plate was positioned within NE Gondwana. It was connected to the Antarctic and Indian plates to the south and

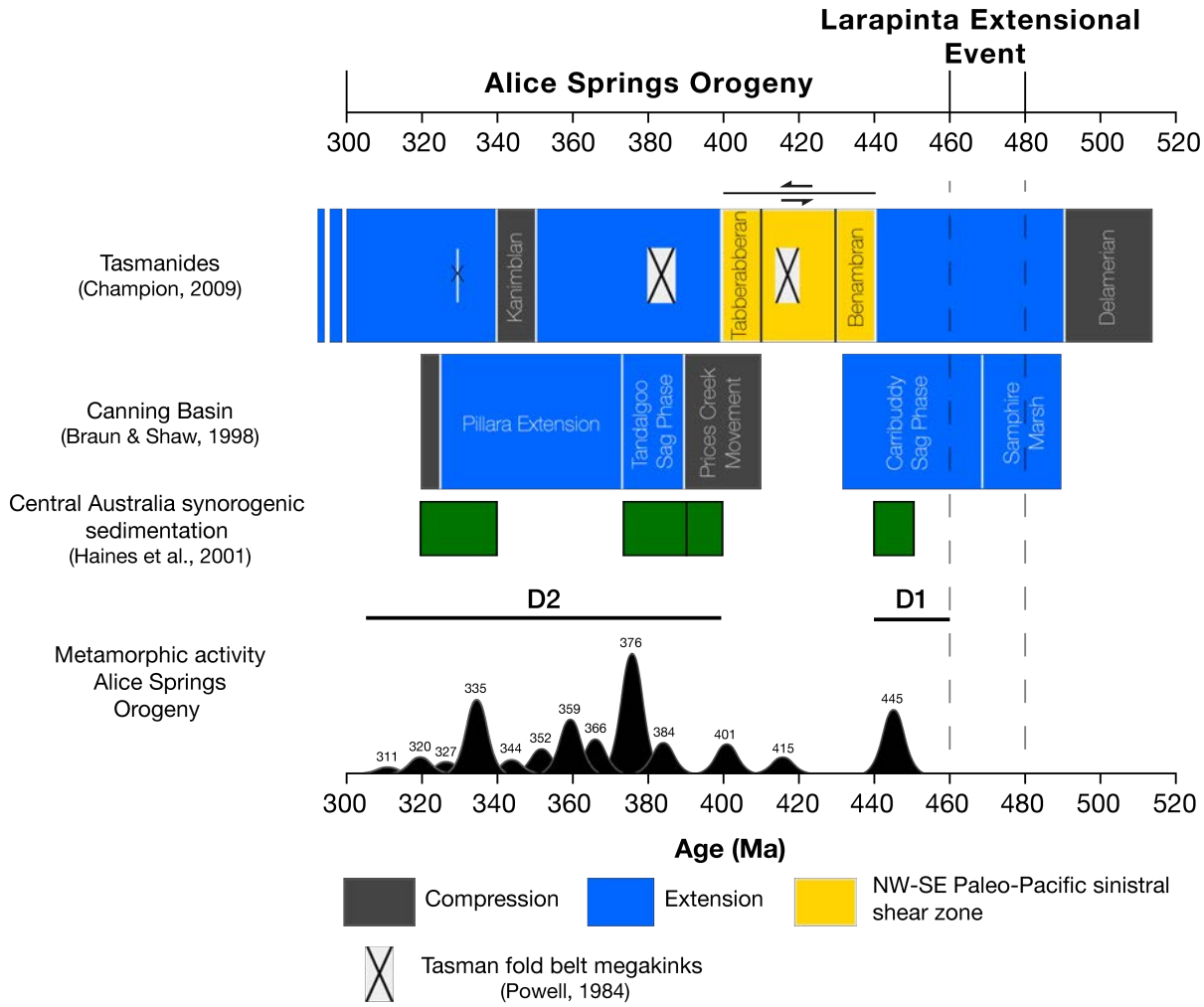

Figure 2. Sequential age comparison between metamorphic activity during the Alice Springs Orogeny (Gaussian deconvolution of frequency probability histogram; modified after Raimondo et al., 2014; Table S1) with the sequential Tasman Orogenic Belt (Tasmanides; Champion et al., 2009; Glen, 2013; Powell, 1984), the Canning Basin (Braun & Shaw, 1998), and the sedimentary record observed in synorogenic basins surrounding the Arunta Region (Haines et al., 2001). The timing of NW-SE sinistral shear between the Australian-Antarctic and Paleo-Pacific plates described by Gray & Foster (2004) is also shown (reconstruction in Figure 3a).

southwest, bounded to the north by the North China Block, and to the east by the Tasmanides and a subduction zone involving westward subduction of the Pacific plate (Klootwijk, 2010; Figure 3a). The Tasmanides of eastern Australia show an early history (approximately 530 Ma) of westward advancing accretionary orogenesis, followed by ~2,000 km of eastward rollback migration of the subduction system, accompanied by back-arc extension and interspersed with Mid- to Late Paleozoic periods of advancing compressional orogenesis (Collins, 2002; Cawood et al., 2009; Champion et al., 2009; Glen, 2013; Figure 2).

The ASO immediately follows a pronounced extensional event at 480–460 Ma (the Larapinta Extensional Event; Buick et al., 2001, 2005), characterized by the opening of the Larapinta Rift and the deposition of protoliths to the HRG (Maidment et al., 2013). Inversion of the rift and compressional tectonics of the ASO initiated at approximately 450 Ma, with metamorphism first recognized at approximately 445 Ma (D1 period; Figure 2) and highly localized south directed reactivation of the Proterozoic

Redbank Shear Zone at approximately 420 Ma (Biermeier et al., 2003; Figure 1b). This early activity in the ASO was contemporaneous with (1) extension and opening of the Canning Basin, Western Australia (Romine et al., 1994), and (2) collision between the Laurasian and Australian plates that began the Qinling Orogeny (Klootwijk, 2013; Meng & Zhang, 2000). At the same time, sediments were deposited in several large basins inside and outside the Arunta Region, including the Amadeus, Georgina, Wiso, and Ngalia Basins (Haines et al., 2001; Figures 1a and 1b).

A period of relative quiescence in the ASO persisted from 440–400 Ma. However, in the east, the Tasmanides experienced active E-W compression (the Benambran Orogeny at approximately 440 Ma and the Tabberabberan Orogeny at approximately 410 Ma; Champion et al., 2009), combined with N-S compression that formed the Tasman fold belt mega-kinks (i.e., a sharp change in tectonic grain orientation dated at approximately 415 Ma; Powell, 1984). During this time, NW-SE sinistral shear was active offshore the NE boundary between the Australian and Pacific plates (Gray & Foster, 2004; Figure 3a). The end of this period (approximately 400 Ma) corresponds with the renewal of metamorphism and sediment deposition in the ASO (Haines et al., 2001).

The second major period of metamorphism during the ASO (D2 from 390 to 320 Ma; Figure 2) was coeval with renewed opening of the Canning Basin (the 373-Ma Pillara Extension; Romine et al., 1994) and the adjacent Bonaparte Basin (Mory & Beere, 1988; Figure 1a). Near the beginning of this period (approximately 370 Ma), the principal compressive stress directions in the ASO shifted from N-S to NNE-SSW. This change was due to displacement of the Euler rotational axes in the Gondwana and Laurussia supercontinents (Kröner et al., 2016). Metamorphism and deformation across the ASO are reduced for the period 360– 340 Ma but spikes again with extensive sedimentation at approximately 340 Ma. After approximately 320 Ma, orogenic activity decreased in the ASO at the same time that the configuration of Gondwana and boundary stresses on the Australian plate significantly changed, possibly due to the shift of the paleo-longitudinal apparent northward wander path (i.e., continental drift) to the south of the Gondwana plate (Klootwijk, 2013).

3-2.3. Current models for the formation of the ASO

Discussion of the Paleozoic tectonics of the Australian continent is largely focused on the compressive N-S stresses responsible for intracontinental orogenesis, with authors rarely discussing the significance of westward paleo-Pacific subduction as one of the tectonic stress actuators for central Australia crustal deformation (e.g., Gray et al., 2004). This is primarily because an ~2,000-km distant westward subduction driver leading to a westward compressional momentum is at odds with the observed E-W structural architecture of the ASO (Figure 3a). Thus, the westward tectonic stress influences on central Australia orogenesis have largely been ignored. Studies by Roberts & Houseman (2001), Klootwijk (2013), and Kröner et al. (2016) correlate

intra-plate reactivation of central Australia with the mainly N-S convergence between Gondwana and Laurasia, forming the Qinling Orogen in the north (Figure 3a). Using numerical models, Roberts & Houseman (2001) showed that rotation of the north Australian block induced simultaneous extension of the Canning Basin in NW Australia and N-S convergence within an area of lithospheric weakness in central Australia. In this scenario, however, heterogeneous deformation within the ASO and the periods of compression and tectonic quiescence remain unexplained. Subsequently, Raimondo et al. (2014) focused attention on the episodic nature of the ASO, suggesting a causal link between ASO activity and periods of alternating E-W compression and extension related to subduction rollback affecting the Tasmanides. In both models, the zone of weakness in the center of the Australian plate is the Ordovician Larapinta seaway.

In the following simulations, we use numerical thin viscous sheet models to test (1) the effect of N-S compression on the deformation pattern within and around a single NW-SE trending weak zone, (2) the effect of the addition of an eastern weak wedge on that deformation pattern, and (3) the effect of compressional or extensional forces at the eastern boundary. With these models, we aim to reconcile the agreed and controversial features identified above (section 2). Our models build upon those performed by Roberts & Houseman (2001) by adding extra complexity, testing the hypothesis that the Tasmanides, as well as the weak crustal wedge comprising the HRG metasedimentary rocks, both played significant roles that influenced the timing and local kinematics of the ASO.

3-3. Numerical implementations

3-3.1. Necessary model components

To simplify modeling of the large-scale effects associated with intracontinental orogeny at midcrustal to lower crustal levels, it is necessary to model behavior at the lithospheric scale with emphasis on the dominant ductile deformation active at shallower crustal depths. In addition, the following ingredients are necessary to perform the tests outlined above:

1 - A regional-scale zone of weakness where strain is accommodated to form the intraplate orogen. This zone needs to be embedded in a relatively stiff continental plate that transmits plate boundary stresses. For the ASO, the proposed zone of weakness is the NW-SE-oriented Larapinta seaway (Maidment et al., 2005) and its sedimentary infill, now largely incorporated into the ASO.

2 - A localized zone of weakness that corresponds to the deep pre-ASO rift basin represented by the Harts Range Group (Maidment, 2005, 2013; Tucker et al., 2015).

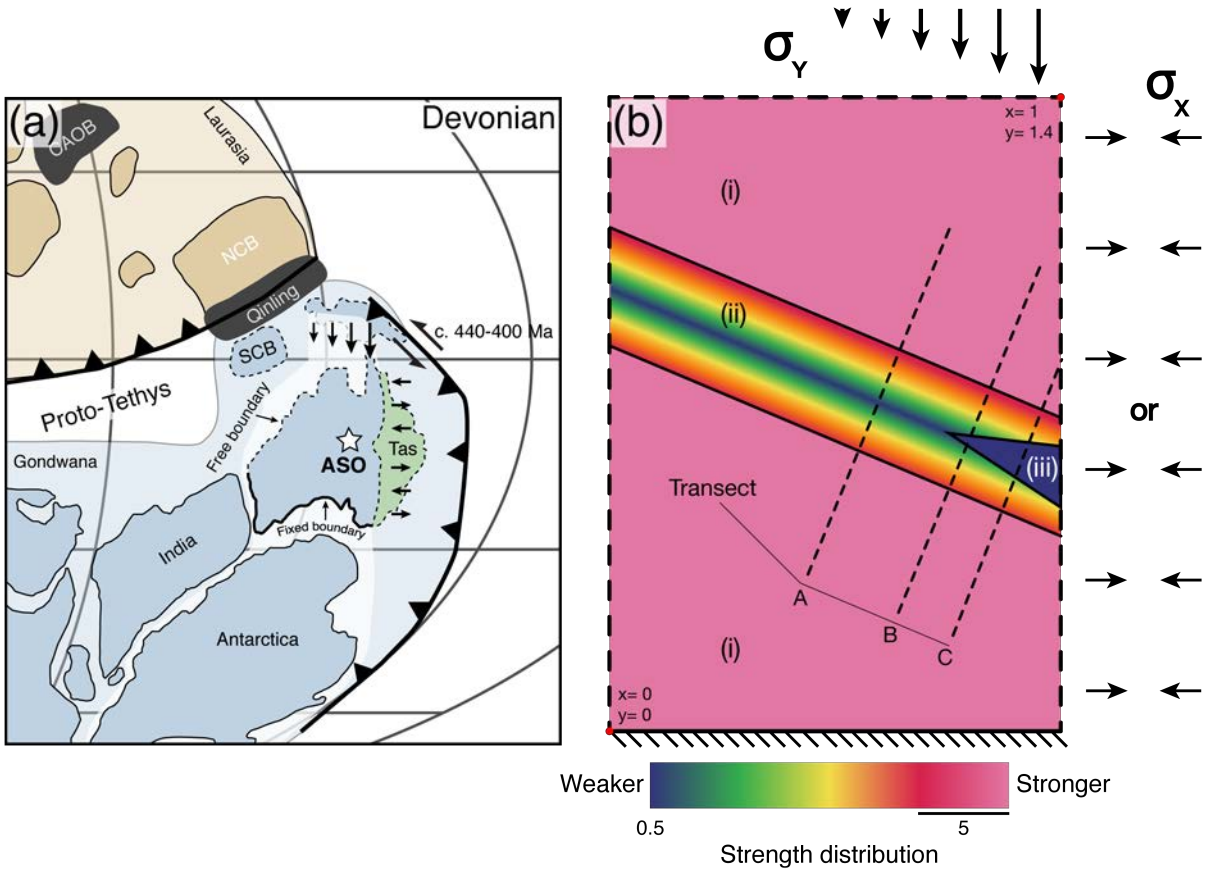

Figure 3. (a): Middle Devonian palaeogeographic reconstruction of the eastern collision between supercontinents Gondwana and Laurussia (future Laurasia; modified after Kröner et al., 2016). Palaeolatitudes are based on the palaeo- magnetic model of Klootwijk (2010). Direction of the active stresses on the margin of the Australian continent is repre- sented based on the aforementioned palaeogeographic reconstruction, the central Australian Alice Springs Orogeny (ASO), and the eastern Australian sequential Tasmanides (see Figure 2). Abbreviations: CAOB, Central Asia Orogenic Belt; NCB, North China Block; SCB, South China Block; Tas, Tasmanides. (b): Geometry of the numerical model, showing the active forces later applied in different simulation sets, and the geometry and strength distribution for each block inserted into the model (see explanatory details in section 3); (i) northern and southern strong blocks, (ii) diagonal weak band showing strength gradient from a relatively strong edge to weak center, and (iii) eastern weak wedge located within the weak band.

3 - Plate boundary conditions that allow the effects of different boundary stresses to be tested. These should include:

(a) A fixed plate boundary to the south to represent the southern part of the Australian continent being stationary in a Gondwana-fixed reference frame;

(b) A northern boundary with N-S compressional stresses and a rotational component that simulates the effect of the Canning Basin opening coupled with N-S collisional forces in the north;

(c) An eastern boundary that may be either tectonically passive, compressional or extensional to model the Tasmanides' variable tectonic character through time.

3-3.2. General numerical model setup: rheological flow laws, model geometry, and boundary conditions

3-.3.2.1. General model used and rheological flow laws

Here we use the nonlinear viscous finite element code BASIL (Barr & Houseman, 1996; Houseman et al., 2008), which allows monitoring of stress, strain, vorticity, and tectonic activity in the form of overthickening of the lithosphere. The continental lithosphere is represented by a thin viscous sheet layer, which deforms coherently. Deformation of the lithosphere is, in response to the deviatoric stress, determined by a nonlinear power law rheology (England & McKenzie, 1982):

$$\bar{\tau}_{ij} = B\dot{E}^{\left(\frac{1}{n}-1\right)}\dot{\varepsilon}_{ij} \tag{1}$$

where $\bar{\tau}_{ij}$ and $\dot{\varepsilon}_{ij}$ are the vertically averaged components of the deviatoric stress and strain rate tensors, respectively; n is a constant referred to as the rheological exponent that determines the degree of nonlinearity; and $\dot{E}$ is the second invariant of the deviatoric stress tensor. B is a rheological constant that includes the dependence of the vertically averaged viscosity of the lithosphere (England & McKenzie, 1982). The distribution and value of the parameter B (i.e., viscosity prefactor) can be spatially variable within the horizontal plane (x, y) to allow for investigation of the effect of a heterogeneous strength distribution in the lithosphere (i.e., values of 5 to 0.5). For the models presented in this contribution, n = 3 is used for the rheological exponent to represent the vertically averaged rheology of the lithosphere dominated by the power law creep of olivine (Karato et al., 1986).

The velocity distribution in the numerical model is used to determine the rate of crustal thickening in terms of the vertical strain rate at each (x, y) location:

$$\frac{1}{S}\frac{\partial S}{\partial t} = \left(\frac{\partial u}{\partial x} + \frac{\partial v}{\partial y}\right) \tag{2}$$

Equation (2) computes the crustal thickness distribution during lithospheric deformation. S is crustal thickness normalized by the length scale. Erosion is not included, so crustal volume is conserved. The relative vorticity vector, perpendicular to the plane of calculation, is also obtained from the horizontal velocity field (u,v):

$$\zeta = \frac{\partial v}{\partial x} - \frac{\partial u}{\partial y} \tag{3}$$

3-.3.2.2. Model geometry

The base geometry of the model has been chosen to be a thin viscous sheet with a ratio width (X)/length (Y) of 1:1.4, representative of the rough geometry of the Australian

plate for this part of Gondwana at the time of ASO formation (Figure 3b). Distance in X corresponds to separation between the western (Canning Basin) and eastern limits of the Larapinta seaway (~1,700 km); distance in Y equals the N-S extent of the North and South Australian Cratons (~2,400 km). We assume a nominal lithospheric thickness representing Z = 100 km. Within the model, a preexisting zone of weakness is defined. It is represented by a lateral variation of the viscosity coefficient within a NW-SE band. In this zone of 450- to 600-km width, the viscosity is greater in the northern and southern parts of the lithospheric sheet but decreases perpendicular to the boundaries to a minimum in the middle of the weak region. In either side of the zone of weakness are located lithospheric blocks of uniform high viscosity. To test the influence of a wedge of extreme weakness to the east, a low-viscosity wedge-shaped block in the eastern extremity of the weak region is incorporated in some models (Figure 3b).

One of the imposed features of the model is that boundaries to the zone(s) of weakness are oriented obliquely to the boundary tractions. Therefore, the model behavior will differ in the *x* and *y* direction. To capture this behavior, results are presented both as XY maps showing the spatial variations but also as transects oriented perpendicular to the structural grain, that is, perpendicular to the weak zone boundary (Figure 3b). Three transects are presented: Transect A cuts the center of the model; Transect B is the same length as Transect A, but displaced 0.77 model units (i.e., ~1,300 km) to the east; and Transect C is close to the eastern boundary of the model (0.6 model units in length). When compared to the ASO, Transects A–C roughly represent N-S profiles through the Reynolds-Anmatjira Ranges, Strangways Range, and Harts Range, respectively (Figures 1 and 3b).

3-.3.2.3. Boundary conditions and simulation setup

The southern boundary (*y* = 0; tick-marked lower boundary in Figure 3b) is fixed with a velocity in *X* and *Y* set to 0 (*u* = 0, *v* = 0). The other boundaries (western: *x* = 0; eastern: *x* = 1; northern: *y* = 1.4; dashed external boundaries in Figure 3b) can all move in response to applied traction, positive or negative, normal or shear. For a model run, boundary forces are imposed on the model. To obtain the desired clockwise rotation of the northern block of the model, a south directed dimensionless stress is applied to the northern boundary (Figure 3b), varying linearly from x = 0.5 to x = 1, with a dimensionless magnitude of σ_y = 0 at *x* = |0.0–0.5|to σ_y = 1 at *x* = 1.0. In order to test the hypothesis that stresses applied to the eastern boundary (*x* = 1; Figure 3b) can influence the intraplate style and periodicity of deformation, two different approaches were used:

1 - A lithostatic-stress boundary condition (Houseman & England, 1993) was imposed on all models for the western, eastern and northern boundaries, where no positive or negative traction is imposed on the boundary. This lithostatic boundary condition assumes that the normal stress is constant and equal to the initial confining stress, and presents zero tangential shear stress along the boundary. It allows the

modelling of a weak external region and consequent free displacement of the boundary during the simulation; in the following, we call this condition *passive.*

2 - On selected models, east- ($-\sigma_x$) or west- (σ_x) directed stresses were imposed on the total length of the eastern boundary (y = 0 to y = 1.4; Figure 3b). When active, the eastern boundary shows an applied dimensionless stress magnitude of 0.15, both for σ_x and $-\sigma_x$.

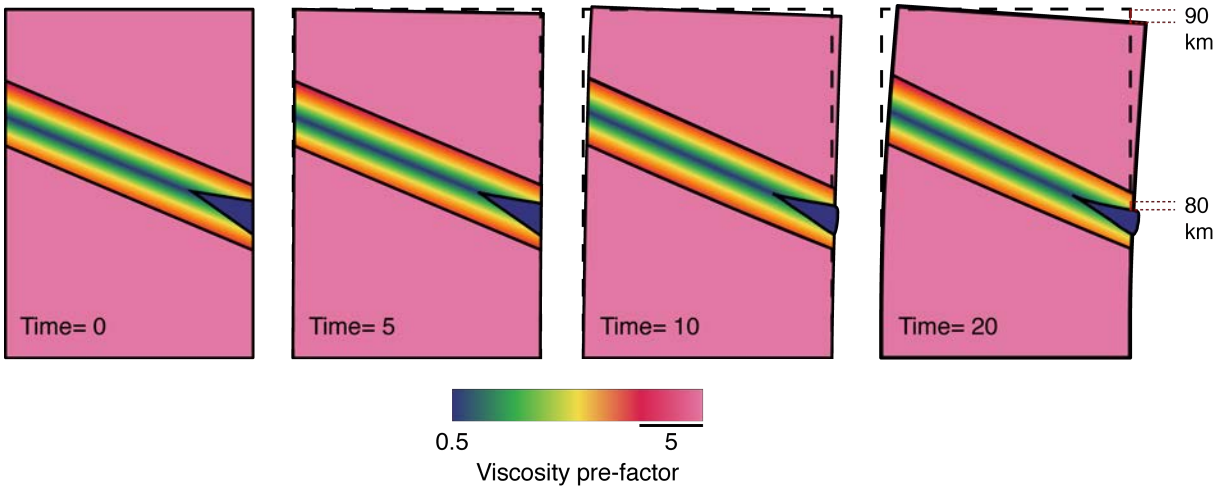

Figure 4. Example of the evolution of the model with (dimensionless) time; here, deformation of model M4b is presented for time 0, 5, 10, and 20. Displacement of the northern model boundary and northern weak wedge boundary in model units converted to kilometers are displayed.

All models are run using 20 dimensionless simulation time units (Figure 4). The running time of the experiment was selected in order to produce a specific amount of southern dislocation of the modeled northern boundary (corresponding in model units to ~100 km; Figure 4), for the model that best fits the observed geology of central Australia (Model M4b).

3-3.3. Models tested

In our study, six models are used to perform our thin viscous sheet modeling. These have been chosen to test the causal relationships between (1) the velocity boundary conditions at the northern and eastern boundaries of the model, that is, whether the eastern boundary is passive or undergoing active compression or extension, and (2)

Models	Weak zone band	Weak zone wedge	Principal stress regime	Secondary stress regime
M1	X		N-S compression	N/A
M2	X	X		N/A
M3a	X			E-W compression
M3b	X			E-W extension
M4a	X	X		E-W compression
M4b	X	X		E-W extension

N= North; S= South; E= East; W= West

Table 1. Summary of simulation sets for the numerical model, providing the individual parameters of stress activity and added block geometry.

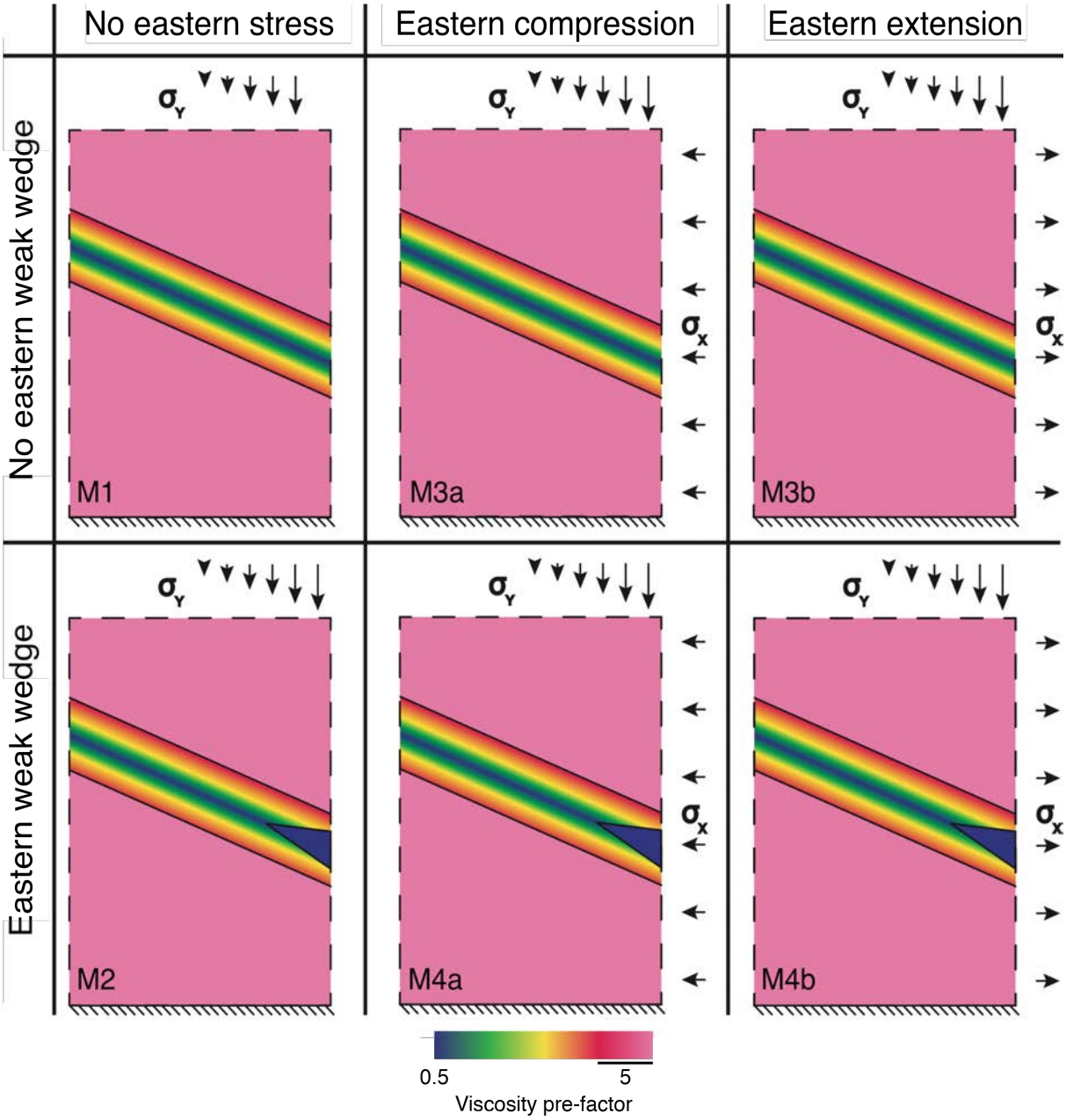

Figure 5. Geometry used in the numerical models. All models present active and equal value of south-directed principal stresses. The top row presents the models with no added weak wedge (M1, M3a, and M3b). The bottom row shows the models with the added weak wedge (M2, M4a, and M4b). The left column displays the models presenting no applied secondary eastern stress (M1 and M2). The middle column shows the models with the added secondary eastern stress- compressional (M3a and M4a). The right column presents the models with the added secondary eastern stress-extensional (M3b and M4b).

the presence or absence of an extremely weak wedge at the eastern end of the weak band (Table 1 and Figure 5).

In all models, a south directed stress is applied to the northern boundary throughout the simulation, while the western boundary is passive. For Models M1 and M2, the eastern boundary is also passive. In contrast, for Models M3a/M4a and M3b/M4b, compressional (west directed) and extensional (east directed) tractions are applied along the eastern boundary, respectively (Table 1 and Figure 5).

All models have two blocks in the northern and southern regions with relatively high-viscosity prefactors of 5 (equation (1)) representing ~80% of the whole model.

These blocks are separated by a weak band with the viscosity prefactor changing gradually perpendicular to the weak band edges, following a logarithmic sinusoidal function where the viscosity prefactor is 5 at the block-weak zone edge and 1 (equation (1)) in the center of the band. Models are presented with increasing complexity. The differentiator between models is the presence (Models M1, M3a, and M3b) or absence (Models M2, M4a, and M4b) of the extremely weak wedge with a viscosity prefactor of 0.5 (equation (1); Table 1 and Figure 5).

3-3.4. Models results and analysis

In thin viscous sheet calculations, there is an implicit assumption that the plane of the calculation is horizontal. Therefore, the relative vorticity is a measure of horizontal local spin, where it is defined that a positive or negative vorticity signifies crustal material flow rotating counterclockwise or clockwise, respectively.

The faulting style expected in a surficial brittle layer that coherently deforms with the viscous lithospheric sheet is quantified. The diagonalized strain rate tensor is decomposed at any point of the solution domain into a pair of double couples, following the method of Houseman & England (1986):

$$p = \left(\frac{3}{4} + \frac{1}{\pi}\ \tan^{-1}\left(\frac{\dot{\varepsilon}_2}{\dot{\varepsilon}_1}\right)\right) \tag{4}$$

The contour quantity between 0 and 1 indicates the expected type of deformation (i.e., style of near-surface faulting) as follows: thrust only ($0 < p < 0.25$), thrust + strike-slip ($0.25 < p < 0.5$), strike-slip only ($p = 0.50$), normal + strike-slip ($0.5 < p < 0.75$), or normal only ($0.75 < p < 1$). The p quantity can thus exhibit the magnitudes of dip-slip and strike-slip deformation. In the range $0.375 < p < 0.625$, the strike-slip deformation rate exceeds the dip-slip deformation.

Model results for the total 20 simulations dimensionless time condition are shown as *XY* maps where only the area containing the weak band and wedge is visualized. In Figures 6 and 7, we present maps of (a) crustal vertical variation, (b) relative vorticity with velocity field vectors, and (c) type of deformation (i.e., style of near-surface faulting).

3-4. The effect of boundary conditions on intracontinental orogenesis: results from numerical modeling

3-4.1. Simulations sets

3-.4.1.1. Model M1: North compression only

Model M1 shows only minor displacement of the N, E, and W boundaries, all of them displaying a small rotational motion in map view (Figures 6 and Supplement 1 (S1) to S3). An incipient protrusion of material toward the east is visible on the eastern boundary close to the central sector of the weak band (Figure 6).

There is significant crustal thickening in the eastern convergent zone and crustal thinning in the western extensional zone, with an overall position and direction following the central E–W weak band from end to end (Figure 6a). All the transects show a crustal thickness distribution that is similar to a Gaussian profile, with minimum thickening at both edges of the transect, and a maximum thickness of 0.53, 0.55, and 0.56 localized in the central sector of the weak band for Transects A–C, respectively (Figure 8a).

The vorticity distribution (Figure 6b) follows a similar pattern to crustal thickness, where the highest values of clockwise vorticity are seen in the center of the weak zone, with increasing values toward the eastern convergent sector. A small area near the eastern boundary, above the higher values and concentration of clockwise vorticity, shows a minor counterclockwise rotation. This pattern is confirmed by the vorticity transects (Figure 8b).

The distribution of the type of deformation (Figure 6c) shows a dichotomy of faulting between the W and E sector. The western sector exhibits primarily normal faulting, whereas the eastern sector presents thrust faults with strike-slip dominating in a transition zone. The northern half of the weak zone displays an area dominated by simple shear and a small amount of compression. Most of the weak band sector and southern area is dominated by thrust and subordinate shear, shifting to an enclaved area of thrust-only faulting in the center. Across the transects, from SW to NE, the faulting style changes from barely dominant shear faulting with subordinate thrusting, to a thrust-dominated area within the weak band for Transects B and C, to a thrust-only area in Transect A, inverting again for all transects toward a shear-dominated area in the northern part of the weak band (Figure 8c). A higher rate of change for the style of deformation is observed from a thrust-dominated region (SW) for Transects B and C to a shear-dominated region (NE), compared to a similar style of deformation change observed for Transect A (in this case from a thrust-only region in the SW).

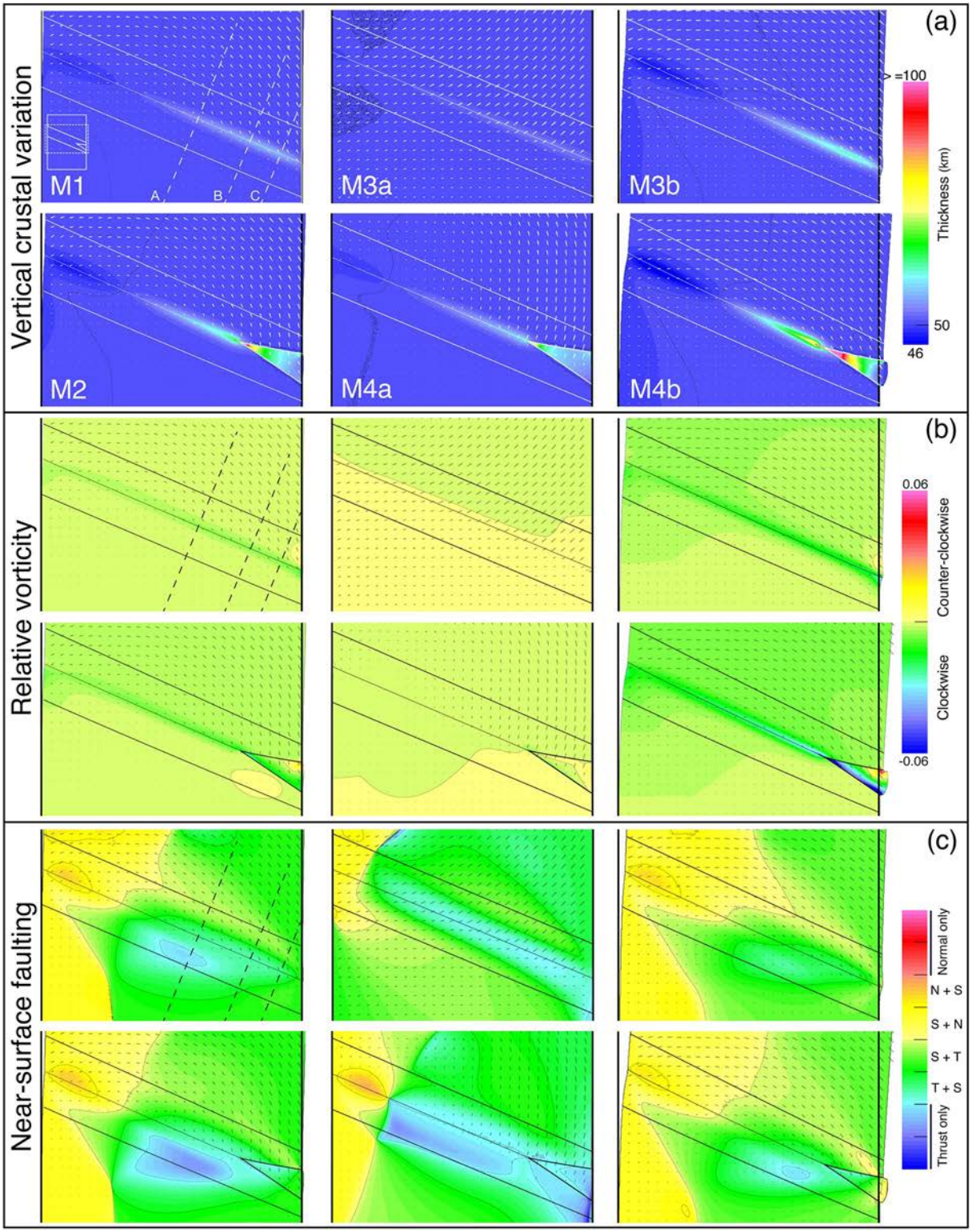

Figure 6. Snapshot at the final simulation dimensionless time 20 for (a) crustal vertical variation, (b) relative vorticity, and (c) near-surface faulting. The figures only display the area containing the weak band for each model, due to most of the relevant deformation observed being concentrated in this region. Transects A–C are displayed in Model M1.

3-.4.1.2. *Model M2: North compression + Eastern weak wedge*

Compared to Model M1, Model M2 exhibits a slightly higher displacement and rotational motion of the northern block, with a slightly enlarged protrusion along the eastern boundary (Figure 6 and S1 to S2). Crustal thicknesses are higher compared to M1,

especially in proximity to the pointed end of the wedge shape and within the eastern area of the weak wedge (Figure 6a). Inside the wedge, crustal thickness decreases from the western boundary to no thickening at the eastern boundary. Transect A (Figure 8a) shows a pattern of crustal thickness variation from time=0 almost identical to M1, except for the absolute thicknesses. In contrast, Transects B and C (Figure 8a) exhibit an abrupt increase in crustal thickness. For Transect B, comparing M1 (weak wedge absent) to M2 (weak wedge present), there is a significant contrast between the second lowest maximum crustal thickening for all simulations (M1) and the highest maximum crustal thickening for all simulations (M2) at approximately the same locale in the model.

A region of clockwise vorticity approximately follows the central region of the weak band (Figure 6b), the intensity of which is higher compared to M1, with the highest vorticity value close to the pointed end of the weak wedge. Within the wedge, two areas of distinct vorticity values are visible. To the south of the weak wedge, a circular area with diminished vorticity values is observable. Transect A follows the same pattern of vorticity seen in M1, only diverging with some higher absolute values (Figure 8b). Transect B shows abrupt increases in clockwise vorticity within the weak wedge, a change that is not observed in M1 without the wedge (Figure 8b). The same pattern observed for Transect B occurs for Transect C, however, instead of an abrupt increase of clockwise vorticity after crossing the northern boundary of the weak wedge, the vorticity builds in intensity toward its southern boundary, before decreasing almost instantaneously to 0 (Figure 8b).

The distribution and type of deformation are similar to M1, with the western sector showing normal faulting, whereas the eastern sector exhibits thrust-related faults (Figure 6c). Two areas show thrust-only faulting: one at the western edge of the weak wedge and a much smaller region external to the SW corner of the weak wedge, which is absent in M1 (Figure 6c). Involving these two areas and most of the weak wedge, a zone of thrust + shear exhibits increasing thrust dominance in the vicinity of the weak wedge boundaries. This thrust-dominant area is also located at the intersection between the two main orientation patterns observed in the model: E-W and NW-SE (Figure 6c). A region of normal faults only is present in the NW corner. Figure 8c reveals for all transects a higher overall amount of thrust-dominated faulting compared to M1. Similarly, all transects exhibit an equivalent distribution of fault types, starting from SW with a shear-dominated region, rapidly changing into a thrust-dominated region, followed by a thrust-only region (in Transects A and B only) near or within the weak band area. At the end of the transects, the faulting pattern returns to a thrust-dominated region. Transects B and C differ from Transect A by crosscutting the weak wedge, displaying an abrupt change from shear-dominated to thrust-dominated in the regions proximal to the boundaries of the weak wedge.

3-.4.1.3. Models M3a and M3b: North compression + active Eastern boundary stress (M3a— compressive; M3b—extension)

Model M3a (compressional eastern boundary) exhibits comparatively no rotation or displacement of the free boundaries, whereas Model M3b (extensional eastern boundary) displays a high rotation and displacement of the northern block. No protrusion is observed for M3a, whereas M3b shows a slightly enlarged protrusion compared to M2 (Figures 6 and S1 to S3).

M3b exhibits localized crustal thickening in the eastern convergent zone and crustal thinning in the western extensional zone, reflecting M1 behavior, although with higher crustal thickening values in the east and a larger area of crustal thinning in the NW corner (Figure 6a). Dissimilar to M3b, M1, and M2, Model M3a presents a limited variation in crustal thickness that nevertheless follows the direction and position of M3b. Transects A–C mirror this crustal behavior, reaching maximum values in the center of the weak band (Figure 8a). Comparing all models, M3a displays lower overall values of vertical crustal variation.

M3b vorticity distribution is similar to that of Model M1, with higher overall values of clockwise vorticity located in the central zone of the weak band and in the eastern convergent sector (Figure 6b). However, absolute vorticity values for M3b are increased relative to M1. The velocity field exhibits a more south directed motion of the crustal flow regime close to the eastern boundary, and by association, is more perpendicular to the weak band (Figure 6b). In M3b, the vorticity magnitude within the weak band also presents higher values compared to M1. To the east of this location, two patches of clockwise and counterclockwise vorticity are discernible. Contrary to M3b, Model M3a shows almost no vorticity for the entire model area (Figure 6b). For Model M3b, Transects A–C exhibit a similarly smooth Gaussian behavior for vertical crustal variation as M1 (Figure 8b). In contrast, Model M3a displays an almost completely flat behavior and close to null values for vorticity (Figure 8b).

M3b exhibits a pattern of deformation similar to that presented by M1. For both models, normal faulting dominates in the west and thrust faulting dominates in the east, with similar localization and relative shape of these isolated regions. However, M3b displays an overall more homogeneous shearing pattern than M1 (Figure 6c). Figure 6c shows that the areas dominated by the coaxial component of deformation in previous models display higher shear stress components in M3b. Model M3b also shows greater invasion of the western normal-dominated faults into the eastern area compared to all previous models. Contrary to M1 and M3b, Model M3a exhibits an almost entirely thrust-related type of deformation, with normal faulting confined to the NW area of the model (Figure 6c). The thrust-dominated area for M3a is mostly localized within the weak band, presenting a more equilibrated thrust/shear ratio in the NE region of the model. All remaining areas of M3a present shear + thrust faulting, with an increased shear component in the southern area of the model (Figure 6c). For

both M3a and M3b, Transects A–C exhibit a gradual variation in the rate of deformation along the length of each transect, when crossing boundaries that mark the change from thrust-dominated to shear-dominated faulting and vice-versa (Figure 8c).

3-.4.1.4. *Models M4a and M4b: North compression + active Eastern boundary stress (M4a— compressive; M4b—extension) + Eastern weak wedge*

Similar to M3a, Model M4a shows no rotation or displacement of the free boundaries, whereas Model M4b displays a high rotation and displacement of the northern block. For M4b, the protrusion at the eastern boundary exhibits a significantly increased displacement of crustal material, whereas M4a exhibits a lack of extrusion similar to that seen in M3a (Figures 6, 7, and S1 to S3).

Despite M4b exhibiting the highest crustal thicknesses, the general pattern of crustal variation is similar to that seen in M2. In contrast, M4a exhibits overall lower crustal variations. For both M4a and M4b, Transects A–C show a progressive increase in crustal thickening (Figure 6a). Similar to M2, Transect A displays a smooth distribution of crustal thickening, whereas Transects B and C present high increases or decreases in crustal thickening when crossing the boundary of the weak wedge.

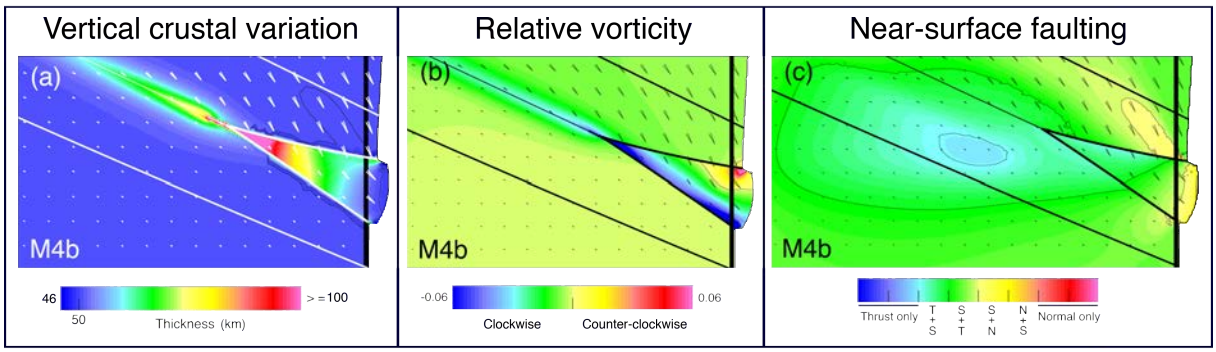

Figure 7. Enlarged region involving the eastern weak wedge for Model M4b, showing details of the features displayed in Figure 6.

M4b exhibits a similar vorticity pattern to M2 but only outside of the weak band (Figures 6b and 7b). Compared to the other models, M4b shows values that are substantially higher for both vertical crustal variation and vorticity. This increase in magnitude is well observed between M4b and M4a, wherein the latter, the spatial pattern of vertical crustal variation and vorticity is similar to M4b, but with significantly lower values. Exclusive to M4b, an apparent stratification of the vorticity intensity inside the eastern weak wedge is discernible, where a gradually shifting pattern of strongly clockwise in the SW to counterclockwise in the NE is seen (Figures 6b and 7b). Within the weak wedge of M4b and opposite to M4a, the velocity vectors show the material flow deflecting from NW-SE to approximately ESE, with higher magnitude close to the northern boundary (Figure 7b). Model M4a displays very small values of vorticity for the entire model, increasing slightly in the southern region of the weak wedge (Figure 6b). For M4b, Transects A–C follow the same vorticity path as M2, only diverging at the highest values (Figure 8b). Transect A exhibits a smooth distribution of vorticity in

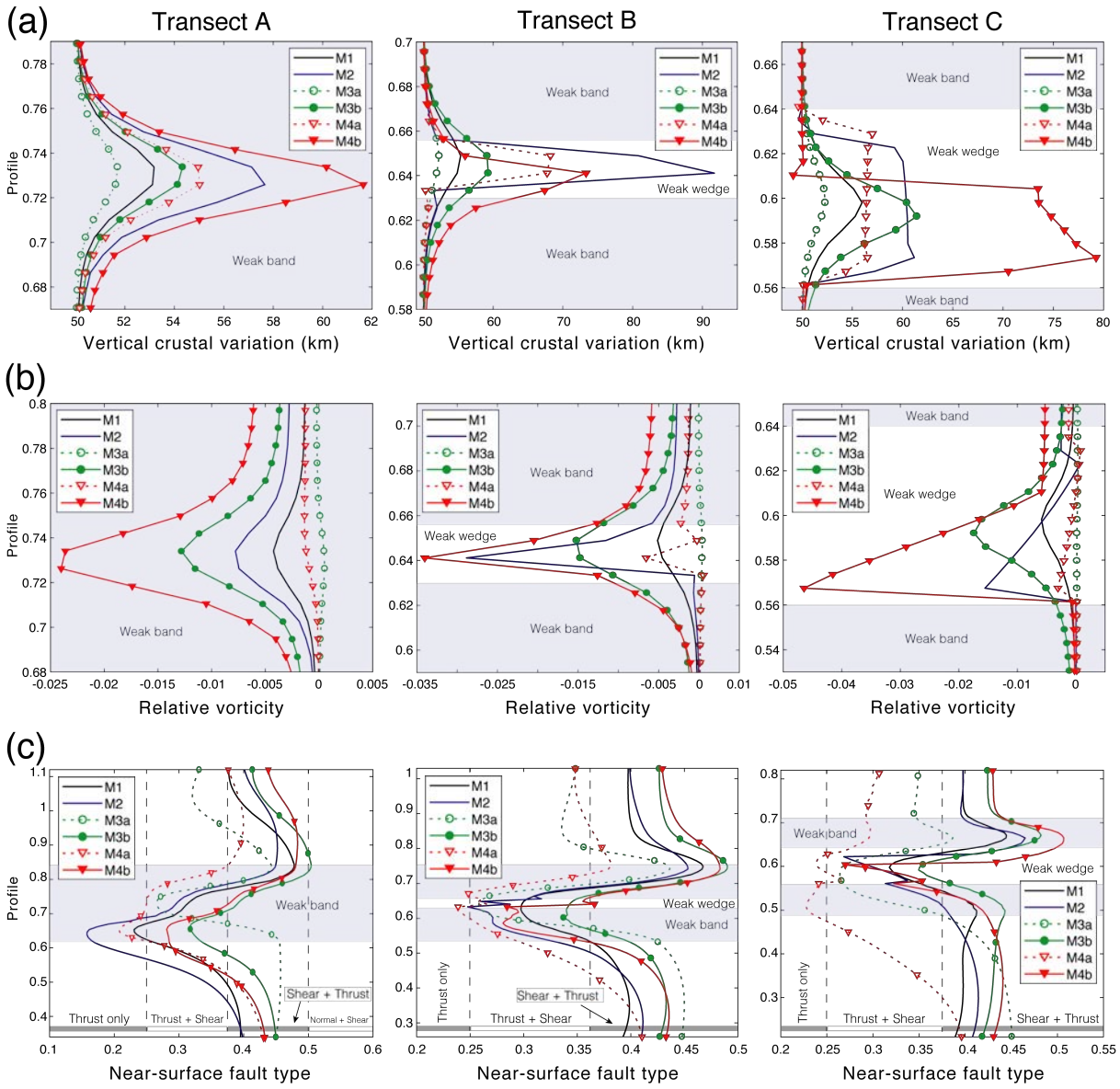

Figure 8. Variation in Transects A–C for the conditions of (a) vertical crustal variation, (b) relative vorticity, and (c) near-surface fault type for all models (M1 to M4b) after simulation dimensionless time 20.

the weak band, whereas Transects B and C present abrupt vorticity variations at the boundaries of the weak wedge and a gradual increase from N to S within the wedge. All transects of Models M4a and M3a present a similar vorticity distribution for low-vorticity values (Figure 8b). The differentiation between these two models resides in the higher vorticity values situated close to the southern boundary of the weak wedge for M4a. These higher values are reflected by a slight increase in vorticity, followed by an abrupt decrease passing the boundary of the weak wedge (Figure 8b).

M4b presents a similar fault distribution to M2 (Figures 6c and 8c) but with a more shear-dominated type of faulting. Two areas of normal faulting are visible close to the eastern boundary: one above the weak wedge with a NW-SE longitudinal direction and the other at the eastern margin of the protrusion from the weak wedge (Figure 8c). The thrust-dominated area is located in the western sector of the weak wedge and its western margin. Within this area, some regions show a higher proportion of thrust versus shear fault displacement, located to the south of the northern and southern

boundaries of the weak wedge and to the west of the weak wedge. In contrast, M4a is characterized by thrust-dominated faulting for the most part (Figure 6c). Thrust-only areas are situated within the weak band and across almost the totality of the weak wedge area. Transect A shows a similar pattern of faulting for both M4a and M4b, specifically in terms of abrupt changes in direction along the x axis (Figure 8c). However, M4a displays a more thrust fault-dominated distribution than M4b, visible as a shift from the center of the weak band in M4a to a region at the south of the weak band in M4b (Figure 6c). Transect B presents a similar pattern to Transect A but with a more extensive and abrupt change in the type of deformation, especially for M4b close to the northern boundary of the weak wedge (Figure 8c). For Transect C, M4b shows the same pattern visible in Transect B of extensive and abrupt changes in fault type when crossing the region close to the weak wedge (Figure 8c). Nevertheless, Transect C exhibits a larger contrast of faulting type between the interior of the weak wedge and the northern area. For Model M4a, Transect C shows a more gradual change in the type of deformation, and an extensive change in fault variability is absent for the top half of the transect.

3-4.2. Effect of primary versus conjugated primary and secondary stress regime on deformation style, crustal thickening, and Eastern extrusion

Our simulations show that the pattern of deformation in terms of crustal thickening, vorticity, and fault-type changes significantly when a secondary boundary stress is applied with a vector at a low angle to the structural grain of the weak zone. For all models, the localization of crustal displacement and deformation in the model is almost exclusively confined to the northern sector (Figures 6 and S1 to S3). The pattern of the velocity field, with the exception of Model M3a, shows that the lithospheric flow of material follows a clockwise rotation with northeast direction and relatively lower magnitude in the NW sector of the models, to a SSE direction and high magnitude along almost all of the eastern boundary (Figures 6 and S1 to S3). This motion is in accordance with Roberts & Houseman (2001), who found that clockwise rotation of the northern block relative to the southern block can activate the simultaneous opening of the Canning Basin to the west and compressional orogenesis in the Arunta Region to the east.

In a general sense, the models that present conjugated south directed compression and east directed traction (M3b and M4b; Figures 6 and S1 to S3), exhibit a higher amount of displacement of the model edges toward east and south relative to the models that present only a primary north stress regime (M1 and M2). Using 90 km of south directed displacement of the northern boundary (Figure 4) and with time constrained by the duration of ASO metamorphic activity (~80 Ma; Figure 2), the localized maximum N-S shortening rate at the northern boundary is 1.125 mm/year (or km/Ma) for the model showing the highest overall deformation (M4b). Due to a shorter southern displacement of 80 km at the northern boundary of the weak wedge (Figure

	Models	Northern block rotation	Protrusion from wedge in East	Crustal thickening	Assymetry in vorticity	Dominant near-surface fault type
Without wedge	M1	*	*	*	*	T + S > S + T
	M3a	-	-	Residual	Residual	T + S
	M3b	***	**	**	**	T + S; S + T
W/ wedge	M2	**	*	****	***	T + S > T only
	M4a	-	-	***	Residual	T only > T + S
	M4b	*****	*****	*****	*****	T + S > S + T

* : Representation of quantity or intensity; T= thrust; S= shear

Table 2. Summary table presenting for each individual model a semiquantitative interpretation of the observed model deformation.

4), the strain rate is reduced to 1 mm/year (or km/Ma) for this area.

The enhanced rotation of the northern block presenting conjugated north and east directed compressive stress regimes allows for a higher amount of crustal thickening in the eastern sector, while also permitting a global increase in vorticity and shearing within the model (Figures 6 and 8). In contrast, models that present conjugated north compressive and west directed extensional stress regimes (M3a and M4a) have edges that are almost stationary or in some cases slightly moved toward the west for parts of the eastern boundary (Figures 6 and S1 to S3). The lack of motion of the northern block in M3a and M4a reflects the competing nature of compressive orthogonal stress regarding the deformation of the model. In these models, all patterns are inverted relative to M3b and M4b, with decreased thickening, vorticity, and a shift from shear-dominated to thrust-dominated faulting (Figures 6 and 8). Furthermore, if secondary stresses are present, a clear difference in thickness variation, vorticity asymmetry, and type of deformation is observed compared to the models where secondary stresses are absent (Figures 6 and 8).

Taking, for example, Models M4a and M4b, if extension as a secondary stress was followed by compression, we would expect rotation of the northern block to be accompanied by a large amount of crustal protrusion within the weak wedge, and a high amount of thickening, asymmetry in vorticity, and thrust-dominated and shear-subordinate type of deformation (Figures 6 and 8). The compressional period that follows would possibly displace the northern block westward and deactivate the crustal flow to the east in the wedge protrusion. It is possible that the protrusion will act as a stress buffer, allowing some N-S stress accommodation within the weak wedge. This stress accommodation would allow for a small amount of the deformation pattern observed in M4b (Figures 6 and 8).

3-4.3. Effect of weak zone geometry on model behavior

The deformational behavior of our simulations is strongly affected by the presence or absence of the eastern weak wedge (Figures 6 and 8). The pattern of the velocity vector shows that for all models except M3a and M4a, the lithospheric material flow

follows a clockwise rotation with NE direction and relatively low magnitude in the NW sector to a SE direction and high magnitude along almost all of the eastern boundary (Figures 6 and 8). Material flows almost perpendicular to the northern boundary of the weak wedge and is then deflected to an approximate ESE direction inside the wedge (Figures 6 and 7) in accordance with the lateral extrusion.

The presence of an eastern weak wedge (Models M2, M4a, and M4b; Figures 6a and 8a) results in higher crustal thicknesses, especially in the western sector of the wedge-shaped zone (Figures 6a and 7a). In contrast, models without the weak wedge show an overall lower and more homogeneous crustal thickness in the eastern sector, with its position and orientation following the central gradual low viscosity band (Figure 6a).

The velocity vector representing the local direction of crustal flow and magnitude shows that all models except M3a and M4a present a central clockwise vorticity band that approximately follows the gradual low-viscosity band (Figure 6b). An apparent stratification of the vorticity intensity is visible inside the eastern weak wedge (Figures 6b and 7b). This vorticity stratification follows a gradual shifting pattern of highly clockwise in the SW to counterclockwise in the NE. Models M3a and M4a present no significant vorticity values or any highly localized vorticity sectors (Figure 6b).

Based on the distribution of deformation types, models that include the eastern weak wedge show an increased heterogeneity of fault patterns for the eastern central sector (Figure 6c). In M2 and M4b, a relative increase in thrust faulting is seen compared with the wedge-absent models, specifically close to the north and south boundaries of the weak wedge (Figures 6c and 7c).

3-5. Discussion

3-5.1. Localization of intracontinental deformation: general model behavior and first-order comparison with the ASO

The deformation pattern of the ASO (Ballèvre et al., 2000; Cartwright et al., 1999; Collins & Teyssier, 1989; Hand & Sandiford, 1999; Mawby et al., 1999; Raimondo et al., 2011, 2014; Figure 1) is generally well represented in our simulations. In particular, Model M4b best represents the deformation history (Table 2). Overall, the localization of thickening at the lithospheric scale is concentrated within weak parts of the crust at a low angle to the principal stress (Figures 6a–8a and 9). This localized deformation is in accordance with two of the requirements to form intracontinental orogens: (1) the transmission of far-field stresses from relatively strong plate margins (Handy & Brun, 2004; Shaw et al., 1991) and (2) a rheologically weak plate interior to accommodate the transmitted stress (Cunningham, 2013; Raimondo et al., 2011, 2012; Sandiford & Hand, 1998; Walter et al., 1995). Stress accommodation in weaker areas translates into

lithospheric-scale thickening, more prominent in models with active extension along the eastern margin, and in areas where N-S compression is facilitated by structural and rheological controls (Figures 5–9 and Table 2). This is accompanied by changes in the type of faults in areas of contrasting crustal rheology, which act as mechanical weaknesses to localize strain (Maidment, 2005; Molnar & Dayem, 2010; Raimondo et al., 2011, 2012). The pattern of vorticity within the weaker areas matches the different types of crustal flow within the models (Figures 5–8 and Table 2). The orientation of preexisting crustal structures in the SE Arunta Region also plays a role in the strain-inducing accommodation of compressive stress (Hurd & Zoback, 2012; Thomas & Powell, 2017). This can be observed in models where crustal deformation is generally oriented at low angle to the principal stress component (Figures 5–9).

3-5.2. The evolution of the ASO with respect to stress evolution and the presence of localized weak zones

3-.5.2.1. *Episodic nature of ASO: causes and effects*

The ASO comprises a series of episodic deformation events spanning the period 450–300 Ma, which reactivated an extensive and anastomosing mesh of Proterozoic shear zones and exhumed lower crustal rocks in the Arunta Region (Ballèvre et al., 2000; Cartwright et al., 1999; Collins & Teyssier, 1989; Hand & Sandiford, 1999; Mawby et al., 1999; Raimondo et al., 2011, 2014; Figures 1 and 2). The ASO exhibits large variations in metamorphic activity and basin evolution over its 150-Myr window of activity. There is a broad correlation between periods of retreating or stagnant westward subduction of the Pacific plate and an increase in metamorphic activity and synorogenic sedimentation across the ASO (Figure 2). In contrast, westward or northwest advancement of the Pacific plate is broadly correlated with a decline in both the metamorphic and sedimentary record of the ASO. This pattern of positive feedback between a retreating or stagnant Pacific plate and deformation in the ASO is observed in the models presenting inactive eastern boundary stresses (M1 and M2) or tractional, extensional eastern boundary stresses (M3b and M4b; Figures 6a–8a and 9). These models show that enhanced mountain building (high crustal thicknesses) and rotation of the northern block occurs when the eastern boundary is passive or actively extending (Roberts & Houseman, 2001; Figure 9). The negative feedback of an advancing Pacific plate on intraplate orogenesis is also visible in the models presenting eastern compressional stresses (M3a and M4a; Figures 6–9), which exhibit lower overall crustal thicknesses and limited northern block rotation due to the constrained displacement and rotation of the northern boundary (Table 2 and Figures S1 to S3).

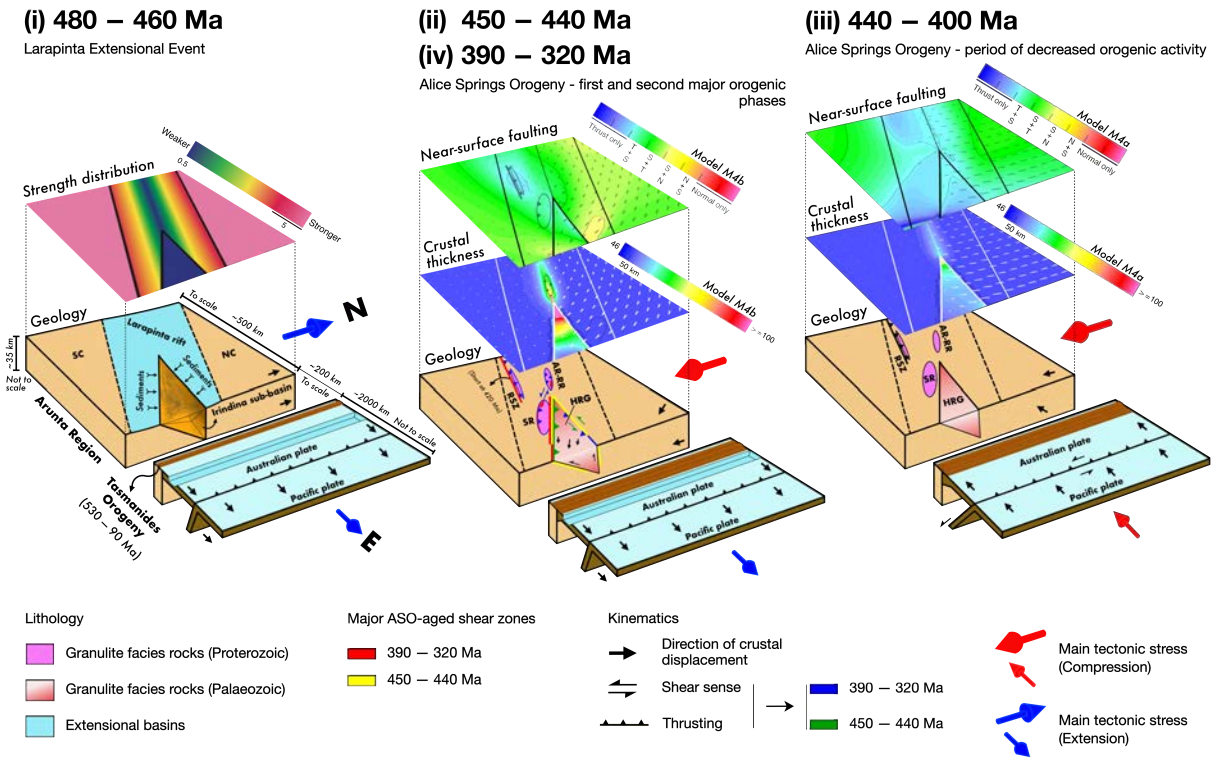

Figure 9. Schematic block models representing the geology of the Arunta Region of central Australia and the Tasmanides Orogeny at the start of the ASO (end of period (i)) and during distinct compressional and/or extensional stress regimes (ii, iii, and iv) at the northern and eastern Australian plate boundaries. The numerical model (M4a or M4b; Figures 6 and 7) best representing the fault and crustal thickening patterns observed on each orogenic phase of the ASO (ii, iii, and iv) is overlain on top of the Arunta Region schematic geology and tectonic setting for each of the previously mentioned time periods. Abbreviations: AR, Anmatjira Range; HRG, Harts Range Group; NC, North Australian Craton; RR, Reynolds Range; RSZ, Redbank Shear Zone; SC, South Australian Craton; SR, Strangways Range.

3-.5.2.2. *Metamorphic grade and exhumation patterns*

The increase in metamorphic grade and pervasiveness of fluid hydration/retrogression in the Arunta Region from the northwest (Reynolds-Anmatjira Ranges) to the southeast (Harts Range) (Mawby et al., 1999; Raimondo et al., 2011, 2014; Tucker et al., 2015) can be explained by an increase in positive vertical crustal variation along the same trajectory observed in models with the eastern weak wedge present. In Models M2, M4a, and M4b (Figures 6a–8a, 9 and Table 2), higher crustal thickening is present toward and inside the eastern weak wedge, corresponding to the highest metamorphic grades of the HRG. This general pattern and the inferred magnitude of crustal exhumation are observed in the vertical crustal variation maps shown in Figure 6. For Transect B (Figure 8a), Models M4a and M4b show crustal thickening values in the order of ~20–25 km. This is likely due to the bivergent shape of the Irindina subbasin and is similar to the observed patterns of exhumation along the western margin of the Harts Range (Maidment, 2005; Tucker et al., 2015).

The localization of higher crustal thickening is not randomly distributed in the Arunta Region (Figure 1b). As proposed by a number of authors (e.g., Cunningham, 2013; Klootwijk, 2013; Molnar & Dayem, 2010; Raimondo et al., 2014; Roberts & Houseman, 2001; Sandiford & Hand, 1998; Shaw et al., 1991), crustal thickening in intracontinental

orogens is usually preferentially located in regions of weakened rheology, leading to enhanced strain accumulation in structures at a low angle relative to the principal stress component and in regions adjacent to crustal strength heterogeneities. In our case, the central sector of the low-viscosity band and the eastern weak wedge (Figures 6–9) model such localization. These two regions correspond to the SE Arunta Region and the western sector of the Harts Range due to their orientation and weakened rheology, respectively (Figure 1b). The opening of the Canning Basin is another example of deformation driven by weakened rheology, as previously discussed by Roberts & Houseman (2001). This feature can be observed in our models as crustal thinning within the western sector of the low-viscosity band, coeval with ASO activity (Figure 6).

Exhumation of granulite facies lower crust is not observed for the whole of the Arunta Region, instead of being concentrated in two major areas (Figure 1b). The kinematics of deformation in Models M2 and M4b (Figures 6c–8c; eastern weak wedge and neutral or extensional Tasmanides) shows two principal areas of thrust-dominated faulting, one proximal to the south of the weak wedge, with thrust predominance near the boundaries of the wedge, and the second to the southwest of the wedge. In the Arunta Region, these features can be spatially related with the development of two major thrust systems that expose lower crustal granulites in their hanging walls: (1) the Redbank Shear Zone, which involves ~25-km displacement of a mantle wedge to shallower crustal levels (e.g., Goleby et al., 1989, 1990; Korsch et al., 1998), and (2) the Harry Creek Shear Zone, which marks the southern margin of the Strangways Range basement terrane (Figures 1b and 9). These results suggest that the variations in metamorphic grade across the ASO are a consequence of differential exhumation. In other words, the general west to east increase in metamorphic grade is not a postorogenic feature caused by tilted exposure but rather represents a primary orogenic feature that implies what is observed in the east is not necessarily predicted to lie beneath the western Arunta Region.

The northern sector of the Harts Range records sinistral shear deformation in the Delny and Entire Point Shear Zone (Collins & Teyssier, 1989; Weisheit et al., 2016). Model M4b, and to a lesser extent Model M2 (Figures 6b– 8b), shows higher values for vorticity in the Harts Range area compared with all remaining models (Table 2). These vorticity values can be explained by the east directed protrusion and flow of crustal material inside the weak wedge (Figures 6b and 7b), similar to the strain distribution within the channel flow extrusion documented in the Himalaya-Tibetan Plateau (Beaumont et al., 2001; Bird, 1991; Godin et al., 2006) and hypothesized by Klootwijk (2013) for the intraplate Australian continent. This movement of material inside the wedge would imply both sinistral and dextral strike-slip kinematics along the northern and southern boundaries of the wedge, respectively (Figure 6b–8b and 9). However, the southern boundary of the Harts Range does not present any major dextral shear sense (Collins & Teyssier, 1989). This can be explained by either the distance of the laminar flow of crustal material (low vorticity) from the southern boundary or the low

velocity of the flow (Figure 8b). The shape of HRG buried beneath the Mesozoic-Cenozoic sediments to the east (Figure 1b; Maidment, 2005) is consistent with the flow velocity of the extrusion having been higher in the northern part of the extrusion than in the south. This N-S dichotomy in the material flow velocity within the weak wedge potentially played an important role in the formation of a pull-apart region in the lower crust of the HRG, essential for the formation of the Entia Gneiss Complex double dome (e.g., Rey et al., 2017; Whitney et al., 2004) during the compressive ASO. Model M4b is the only model that shows a similar N-S dichotomy in the extrusion flow velocity (Figures 6b–8b), indicating that the presence of the eastern weak wedge conjugated with eastern extensional boundary forces is necessary to achieve this flow pattern.

3-.5.2.3. Fault zone types and their distribution: reactivation and changing character

The Arunta Region shows widespread reactivation of Proterozoic shear zones throughout most of its SE domain during the ASO (Ballèvre et al., 2000; Cartwright et al., 1999; Raimondo et al., 2011, 2014). Reactivation is enhanced in areas proximal to the HRG (e.g., West Bore, Gough Dam, Entire Point, and Delny Shear Zones) and the Redbank Shear Zone (Figure 1). Adjacent to the West Bore and Gough Dam Shear Zone, and in a lesser amount between the Entire Point and Delny Shear Zones, a network of kilometer-scale hydrous shear zones is observed. The presence of hydrous shear zones bounding the HRG can be explained by local weaknesses and strain localization at the transition between the Paleozoic HRG and Paleoproterozoic granulites of the Strangways Range (West Bore and Gough Dam Shear Zones), due to rheological heterogeneities between these two terranes (Molnar & Dayem, 2010; Figure 1c).

Such local weaknesses are observed in Transects B and C, with abrupt changes in crustal thickness variation, local vorticity, and shifting of fault kinematics to thrust-dominated deformation at the boundaries of the eastern weak wedge (Figure 8). Since a local area of weakness governs the observed differences in movement, a large-scale Rayleigh-Taylor instability is incompatible because it is not predicted to cause localized changes in viscosity/rheology (Neil & Houseman, 1999; Raimondo et al., 2014). Compared with models including the eastern weak wedge, those excluding the weak wedge (M1, M3a, and M3b; Figure 6) do not show the same heterogeneity of crustal variation, vorticity, or kinematics of deformation. Instead, the strain deformation follows a smoother pattern due to the rheological control on the gradual change of viscosity in the weak band (Figure 6c). The lack of spatial heterogeneity for all calculated crustal parameters does not agree with the complex knematic pattern and structural control observed in central Australia (Figure 1).

The orientation of preexisting Proterozoic structures also influences the timing of reactivation and the large-scale orogenic architecture. During the first major period of metamorphic activity (D1; Figure 2), the principal stress component is oriented N-S (Kröner et al., 2016), leading to the reactivation of structures oriented E-W, orthogonal

to the first-order compressional stress (e.g., the Redbank Shear Zone; Biermeier et al., 2003). In our simulations, this area is approximately located in the domain representing the SW Arunta Region, where the thrust regime is dominant (Figures 6c, 7c and 9). This thrust-dominant area is also located at the intersection between the two main orientation patterns observed in the models: E-W and NW-SE (Figures 6c, 7c and 9). These two orientations match the dominant structural fabric of shear zones and thrust faults throughout the Arunta Region (Figure 1). During the second major period of metamorphic activity (D2; Figure 2), the principal stress was oriented NNE-SSW (Kröner et al., 2016), reactivating most of the shear zones and thrust faults oriented NW-SE to WNW-ESE (e.g., anastomosing shear zones in the Reynolds-Anmatjira Ranges and Strangways Range; Ballèvre et al., 2000; Cartwright et al., 1999; Raimondo et al., 2011, 2014). In our model, these structures are in a similar orientation to the main weak zones (i.e., the weak band and weak wedge), representing the Larapinta Rift and the Harts Range, respectively (Figures 6c and 9).

3-6. Conclusion: how to make an intracontinental orogen: relationships and predictions

Here we demonstrate that in order to obtain a pattern of deformation similar to that observed for the Alice Springs Orogen, central Australia, external tectonic stresses acting on the margins of the Australian plate are required to be transmitted into areas of weak intraplate lithosphere. Secondary stresses orthogonal to the principal stresses may have positive or negative feedback on crustal thickness and rotation in the developing intracontinental orogen, by either enhancing or neutralizing the horizontal stress state acting on the weak areas. For the case study presented, our models show that the secondary stresses acting on the Australian continent contributed to marked periodicity during the ASO, as indicated by a strong temporal link between tectonic activity in eastern and central Australia.

Intracontinental orogenesis is sensitive to stress reconfigurations at plate margins. Primary features such as the geometry of the orogenic system, preexisting crustal structures, and transmitted stresses are highly relevant in the accommodation and concentration of differential stress within continental plates. When the principal transmitted stresses are oriented at a low angle to the weak intraplate zone, intracontinental orogenesis is enhanced. A higher magnitude of crustal thickening rates in the context of these models suggest exhumation of higher grade metamorphic rocks, augmented by enhanced thrusting when coupled with proximal boundaries of contrasting rheological terranes or the presence of previous crustal weaknesses (e.g., shear zones or a failed rift). Secondary stresses may also provide a positive effect for the principal stresses and enhance the extrusion of lower crustal material from the weak areas.

3-7. Acknowledgements

This is contribution 1209 of the Australian Research Council (ARC) Centre of Excellence for Core to Crust Fluid Systems. This work was carried out as part of a PhD study at Macquarie University and was supported by ARC Discovery grant DP160103449. We thank Russ Pysklywec and an anonymous reviewer for constructive reviews and Taylor Schildgen for editorial handling. We are grateful to Robyn Gardner for invaluable help in using Basil software and for useful modelation discussions. The data used are listed in the references, figures, tables, and supporting information.

3-8. References

Aitken, A. R. A., Betts, P. G., Ailleres, L., 2009. The architecture, kinematics, and lithospheric processes of a compressional intraplate orogen occurring under Gondwana assembly: The Petermann orogeny, central Australia. Lithosphere, 1(6): 343-357.

Andeweg, B., De Vicente, G., Cloetingh, S., Giner, J., Muñoz Martin, A., 1999. Local stress fields and intraplate deformation of Iberia: variations in spatial and temporal interplay of regional stress sources. Tectonophysics, 305(1–3): 153–164.

Ballèvre, M., Möller, A., Hensen, B. J., 2000. Exhumation of the lower crust during crustal shortening: an Alice Springs (380 Ma) age for a prograde amphibolite facies shear zone in the Strangways Metamorphic Complex (central Australia). Journal of Metamorphic Geology, 18(6): 737–747.

Barr, T. D. & Houseman, G. A., 1996. Deformation fields around a fault embedded in a non-linear ductile medium. Geophysical Journal International, 125(2): 473–490.

Beaumont, C., Jamieson, R. A., Nguyen, M. H., Lee, B., 2001. Himalayan tectonics explained by extrusion of a low-viscosity crustal channel coupled to focused surface denudation. Nature, 414(6865): 738-742.

Bendall, B., 2000. Mid-Palaeozoic shear zones in the Strangways Range: a record of intracratonic tectonism in the Arunta Inlier, Central Australia (Doctoral dissertation). University of Adelaide, Adelaide, Australia.

Biermeier, C., Stüwe, K., Foster, D. A., Finger, F., 2003. Thermal evolution of the Redbank thrust system, central Australia: Geochronological and phase–equilibrium constraints. Tectonics, 22(1): 1002.

Bird, P., 1991. Lateral Extrusion of Lower Crust from Under High Topography in the Isostatic Limit. Journal of Geophysical Research, 96(B6): 10275-10286.

Braun, J. & Shaw, R., 1998. Contrasting styles of lithospheric deformation along the northern margin of the Amadeus basin, central Australia. Structure and Evolution of the Australian Continent, 139–156.

Braun, J. & Shaw, R., 2001. A thin–plate model of Palaeozoic deformation of the Australian lithosphere: Implications for understanding the dynamics of intracratonic deformation. Geological Society, London, Special Publications, 184(1): 165–193.

Buick, I. S., Hand, M., Williams, I. S., Mawby, J., Miller, J. A., Nicoll, R. S., 2005. Detrital zircon provenance constraints on the evolution of the Harts Range metamorphic complex (central Australia): Links to the centralian superbasin. Journal of the Geological Society 162(5): 777–787.

Buick, I., Miller, J., Williams, I., Cartwright, I., 2001. Ordovician high-grade metamorphism of a newly recognised late Neoproterozoic terrane in the northern Harts Range, central Australia. Journal of Metamorphic Geology, 19(4): 373–394.

Buick, I., Storkey, A., Williams, I., 2008. Timing relationships between pegmatite emplacement, metamorphism and deformation during the intra-plate Alice Springs orogeny, central Australia. Journal of Metamorphic Geology, 26(9): 915–936.

Burov, E. B. & Watts, A. B., 2006. The long-term strength of continental lithosphere: “jelly sandwich” or “crème brûlée”? GSA today, 16(1): 4.

Camacho, A. & McDougall, I., 2000. Intracratonic, strike-slip partitioned transpression and the formation and exhumation of eclogite facies rocks: An example from the Musgrave Block, central Australia. Tectonics, 19(5): 978-996.

Cartwright, I. & Buick, I. S., 1999. Meteoric fluid flow within Alice Springs age shear zones, Reynolds Range, central Australia. Journal of Metamorphic Geology, 17: 397-414.

Cartwright, I., Buick, I. S., Foster, D. A., Lambert, D. D., 1999. Alice Springs age shear zones from the southeastern Reynolds Range, central Australia. Australian Journal of Earth Sciences, 46(3): 355-363.

Cawood, P. A., Kröner, A., Collins, W. J., Kusky, T. M., Mooney, W. D., Windley, B. F., 2009. Accretionary orogens through Earth history. Geological Society, London, Special Publications, 318(1): 1–36.

Champion, D., Kositcin, N., Huston, D., Mathews, E., Brown, C., 2009. Geodynamic synthesis of the Phanerozoic of eastern Australia and implications for metallogeny. Geoscience Australia Record, 18(2009): 254p.

Coblentz, D. D., Zhou, S., Hillis, R. R., Richardson, R. M., Sandiford, M., 1998. Topography, boundary forces, and the Indo–Australian intraplate stress field. Journal of Geophysical Research: Solid Earth, 103(B1): 919-931.

Collins, W. & Shaw, R., 1995. Geochronological constraints on orogenic events in the Arunta inlier: A review. Precambrian Research, 71(1): 315–346.

Collins, W. & Teyssier, C., 1989. Crustal scale ductile fault systems in the Arunta inlier, central Australia. Tectonophysics, 158(1): 49–66.

Collins, W. J., 2002. Nature of extensional accretionary orogens. Tectonics, 21(4).

Cunningham, D., 2005. Active intracontinental transpressional mountain building in the mongolian Altai: Defining a new class of orogen. Earth and Planetary Science Letters 240(2): 436–444.

Cunningham, D., 2013. Mountain building processes in intracontinental oblique deformation belts: Lessons from the Gobi corridor, central Asia. Journal of Structural Geology, 46: 255–282.

Dunlap, W. J., Teyssier, C., McDougall, I., Baldwin, S., 1995. Thermal and structural evolution of the intracratonic Arltunga Nappe Complex, central Australia. Tectonics, 14(5): 1182–1204.

England, P. & McKenzie, D., 1982. A thin viscous sheet model for continental deformation. Geophysical Journal International, 70(2): 295–321.

Glen, R., 2013. Refining accretionary orogen models for the Tasmanides of eastern Australia. Australian Journal of Earth Sciences, 60(3): 315–370.

Godin, L., Grujic, D., Law, R. D., Searle, M. P., 2006. Channel flow, ductile extrusion and exhumation in continental collision zones: an introduction. Geological Society, London, Special Publications, 268: 1–23.

Goleby, B. R., Kennett, B. L. N., Wright, C., Shaw, R. D., Lambeck, K., 1990. Seismic reflection profiling in the Proterozoic Arunta Block, central Australia: processing for testing models of tectonic evolution. Tectonophysics, 173(1-4): 257-268.

Goleby, B. R., Shaw, R. D., Wright, C., Kennett, B. L. N., Lambeck, K., 1989. Geophysical evidence for 'thick-skinned' crustal deformation in central Australia. Nature, 337(6205): 325-330.

Gorczyk, W. & Vogt, K., 2015. Tectonics and melting in intra-continental settings. Gondwana Research, 27(1): 196-208.

Gorczyk, W., Hobbs, B., Gessner, K., Gerya, T., 2013. Intracratonic geodynamics. Gondwana Research, 24(3-4): 838-848.

Gray, D. & Foster, D., 2004. Tectonic evolution of the Lachlan orogen, southeast Australia: Historical review, data synthesis and modern perspectives. Australian Journal of Earth Sciences, 51(6): 773–817.

Haines, P. W., Hand, M., Sandiford, M., 2001. Palaeozoic synorogenic sedimentation in central and northern Australia: A review of distribution and timing with implications for the evolution of intra-continental orogens. Australian Journal of Earth Sciences, 48(6): 911–928.

Hand, M. & Sandiford, M., 1999. Intraplate deformation in central Australia, the link between subsidence and fault reactivation. Tectonophysics, 305(1): 121–140.

Hand, M., Mawby, J., Kinny, P., Foden, J., 1999a. U–Pb ages from the Harts Range, central Australia: Evidence for early Ordovician extension and constraints on Carboniferous metamorphism. Journal of the Geological Society, 156(4): 715–730.

Handy, M. R., & Brun, J. P., 2004. Seismicity, structure and strength of the continental lithosphere. Earth and Planetary Science Letters, 223(3-4): 427–441.

Heron, P. J. & Pysklywec R. N., 2016. Inherited structure and coupled crust-mantle lithosphere evolution: Numerical models of Central Australia. Geophysical Research Letters, 43(10): 4962-4970.

Heron, P. J., Pysklywec, R. N., Stephenson, R., 2016. Lasting mantle scars lead to perennial plate tectonics. Nature communications, 7: 11834.

Houseman, G. & England, P., 1986. Finite strain calculations of continental deformation: 1. Method and general results for convergent zones. Journal of Geophysical Research: Solid Earth, 91(B3): 3651–3663.

Houseman, G. & England, P., 1993. Crustal thickening versus lateral expulsion in the Indian–Asian continental collision. Journal of Geophysical Research: Solid Earth, 98(B7): 12233–12249.

Houseman, G., Barr, T., Evans, L., 2008. Basil: stress and deformation in a viscous material. Microdynamics simulation. Berlin, Springer-Verlag, 139-154.

Hurd, O. & Zoback, M. D., 2012. Intraplate earthquakes, regional stresses and faults mechanics in the Central and Eastern U.S. and Southern Canada. Tectonophysics, 581: 182–192.

Karato, S. I., Paterson, M. S., FitzGerald, J. D., 1986. Rheology of synthetic olivine aggregates: influence of grain size and water. Journal of Geophysical Research: Solid Earth, 91(B8): 8151–8176.

Klootwijk, C., 2010. Australia's controversial Middle-Late Palaeozoic pole path and Gondwana–Laurasia interaction. Palaeoworld, 19(1): 174–185.

Klootwijk, C., 2013. Middle–late Paleozoic Australia-Asia convergence and tectonic extrusion of Australia. Gondwana Research, 24(1): 5–54.

Korsch, R. J., Goleby, B. R., Leven, J. H., Drummond, B. J., 1998. Crustal architecture of central Australia based on deep seismic reflection profiling. Tectonophysics, 288(1-4): 57-69.

Kröner, A., 1977. Precambrian mobile belts of southern and eastern Africa—ancient sutures or sites of ensialic mobility? A case for crustal evolution towards plate tectonics. Tectonophysics, 40(1-2): 101-135.

Kröner, U., Roscher, M., Romer, R. L., 2016. Ancient plate kinematics derived from the deformation pattern of continental crust: Paleo-and Neo-Tethys opening coeval with prolonged Gondwana–Laurussia convergence. Tectonophysics, 681: 220–233.

Kusznir, N. J. & Park, R. G., 1987. The extensional strength of the continental lithosphere: its dependence on geothermal gradient, and crustal composition and thickness. Geological Society, London, Special Publications, 28(1): 35-52.

Livaccari, R. F., 1991. Role of crustal thickening and extensional collapse in the tectonic evolution of the Sevier-Laramide orogeny, western United States. Geology, 19(11): 1104-1107.

Maidment, D., Hand, M., Williams, I., 2005. Tectonic cycles in the Strangways metamorphic complex, Arunta inlier, central Australia: Geochronological evidence for exhumation and basin formation between two high–grade metamorphic events. Australian Journal of Earth Sciences, 52(2): 205–215.

Maidment, D., Hand, M., Williams, I., 2013. High–grade metamorphism of sedimentary rocks during Palaeozoic rift basin formation in central Australia. Gondwana Research, 24(3): 865–885.

Marshak, S., Karlstrom, K., Timmons, J. M., 2000. Inversion of Proterozoic extensional faults: An explanation for the pattern of Laramide and Ancestral Rockies intracratonic deformation, United States. Geology, 28(8): 735-738.

Mawby, J., Hand, M., Foden, J., 1999. Sm–Nd evidence for high–grade ordovician metamorphism in the Arunta block, central Australia. Journal of Metamorphic Geology, 17: 653–668.

McLaren, S., Sandiford, M., Dunlap, W. J., Scrimgeour, I., Close, D., Edgoose, C., 2009. Distribution of Palaeozoic reworking in the western Arunta region and northwestern Amadeus basin from 40ar/39ar thermochronology: Implications for the evolution of intracratonic basins. Basin Research, 21(3): 315–334.

Meng, Q. R. & Zhang, G. W., 2000. Geologic framework and tectonic evolution of the Qinling orogen, central China. Tectonophysics, 323(3): 183–196.

Molnar, P. & Tapponnier, P., 1975. Cenozoic tectonics of Asia: Effects of a continental collision. Science, 189(4201): 419–426.

Molnar, P., & Dayem, K. E., 2010. Major intracontinental strike-slip faults and contrasts in lithospheric strength. Geosphere, 6(4): 444–467.

Mory, A. & Beere, G., 1988. Geology of the onshore Bonaparte and Ord basins in western Australia. Geological Survey Western Australia, Bulletin, 134.

Myers, J. S., Shaw, R. D., Tyler, I. M., 1996. Tectonic evolution of Proterozoic Australia. Tectonics, 15(6): 1431–1446.

Neil, E. A. & Houseman, G. A., 1999. Rayleigh–Taylor instability of the upper mantle and its role in intraplate orogeny. Geophysical Journal International, 138(1): 89–107.

Neves, S. P., 2003. Proterozoic history of the Borborema province (NE Brazil): Correlations with neighboring cratons and Pan–African belts and implications for the evolution of western Gondwana. Tectonics, 22(4).

Perry, H.K.C., Mareschal, J.C., Jaupart, C., 2006. Variations of strength and localized deformation in cratons: the 1.9 Ga Kapuskasing uplift, Superior Province, Canada. Earth and Planetary Science Letters, 249(3–4): 216–228.

Powell, C. M., 1984. Terminal fold–belt deformation: Relationship of mid–Carboniferous megakinks in the Tasman fold belt to coeval thrusts in cratonic Australia. Geology, 12(9): 546–549.

Pysklywec, R.N. & Beaumont, C., 2004. Intraplate tectonics: feedback between radioactive thermal weakening and crustal deformation driven by mantle lithosphere instabilities. Earth and Planetary Science Letters, 221(1–4): 275–292.

Raimondo, T., Clark, C., Hand, M., Cliff, J., Anczkiewicz, R., 2013. A simple mechanism for mid-crustal shear zones to record surface-derived fluid signatures. Geology, 41(6): 711-714.

Raimondo, T., Clark, C., Hand, M., Cliff, J., Harris, C., 2012. High-resolution geochemical record of fluid-rock interaction in a mid-crustal shear zone: A comparative study of major element and oxygen isotope transport in garnet. Journal of Metamorphic Geology, 30(3): 255–280.

Raimondo, T., Clark, C., Hand, M., Faure, K., 2011. Assessing the geochemical and tectonic impacts of fluid-rock interaction in mid-crustal shear zones: A case study from the intracontinental Alice Springs orogen, central Australia. Journal of Metamorphic Geology, 29(8): 821–850.

Raimondo, T., Collins, A. S., Hand, M., Walker–Hallam, A., Smithies, R. H., Evins, P. M., Howard, H. M., 2010. The anatomy of a deep intracontinental orogen. Tectonics, 29(4): TC4024.

Raimondo, T., Hand, M., Collins, W. J., 2014. Compressional intracontinental orogens: Ancient and modern perspectives. Earth–Science Reviews, 130: 128–153.

Ramdani, F., 1998. Geodynamic implications of intermediate-depth earthquakes and volcanism in the intraplate Atlas mountains (Morocco). Physics of the Earth and Planetary Interiors, 108(3): 245–260.

Ranalli, G. & Murphy, D. C., 1987. Rheological stratification of the lithosphere. Tectonophysics, 132(4): 281-295.

Regenauer-Lieb, K., Veveakis, M., Poulet, T., Paesold, M., Rosenbaum, G., Weinberg, R. F., Karrech, A., 2015. Multiscale, multiphysics geomechanics for geodynamics applied to buckling instabilities in the middle of the Australian craton. Philosophical Magazine, 95(28-30): 3055-3077.

Rey, P. F., Mondy, L., Duclaux, G., Teyssier, C., Whitney, D. L., Bocher, M., Prigent, C., 2017. The origin of contractional structures in extensional gneiss domes. Geology, 45(3): 263–266.

Roberts, E. A. & Houseman, G. A., 2001. Geodynamics of central Australia during the intraplate Alice Springs orogeny: Thin viscous sheet models. Geological Society, London, Special Publications, 184(1): 139–164.

Romine, K., Southgate, P., Kennard, J., Jackson, M., 1994. The Ordovician to Silurian phase of the Canning basin, WA: Structure and sequence evolution. The sedimentary basins of Western Australia, 677–696.

Sandiford, M. & Hand, M., 1998. Controls on the locus of intraplate deformation in central Australia. Earth and Planetary Science Letters, 162(1): 97–110.

Sandiford, M., Hand, M., McLaren, S., 2001. Tectonic feedback, intraplate orogeny and the geochemical structure of the crust: A central Australian perspective. Geological Society, London, Special Publications, 184(1): 195–218.

Scrimgeour, I. R., 2013. Aileron Province, in Ahmad M. and Munson T. J., Geology and mineral resources of the Northern Territory. Northern Territory Geological Survey, Special Publication, 5.

Shaw, R., Etheridge, M., Lambeck, K., 1991. Development of the late–Proterozoic to mid-Paleozoic intracratonic Amadeus basin in central Australia: A key to understanding tectonic forces in plate interiors. Tectonics, 10(4): 688–721.

Shaw, R., Wellman, P., Gunn, P., Whitaker, A., Tarlowski, C., Morse, M., 1995. Australian crustal elements map. AGSO Research Newsletter, 23: 1–3.

Teixell, A., Arboleya, M.-L., Julivert, M., Charroud, M., 2003. Tectonic shortening and topography in the central High Atlas (Morocco). Tectonics, 22(5): 1051.

Teyssier, C., 1985. A crustal thrust system in an intracratonic tectonic environment. Journal of Structural Geology, 7(6): 689–700.

Thomas, W. A. & Powell, C. A., 2017. Necessary conditions for the intraplate seismic zones in north America. Tectonics, 36: 2903–2917.

Tommasi, A., Vauchez, A., Daudré, B., 1995. Initiation and propagation of shear zones in a heterogeneous continental lithosphere. Journal of Geophysical Research: Solid Earth, 100(B11): 22083-22101.

Tucker, N. M., Hand, M., Payne, J. L., 2015. A rift–related origin for regional medium–pressure, high–temperature metamorphism. Earth and Planetary Science Letters, 421: 75–88.

Walter, M. R., Veevers, J. J., Calver, C. R., Grey, K., 1995. Neoproterozoic stratigraphy of the centralian superbasin, Australia. Precambrian Research, 73(1–4): 173–195.

Webby, B. D., 1978. History of the Ordovician continental platform shelf margin of Australia. Journal of the Geological Society of Australia, 25(1–2): 41–63.

Weisheit, A., Reno, B. L., Beyer, E. E., Whelan, J. A., McGloin, M., 2016. Multiply reactivated crustal–scale structures and a long– lived counter–clockwise P–T path: New insights into the 1.5 billion year tectonothermal evolution of the eastern Arunta region, central Australia. Annual Geoscience Exploration Seminar (AGES) Proceedings, 56–62.

Whitney, D. L., Teyssier, C., Vanderhaege, O., 2004. Gneiss domes and crustal flow, in Whitney, D.L, Teyssier, C., and Siddoway, C.S., Gneiss domes in orogeny. Geological Society of America, Special Paper, 380: 15–3

Wright, C., Goleby, B. R., Collins, C. D. N., Korsch, R. J., Barton, T., Greenhalgh, S. A., Sugiharto, S., 1990. Deep seismic profiling in central Australia. Tectonophysics, 173(1–4): 247–256.

Zoback, M. L., Zoback, M. D., Adams, J., Assumpcao, M., Bell, S., Bergman, E. A., Blumling, P., Brereton, N. R., Denham, D., Ding, J., Fuchs, K., Gay, N., Gregersen, S., Gupta, H. K., Gvishiani, A., Jacob, K., Klein, R., Knoll, P., Magee, M., Mercier, J. L., Muller, B. C., Paquin, C., Rajendran, K., Stephansson, O., Suarez, G., Suter, M., Udias, A., Xu, Z. H., Zhizhin, M., 1989. Global patterns of tectonic stress. Nature, 341: 291–298.

Chapter 4. Glimmerite: a product of melt-rock interaction within a crustal-scale high-strain zone

David Silva[1*], Nathan R. Daczko[1], Sandra Piazolo[1,2], Tom Raimondo[3,4]

[1]ARC Centre of Excellence for Core to Crust Fluid Systems and GEMOC, Department of Earth and Planetary Sciences, Macquarie University, NSW 2109, Australia

[2]School of Earth and Environment, Institute of Geophysics and Tectonics, University of Leeds, Leeds, UK

[3]School of Natural and Built Environments, University of South Australia, GPO Box 2471, Adelaide, SA 5001, Australia

[4]Future Industries Institute, University of South Australia, GPO Box 2471, Adelaide, SA 5001, Australiaa

*E-mail address: david.barbosa-da-silva@hdr.mq.edu.au

Keywords: Glimmerite; high-strain zone; continental crust; metasomatism; melt-rock interaction

Abstract

High-strain zones are crucial for the migration of fluids through the crust. The paradigm for hydrous high-strain zones that cut dry host rocks is for fluid-rock interaction to have involved aqueous fluids. However, the role of silicate melt driving such hydration is increasingly recognised. In this contribution, we examine the formation of glimmerite (biotitite) bands during melt migration in the Gough Dam shear zone, a high-strain zone in central Australia active during the Alice Springs Orogeny (c. 450–300 Ma). These glimmerite bands cut and replace a range of felsic protoliths, including granitic gneiss and quartzite. Melt migrating through the high-strain zone is interpreted to have penetrated relict layers of protolithic rocks along a network of fractures parallel and orthogonal to the shear zone foliation, enhancing dissolution of precursor rock and replacement by glimmerite. Microstructures indicative of the former presence of melt in the high-strain zone include: (i) pseudomorphs of former melt pockets of granitic composition; (ii) small dihedral angles of interstitial phases; (iii) elongate grain boundary melt pseudomorphs; (iv) small grain aggregates connected in three dimensions; and (v) localized static grain growth and recovery. Other microstructures indicative of melt-present deformation includes neoformed grains with evidence for activation of multiple slip systems and a random orientation distribution. The degree

of modification of quartzite to glimmerite is documented by an increase in biotite mode and correlates with changes in biotite chemistry to higher Ti content (higher apparent temperature) and changes to trace element and REE composition. Melt-assisted coupled dissolution-precipitation reactions during melt flux are interpreted to partially reset Proterozoic monazite U-Pb ages inherited from the protolith (c. 1740–1630 Ma) to younger Palaeozoic ages, with a complex age pattern congruent with the Alice Springs Orogeny (c. 606–371 Ma, with a dominant age maxima at c. 451 Ma). We propose that the glimmerite formed during dynamic melt migration of an externally derived hydrous peraluminous melt, driving reaction replacement of various felsic protolithic rocks during this orogenic event.

4-1. Introduction

Fluid or the lack thereof is key in crustal tectonometamorphic processes because it plays a major role in the progression of reactions, changes to mineral assemblages, metastability, activation of deformation processes and coupled rheological consequences (Yardley, 2009 and references therein). Both water or solute-rich fluids such as silicate melts have a first order effect on a wide range of geochemical and deformation processes, acting as important agents at all scales. For example, fluids increase grain boundary mobility (e.g. Piazolo et al., 2002; Mancktelow & Pennacchioni, 2004), cause crystal hydrolytic weakening (e.g. Griggs & Blacic, 1965; Green et al., 1970; Kronenberg et al., 1990; Girard et al., 2013) and rheological weakening through fluid overpressure (e.g. Thompson & Connolly, 1992; Sibson, 1994), induce water-fluxed melting (e.g. Weinberg & Hasalová, 2015 and references therein), facilitate metasomatism (e.g. Etheridge et al., 1983; Ferry, 1994; Putnis & Austrheim, 2010), enable fast intra- and inter-grain diffusion pathways (e.g. Watson & Baxter, 2007; Wheeler, 2014; Chapman et al., 2019), and drive coupled dissolution-precipitation replacement reactions (e.g. Putnis & Putnis, 2007; Putnis, 2009; Seydoux-Guillaume, 2012). These fluid-aided processes can have major effects at the macroscale for the exhumation of deep crust (Raimondo et al., 2014 and references therein), rates and style of subduction (e.g. Le Pichon et al., 1993; Stern, 2002), arc volcanism (e.g. Morris et al., 1990; Sobolev & Chaussidon 1996; Schmidt & Poli, 1998), and progression and character of orogenesis (e.g. Beaumount et al., 2001; Bercovici, 1998; Jamieson et al., 2011).

Importantly, externally sourced fluids are commonly in disequilibrium with the host rocks through which they migrate and are therefore likely to trigger mineral reactions (Yardley, 2009; Putnis, 2009). The most extreme examples of fluid-rock interaction and associated reaction are usually observed in high-strain zones where time-integrated fluid fluxes and reactive surface area at any one time are high and fluid migration is channelized (Etheridge et al., 1983; Oliver et al., 1990; Selverstone et al., 1991; Cartwright & Barnicoat, 2003; Clark et al., 2005; Daczko et al., 2016; Stuart et al., 2016, 2017, 2018a). In these cases, the rheological consequences are

pronounced and fall into four general categories: (i) fluid-rock interaction results in the production of minerals that have a different rheological behaviour than their precursors (e.g. Brodie & Rutter, 1985; Wintsch et al., 1995; Smith et al., 2015); (ii) fluids cause grain size changes which may change the dominant deformation mechanism (Smith et al., 2015; Menegon et al., 2015); (iii) fluids change the rate of the dominant deformation mechanism (e.g. Karato, 1986); and/or (iv) the actual physical presence of the fluid itself has a rheological effect (e.g. Faulkner & Rutter, 2001, Handy et al., 2001).

Until recently, the observation of hydrated high-strain zones has been focused on zones that experienced interaction with water-rich fluids, most commonly during retrograde metamorphic conditions (e.g. White & Knipe, 1978; McCraig et al., 1990; Menegon et al., 2008; Gonçalves et al., 2012). Often, such fluid-fluxed areas exhibit extensive metasomatism, changing not only the mineral assemblage but also the bulk chemistry of the fluid-fluxed rock (e.g. Spruzeniece & Piazolo, 2015 and references therein). However, recently it has been shown that hydration and strain localization can also occur when a hydrous silicate melt fluxes lower crustal rocks in the roots of magmatic arcs (Stuart et al., 2016, 2017, 2018a; Daczko et al., 2016; Meek et al., 2019). In these cases, the main hydrous minerals produced are amphibole and clinozoisite, controlled by the mafic to intermediate silicate melts inferred to have migrated through the actively deforming high strain zone. A similar process of melt-rock interaction as melt migrates up high strain-zones has also recently been recognised (Ghatak, 2017) in mid-crustal granulite facies rocks of central Australia during the Alice Springs Orogeny. In this particular case, melt metasomatism is inferred to have involved hydrous S-type granitic melts and produced metasomatic rocks rich in biotite and garnet at pressure of 6–8 kbar. The enrichment in biotite and garnet and depletion (i.e. replacement) of quartz and feldspar in precursor rocks suggests the melt temperatures were close to the melt liquidus, where fewer minerals are in equilibrium with the high-temperature melt (i.e. at temperatures above the stability of quartz and feldspar such that these dissolve into the melt; Ghatak, 2017).

Due to the increased porosity and permeability that accompanies deformation, high-strain zones are ideal pathways for fluid migration, either by aqueous fluids or melts (e.g. White & Knipe, 1978; Hutton, 1988; McCaig & Knipe, 1990; D'Lemos et al., 1992; Brown & Solar, 1998; Rosenberg, 2004; Menegon et al., 2008; Gonçalves et al., 2012; Menegon et al., 2015; Stuart et al., 2018a). Both types of fluid migration in high-strain zones are well understood and easily recognised if, in the case of melt, a certain threshold of interconnected fluid (>10%) is present during deformation (e.g. Brown & Solar, 1998; Collins & Sawyer, 1996; Weinberg & Hasalová, 2015; Zavada et al., 2018). Such high proportions are identified in the field by the high percentage of leucosome (Sawyer, 2008). In contrast, lower proportions of melt in a deforming rock (<10%) will have only limited rheological effect (Rosenberg & Handy, 2005), although this is debatable.

However, a lack of field evidence for high proportions of melt does not exclude

the possibility of melt-present rheological weakening, as during the last stages of deformation the melt phase may have been largely expelled (Schulmann et al., 2008; Stuart et al., 2018b). Additionally, recent work has shown that high-strain rocks lacking typical sub-solidus crystal-plastic deformation microstructures (e.g. crystallographic preferred orientations, dynamic recrystallisation, undulose extinction) may be used as an indicator of former melt-present deformation and is suggestive of weakened rocks (Stuart et al. 2018b). Key microstructures used to recognise former melt flux through high-strain zones include: (1) small dihedral angles of interstitial phases; (2) elongate interstitial grains; (3) small aggregates of quartz or feldspar grains connected in three dimensions; (4) fine-grained multiphase aggregates representing melt inclusions (e.g. Cesare et al., 2015); and (5) mm- to cm-scale felsic dykelets (Stuart et al., 2018b). Other melt microstructures such as those observed in migmatites (Sawyer, 1999; Vernon, 2011) may also be useful indicators of former melt-present deformation in high-strain zones.

Glimmerites ("biotitite" in the IUGS classification) are defined as rocks with a very high proportion of mica (>75%, mainly biotite) and have been reported globally in diverse geological settings (e.g. Waters, 1987; Rakotondrazafy et al., 1997; Becker et al., 1999; Fuertes-Fuente et al., 2000; Gregoire et al., 2002, Rajesh et al., 2004, Lin & Sawyer, 2019). Glimmerite is exceptionally hydrous, and its bulk composition does not resemble any classic sedimentary or igneous rock type, apart from small-scale gradational concentrations of mafic minerals in granites and migmatites, i.e. schlieren (Weinberg et al., 2001; Milord and Sawyer, 2003; Zak et al., 2008). Hence, it is likely that glimmerites represent rocks that have undergone extreme chemical change or metasomatism, sensu lato. The most commonly reported occurrence of glimmerite is associated with highly metasomatized mantle rocks caused by interaction with a percolating melt/fluid (e.g. Becker et al., 1999; Gregoire et al., 2002). Glimmerites have also been reported to occur adjacent to felsic intrusions in mantle rocks (e.g. Fuertes-Fuente et al., 2000) and have been interpreted to represent progressive fractional crystallization of mantle melts injected into the lower crust (e.g. Rajesh et al., 2004).

Contrary to these latter examples, the glimmerites studied here are located in a high-strain zone known as the Gough Dam shear zone, central Australia. They are spatially adjacent to and/or surrounded by felsic mid-crustal material (granitic and felsic gneisses). The chosen field example forms part of a regional-scale, 10 km long and 2–4 kilometre-thick belt of glimmerite and other biotite-rich schistose rocks of varying biotite mode. In this contribution, we explore the mechanism of formation of glimmerite by examining well-exposed continuous outcrops that allow detailed field and multi-technique analysis. Based on the glimmerite assemblage, geochemistry, deformation and reaction features and geochronology, we suggest that this intriguing rock type formed as a consequence of extreme melt-rock interaction during felsic peraluminous melt migration through high-strain zones of the Palaeozoic Alice Springs Orogeny.

4-2. General geological background

The area of interest lies in the Strangways Metamorphic Complex (SMC), Arunta Region, central Australia. This basement terrane is a broad belt of dominantly anhydrous upper amphibolite and granulite facies rocks, up to ~125 km wide, metamorphosed during the Strangways Orogeny at c. 1780–1730 Ma (Figure 1) (Shaw et al., 1984; Collins & Teyssier, 1989). Subsequently, it was extensively reworked during the Alice Springs Orogeny (ASO), an intracontinental orogeny during the middle to late Palaeozoic (450–300 Ma) (Collins & Teyssier, 1989; Raimondo et al., 2014). This event caused crustal thickening and deep exhumation of ensialic granulitic basement in the Arunta Region, resulting in an orogen with an estimated horizontal shortening of up to 100 km at its eastern margin (Shaw et al., 1984; Teyssier, 1985; Collins & Teyssier, 1989; Figure 1). An extensive regional network of anastomosing, km-wide high-strain zones bounding the Strangways Metamorphic Complex were reactivated during the ASO, facilitating much of the observed exhumation (e.g. Cartwright et al., 1999; Hand & Sandiford, 1999; Mawby et al., 1999; Ballèvre et al., 2000; Scrimgeour, 2013; Raimondo et al., 2011, 2014; Figure 1). These schistose high strain zones include the West Bore shear zone and Gough Dam shear zone at the northern boundary of the SMC, and the Harry Creek shear zone toward the south.

The studied glimmerite occurs in the Gough Dam shear zone (GDSZ; labelled #1 in Figure 1), located at the northern boundary of the Strangways Metamorphic Complex. The GDSZ trends roughly E-W to NNW-SSE, is steeply dipping 60–90° to the north, and presents a typical width of 1-2 km, but can reach up to 4 km wide. The high-strain zone is described as a significant tectonic discontinuity in the Arunta Region, controlling crustal block separation and reverse south-directed thrusting of the Harts Range Group relative to the Strangways Metamorphic Complex, kinematically informed by shear bands and sigma-type porphyroclasts (Collins & Shaw, 1995; Bendall, 2000; Figure 1). It is characterized by hydration of the bi-modal interlayered originally anhydrous mafic-felsic granulites, quartzofeldspathic and quartzitic gneisses, and minor calcsilicate and amphibolite rocks constituting the Paleoproterozoic basement of the Arunta Region.

4-2.1. Gough Dam shear zone field relationships

The GDSZ features different rock types throughout the schist belt, the most recurrent being phyllonitic biotite-rich quartzo-feldspathic gneiss, felsic and mafic granulite low strain pods, and quartz-rich rafts (Ballèvre et al., 1997). Some low strain areas of the GDSZ include garnet-bearing granulites with garnet crystals up to 8 cm in diameter. A mineral lineation is defined by biotite and sillimanite, and locally kyanite, and shows a steep plunge to the northeast. The selected study area comprises an outcrop of approximately 10 m width by 15 m length of feldspar-biotite-quartz schist (identified hereafter in the text as glimmerite schist) that contains cm to dm scale lenses and layers of strained quartzite (up to 50 cm thick and 10 m in length; Figure 2a, d–f), felsic granulite

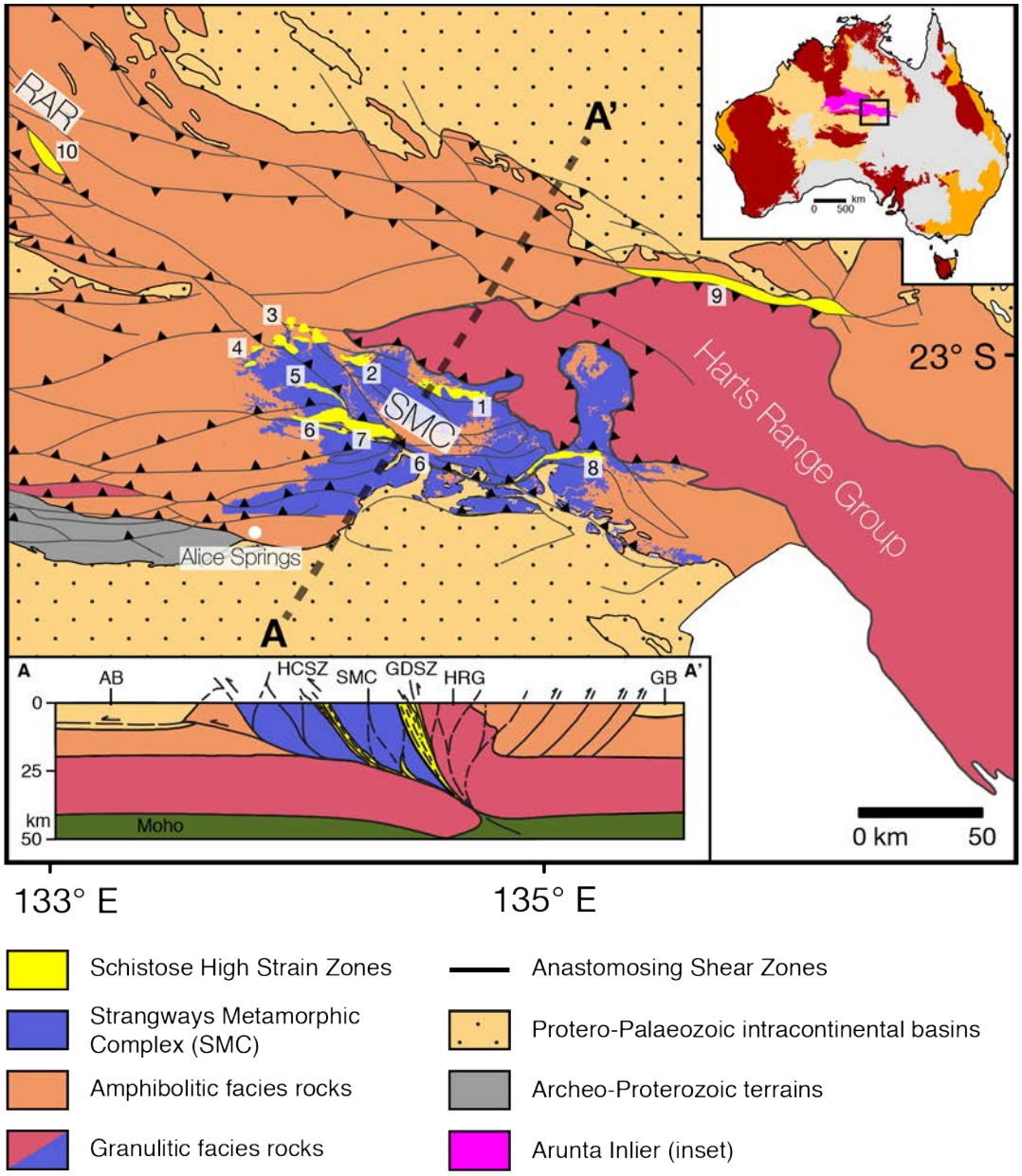

Figure 1. Generalised geological map of the southeastern Arunta Region, emphasizing the distribution of regional schistose belts (e.g. Gough Dam shear zone; yellow structures numbered on map) that cross-cut the dominantly granulite and amphibolite facies rocks comprising this basement terrane. Also represented are the regional anastomosing high-strain zones and thrust faults. Simplified structural cross-section (modified after Raimondo et al., 2014) shows the principal crustal discontinuities and high-strain zones in the Arunta Region associated with the Alice Springs Orogeny (Collins & Teyssier, 1989; Ballèvre et al., 2000; Maidment, 2005; Raimondo et al., 2011; Scrimgeour, 2013). #1 Gough Dam shear zone (GDSZ); #2 West Bore shear zone; #3 Wallaby Knob shear zone; #4 Yambah shear zone; #5 Southern Cross shear zone; #6 Harry Creek shear zone (HCSZ); #7 Erontonga/Two Mile Bore shear zone; #8 Illogwa shear zone; #9 Delny shear zone; #10 Yalbadjandi shear zone (Reynolds–Anmatjira Range (RAR)).

and granitic gneiss that are elongate parallel to the schistose foliation (Figure 2a–c, g). The matrix of the glimmerite schist is dominated by biotite (~50%) with subordinate quartz, muscovite and sillimanite, with mm to cm-wide feldspar grains (Figure 2a–f). Within 200m to the study area, kyanite and staurolite were also observed. Glimmerite dominated by biotite (>75%) is present as cm-wide sleaves adjacent to, crosscutting or ‘invading’ felsic bodies (i.e. quartzite mylonites, granitic gneisses and pegmatites), dispersed as elongated lenses within glimmerite schist (Figure 2c–f). The relationships

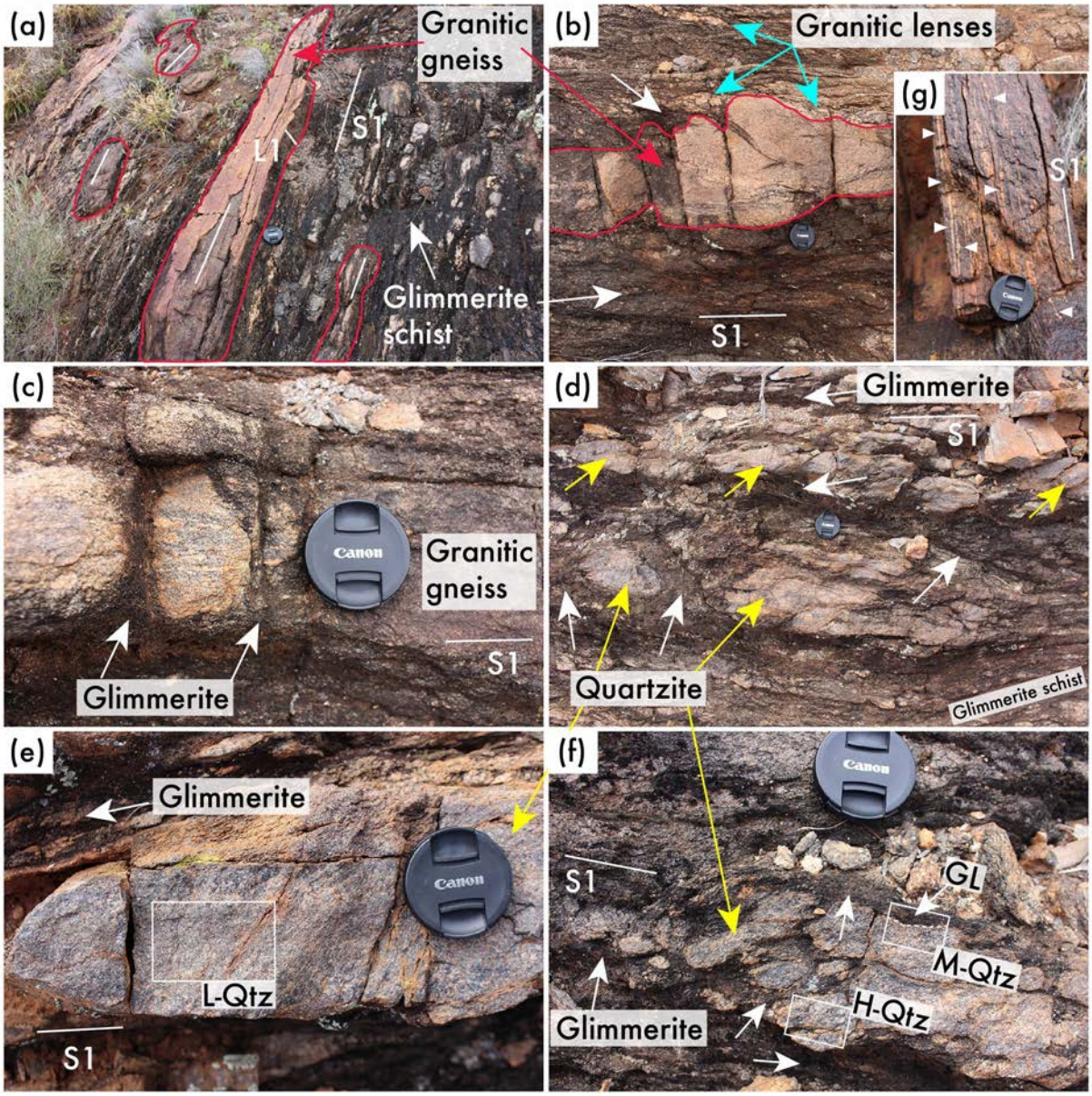

Figure 2. (a) Outcrop looking west of meter-scale glimmerite schist with a well-developed foliation (S1, white line) that contains layers and lenses of felsic rock types, i.e. granitic gneiss and quartzite mylonite. Elongated quartzite mylonite (along S1) and granitic gneiss bodies are surrounded by glimmerite schist. Field sense of shear is north-up reverse (along a steeply-plunging L1); (b) Granitic gneiss elongated along S1 surrounded by glimmerite schist and pegmatite lenses. Granite lenses in glimmerite schist are elongate parallel to S1 foliation. Glimmerite embayments are observed in the granitic gneiss body; (c) Magnification of granitic gneiss lenses 'invaded' by glimmerite along fractures, similar to (a), at a high angle to the foliation; (d) Quartzite mylonite in glimmerite schist unit surrounded and crosscut at a high angle to the foliation by glimmerite seams. Some K-feldspar grains are present in the glimmerite schist; (e) Magnification of the sampled quartzite mylonite hosting sample GD1609A (L–Qtz sample) within the glimmerite schist unit surrounded by glimmerite seams. Less glimmerite 'invaded' along high angle fractures to the foliation is observed; (f) Quartzite mylonite samples GD1609B–C (H–Qtz, H–Qtz and GL sample, respectively). Glimmerite seams warp around and 'invade' the quartzite mylonite, involving most of the H-Qtz sample; (g, top right in figure) Granitic gneiss mylonite displaying plastic deformation of feldspar along S1.

detailed at our study site and focused on for this study are representative of the most extremely hydrated rocks within the hydrous shear zones of the Alice Springs Orogeny.

In the field, the quartzite exhibits classic mylonite features including a strong alignment of biotite and quartz to form a steeply plunging lineation. The mylonitic foliation in the quartzite and granitic gneiss foliation are parallel to the glimmerite foliation

(Figure 2b, c, g). The quartzite mylonite and granitic gneiss is partially dismembered by perpendicular fractures of mm to cm size, exhibiting a range of isolated lenses and blocks ranging from mm to dm size (Figure 2a–f). Glimmerite is seen in brittle fractures oriented perpendicular to the foliation, embayments and irregular partings that define the lenses and blocks (Figure 2a–f). The glimmerite in these dismembered zones contains the same mineral assemblage as observed in the main glimmerite unit. Field evidence suggests that there is a near continuum between quartzite mylonite and glimmerite, with an increasing amount of biotite content from <10% biotite (Bt) representing the original quartzite mylonite to >80% Bt forming the glimmerite (Figure 2 e, f). This progressive increase in Bt content, commonly associated with structural features such as fractures, suggests that there is a causal relationship between Bt content and dismemberment. Hence, field observations suggest an association between chemical change (i.e. reduced quartz and feldspar content and increased Bt content), reaction and dismemberment commonly observed in metasomatic zones (Ferry, 1994).

4-3. Sample selection and analysis

4-3.1. Sample selection

Samples were collected from the Gough Dam shear zone (GPS coordinates 23.1469°S, 134.56517°E, WGS84) and include components of quartz-rich mylonite and glimmerite in contact between them. The samples were selected to represent the observed change in Bt content from a highly quartz-rich mylonite (<10 vol.% biotite) to glimmerite sleeves (>80 vol.% biotite). We therefore selected a sequence of four domains represented by three hand specimens and thin sections: (i) low, <10% Bt content, least-reacted quartzite (Sample L-Qtz [field ID number GD1609A]); Figure 2e and Figure 3a), (ii) medium, ~10% Bt content, medium-reacted quartzite (sample M-Qtz [field ID number GD1609C]); Figure 2f and lower part of Figure 4a), (iii) high, ~15% Bt content, highly-reacted quartzite (sample H-Qtz [field ID number GD1609B]); Figure 2f and Figure 3b) and (iv) glimmerite with >80% Bt (Sample GL [field ID number GD1609C]); Figure 2d–f and Figure 4a). It should be noted that within one hand specimen [field ID number GD1609C], the boundary between M-Qtz and GL is contained. Unless otherwise stated, the two parts of the same samples will be treated separately.

4-3.2. Methods of analysis

4-.3.2.1. Petrography and quantitative orientation analysis

Polished thin sections (30 µm thick) were made from blocks cut perpendicular to foliation and parallel to lineation in both the quartz mylonite and glimmerite.

Petrographic observations of the mineral assemblages were made using a petrographic microscope, the Virtual Petrographic Microscope (Tetley & Daczko, 2014) and ImageJ 1.47v (Rasband, 1997-2018). Microstructural/crystallographic characterisation of thin sections was performed using a FEI Quanta 650 FEG-ESEM with AZtec software and an Oxford/HKL Nordlys S EBSD system at the University of Leeds, UK. EBSD mapping was performed covering large areas of the thin section. Working conditions were: 20 kV accelerating voltage, 20–26 mm working distance, 70° specimen tilt and step size of 8 µm. Automatic indexation was performed using AZtec software (Oxford Instruments). HKL software was used to execute standard noise reduction and to extrapolate missing data using at least and in succession 8, 7, 6 and finally 5 identical neighbours with similar orientation. Grain orientation maps using Euler angles and an inverse pole figure (IPF) were generated using the MTex package (Bachmann et al., 2010; Henry et al., 2017; Henry, 2018). Grains were calculated using a boundary angle >10° misorientation. Dauphine twin boundaries for quartz were defined as quartz-quartz grain boundaries with a 60° rotation around the c-axis. Crystallographic preferred orientation (CPO) of quartz was assessed using pole figures plotted on the lower hemisphere, equal area projection with one point per grain. To quantify the intensity of the CPO, J- and M-indices (Bunge, 2013; Skemer et al., 2005) were computed. Average grain size of minerals was determined using the EBSD data. We present grain size data where Dauphine twins were disregarded.

4-.3.2.2. Imaging and geochemical analysis

Micro X-ray Fluorescence (µ-XRF) analysis of the polished thin sections was used for mineral identification and spatial distribution mapping, quantification of modal proportions, and analysis of thin section scale “whole-rock” major oxides. µ-XRF analyses were performed using the Bruker M4 Tornado spectrometer at Macquarie University Geoanalytical (MQGA), Sydney, Australia. The µ-XRF analyses were run with a tube voltage of 50 kV, a beam current of 200 µA, a chamber pressure of 20 mbar, an acquisition time of 15 ms/pixel and using a step size of 25 µm. AMICS (Advanced Mineral Identification and Characterization System) was used to convert the X-ray fluorescence spectra to produce detailed mineral maps.

High-resolution, high-sensitivity element mapping of polished thin sections on pure silica glass slides was performed to assess the trace element distribution within the reacted quartzite. Mapping was completed using the X-Ray Fluorescence Microscopy beamline and the Maia-384 detector on the Kirkpatrick-Baez mirror microprobe at the Australian Synchrotron, Melbourne (Ryan et al., 2010; Paterson et al., 2011). A beam energy of 18.5 keV focussed to a 2 µm spot size was used. Samples were scanned using a 4 mm step size in both the x and y directions, at a speed of 4 mm/s and a dwell time of 1 ms/pixel. A set of standard foils (Pt, Mn, Fe, YF3) were periodically analyzed for calibration. Data reduction was performed using GeoPIXE (Ryan et al., 1990), which uses the fundamental parameter model for the layered sample, the Maia

detector efficiency model, and the DA matrix method to deconvolute spectra (Ryan et al., 1995, 2015).

Backscatter Electron (BSE) images and associated *EDS* point analysis were used for both mineral identification and imaging of microstructures. Polished thin sections were carbon coated and imaged in a Hitachi Desktop Scanning Electron Microscope (SEM) at the OptoFab node of the Australian National Fabrication Facility, Macquarie University, Sydney, Australia. The operating conditions of the SEM were low vacuum and 15 kV accelerating voltage. For rapid identification of monazite grains the BSE image based Mineral Liberation Analysis on the FEI 650 ESEM at the University of Tasmania, Australia, was used at low vacuum and 20 kV accelerating voltage.

Cathodoluminescence (CL) images were used to identify alteration of elemental concentration and/or crystallographic defects within quartz grains by migrating fluids interacting with the quartzite samples from the study area. The CL images were acquired using a Tescan VEGA3 XM SEM (University of Leeds, UK), operating at 20 kV and a beam current of 20 nA.

Electron microprobe analysis was used to acquire compositional data of silicates using a JEOL JXA 8530F Plus field emission electron microprobe at the Central Science Laboratory, University of Tasmania. The instrument is equipped with a field emission source, running an accelerating voltage of 15 kV, a beam current of 15 nA and a beam size of 10 µm. The instrument has 5 wavelength dispersive spectrometers and is operated using the Probe Software Inc. “Probe For EPMA” software package. Plagioclase Lake County, Hornblende Kakanui, Augite Kakanui, Pyrope Kakanui, Olivine Springwater, Garnet Roberts Victor Mine (all Smithsonian; Jarosewich et al., 1980) and Orthoclase from P&H Developments UK were analysed as secondary standards to confirm the quality of the analysis of the unknown material. A time dependent intensity correction was applied on Na and K if applicable. Oxygen was calculated by cation stoichiometry and included in the matrix correction. Hydrogen was calculated based on the mineral formula and included in the matrix correction as well. The matrix correction algorithm utilized was Armstrong/Love Scott (Armstrong, 1988) and the mass absorption coefficients dataset was LINEMU <10 keV (Henke, 1985) and CITZMU >10 keV (Heinrich, 1966).

Laser Ablation Inductively Coupled Plasma Mass Spectrometry (LA-ICP-MS) was used to collect monazite U-Pb data for age determination using a Resonetics M-50-LR 193 nm excimer laser coupled to an Agilent 7700x Quadrupole ICP-MS housed at Adelaide Microscopy, University of Adelaide. Data was collected from thin sections using 5 pre-ablation shots, 30 seconds of background measurement and 30 seconds sample ablation at 5 Hz, 2 J/cm2 fluence and a spot size of 19 or 13 µm. The raw data signal was reduced using Iolite software (Paton et al., 2011). U–Pb fractionation was corrected using the MAdel monazite standard (TIMS normalisation data: 207Pb/206Pb age = 492.01 ± 0.77 Ma; 206Pb/238U age = 517.9 ± 2.6 Ma; 207Pb/235U age = 513.13 ± 0.20 Ma; updated from Payne et al. (2008) with additional

TIMS analyses). Accuracy was also monitored by repeat analyses of the in-house internal standard 94-222/Bruna-NW (206Pb/238U = 450.2 ± 3.4 Ma; Maidment et al., 2005).

The concentration of rare earth elements in biotite was determined in thin section using a Teledyne Analyte Excite 193 nm excimer laser coupled to an 7700x ICP-MS housed at Macquarie University Geoanalytical (MQGA), Sydney, Australia. Data was collected from thin sections using 30 seconds of background measurement and 30 seconds sample ablation at 10 Hz, 5 J/cm2 fluence and spot size of 150 µm. Silicon (measured by EMP) was used as internal standard for all minerals, and NIST 610 and 612, and basalt from the Columbia River (BCR-2) were used as external standards. The raw data signal was reduced using GLITTER software (Griffin et al., 2008).

4-.3.2.3. Biotite and phengite geothermobarometers

The P–T conditions for each sample are estimated using the titanium-in-biotite thermometer of Henry et al. (2005) and the silicon-in-phengite geobarometer of Massonne & Schreyer (1987). The Henry et al. (2005) geothermometer is based on the titanium (Ti a.p.f.u.) composition of biotite in a peraluminous metapelite with Ti–bearing minerals (ilmenite or rutile) and graphite in the mineral assemblage, equilibrated at 4–6 kbar. Temperature estimates are made by using the concentration of Ti, Fe and Mg in the biotite present in all samples (Table 2). Compared to the Henry et al. (2005) experimental conditions for the geothermometer, the expected accuracy of the temperature estimates is approximately ± 50 °C. This high error is due to the absence of graphite and accessory Ti-bearing minerals in the samples from this study (Figure 3 and 4). Henry et al. (2005) describes the Ti-in-biotite temperature estimate calculations in the absence of Ti-saturating phases as being minimum temperatures estimates.

The Massonne & Schreyer (1987) geobarometer is based on the silicon (Si) composition in magnesium muscovites (phengites) coexisting with alkali feldspar, phlogopite/biotite and quartz minerals. The maximum Si composition in phengite can only be attained if the phengite coexists with the aforementioned mineral assemblage for the geobarometer calculation. For phengites present in the glimmerites, the pressure estimates are expected to be precise since all the necessary minerals for the best pressure calculations are present (Figure 3 and 4). Phengite in quartzite does not coexist with alkali feldspar, limiting the pressure estimates into a minimum pressure formation (Figure 3 and 4).

4-4. Results

4-4.1. Petrography and microstructures

4-.4.1.1. Least Reacted Quartzite (sample L–Qtz; <10vol.% biotite)

Sample L–Qtz (field ID number GD1609A) comprises the mineral assemblage quartz (Qz; ~90 vol.%), biotite (Bt; 8 vol.%) and magnetite (Mt; <1 vol.%) (Figure 3a), along with accessory zircon and monazite (for more details see Section 4.4 – Geochronology). The quartz grains show a variation in morphology from equidimensional, mostly visible in the smaller grains, to an elongated and ribbon-like morphology in the coarser grains (Figure 3a). The majority of quartz grains lack elongation, with small areas showing a weak grain elongation along shear bands. Most quartz grains show signs of high mobility of the grain boundaries, presenting deeply sutured, curved, interlobate quartz-quartz boundaries (Figure 3a). In areas of interstitial biotite between quartz grains, the mobility of the quartz grain boundaries is retarded, shifting from curved or lobate quartz-quartz boundaries to more rectilinear quartz-biotite boundaries (Figure 3a).

The biotite grains in the quartzite are light to dark green and show variable grain dimensions from 100 µm to 5 mm in length and up to 1 mm in width (Figure 3a). Magnetite and biotite are rarely associated and share straight grain boundaries. However, magnetite shares irregular boundaries with quartz. The biotite grains show a shape preferred orientation consistent with the tectonic reverse sense of shear for the high strain zone. Biotite is concentrated between quartz grains or in fractures present in the quartzite (Figure 3a).

4-.4.1.2. Highly Reacted Quartzite (sample H–Qtz; <15 vol.% biotite)

In comparison to sample L–Qtz, sample H–Qtz (field ID number GD1609B) is similarly dominated by quartz (>80 vol.%) and biotite (~15 vol.%) but shows a decrease in the accessory magnetite content to a few isolated grains and the appearance of sillimanite (Sil, <5 vol.%) (Figure 3b, c). It also contains accessory zircon and monazite. Sample H–Qtz displays quartz grains with an overall elongated or ribbon-shaped morphology and a coarsening of the quartz granulometry when compared with sample L–Qtz (Figure 3b). The shape preferred orientation of the quartz elongation is consistent with the tectonic sense of shear observed in the sample. Similar to sample L–Qtz, sample H–Qtz shows a high degree of grain boundary mobility in the quartz grains, leading to deeply sutured, curved, interlobate quartz-quartz boundaries (Figure 3b). However, in contrast to L–Qtz, sillimanite-rich bands are observed in the lower area of sample H–Qtz and here quartz grains show a decreased amount of lobate quartz-quartz boundaries, inverting the overall boundary migration to more rectilinear quartz-quartz boundaries and an increase in ribbon quartz morphology (Figure 3b).

The biotite grains are light to dark green, as observed in sample L–Qtz (Figure 3c). The two-fold increase in biotite in sample H–Qtz compared with L–Qtz accompanies

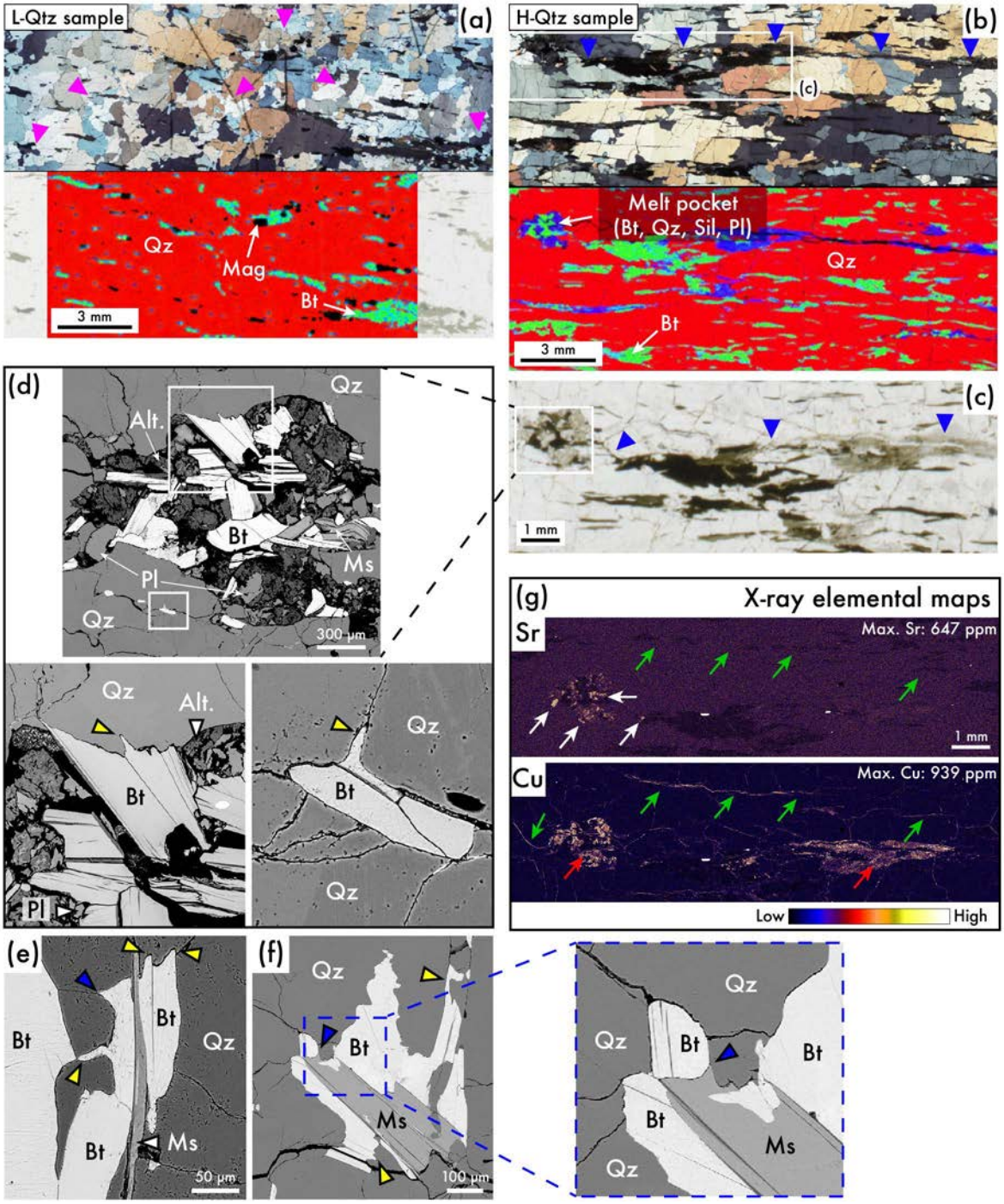

Figure 3. (a–b): Petrography and elemental mapping of quartzite samples. Top: Crossed-polarised light thin section photomicrographs and bottom: thin section µ-XRF maps. Magenta triangles highlight high grain mobility features in quartz grains; blue triangles highlight bands rich in sillimanite that are inferred to be former melt migration pathways that include lenses inferred to have pseudomorphed melt; (c): Plane-polarised light photomicrograph of magnification of H–Qtz sample sillimanite-rich bands (blue triangles); (d): Inferred melt pocket displayed in image (b, c) presenting S-type granite mineral assemblage. Biotite presents interlocking boundaries with surrounding quartz and finger-like protrusions (yellow arrows). (e–f): Biotite, muscovite and sillimanite microstructures; (e): Biotite located in sample H-Qtz showing interlocking boundary with quartz (yellow arrow); (f): Biotite and muscovite grains presenting elongated interstitial grains/finger-like protrusions (yellow arrows) and low apparent dihedral angles (blue arrows) between other grains; (g): Synchrotron X-ray elemental concentration maps of Sr and Cu for area shown in image (c). Mineral abbreviations following Whitney & Evans (2010).

an overall increase in the dimension of the biotite grains and in the formation of contiguous bands (Figure 3b). Biotite grains present rare finger-like protrusions into adjacent quartz grains and quartz-quartz boundaries (Figure 3d, e). The protrusions terminate with low apparent dihedral angles between the quartz-quartz grains (Figure 3e, f). The biotite and muscovite are sometimes intergrown or muscovite may cut biotite (Figure 3e, f). A sillimanite–biotite-rich band is observed in the ribbon quartz area of the sample and is highlighted by blue arrows on Figure 3b and 3c. At the left margin of this band, a circular-shaped lens contains equigranular, euhedral to subhedral biotite, plagioclase, muscovite and quartz, with the biotite interlocking with the host quartz (Figure 3b–d). This lens is inferred to have pseudomorphed melt, showing a spatial concentration of Sr in this particular area due to the presence of plagioclase (Figure 3g). A very fine-grained Al–Si-rich alteration product after plagioclase and sillimanite, inferred to be kaolinite or pyrophyllite (labelled on figures as Alt.), fills grain boundaries and micro-fractures (Figure 3b–d, g).

4-.4.1.3. *Medium Reacted Quartzite and Glimmerite contact (samples M-Qtz–GL; ~10vol.% and ~80vol.% biotite)*

The M-Qtz and GL composite sample (field ID number GD1609C) shows the contact between a sample similar to H-Qtz described above (labelled M-Qtz) and a glimmerite seam (labelled GL; both in Figure 4a). The GL domain is constituted by 80 vol.% biotite, 8 vol.% quartz, 6 vol.% sillimanite and 6 vol.% muscovite (Figure 4a), along with accessory zircon and monazite (for details see Section 4.4 – Geochronology).

Quartz grains in sample M-Qtz show strong similarities in their shape and boundary migration behaviour to the previously described quartz grains present in sample H–Qtz. Dissimilar to H-Qtz, unusual-shaped quartz grains are observed in proximity of the large sillimanite-rich band present in the quartzite when compared to the remaining quartz grains in the M-Qtz sample (Figure 4a–f). These unusually shaped quartz grains present a variation in crystallographic grain orientation less than or equal to 10° between the majority of the targeted quartz grains or within spatially close groups of quartz grains (Figure 4d, e). Multiple quartz grains near the quartzite–glimmerite contact are isolated and surrounded by biotite, in multiple locations, creating biotite filled embayments in quartz grains displaying similar extinction when observed in the crossed polarised light microscope (embayment's highlighted by white arrows in Figure 4f).

Biotite displays generally similar grain shape and microstructures to that described previously in sample H-Qtz, with the presence of finger-like protrusions into adjacent quartz-quartz boundaries (Figure 4g). Sillimanite is present in bands within the quartzite in association with biotite (Figure 4a). The sillimanite grains show an elongated prismatic morphology and extension fractures perpendicular to the sense of elongation. An unidentified material of Si-Al composition fills the fractures (Figure 4h).

A notable increase in monazite and zircon grains is observed in the GL

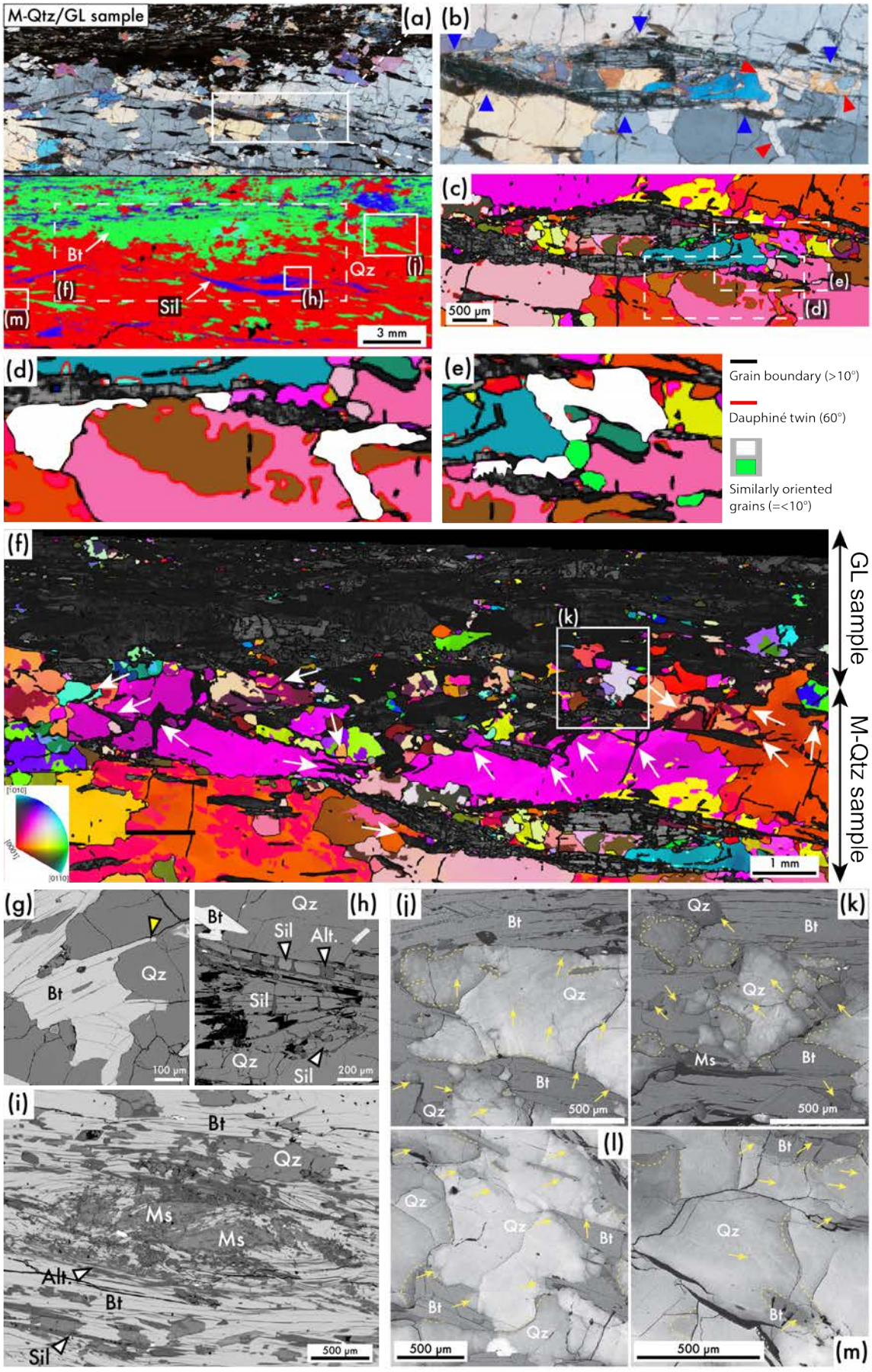
M-Qtz/GL sample
(a)
(b)
(c)
Bt
Qz
(j)
(f)
Sil
(h)
(m)
3 mm
500 µm
(e)
(d)
(d)
(e)
Grain boundary (>10°)
Dauphiné twin (60°)
Similarly oriented grains (=<10°)
(f)
(k)
GL sample
M-Qtz sample
1 mm
(g)
(h)
(j)
(k)
Qz
Bt
Sil
Alt.
100 µm
200 µm
500 µm
Ms
(i)
(l)
(m)

component compared to the quartzite domain and other L–Qtz or H–Qtz samples (for details see Section 4.4 – Geochronology). All the major minerals show a strong preferred orientation in the GL domain (Figure 4i). Similar to sample H-Qtz, biotite and muscovite are sometimes intergrown or may cut each other (Figure 4i), with muscovite crosscutting biotite more often than not. Sillimanite shows a similar elongate morphology, with fractures perpendicular to the long axis (Figure 4h) and is similarly concentrated into bands, as observed in sample M-Qtz and H–Qtz (Figure 4a). Some of the coarser muscovite grains show a sigmoidal shape with biotite warping the larger grains (Figure 4i).

SEM cathodoluminescence (CL) images (Figure 4j–m) show darker CL bands that transgress single grains of quartz. The darker luminescence intensity is also observed at grain boundaries in the majority of quartz grains. These microstructures observed in the CL images are more prominent in domains where the biotite modal distribution is higher, i.e. within or close to sample GL (Figure 4j, k), and are less common in domains with lower biotite mode i.e. sample M–Qtz (Figure 4l, m).

4-4.2. Quantitative quartz orientation analysis

Inverse pole figure (IPF) colored maps for both the M–Qtz and H–Qtz samples show a crystallographic preferred orientation (CPO) of the quartz grains. The majority of grains contain c-axes oriented perpendicular, in the X-axis, to the stretching lineation of the sample (Figure 5a, d).

Crystallographic orientation data for quartz grains present in samples M–Qtz, GL and H–Qtz are represented as pole figures in Figure 5b, e. J-index for all the quartz grains present in the mapping area is 2.86 and 3.35 for the combined M–Qtz/GL samples and H–Qtz sample, respectively (Figure 5b, e). Sample M–Qtz/GL quartz CPO features a [c]–axis maximum parallel to the Y–axis and spreading 45° in the NE sector of the pole figure. <a> axes define a distribution close to the great circle with a main cluster for the <a> axis at ~30–45° from X–axis (Figure 5b).

Results from the three regions delineated for the composite M–Qtz and GL

Figure 4. (a): Petrography and elemental mapping of samples M-Qtz and GL. Top: Crossed-polarised light thin section photomicrograph and bottom: thin section μ-XRF maps; (b): Crossed-polarised light thin section photomicrograph magnification of sillimanite-rich bands in sample M-Qtz. Blue triangles indicate sillimanite-rich bands and red triangles indicate irregular quartz grain shapes; (c): Euler map of quartz grains for the area of image (b), displaying in image (d) and (e) similarly oriented intragranular quartz grains adjacent to sillimanite grain agglomeration; (f): Quartz IPF orientation map and remaining mineralogy band contrast for magnification of samples M-Qtz and GL contact region. White arrows highlight quartz dissolution, dominantly replaced by biotite grains. (g–i): Biotite, muscovite and sillimanite microstructure; (g): Biotite grain presenting elongated interstitial grains/finger-like protrusions (outside field of view of thin section representation in image (a); yellow arrows); (h): Sillimanite grains in quartzite showing perpendicular fractures filled with a cryptic alteration product of Si-Al composition (labelled Alt.); (i): Biotite and quartz grains warping around large deformed muscovite grain (outside field of view of thin section representation in (a)); (j–m): Cathodoluminescence images for selected regions in M-Qtz showing quartz and biotite grain contacts. Dashed lines highlight darker luminescent regions mostly at the quartz grain boundaries when in contact with biotite grains. Yellow arrows highlight narrow dark bands inferred to be healed small fractures within or at the quartz grain boundaries. Mineral abbreviations following Whitney & Evans (2010).

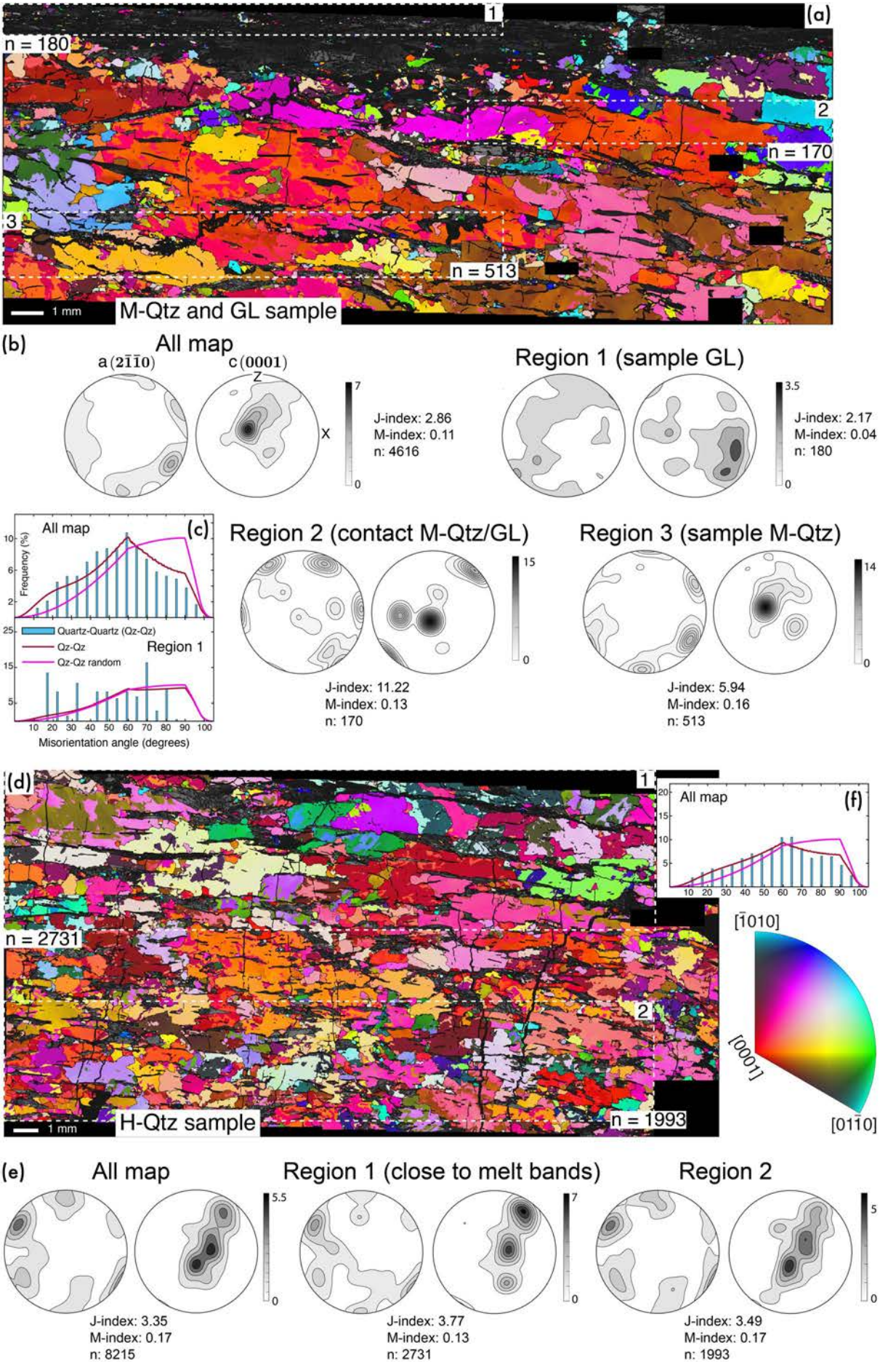

Figure 5. Quartz IPF map relative to the Y-axis for (a) samples M–Qtz and GL, and (d) sample H–Qtz. Regions displayed in each sample represent individual quartz orientation calculation subsets; (b, c)–(e, f): EBSD-derived quartz crystallographic orientation pole figures and neighbouring quartz pair misorientation distribution (blue bars) for respective sample and displayed region.

sample map shows a discrepancy in the quartz grains CPO, J– and M–index between the different regions (region 1 vs region 2 and 3), or put simply, sample GL vs sample M-Qtz (Figure 5b). Region 1 quartz CPO presents a [c]–axis maximum close to the great circle at ~45° from X and Z in the SE sector. This distribution of the <c> axes in region 1 contrasts from the observed <c> axes distribution close to Y for both region 2, 3 in sample M–Qtz. Overall, axes are more randomly distributed in region 1, i.e. sample GL, when compared to region 2 and 3, i.e. sample M–Qtz (Figure 5b). In region 2 and 3, a clustering of <a> axes close to the great circle is distinguishable (Figure 5b).

For quartz in sample H–Qtz, variations between regions are not as extreme as those observed for the composite M–Qtz/GL sample. The <c> axes in region 1 and 2 are similar to the entirety of quartz in the H–Qtz sample – a NE–SW oriented girdle distribution. However, a [c]–axis maximum is observed in region 1 to be close to the great circle, whereas for region 2, the two maxima are displayed close to Y. The <a> axes show similar orientation and distribution for both regions, with a slightly higher girdle like distribution in region 1 (Figure 5e).

The distribution of misorientation between pairs of quartz grains shows a higher proportion of angles below 60° than that expected for a random quartz distribution for the composite sample M–Qtz/GL (Figure 5c), when compared to sample H-Qtz data (Figure 5f). In sample M–Qtz/GL, a contrasting behavior of quartz misorientation between region 1 and the full quartz misorientation data set for sample M-Qtz/GL is observed (Figure 5c). Region 1 shows a nearly perfect random distribution, while sample M-Qtz/GL show a stronger correlated misorientation distribution. H–Qtz quartz misorientations are similar to sample M-Qtz/GL, a slightly correlated distribution below 60° (Figure 5f).

Mean area weighted quartz grain size analysis was performed for the regions included and described in samples M–Qtz/GL and H–Qtz from Figure 5. An increased mean quartz grain size data is observed for region 2 in sample M-Qtz and region 1 in sample H-Qtz, compared to quartz grains present in region 3 and region 2 for samples M-Qtz and H–Qtz, respectively. Quartz grains in sample GL present two orders of magnitude lower mean area weighted quartz grain size compared to the remaining regions described above (Figure 6).

4-4.3. Geochemistry

4-.4.3.1. Glimmerite whole-rock major oxides

Harker diagrams (Figure 7) for whole rock compositions of representative samples of the Strangways Metamorphic Complex (mafic granulites, felsic granulites, metasedimentary rocks and the schistose high strain zones that cut them; references given in Table 1) are presented and compared with data from sample GL. The felsic and mafic granulites generally fall on an array similar to fractionation trends in igneous

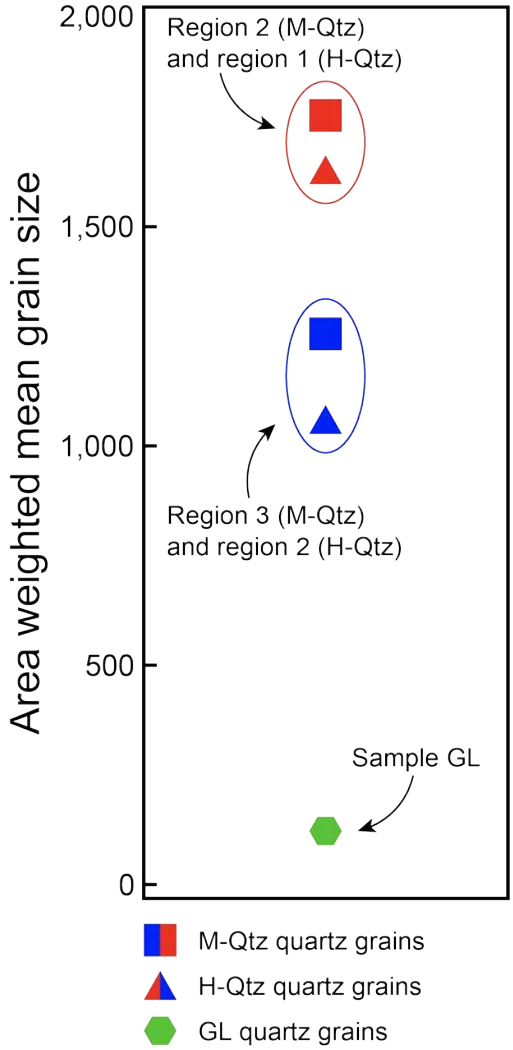

Figure 6. Graphical description of the mean area weighted quartz grain size for the different regions described in Figure 5.

suites (e.g. Winter, 2013; Frost & Frost, 2013). The data for granulite facies metasedimentary rocks of the SMC and the schistose high strain zones largely follow the same trends, forming an array from lower SiO2 metapelitic rocks to higher SiO2 metapsammitic rocks. Felsic granulites are distinct in their high SiO2 content and low Al, Ti, Fe, and Mg. The data for schistose high strain zones is distinguishable from the array of metasedimentary rocks only by having generally lower K2O concentrations. The GL sample of this study shows low Al2O3, high K2O and high TiO2 compared to the majority of the other schistose high strain zones in the region, and lower concentration of TiO2 and FeO compared to average biotite in peraluminous granite.

4-.4.3.2. *Mineral major element chemistry and geothermobarometry*

The totals for added H2O in biotite from all samples averages 3.97 wt% (Table 2). Biotite in sample L–Qtz has variable composition, whereas biotite in the remaining samples is more homogeneous (Table 2, Figure 8a–c). Comparison between samples reveals an increasing biotite TiO2 content, ranging from 0.29 to 2.7 wt%, and Al2O3 (16.64 to 22.03 wt%) from sample L–Qtz to samples H-Qtz/GL (Table S2). Conversely, XMg [= Mg/(Fe+Mg)] shows a decreasing trend from sample L–Qtz to sample H-Qtz (Figure 8a). Biotite in all samples shows moderate concentrations of F (average 0.71 wt%) and Cl (average 0.26 wt%; Table 2) compared to igneous biotite data in literature (Neiva et al., 2002; Cesare et al., 2008).

Figure 8b employs the Nachit et al. (1985) classification and the vast majority of biotite analyses plot in the peraluminous fluid domain. Samples H–Qtz, M–Qtz and GL plot tightly in the same region of the diagram, each cluster showing a minor range in Al and Mg. In contrast, biotite from sample L–Qtz contains noticeably higher Mg and a broader spread of values (Figure 8b). Using the Nachit et al. (2005) biotite classification diagram (Figure 8c), based on the assumption that magmatic biotite composition (primary biotite) changes with hydrothermal interaction (reequilibrated biotite) or neocrystallization at equilibrium with that fluid (neoformed biotite), most analyses from samples M-Qtz, H-Qtz and GL plot in a cluster within the reequilibrated

	SiO_2 wt.%	TiO_2	Al_2O_3	FeO_{total}	MnO	MgO	CaO	Na_2O	K_2O	Total
Average granitic biotite[1] (n=24)	35.50	2.46	19.81	23.19	0.42	4.92	0.12	0.25	9.21	**96.43**
GL sample										
GD1609C	40.63	1.47	18.67	12.64	0.04	6.13	0.00	0.00	9.37	**97.30**
Felsic granulites										
YB10[2]	75.18	0.61	10.30	4.74	0.04	5.86	0.05	0.10	1.30	**99.15**
YB11[2]	65.11	1.17	13.13	8.86	0.11	2.31	5.26	2.27	0.49	**99.67**
YB12[2]	75.26	0.43	11.83	4.04	0.07	4.39	0.19	0.21	1.15	**98.91**
YB13[2]	73.56	0.72	11.21	4.78	0.06	1.28	1.33	2.50	2.66	**99.37**
YB14[2]	73.25	0.65	11.52	4.36	0.06	1.50	1.80	2.71	2.37	**99.24**
A91[3]	73.78	0.10	11.03	4.72	0.03	1.42	1.54	2.99	2.76	**99.72**
A129[3]	76.86	0.81	11.29	5.08	0.25	0.96	1.88	0.62	1.80	**100.28**
12C[4]	73.38	0.42	12.63	2.86	0.02	0.44	1.37	2.64	5.12	**99.44**
14B[4]	75.82	0.41	12.33	1.09	0.02	0.26	1.85	3.28	4.12	**99.57**
15[4]	72.82	0.48	12.56	3.13	0.02	0.69	1.56	2.22	5.53	**99.77**
16[4]	73.43	0.40	13.02	1.98	0.03	0.66	1.61	2.22	5.82	**99.84**
17[4]	73.15	0.42	12.75	3.09	0.03	0.56	1.45	2.40	5.27	**99.77**
18A[4]	71.38	0.60	12.07	4.66	0.02	1.04	0.71	1.90	6.30	**99.49**
18B[4]	75.16	0.60	13.53	0.82	0.02	0.13	3.07	3.40	2.24	**99.59**
19[4]	72.85	0.46	12.58	2.92	0.01	0.67	1.65	2.05	5.46	**99.24**
25[4]	73.01	0.04	14.38	0.28	0.01	0.08	0.59	1.76	9.05	**99.72**
31[4]	73.89	0.03	14.33	0.18	0.01	0.03	0.51	1.43	9.34	**100.15**
30[4]	73.54	0.50	12.24	3.00	0.01	0.36	1.19	1.71	6.31	**99.68**
36[4]	73.09	0.30	12.47	2.61	0.01	0.34	0.14	1.37	8.76	**99.73**
37[4]	73.00	0.51	12.50	2.89	0.01	0.73	1.64	2.34	5.32	**99.65**
38[4]	72.02	0.44	12.73	3.52	0.02	0.62	1.37	2.33	5.83	**99.59**
39B[4]	73.93	0.44	12.90	2.25	0.02	0.66	1.36	3.08	4.37	**99.77**
45[4]	75.38	0.14	13.13	1.20	0.03	0.26	1.30	2.76	5.40	**100.08**
48A[4]	70.73	0.65	13.87	3.10	0.04	0.70	1.78	2.08	6.43	**100.25**
49A[4]	70.54	0.66	12.60	5.45	0.04	0.81	2.07	2.37	4.24	**99.67**
50[4]	74.73	0.28	11.71	2.04	0.02	1.10	0.71	1.60	6.74	**99.65**
54[4]	72.05	0.42	12.50	4.69	0.03	0.22	0.29	1.22	8.01	**100.02**
Mafic granulites										
YB2[2]	62.82	0.61	14.58	7.88	0.08	3.07	8.80	0.54	0.19	**99.98**
YB32[2]	60.42	0.64	16.90	7.82	0.12	2.42	9.42	0.87	0.13	**99.93**
YS148[2]	66.14	0.58	16.01	8.19	0.13	2.03	5.19	0.40	0.06	**99.92**
YS149[2]	52.45	0.53	13.02	19.18	0.23	5.53	6.81	0.53	0.15	**100.49**
YB22[2]	60.89	0.64	14.30	8.08	0.06	2.08	11.42	0.36	0.23	**100.01**
WK55[2]	51.01	0.84	21.02	10.29	0.15	3.80	0.84	1.38	6.29	**98.90**
WK56[2]	45.81	0.93	24.51	10.26	0.10	3.91	0.05	0.74	7.46	**98.73**
A92[3]	48.14	1.43	13.18	14.37	0.30	7.18	9.20	2.02	0.47	**99.27**
A89[3]	46.67	0.92	14.19	13.26	0.29	8.03	11.62	1.42	0.74	**100.51**
A4[3]	52.83	1.83	13.63	9.21	0.12	8.09	11.89	0.69	0.07	**100.46**
A16[3]	67.76	1.17	11.06	5.52	0.04	7.51	2.13	1.03	0.09	**99.97**
A33[3]	64.24	0.73	15.15	5.80	0.07	2.30	9.85	0.85	0.23	**100.32**
A44[3]	63.19	0.68	13.73	8.23	0.11	2.13	8.97	0.61	0.09	**99.54**
10[4]	47.78	1.42	15.11	13.04	0.16	7.90	10.41	1.44	0.76	**99.63**
13A[4]	50.44	2.65	15.36	8.39	0.09	7.60	9.39	1.90	2.01	**99.43**
21[4]	51.52	1.56	15.67	13.55	0.08	6.47	8.30	1.18	0.39	**99.86**
40[4]	47.74	2.11	14.04	13.91	0.16	6.70	9.46	2.83	0.94	**99.48**
42[4]	54.77	1.44	14.46	10.22	0.08	5.13	9.24	3.20	0.58	**99.84**

Table 1. Whole rock major oxides micro-XRF analysis for GL sample and literature average peraluminous granite biotites and SMC major rock types.

Table 1. (continued)

43[4]	49.56	0.73	20.41	6.63	0.07	5.51	12.52	2.98	0.55	**99.75**
44B[4]	50.63	1.36	14.58	13.73	0.17	5.53	8.82	2.99	0.71	**99.69**
48B[4]	54.39	1.55	14.65	12.84	0.18	3.39	7.41	3.32	0.69	**99.79**
49C[4]	47.11	0.72	14.74	14.45	0.15	8.58	8.84	2.18	1.08	**99.12**
51[4]	50.80	0.55	15.76	10.93	0.15	9.02	9.12	2.08	0.22	**99.38**
Metapelites										
YB6[2]	78.80	0.32	10.37	2.25	0.03	1.50	1.63	1.72	1.71	**99.59**
YB8[2]	73.95	0.32	7.85	5.51	0.09	5.81	0.10	0.15	3.76	**99.03**
WK62[2]	77.56	0.32	7.61	6.10	0.05	2.46	1.51	1.03	1.78	**99.57**
WK61[2]	75.85	0.40	10.96	2.30	0.03	2.97	0.48	0.23	3.79	**99.18**
A93[3]	73.96	0.51	11.34	3.69	0.02	2.02	1.33	2.16	3.61	**100.12**
A128[3]	76.45	0.81	11.29	4.97	0.00	1.11	1.98	0.58	1.81	**99.90**
A1[3]	73.84	0.71	10.99	4.47	0.06	0.75	1.48	2.69	3.12	**99.94**
A22[3]	61.91	0.61	17.63	7.80	0.45	1.95	4.10	1.92	2.11	**100.31**
A107[3]	73.51	0.25	13.85	3.55	0.05	0.80	1.83	1.73	2.80	**100.48**
23[4]	54.05	0.78	21.17	8.11	0.08	2.70	0.70	1.45	9.52	**99.63**
28[4]	53.35	0.78	22.45	8.27	0.10	2.69	0.80	1.33	8.21	**99.6**
29[4]	56.80	0.68	20.88	6.23	0.06	2.65	0.85	2.32	7.80	**99.59**
601[4]	53.56	1.05	24.01	9.81	0.13	3.61	0.41	0.78	5.20	**99.96**
621[4]	50.41	1.13	26.68	11.71	0.09	3.35	0.21	0.32	4.25	**99.84**
701[4]	53.88	0.88	24.70	9.84	0.08	2.94	0.31	0.57	5.10	**100.04**
709[4]	55.88	0.69	19.82	9.51	0.10	1.78	0.72	1.63	8.49	**100.24**
728[4]	51.43	1.04	24.20	11.56	0.27	3.58	1.44	0.28	4.25	**100.2**
757[4]	60.71	1.06	17.80	10.99	0.11	3.47	1.36	0.66	2.39	**100.29**
784[4]	50.53	0.87	24.65	16.79	0.22	5.07	0.52	0.00	0.17	**100.29**
807[4]	43.93	1.04	30.97	11.31	0.14	3.88	1.33	0.75	4.22	**100.31**
822[4]	47.73	0.66	27.23	12.25	0.21	3.97	1.29	1.34	3.26	**99.96**
Metapelites SHSZ										
YB19[2]	53.93	0.72	24.20	8.40	0.05	3.00	0.14	0.43	5.18	**99.36**
YB30[2]	52.75	0.53	29.76	7.22	0.11	4.53	0.09	0.17	2.43	**99.38**
YB31[2]	42.17	1.63	27.40	17.40	0.20	3.98	0.06	0.29	3.22	**99.4**
WK59[2]	56.28	0.63	17.74	7.57	0.23	2.55	6.99	0.18	3.93	**99.25**
WK59A[2]	55.36	0.72	16.15	8.95	0.25	2.49	6.23	0.22	5.33	**99.06**
WK60[2]	55.58	0.65	14.69	7.78	0.20	2.87	15.70	0.17	0.05	**100.17**
A18[3]	59.52	0.68	23.59	7.56	0.22	2.94	0.83	0.84	2.13	**100.79**
A43[3]	57.58	0.76	22.94	8.29	0.08	3.89	0.44	0.56	3.36	**100.45**
A99[3]	54.28	0.80	22.80	11.52	0.10	2.42	1.31	1.01	3.54	**100.55**

[1] Neiva et al., 2002; [2] Bendall, 2000; [3] Iyer, 1974; [4] Norman, 1991; SHSZ: Schistose High Strain Zone

biotite domain and adjacent to the primary biotite domain, whereas sample L–Qtz is scattered between the neoformed and reequilibrated domains (Figure 8c).

A plot of Ti a.p.f.u. vs XMg shows a trend of increasing Ti with decreasing XMg in biotite from samples L–Qtz to M–Qtz–GL (Figure 8a). The application of the Ti-in-biotite thermometer of Henry et al. (2005) indicates highly variable minimum formation temperatures, 300–570 ± 50 °C for sample L–Qtz, ~630 ± 50 °C for biotite in the quartzite and glimmerite domains of sample M–Qtz–GL, and ~660 ± 50 °C for sample H–Qtz (Figure 8d). In samples were phengites are present (H–Qtz and M–Qtz–GL), the Si-in-phengite geobarometer of Massonne & Schreyer (1987) was applied. Phengites from these samples present Al slightly lower than 3.1 a.p.f.u., which in combination with the Ti-in-biotite thermometer (Henry et al., 2005) allows us to discriminate their pressure formation at ~5–6 kbar (Figure 8d).

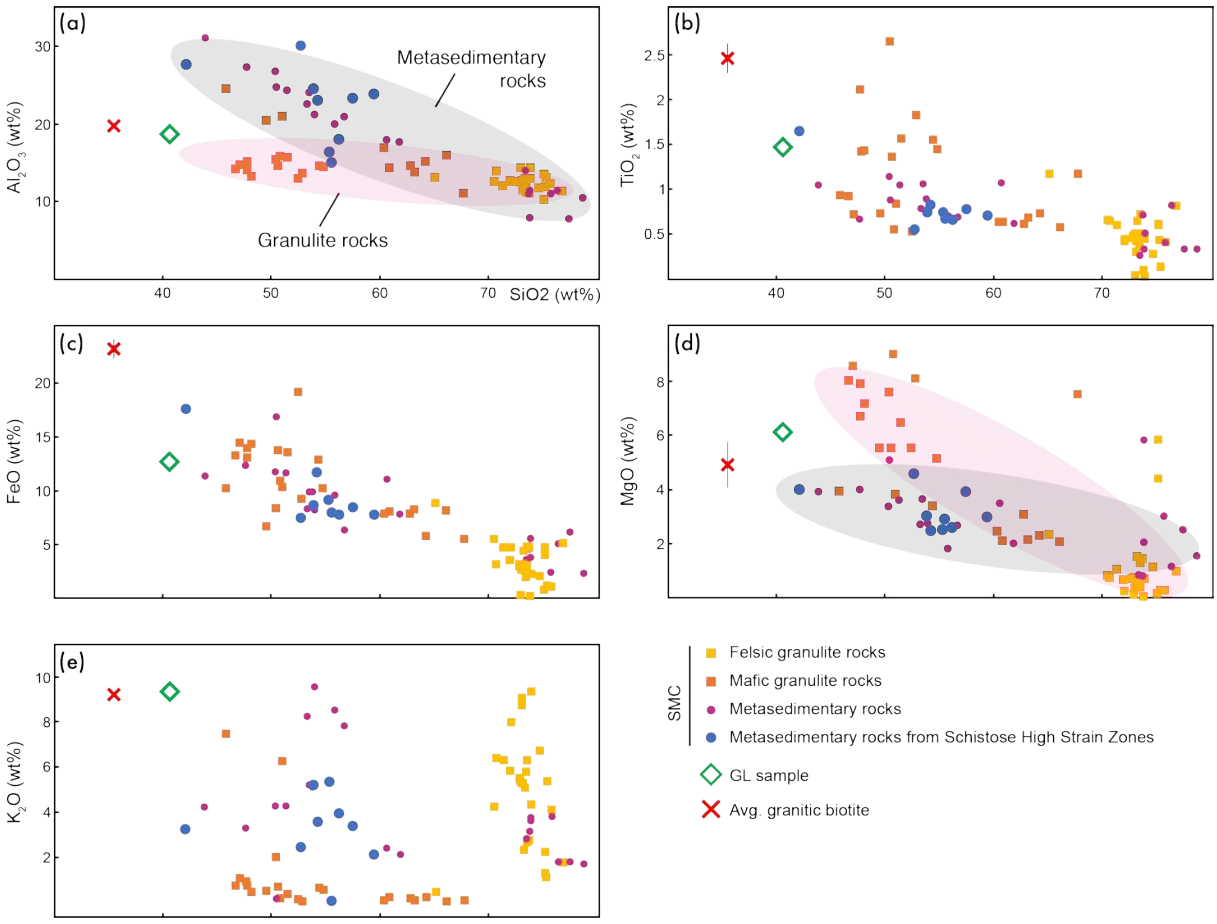

Figure 7. Harker diagrams for whole rock major oxides (Al2O3, TiO2, FeO, MgO and K2O vs SiO2) for selected rock types present in the Strangways Metamorphic Complex, sample GL (this study) and average biotite composition for peraluminous granites (Neiva et al., 2002). See Table 1 for all data references. Standard deviation for average biotite composition displayed only if larger than the symbol.

4-.4.3.3. *Biotite trace element chemistry*

For all samples, the biotite concentrations for Zr, Hf, Nb, Ta (Table 3) normalized to chondrite (McDonough & Sun, 1995) follow similar patterns. Zr values are consistently below chondrite (Figure 9a–c), except for a single biotite analysis from the M–Qtz–GL sample (Figure 9c). Hf values are likewise depleted but to a lesser extent (Figure 9a–c), again with the exception of the previous distinctive Zr-enriched biotite grain conjointly enriched in Hf (Figure 9c). In contrast, Nb and Ta show consistently enriched values (Figure 9a–c). A distinction in Nb and Ta concentration is observed between the values for sample L–Qtz and the remaining samples (H–Qtz and M–Qtz–GL), with the former displaying lower concentrations of Nb (Figure 9a) compared to the remaining samples (Figure 9b,c), while showing equivalent values of Ta (L–Qtz ~167–232; pair H–Qtz ~143–225 times chondrite; Table 3; Figure 9a–c and Figure 10c).

Biotite grains in all samples show a consistent depletion in rare-earth elements (REE) compared to the chondrite values (Table 3 and Figure 9a–c). Similar behaviour is observed for all chondrite-normalized REE patterns, with a slight decrease in LREE trending down from La to Sm in comparison to the HREE (Figure 9a–c). Compared to biotite in samples H–Qtz and M-Qtz/GL, sample L–Qtz shows a more variable pattern of LREE enrichment and an overall increased concentration of LREE (Figure

Sample	L-Qtz		H-Qtz			M-Qtz			GL		
Mineral	Bt	Mag	Bt	Ms	Pl	Bt	Ms	Sil	Bt	Ms	Sil
SiO_2 wt%	36.74	b.d.l.	35.70	44.49	62.89	35.89	44.55	36.03	35.64	44.56	36.06
TiO_2	0.83	0.03	2.35	0.86	b.d.l.	1.86	0.60	b.d.l.	1.97	0.60	b.d.l.
Al2O3	17.49	0.43	18.23	32.82	23.00	18.28	33.32	63.23	18.36	33.07	63.41
V_2O_3	b.d.l.	0.06	0.05	b.d.l.	b.d.l.	0.06	0.03	b.d.l.	0.04	0.03	b.d.l.
Cr_2O_3	b.d.l.	b.d.l.	b.d.l.	b.d.l.	b.d.l.	b.d.l.	b.d.l.	b.d.l.	0.04	b.d.l.	b.d.l.
FeO_{total}	13.92	92.19	16.22	3.24	0.05	15.70	3.36	0.84	15.20	3.21	0.83
NiO	b.d.l.	b.d.l.	b.d.l.	b.d.l.	b.d.l.	b.d.l.	b.d.l.	b.d.l.	0.06	b.d.l.	b.d.l.
MnO	0.05	0.07	0.07	b.d.l.	b.d.l.	0.06	b.d.l.	b.d.l.	0.05	b.d.l.	b.d.l.
MgO	15.32	0.06	12.15	0.97	b.d.l.	12.53	0.96	b.d.l.	12.66	0.90	b.d.l.
CaO	0.03	b.d.l.	b.d.l.	b.d.l.	3.67	b.d.l.	0.02	b.d.l.	b.d.l.	b.d.l.	b.d.l.
Na_2O	0.16	b.d.l.	0.19	0.51	9.36	0.26	0.63	b.d.l.	0.23	0.56	b.d.l.
K_2O	9.72	b.d.l.	9.86	10.53	0.19	9.82	10.00	0.01	9.79	10.63	b.d.l.
P_2O_5	b.d.l.	b.d.l.	b.d.l.	b.d.l.	0.07	0.03	b.d.l.	b.d.l.	b.d.l.	b.d.l.	b.d.l.
SO_3	b.d.l.	b.d.l.	b.d.l.	b.d.l.	b.d.l.	b.d.l.	b.d.l.	b.d.l.	b.d.l.	b.d.l.	b.d.l.
Cl	0.26	b.d.l.	0.18	b.d.l.	0.02	0.18	0.06	b.d.l.	0.19	0.02	b.d.l.
F	0.92	b.d.l.	0.67	0.06	b.d.l.	0.66	0.12	b.d.l.	0.71	0.08	b.d.l.
O	-0.45	0.04	-0.32	-0.03	-0.02	-0.32	-0.07	0.00	-0.34	-0.04	-0.01
H_2O	3.99	0.00	3.96	4.45	0.00	3.97	4.45	0.00	3.98	4.45	0.00
Total	98.99	92.89	99.30	97.89	99.25	99.00	98.04	100.11	98.57	98.07	100.30

Mineral abbreviation following Whitney and Evans (2010). B.d.l.: Bellow detection limit. The complete dataset is available in Supplementary Data.

Table 2. Selected electron microprobe data on multiple minerals for the reacted quartzites and glimmerite seams in Gough Dam shear zone.

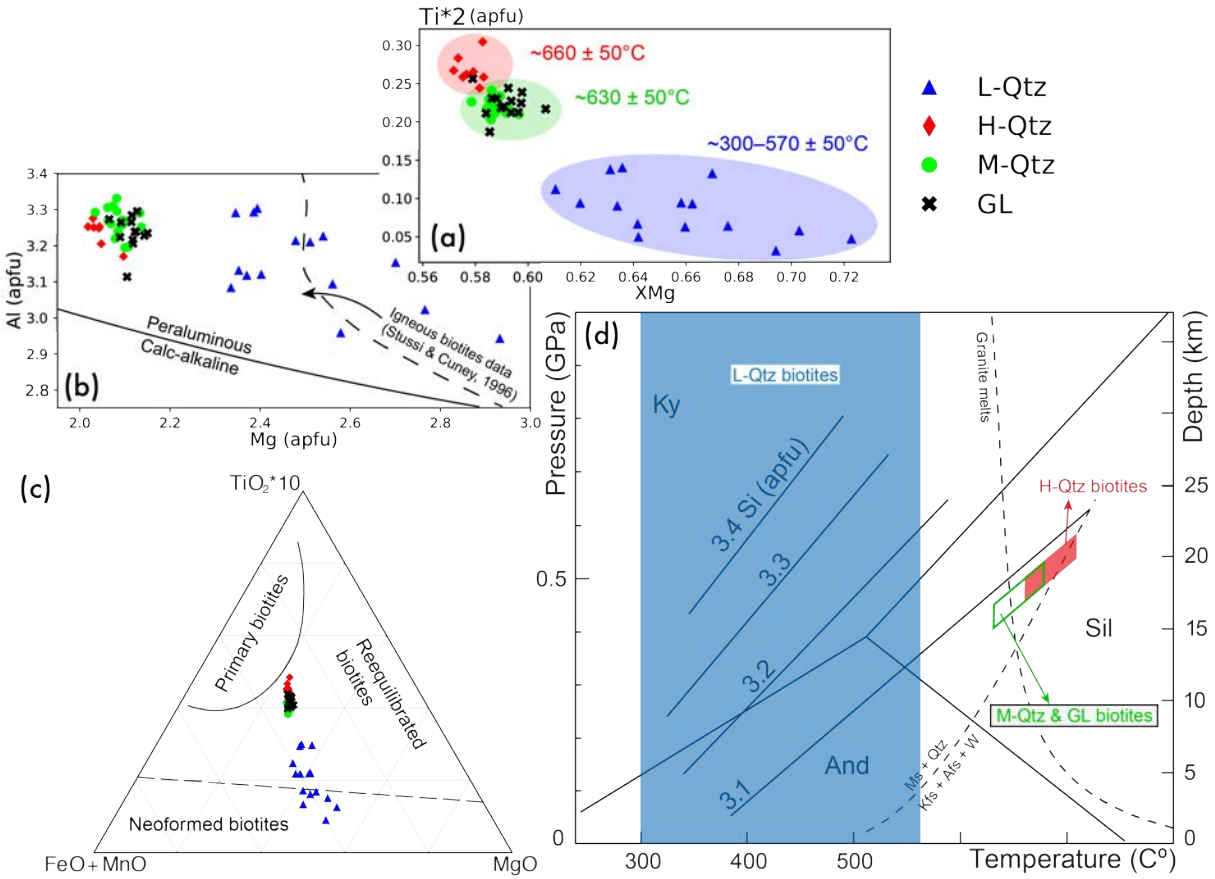

Figure 8. (a) Ti atoms per formula unit (a.p.f.u.) vs XMg diagram for biotite from all samples; (b) Al vs Mg a.p.f.u. classification diagram for biotite in igneous rocks (after Nachit et al., 1985 and Stussi & Cuney, 1996); (c); Ternary diagram TiO2 x10–(FeO+Mn)–MgO for discrimination between primary magmatic, reequilibrated and neoformed biotites (Nachit et al., 2005); (d) P-T diagram for Gough Dam shear zone samples, using Ti in biotite for temperature (Henry et al., 2005) and Si in phengite for barometry (Massonne & Schreyer, 1987).

	Gough Dam Shear Zone			Compilation of published biotite compositions						
Sample	L-Qtz (GD1609A)	H-Qtz (GD1609B)	M-Qtz & GL (GD1609C)	Two-mica granite[1]	Diatexite migmatite[2]	Metapelite xenolith[3]	Pegmatite[4]	Mica schist[5]	Rhyolite/ Rhyodacite[6]	Experiment[7]
Zr	0.21	0.35	0.28	n.a.	n.a.	1.41	n.a.	n.a.	40.05	n.a.
Hf	0.66	0.96	0.66	n.a.	n.a.	2.52	n.a.	n.a.	27.77	n.a.
Nb	85.13	221.75	188.88	n.a.	197.08	341.67	n.a.	n.a.	283.33	208.33
Ta	134.71	216.18	183.09	n.a.	462.50	323.53	n.a.	n.a.	119.85	1397.06
La	b.d.l.	0.016	0.009	0.717	0.169	0.253	7.890	107.173	342.194	n.a.
Ce	0.013	0.002	0.002	0.277	0.196	0.016	5.726	81.240	274.062	n.a.
Pr	0.018	0.008	b.d.l.	0.970	0.108	0.216	5.065	n.a.	n.a.	n.a.
Nd	0.014	0.009	0.009	0.700	0.088	0.131	4.136	52.516	133.479	n.a.
Sm	b.d.l.	b.d.l.	0.107	0.405	0.068	0.068	8.851	24.662	53.243	n.a.
Eu	0.357	0.702	0.444	0.533	0.355	2.664	0.710	11.368	7.105	n.a.
Gd	b.d.l.	b.d.l.	0.068	0.452	0.050	0.653	13.920	16.332	n.a.	n.a.
Dy	b.d.l.	b.d.l.	b.d.l.	0.122	0.033	0.081	19.553	10.163	17.195	n.a.
Er	0.018	b.d.l.	b.d.l.	0.125	0.044	0.063	11.000	n.a.	n.a.	n.a.
Yb	b.d.l.	b.d.l.	b.d.l.	0.124	0.050	0.124	10.932	6.832	15.466	n.a.
Lu	0.043	0.067	0.031	n.a.	0.081	n.a.	9.756	69.106	15.041	n.a.

REE and trace elements values were normalised using McDonough & Sun (1995) chondritic values.

(1) Bea et al., 1994a; (2) Bea et al., 1994b; (3) Acosta-Vigil et al., 2010; (4) Hulsbosch et al., 2014; (5) Laul & Lepel, 1987; (6) Nash & Crecraft, 1985; (7) Stepanov & Herman, 2013. The complete dataset is available in Supplementary Data. b.d.l.: Bellow detection limit; n.a.: Non available.

Table 3. Representative LA-ICP-MS trace element and REE composition data for biotite grains from the Gough Dam shear zone, and comparison to published data from multiple locations and formation settings exogenous to the study area.

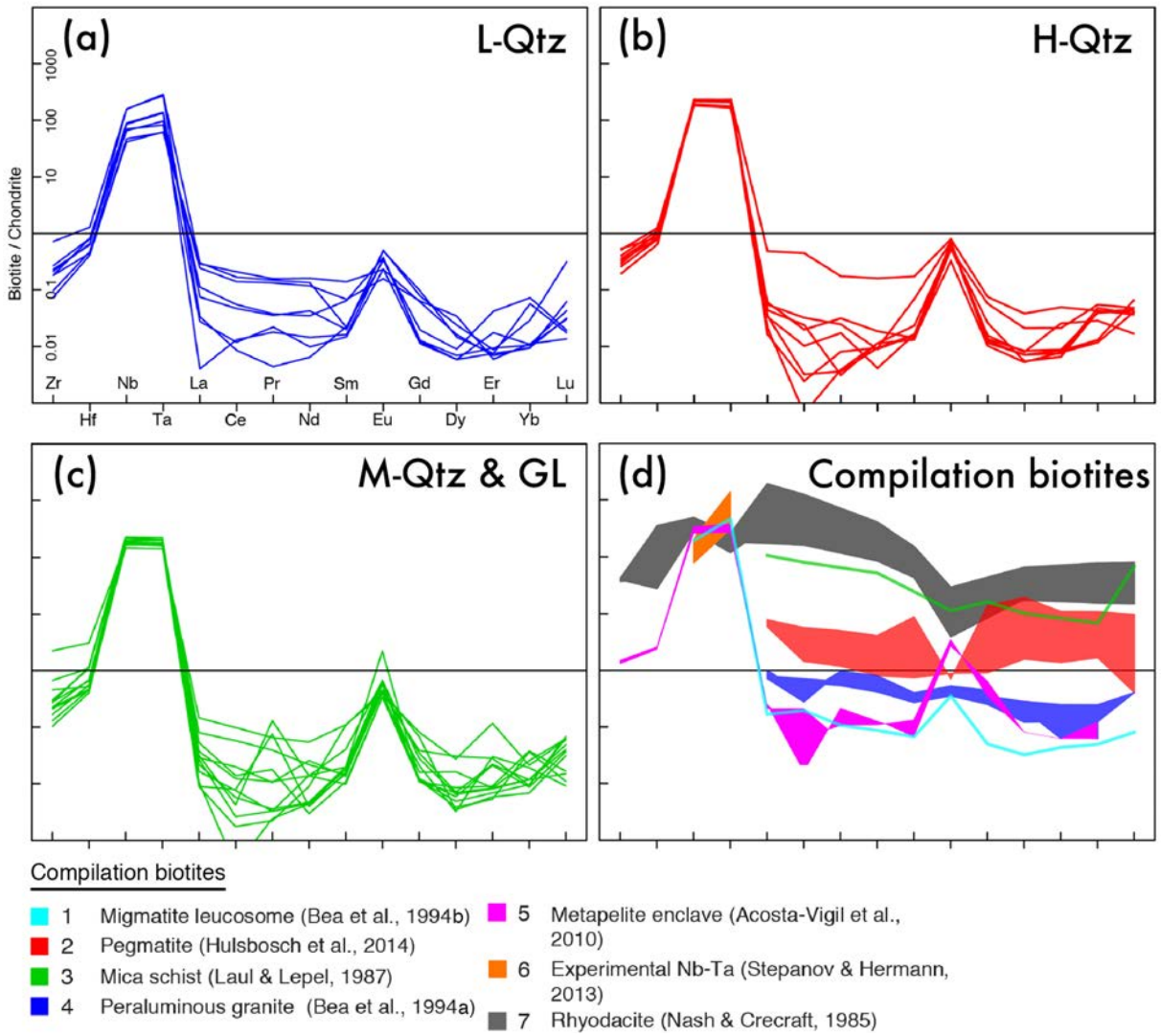

Figure 9. Chondrite-normalized trace elements and REE patterns for biotite in (a–c) Gough Dam shear zone samples and (d) literature compilation (detailed in Table S1).

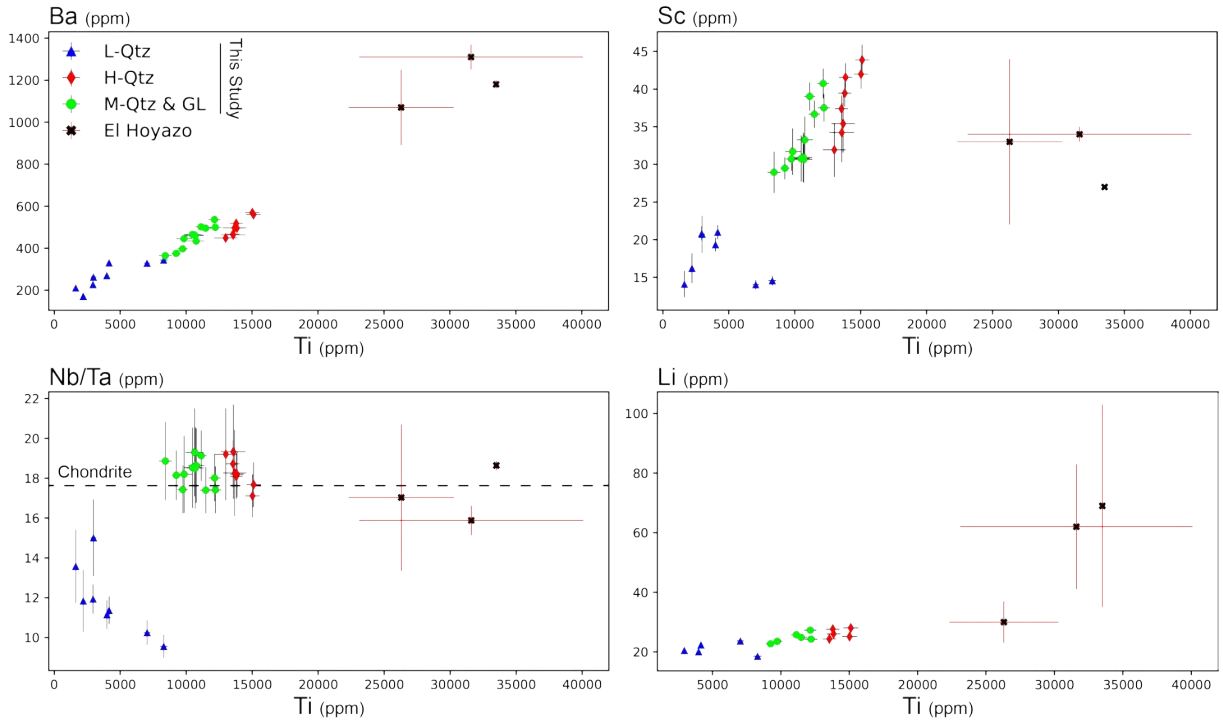

Figure 10. Correlation diagrams for Ti vs Ba, Ti vs Sc, Nb vs (Nb/Ta) and Ti vs Li from Gough Dam shear zone samples and additional data from El Hoyazo enclaves (Table S1; Acosta-Vigil et al., 2010). Black error bars: measured uncertainty of individual analysis; Red error bars: Standard deviation of multiple analyses.

9a–c). Overall, biotite HREE patterns show a concave-up shape due to higher Lu concentrations compared to the remaining HREE. All data present a pronounced positive Eu anomaly (Figure 9a–c) for sample H–Qtz and the combined M–Qtz and GL biotite analyses, with a slightly weaker anomaly for sample L–Qtz.

Figure 9d and Table S1 compile published values and sample descriptions for natural and experimental igneous and metamorphic biotite normalized to chondritic concentrations (McDonough & Sun, 1995). The Gough Dam samples present lower concentrations of Zr, Hf and REE compared to the compiled data, but have similar values of Nb and Ta, especially in relation to the metapelitic peraluminous El Hoyazo enclaves (Figure 9; Cesare et al., 1997; Acosta-Vigil et al., 2010) and the peraluminous migmatite biotite of Bea et al. (1994b).

Two groups of biotite composition are distinguishable on bivariate plots of niobium/tantalum (Nb/Ta) versus Nb, and barium (Ba), scandium (Sc) and lithium (Li) versus Ti (Figure 10). Sample L–Qtz is depleted compared to H–Qtz and the combined M–Qtz and GL biotite analyses, with the pooled data forming a positive correlation trend. The enrichment trend is also visible if compared to El Hoyazo biotite (Acosta-Vigil et al., 2010), which plots as either the most Ba and Li enriched analyses or at equivalent Nb/Ta and Sc concentrations with samples H-Qtz, M-Qtz and GL (Figure 10). Within the group of Nb-enriched biotite (samples H–Qtz, M–Qtz and GL), Nb values above the chondritic concentrations of McDonough & Sun (1995) is observed for samples H–Qtz and M–Qtz/GL. In general, the order of Ba, Li and Sc in biotite concentration is observed as L–Qtz< M–Qtz/GL≤ H–Qtz.

4-4.4. Geochronology (U–Pb monazite)

Monazites from samples M–Qtz (low biotite vol.%; Figure 11a–b) and GL (high biotite vol.%; Figure 11c–d) are generally located in contact with or surrounded by biotite and sillimanite, with few grains located adjacent to quartz grain boundaries or fractures. Monazite grains are rounded to elongate and 50–200 μm in the longest dimension (Figure 12a), but with a range in size and shape observed for all samples. Several grains show zonation in BSE images, usually with higher BSE response in core domains or multiple zones of variable BSE response (Figure 12a). Curved, inward-penetrating boundaries between core and rim domains and cross-cutting textures in BSE images are visible in some grains. Thorite inclusions, inferred to have formed during the breakdown and regrowth of monazite, are mostly contained in brighter zones of monazite near the contact with small darker patches or in small micro-fractures (Figure 12a). The remaining grains, usually tending to smaller dimensions, do not present any observable zonation.

From all samples described above, 56 spot analyses on 39 monazite grains were obtained. Data with <2% discordance show two discernible age groups (Figure 12b and Table S2): (i) Palaeoproterozoic ages ranging from 1740 ± 16 Ma to 1630 ± 19 Ma with a density age estimation at c. 1669 Ma; and (ii) Neoproterozoic to Palaeozoic ages ranging from 606.1 ± 5.8 Ma to 370.9 ± 3.6 Ma with a density age estimation at c. 451 Ma. By including the spread of discordant analyses, the upper intercept age is 1660 ± 2.3 Ma with a lower intercept age of 477 ± 0.85 Ma, although with large dispersion resulting in an MSWD of 17 (Figure 12b). A significant portion of discordant analyses are spread along the discordia line towards its upper intercept, leaving the remaining analyses located closer to the intersection between the discordia line and the younger concordant Palaeozoic age group, creating a complex age distribution at the lower intercept (Figure 12b).

The obtained monazite ages are not homogenously distributed throughout samples M–Qtz and GL (Figure S1). Sample M–Qtz includes all the Early Palaeoproterozoic analyses, broadly coinciding with the timing of peak metamorphism during the Strangways Orogeny (c. 1780–1730 Ma). It also contains isolated grain clusters that record a spread of Neoproterozoic–Palaeozoic ages (Figure S1). In contrast, the adjacent glimmerite component (sample GL) hosts a much narrower age span, with most monazites recording Palaeozoic ages and a greater proportion falling within the age bounds of the ASO (450–300 Ma; Figure S1). Discordant ages from both samples reflect the lower BSE response zones and/or rim areas of monazite grains (Figure 12a).

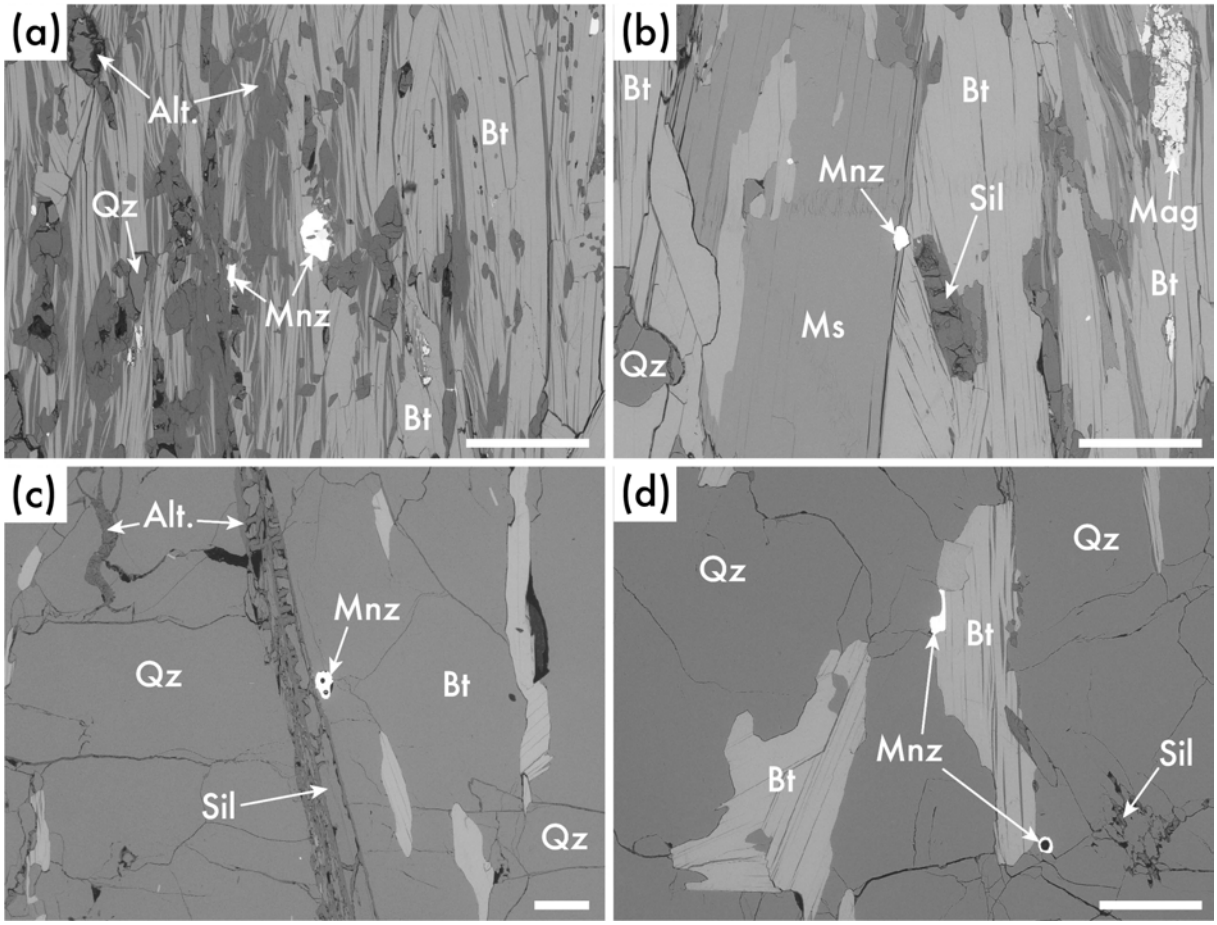

Figure 11. Textural relationship for monazite grains present in the low biotite modal composition, sample M–Qtz, and the high biotite modal composition, sample GL. Scale 200 μm.

4-5. Discussion

4-5.1. Conditions and timing of glimmerite formation

Combined petrography, mineral geochemistry and monazite geochronology across the cm-scale transect of variably modified quartzites from the Gough Dam shear zone provides insight into the geological environment that formed the biotite-rich mineral assemblages and the P-T-t conditions of this process. The P–T estimation using mica in the studied samples suggests mid-crustal conditions of formation at P >4–5 kbar and T >570–660°C (Figure 8), similar to previously published conditions from the GDSZ and other Palaeozoic shear zones in the Strangways region (Ballèvre et al., 2000; Bendall, 2000). Due to the lack of graphite and Ti-bearing accessory minerals in all samples, temperature estimates are minimum values. Note also that this influences the pressure estimates, suggesting they are also minimum values. The upper end of the calculated temperature range lies above the hydrous granite solidus and is consistent with field observations of syn-deformational granitic lenses in the GDSZ (Figure 2b, g).

The relationship between age and textural position of monazite grains in the studied samples suggests the precursor quartzite initially experienced metamorphism during the Strangways Orogeny (c. 1730 Ma), followed by a subsequent metamorphic

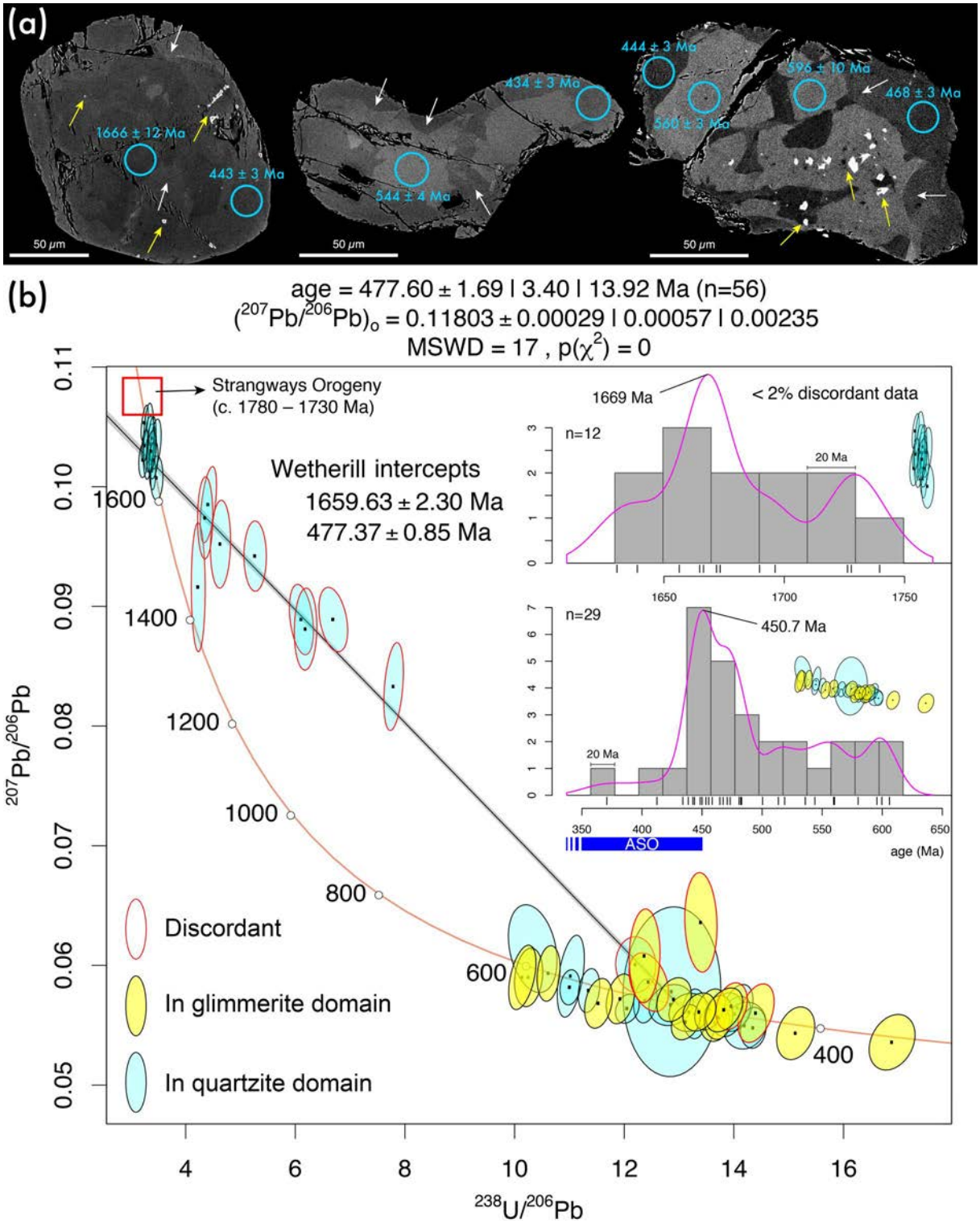

Figure 12. (a) Morphology and textures of representative monazite grains in back-scattered electron imaging. 206Pb/238U ages with associated errors (2 SE) are displayed, and full analytical results are given in Table S2. White arrows indicate inward-penetrating boundary interfaces and yellow arrows indicate thorite inclusions; (b) Tera-Wasserburg concordia plot showing U–Pb geochronological data from samples M–Qtz and GL and kernel density estimation for data with < 2% discordance.

event during the Alice Springs Orogeny (c. 450–300 Ma) that is largely recorded in the cross-cutting glimmerite (Figure 12). The morphology of the monazite grains and zonation patterns in BSE intensity suggests that the monazites were modified by fluid-assisted (melt-assisted) coupled dissolution-precipitation reactions (Figure 12a). The concordia lower intercept age at c. 477 Ma intersects a significant spread

of Neoproterozoic to Paleozoic ages (c. 606–371 Ma; Figure 12). These complex age data can be interpreted in two ways: (i) the individual age data are geologically meaningful and reflect multiple reactivation and fluid flow events in the GDSZ; or (ii) the data reflect partial age-resetting of inherited monazite grains during one or more Palaeozoic reactivation and fluid flow events in the GDSZ.

On the basis of coupled dissolution-precipitation experiments which demonstrate that the replacement of precursor monazite may be incomplete, forming nanomixtures of old and new monazite (Grand-Homme et al., 2016, 2018), we prefer the interpretation that some of the Neoproterozoic to Paleozoic monazite ages are unlikely to be geologically meaningful. This young age cluster is therefore difficult to use to precisely date the timing of glimmerite formation, beyond stating that it occurred broadly during the Alice Springs Orogeny. Notably, however, the most significant age peak from the kernel density estimation occurs at 451 Ma, consistent with U-Pb monazite ages from similar shear zones of the Strangways Range (Möller et al., 1999; Howlett et al., 2014; Fournier et al., 2016). This timing reflects the earliest onset of the Alice Springs Orogeny recorded regionally (Mawby et al., 1999; Raimondo et al., 2014), perhaps suggesting a peak in melt-rock interaction associated with large-scale changes to deep crustal architecture and basin dynamics that initiated at this time. The observed spread in Neoproterozoic–Palaeozoic ages terminating at this age maxima suggests that pervasive replacement and resetting of inherited monazite grains was driven by an intensification of activity marking the beginning of the ASO.

4-5.2. Microstructural evidence for melt-present deformation and glimmerite formation

Of the five key microstructures indicative of the former presence of melt in high-strain zones outlined by Stuart et al. (2018b), four were observed in the GDSZ samples: (1) small dihedral angles between biotite, muscovite and quartz (Figure 3e, f); (2) elongated grain boundary films pseudomorphed by biotite (Figure 3d–f and 4g, h); (3) small quartz grain aggregates connected in three dimensions (Figure 4a, d, e), presenting less than ten degrees of crystallographic misorientation between grains; (4) pseudomorphs of inferred cm-scale granitic melt pockets (Figure 3b, i). Other microstructures that support our interpretation of melt-present deformation in the GDSZ include biotite finger-like protrusions into adjacent quartz grains (Figure 3d–f and 4g) and CL images highlighting bands of darker CL response in quartz near biotite (Figure 4j–m), possibly reflecting microscale fracturing, melt migration pathways or a CL signature of quartz grain boundary migration (Holness & Watt, 2001; Bergman & Piazolo, 2012).

Crystallographic orientation data of quartz also supports the former presence of melt in the GDSZ. Quartz grains in the H–Qtz and M-Qtz samples display a strong CPO, while the quartz grains present in sample GL show a weak CPO and activation of multiple slip systems (Figure 5). The strong CPO for the highly strained quartzite sample

is not accompanied by intense recrystallisation of the quartz grains, instead showing widespread quartz grain boundary migration, implying deformation temperatures >500°C (Stipp et al., 2002a, b). The observed CPO in quartzite is most probably an inherited structure formed at granulite facies, indicative of activation of the prism <a> slip system, during the Strangways Orogeny, and not a feature formed during the ASO. This affirmation is informed by the lack of ductile shear bands microstructures in the quartzite samples and quartz grains (Gapais & White, 1982; Menegon et al., 2011) or quartz grain size reduction by recrystallization (Hobbs, 1968; Lloyd, 1994, 2004; Stipp et al., 2010)(Figure 3b, 4a and 5–6), leading to the interpretation that melt flux pathways initiated within the quartzite mylonite, later pseudomorphed by biotite-sillimanite-muscovite, and result from shear or dilation fractures in a brittle regime (Lloyd & Knipe, 1992). The small quartz grains in sample GL (Figure 5a) show a weak CPO and activation of multiple slip systems (Figure 5b, c) suggesting that these grains are not relict grains from the main quartzite present in sample M–Qtz, but instead are the product of neoformed quartz grains that may reflect melt pseudomorphs. These results indicate that the deformation of the quartz grains was concomitant with the presence of melt, leading the strain to be accommodated into the weaker surrounding melt, not allowing a strong CPO similar to that observed for the quartz grains in samples M- and H-Qtz (Figure 5; Lee et al., 2018, Stuart et al., 2018b, Prakash et al., 2018). An increase of the mean quartz grain size is observed for areas of the sample close or in contact to the inferred melt pathways, when compared to quartz grains more distant to the inferred melt pathways (Figure 6). This increase in the mean quartz grain size can be explained by the increase in temperature in proximity to the melt pathways (Figure 5a, d), leading to static grain growth and recovery of the quartz grains for sample M–Qtz (close to glimmerite) and sample H–Qtz (far from glimmerite). The fact that there is quite a strong local effect suggests that melt flux must have been short-lived, probably involving several pulses, rather than continuous long-lived melt flux that would anneal a larger area of the sample. During such annealing, grain boundaries migrate to cross biotite boundaries (e.g. Piazolo et al., 2006), hence the increase in biotite enclosure with proximity to the inferred melt pathways (Figure 4f and 5). Furthermore, during annealing, subgrain boundaries get rearranged and decrease in abundance (e.g. Borthwick & Piazolo, 2010). At the same time, the intensity of CPO increases (Piazolo et al., 2010). The much smaller mean size of the quartz present in sample GL can be related to the neoformation of quartz by melt pseudomorphism previously described.

4-5.3. Glimmerite: an under-recognised product of melt-rock interaction

In addition to the P-T-t and microstructural evidence for melt-present deformation being important at the time of the formation of glimmerite in the GDSZ, the biotite geochemical data are also consistent with the system being driven by melt-rock interaction. Micas, and in particular biotite, are observed as dominant in the mineral assemblage of the glimmerite, and in the inferred reactive melt pathways within the partially modified

quartzite samples (Figures 2–6).

The discrimination of biotite that formed at supra-solidus metamorphic or igneous conditions versus grains formed at lower-T sub-solidus metamorphic conditions is not straightforward. Here, the discrimination diagram of Nachit et al. (1985) is used, based on the inference of melt-present conditions (Figure 8b). The diagram is potentially useful to inform on the type of melt involved in the melt-rock interaction that formed the glimmerite rocks. The peraluminosity of the melt is inferred to be reflected by the aluminium content of the equilibrated crystalized biotite (Nachit et al., 1985; Stussi & Cuney, 1996) and our data suggest that the glimmerite biotite grains share similarities with magmatic biotite grains that formed from and are partially reequilibrated with a peraluminous melt.

The highly dispersed and overall lower concentrations of Al, Ti, Fe and Mn of the biotite in the L–Qtz sample likely reflects a dominance of chemical components from the precursor quartzite rock over the externally-derived melt, compared to H–Qtz/M–Qtz/GL biotites which are dominated by the chemistry of the melt (Figure 8). About half of the L–Qtz biotites present formation conditions trending towards the formation conditions observed for the L–Qtz to H–Qtz/M–Qtz/GL biotites, showing an increase of apparent temperature of formation and peraluminosity of crystalizing fluid concordant with the igneous biotite data compiled by Stussi & Cuney (1996). This wide range of L–Qtz biotite compositions likely reflects variable but low ultra-local melt volumes in the quartzite domains and limited equilibration with the fluxing melt.

The trace element analyses of biotite in all samples shows low concentrations of chondritic normalised REE, Zr and Hf, and above chondritic concentrations of Nb and Ta (Figure 9 and 10). The high concentration of Nb and Ta likely results from the high partition coefficient between biotite and granitic melt (Stepanov & Herman, 2013). In their experiments and analysis of natural examples, Stepanov & Herman (2013) observed that biotite in partial melting environments preferentially incorporates Nb over Ta and they conclude that the biotite plays an important role for the missing Nb-paradox observed in the continental crust. Such behaviour of Nb incorporation over Ta in biotite is observed in our data, with most of the L–Qtz biotite grains presenting lower Nb concentration and overall lower Nb/Ta ratios when compared to H–Qtz, M–Qtz and GL biotite grains (Figure 9 and 10). Concentration of Zr and Hf in biotite for all samples shows similar values, although presenting lower concentration to the biotite present in the partially melted metapelite enclaves of El Hoyazo (Acosta-Vigil et al., 2010), while presenting 2–3 orders of magnitude lower values when compared to rhyodacite biotite (Nash & Crecraft, 1985) (Figure 9). The similarity in the concentration of Zr and Hf between our biotite and the El Hoyazo and dissimilitude with rhyodacite biotite can be explained by the presence of abundant zircon grains in equilibrium with biotite in our samples and El Hoyazo metapelites and trace proportions of zircon in the rhyodacite, possibly allowing the zircon grains to buffer the concentration of Zr and Hf in the melt (Acosta-Vigil et al., 2010; Nash & Crecraft, 1985). The studied biotite

REE concentrations show decreased values, i.e. chondrite normalised concentration below unity and a slight increase of LREE over HREE (Figure 9a–c), similar to the biotite REE concentration in partial melting environments of the El Hoyazo enclave and Pena Negra Complex migmatite leucosomes (Acosta-Vigil et al., 2010; Bea et al., 1994b) or closed system fractional crystallization from a peraluminous melt in the Pedrobernardo pluton (Bea et al., 1994a) (Figure 9d). The biotite REE–depleted pattern observed for El Hoyazo, Pena Negra and Pedrobernardo samples (Table S1 and Figure 9d) are explained by the authors by the presence of accessory minerals with higher REE mineral/melt partitioning than biotite, i.e. monazite, zircon and apatite, or by REE-depleted melt due to the retention of REE in the same previously described residual accessory minerals in the palaeosome. Each of these mechanisms, or a combination of both, can be considered viable explanations for the REE concentration in H–Qtz, M–Qtz and GL biotite in our study, due to the presence of monazite and apatite in equilibrium within the glimmerite mineral assemblage, or by the externally-derived melt becoming depleted in REE following crystallization and fractionation of mineral phases rich in REE during prior melt flow. Another explanation for our biotite REE-depleted signature can be attributed to the smaller equilibration volume and /or variation in the composition of fluxing melt signatures proposed by Stuart et al. (2018a) for the observed variation in the igneous-like mineral REE patterns they measured in the Pembroke Granulite (lower crust of a magmatic arc) metasomatic reactions. The presence of melt in the GDSZ is also suggested by the overall enrichment in incompatible elements in biotite from L–Qtz to the group of samples: H–Qtz, M–Qtz and GL (Figure 10). This increase in incompatible elements follows an almost linear trend with the apparent increase in temperature informed by the increase in biotite Ti concentration. The increase in biotite incompatible elements can be attributed to a more fractionated melt, enriched in incompatible elements (Cerny, 1991; O'Connor et al., 1991; Bea et al., 1994a) or by a higher equilibration volume of melt trending from the L–Qtz to the most reacted samples, possibly also explaining the apparent temperature increase from sample L–Qtz to sample H–Qtz.

Comparing the whole rock major oxide concentration in sample GL and the range of precursor rock types present in the SMC is necessary to understand the chemical evolution between the different glimmerites present in the study area, and their possible protoliths. The glimmerite composition is different to the possible precursor rocks (Figure 7), plotting most of the time in between the oxide values presented by the mafic granulites, schistose high strain zone metapelites and the average peraluminous granitic biotite. The concentration of major oxides does not indicate a strong relationship between the glimmerite rock observed in the GDSZ and the surrounding rocks from the SMC. This suggests that the process of forming glimmerite involved a high degree of geochemical modification (i.e. metasomatism, sensu lato). We infer this involved reactive flow of melt through high strain zones, leading to dissolution of much of a SMC protolithic rock, likely one of the felsic protoliths observed in SMC based on the largely replaced layers and lenses within the glimmerite outcrop. Coupled precipitation

of mostly biotite pushed the whole rock composition of the resulting glimmerite rock to values similar to the average composition of peraluminous granitic biotite (Figure 7).

This proposed mode of glimmerite formation is distinct to the seminal examples of glimmerite where they formed by metasomatism of mantle (Becker et al., 1999; Gregoire et al., 2002; Rajesh et al., 2004). The “classic” glimmerite rocks generally show a spatial relationship in outcrop between mantle rocks and either a K-rich metasome with or without a third component involving felsic igneous intrusions (Fyfe & McBirney, 1975; Wyllie & Sekine, 1982; Rakotondrazafy et al., 1997; Fuertes-Fuente et al., 2000). The K-rich mantle metasomes are characterised by an assemblage composed usually of biotite + amphibole ± pyroxene (Menzies & Murthy, 1980; Smart et al., 2019). These characteristics of “classic” glimmerites are not observed in sample GL. However, similarities between our proposed mode of glimmerite formation and the classic examples include melt-rock interaction involving a felsic melt, and modification of a protolithic rock (however, felsic versus ultramafic) by melt-mediated coupled dissolution-precipitation, forming mostly biotite (Figure 3, 4 and 5). Genetically and mineralogically, sample GL shows a higher degree of similarity to the formation of “back reactive melanosome” in anatectic migmatites described by Kriegsman (2000). In that model, locally-derived in-situ melt is invoked to interact with the mesosome. This diverges from our proposed mode of protolith (quartzite) modification and glimmerite formation as we invoke an externally-sourced melt to drive dissolution of protolith minerals and precipitation of glimmerite minerals, mainly quartz and biotite, respectively, in our example.

The modal percentage of hydrous phases is a consequence of the volume of reactive melt flux calculated for the GDSZ. Arrested melt flux may occur upon draining of source magma or cooling and freezing of the system. Regardless, cessation of reactive melt flux formed the microstructures observed in the studied samples and the patterns suggest that melt flux through the quartzite occurred mainly via intergranular mechanisms and focused along structurally controlled planes such as fractures and the main foliation. In the glimmerite domain, the extreme metasomatism implies higher reactive melt flux, where the protolithic rock is partially or entirely dissolved by the reactive melt, enhancing porosity and permeability (e.g. Daczko et al., 2016), and providing a positive feedback that allows a higher volume of melt flow and consequent increase in the formation of the hydrous minerals.

4-5.4. Estimates of reactive hydrous melt volume forming glimmerite

In this section, the minimum volume of reactive hydrous melt needed to form the glimmerite is estimated for each of the Gough Dam samples presented and discussed in this study. As previously discussed, melt-rock interaction and subsequent formation of hydrous phases observed in the study area implies open system melt migration through a felsic protolith located in the Gough Dam shear zone (GDSZ). The observed

	Hydrous minerals wt%	
Sample	L-Qtz	H-Qtz
Biotite (3.97 H_2O wt%)	8.0	15.0
Muscovite (4.44)	0.0	2.0
Total sample H_2O (wt%)	0.32	0.68
Melt H_2O (wt%)	Volume of melt per m^3 rock	
3.0	0.11	0.23
6.0	0.05	0.11
9.0	0.04	0.08
12.0	0.03	0.06

Table 4. Calculation of melt volume forming hydrous minerals in a high-strain zone for samples L–Qtz and H–Qtz.

increase in modal biotite and muscovite of the GDSZ is relatable to a melt flow-derived hydrous metasomatism mechanism. With this interpretation in mind, the calculation for a minimum volume of reactive melt flux can be achieved (following the method of Stuart et al., 2018a).

The minimum volume of reactive melt flux is calculated considering a theoretical cube of quartzite rock showing no hydrous phases and an H2O content virtually close to 0%. The proportions and average H2O content of the hydrous phases, i.e. biotite and muscovite present in this study, formed during the melt-rock hydrous metasomatism are used to calculate the final H2O composition of our hypothetic quartzite cube. Calculated H2O content for biotite and muscovite from EMP analyses are 3.97 wt% (n=75) and 4.44 wt% (n=24), respectively (Table 2). Totalling the proportion of biotite and muscovite in each sample gives the final H2O content of 0.3 wt% and 0.7 wt% for samples L–Qtz and H–Qtz, respectively (Table 4).

The reactive melt flux is calculated by using the volume of melt necessary to drive the increase of the H2O content. Four melts of variable H2O content are considered (3, 6, 9 and 12 wt%) which represent a typical range of water contents in granitic melts (Holtz et al., 2001). Two simplifying theoretical assumptions are made for the calculation: (1) the totality of the H2O present in the melt is partitioned into the new hydrous phases; and (2) homogeneous melt flux throughout the rock cube. In nature, this perfect behaviour of H2O partitioning and homogeneous flux wouldn't be expected. The model is also restricted by disregarding some anhydrous phases (plagioclase, sillimanite, K-feldspar) into the H2O partition calculation, leading to an underestimation of the amount of melt flux for the sample H–Qtz. The underestimation of melt flux is considered likely in this study due to the possibility of armoured and unreactive melt flux following formation of glimmerite layers, analogous to hornblendite channels observed in arc environments (Daczko et al., 2016; Stuart et al., 2018a) or dunnite channels observed in the mantle (Kelemen, et al. 1995). Calculated minimum melt flux volumes range between 0.03 to 0.23 m3 of melt per m3 of rock. Values of melt flux volume varies accordingly to the interplay of the initial H2O present in the fluxing melt and the proportion of reactive hydrous phases observed in the samples. Sample

L–Qtz shows the lower values of melt flux with H–Qtz approximately double the L–Qtz values.

4-5.5. Implications for the geotectonic significance of glimmerite schist belts

A key feature of the Earth's crust is an intracrustal heterogeneity in, among others, chemical composition, with the upper crust showing an increased silicic composition and concentration of granitic material, while the lower crust presents a more mafic composition (Vigneresse, 1995; Brown & Rushmer, 2006). Deeply seated high-strain zones in the lower to middle crust are considered part of the crustal system of melt migration. These function as major pathways for the ascent of melt originated from anatectic processes in the lower to middle crust and are partially responsible for batch mass transfer of melt to the upper crust (Hutton, 1988; Sawyer et al., 2011; Daczko et al., 2016).

Melt generation in the crust can be achieved by two main types of anatectic process: water-absent or dehydration melting (Thompson, 1982; Le Breton & Thompson, 1988; Patiño-Douce & Beard, 1995) and water-fluxed or hydration melting (Hasalová et al., 1998; Beard, 2004; Daczko et al., 2016; Stuart et al., 2017). In the dehydrated middle to lower regions of the crust, the influx of locally- or externally-derived fluids forms pronounced local chemical gradients between fluid and rock, which paired with high differential stresses, enhances metamorphic reactions (Putnis & Austrheim, 2010; Wheeler et al., 2014, Stuart et al., 2016, 2017). If the fluid presents high enough water concentration and appropriate fugacity, exothermic hydration (or retrograde) metamorphic reactions of anhydrous minerals occurs. The intracontinental ASO, involving the GDSZ in particular and possibly other schistose high strain zones present in central Australia, are good examples of pathways of melt flow in high-strain zones that lead to melt-rock interaction and hydration of protolith granulites.

The physical presence of melt and metamorphic reactions that produce rheologically weak minerals (i.e. reaction softening) in high-strain zones favours a decrease in the strength of the high-strain zone. This increases the accommodation of stress transmitted from the surrounding, relatively more competent host rocks and facilitates strain localization and enhances the displacement across the high-strain zone (Hollister & Crawford, 1986; Brown & Solar, 1998; Molnar & Dayem, 2010; Cunningham, 2013). Reaction softening such as that presented in this study with the formation of layers containing high proportions of phyllosilicates within a competent anhydrous granulite terrain, can be considered a textbook example of decreased rock strength, enabling stress accommodation and consequent strain localization within structures such as the GDSZ. However, we do not observe classic solid-state deformation microstructures in any off our samples, suggesting that (1) melt was involved in any/all reactivation events, forming microstructures indicative of the former presence of melt and (2) stresses interior to the continent were never high enough to reactivate reaction softened high-strain zones.

Weakening of high-strain zones is proposed by various authors as an important mechanism to enhance orogenesis, especially true for far-field compressional intracontinental orogenies (e.g. Alice Springs and Altai orogenies; Hand & Sandiford, 1999; Raimondo et al., 2014 Cunningham, 2005, Silva et al., 2018), where stress regimes are comparatively lower compared to those observed in areas proximal to collisional plate boundaries (Coblentz et al., 1998; Heidbach et al., 2010). Moreover, weakened high-strain zones are described by various authors to be significant in the multiple reactivation events documented in the ASO (Raimondo et al., 2014; Silva et al., 2018) as these facilitate the accommodation of lithospheric horizontal stresses formed during increased early Palaeozoic dextral rotation of the northern Australian block (Roberts & Houseman, 2001; Silva et al., 2018). The formation and presence of meter-scale glimmerites, such as that documented here in the GDSZ and for hydrated high-strain zones elsewhere in the SMC, indicates that this specific rock type, characterised by its intrinsic low competence and enhanced by the physical presence of melt, is an ideal candidate to intensify intracontinental orogenesis in central Australia.

4-6. Conclusions

Glimmerite in the study area of the Gough Dam shear zone (GDSZ) formed during the migration of a hydrous peraluminous melt and interaction with protoliths of felsic composition, during the Alice Springs Orogeny (ASO). In addition to melt migration through high-strain rocks, fractures parallel and perpendicular to the shear zone foliation created melt pathways that enhanced melt infiltration into the protolith. High-temperature melt-rock interaction at conditions close to the liquidus of the melt promoted dissolution of the protolith and precipitation of largely biotite. Localized temperature-dependent quartz grain growth recovery is observed in highly organized modified quartzite mylonite and random quartz grain orientation is observed in glimmerite. The mode of hydrous minerals in the various rock types is inferred to relate to variable volumes of reactive melt flux. Zones of larger melt volume fluxing through the shear zone show increased equilibration and homogenisation of the neoformed hydrous minerals. For example, a calculated melt flux between 0.06 and 0.23 m3 per m3 of rock allowed the increase of the host rock vol.% hydrous mineral assemblage by at least two-fold (8% to 17%), increasing the concentration of trace elements (Ti, Nb, Zr, Hf, Sc, Ba and Li) and REE (mostly Eu). Proterozoic-aged monazite is variably reset to early-ASO ages by coupled dissolution-precipitation processes, indicating the mobility of Pb was low, leading to high dispersion in the age population. The formation of glimmerite layers in anhydrous terrains has the potential to be an important mechanism for stress localisation, and by consequence strain localization, facilitating orogenesis in intracontinental regions, such is the proposed case for the ASO.

4-7. Acknowledgments

M. Bebbington and T. Murphy (Macquarie University) assisted with making thin sections and geochemical analysis. Sandrin Feig (Univ. of Tasmania) assisted with electron microprobe analysis. Duncan Hedges and Richard Walshaw (University of Leeds) assisted with EBSD data collection. This study used instrumentation funded by ARC LIEF and DEST Systemic Infrastructure Grants, Macquarie University and Industry. This is contribution 1380 from the ARC Centre of Excellence for Core to Crust Fluid Systems (http://www.CCFS.mq.edu.au) and GEMOC Key Centre (http://www.GEMOC.mq.edu.au). This work was carried out as part of a PhD study at Macquarie University and was supported by ARC Discovery grant DP160103449 to Putnis, TR and ND. We thank S. Cruden (Monash University) and A. Tommasi (University of Montpellier) for constructive comments on an earlier version of this manuscript. We thank the land owners for permission to visit and sample localities in the Gough Dam shear zone.

4-8. References

Acosta-Vigil, A., Buick, I., Hermann, J., Cesare, B., Rubatto, D., London, D., Morgan, G. B., 2010. Mechanisms of crustal anatexis: a geochemical study of partially melted metapelitic enclaves and host dacite, SE Spain. Journal of Petrology, 51(4): 785–821.

Bachmann, F., Hielscher, R., Schaeben, H., 2010. Texture analysis with MTEX–free and open source software toolbox. Solid State Phenomena, 160: 63–68.

Ballèvre, M., Hensen, B. J., Reynard, B., 1997. Orthopyroxene-andalusite symplectites replacing cordierite in granulites from the Strangways Range (Arunta block, central Australia): A new twist to the pressure-temperature history. Geology, 25(3): 215–218.

Ballèvre, M., Möller, A., Hensen, B. J., 2000. Exhumation of the lower crust during crustal shortening: an Alice Springs (380 Ma) age for a prograde amphibolite facies shear zone in the Strangways Metamorphic Complex (central Australia). Journal of Metamorphic Geology, 18(6): 737–747.

Bea, F., Pereira, M. D., Corretgé, L. G., Fershtater, G. B., 1994a. Differentiation of strongly peraluminous, perphosphorus granites: the Pedrobernardo pluton, central Spain. Geochimica et Cosmochimica Acta, 58(12): 2609–2627.

Bea, F., Pereira, M. D., Stroh, A., 1994b. Mineral/leucosome trace-element partitioning in a peraluminous migmatite (a laser ablation-ICP-MS study). Chemical Geology, 117(1–4): 291–312.

Beard, J. S., Ragland, P. C., Rushmer, T., 2004. Hydration crystallization reactions between anhydrous minerals and hydrous melt to yield amphibole and biotite in igneous rocks: description and implications. The Journal of Geology, 112(5): 617–621.

Beaumont, C., Jamieson, R. A., Nguyen, M. H., Lee, B., 2001. Himalayan tectonics

explained by extrusion of a low-viscosity crustal channel coupled to focused surface denudation. Nature, 414(6865): 738.

Becker, H., Wenzel, T., Volker, F., 1999. Geochemistry of glimmerite veins in peridotites from Lower Austria—implications for the origin of K-rich magmas in collision zones. Journal of Petrology, 40(2): 315–338.

Bendall, B., 2000. Mid-Palaeozoic shear zones in the Strangways Range: a record of intracratonic tectonism in the Arunta Inlier, Central Australia (Doctoral dissertation). University of Adelaide, Adelaide, Australia.

Bercovici, D., 1998. Generation of plate tectonics from lithosphere–mantle flow and void–volatile self-lubrication. Earth and Planetary Science Letters, 154(1–4): 139–151.

Bergman, H., & Piazolo, S., 2012. The recognition of multiple magmatic events and pre-existing deformation zones in metamorphic rocks as illustrated by CL signatures and numerical modelling: Examples from the Ballachulish contact aureole, Scotland. International Journal of Earth Sciences, 101(5): 1127–1148.

Borthwick, V. E., & Piazolo, S., 2010. Post-deformational annealing at the subgrain scale: Temperature dependent behaviour revealed by in-situ heating experiments on deformed single crystal halite. Journal of Structural Geology, 32(7): 982–996.

Brodie, K. H., & Rutter E. H., 1985. On the relationship between deformation and metamorphism, with special reference to the behaviour of basic rocks. Metamorphic Reactions: Kinetics, Textures and Deformation: Advances in Physical Geochemistry, 4: 138–179.

Brown, M., & Rushmer, T., 2006. Evolution and Differentiation of the Continental Crust. Cambridge University Press, Cambridge.

Brown, M., & Solar, G. S., 1998. Shear-zone systems and melts: Feedback relations and self-organization in orogenic belts. Journal of Structural Geology, 20: 211–227.

Bunge, H. J., 2013. Texture analysis in materials science: Mathematical methods. Elsevier, Amsterdam, Netherlands.

Cartwright, I., & Barnicoat, A. C., 2003. Geochemical and stable isotope resetting in shear zones from Täschalp: constraints on fluid flow during exhumation in the Western Alps. Journal of Metamorphic Geology, 21(2): 143–161.

Cartwright, I., Buick, I. S., Foster, D. A., Lambert, D. D., 1999. Alice Springs age shear zones from the southeastern Reynolds Range, central Australia. Australian Journal of Earth Sciences, 46(3): 355–363.

Cerny, P., 1991. Fertile granites of Precambrian rare-element pegmatite fields: is geochemistry controlled by tectonic setting or source lithologies? Precambrian Research 51: 429–468.

Cesare, B., Acosta-Vigil, A., Bartoli, O., Ferrero, S., 2015. What can we learn from melt inclusions in migmatites and granulites? Lithos, 239: 186–216.

Cesare, B., Mariani, E. S., Venturelli, G., 1997. Crustal anatexis and melt extraction during deformation in the restitic xenoliths at El Joyazo (SE Spain). Mineralogical Magazine, 61(1): 15–27.

Cesare, B., Satish-Kumar, M., Cruciani, G., Pocker, S., Nodari, L., 2008. Mineral chemistry of Ti-rich biotite from pegmatite and metapelitic granulites of the Kerala Khondalite Belt (southeast India): Petrology and further insight into titanium substitutions. American Mineralogist, 93(2–3): 327–338.

Chapman, T., Clarke, G. L., Piazolo, S., Robbins, V. A., Trimby, P. W., 2019. Grain-scale dependency of metamorphic reaction on crystal plastic strain. Journal of Metamorphic Geology.

Clarke, G. L., Daczko, N. R., Klepeis, K. A., Rushmer, T., 2005. Roles for fluid and/or melt advection in forming high-P mafic migmatites, Fiordland, New Zealand. Journal of Metamorphic Geology, 23(7): 557-567.

Coblentz, D. D., Zhou, S., Hillis, R. R., Richardson, R. M., Sandiford, M., 1998. Topography, boundary forces, and the Indo-Australian intraplate stress field. Journal of Geophysical Research: Solid Earth, 103(B1): 919–931.

Collins, W. J., & Sawyer, E. W., 1996. Pervasive granitoid magma transfer through the lower–middle crust during non-coaxial compressional deformation. Journal of Metamorphic Geology, 14(5): 565–579.

Collins, W., & Shaw, R., 1995. Geochronological constraints on orogenic events in the Arunta inlier: A review. Precambrian Research, 71(1): 315–346.

Collins, W., & Teyssier, C., 1989. Crustal scale ductile fault systems in the Arunta inlier, central Australia. Tectonophysics, 158(1): 49–66.

Cunningham, D., 2005. Active intracontinental transpressional mountain building in the mongolian Altai: Defining a new class of orogen. Earth and Planetary Science Letters 240(2): 436–444.

D'lemos, R. S., Brown, M., Strachan, R. A., 1992. Granite magma generation, ascent and emplacement within a transpressional orogen. Journal of the Geological Society, 149(4): 487–490.

Daczko, N.R., Piazolo, S., Meek, U., Stuart, C. A., Elliott, V., 2016. Hornblendite delineates zones of mass transfer through the lower crust. Scientific Reports, 6: 31369.

Donovan, J. J., Snyder, D. A., Rivers, M. L., 1993. An improved interference correction for trace element analysis. Microbeam Analysis, 2: 23–28.

Etheridge, M. A., Wall, V. J., Vernon, R. H., 1983. The role of the fluid phase during regional metamorphism and deformation. Journal of Metamorphic Geology, 1(3): 205–226.

Faulkner, D. R., & Rutter, E. H., 2001. Can the maintenance of overpressured fluids in large strike-slip fault zones explain their apparent weakness? Geology, 29(6): 503–506.

Ferry, J. M., 1994. A historical review of metamorphic fluid flow. Journal of Geophysical Research, 99: 15487–98.

Fournier, H. W., Camacho, A., Lee, J. K. W., 2016. High-strain deformation and fluid infiltration diachronism of the middle crust: New Devonian–Permian Alice Springs ages (365–290 Ma) of shear zones in the Strangways Metamorphic Complex, Central Australia. Chemical Geology, 443: 39–5.

Frost, B. R., & Frost, C. D., 2013. Essentials of igneous and metamorphic petrology. Cambridge University Press, Cambridge.

Fuertes-Fuente, M., Martin-Izard, A., Boiron, M. C., Viñuela, J. M., 2000. P–T path and fluid evolution in the Franqueira granitic pegmatite, central Galicia, northwestern Spain. The Canadian Mineralogist, 38(5): 1163–1175.

Fyfe, W. S., & McBirney, A. R., 1975. Subduction and the structure of andesitic volcanic belts. American Journal of Science, 275(1): 285–297.

Gapais, D., & White, S.H., 1982. Ductile shear bands in a naturally deformed quartzite. Texture, Stress, and Microstructure, 5(1): 1–17.

Ghatak, 2017. Distinguishing hydration in shear zones by aqueous fluid versus silicate melt (Masters dissertation). Macquarie University, Sydney, Australia.

Girard, J., Chen, J., Raterron, P., Holyoke III, C. W., 2013. Hydrolytic weakening of olivine at mantle pressure: Evidence of [1 0 0] (0 1 0) slip system softening from single-crystal deformation experiments. Physics of the Earth and Planetary Interiors, 216:12–20.

Goncalves, P., Oliot, E., Marquer, D., Connolly, J. A. D., 2012. Role of chemical processes on shear zone formation: an example from the Grimsel metagranodiorite (Aar massif, Central Alps). Journal of Metamorphic Geology, 30(7): 703¬722.

Grand'Homme, A., Janots, E., Seydoux-Guillaume, A. M., Guillaume, D., Magnin, V., Hövelmann, J., Höschen, C., Boiron, M. C., 2018. Mass transport and fractionation during monazite alteration by anisotropic replacement. Chemical Geology, 484: 51–68.

Grand'Homme, A., Janots, E., Seydoux-Guillaume, A. M., Guillaume, D., Bosse, V., Magnin, V., 2016. Partial resetting of the U-Th-Pb systems in experimentally altered monazite: Nanoscale evidence of incomplete replacement. Geology, 44(6): 431–434.

Grégoire, M., Bell, D., Le Roex, A., 2002. Trace element geochemistry of phlogopite-rich mafic mantle xenoliths: their classification and their relationship to phlogopite-bearing peridotites and kimberlites revisited. Contributions to Mineralogy and Petrology, 142(5): 603–625.

Griffin, W. L., 2008. GLITTER: data reduction software for laser ablation ICP-MS. Laser Ablation ICP-MS in the Earth Sciences: Current practices and outstanding issues: 308–311.

Griggs, D. T., & Blacic, J. D., 1965. Quartz: anomalous weakness of synthetic crystals. Science, 147(3655): 292–295.

Hand, M., & Sandiford, M., 1999. Intraplate deformation in central Australia, the link between subsidence and fault reactivation. Tectonophysics, 305(1): 121–140.

Handy, M. R., Mulch, A., Rosenau, M., Rosenberg, C. L., 2001. The role of fault zones and melts as agents of weakening, hardening and differentiation of the continental crust: a synthesis. Geological Society, London, Special Publications, 186(1): 305–332.

Hasalová, P., Stipska, P., Powell, R., Schulmann, K., Janousek, V., Lexa, O., 1998. Transforming mylonitic metagranite by open-system interactions during melt flow. Journal of Metamorphic Geology, 26(1): 55–80.

Heidbach, O., Tingay, M., Barth, A., Reinecker, J., Kurfess, D., Müller, B., 2010. Global crustal stress pattern based on the World Stress Map database release 2008. Tectonophysics, 482(1–4): 3–15.

Heinrich, K.F.J., 1966. X-ray absorption uncertainty. The electron microprobe: 296.

Henke, B.L., 1985. Lawrence Berkeley Laboratories, unpublished.

Henry, D. J., Guidotti, C. V., Thomson, J. A., 2005. The Ti-saturation surface for low-to-medium pressure metapelitic biotites: Implications for geothermometry and Ti-substitution mechanisms. American Mineralogist, 90(2-3): 316–328.

Henry, H., 2018 Mantle Pyroxenites: Deformation and Seismic Properties. (Doctoral dissertation). Macquarie University, Sydney, Australia.

Henry, H., Tilhac, R., Griffin, W. L., O'Reilly, S. Y., Satsukawa, T., Kaczmarek, M. A., Ceuleneer, G., 2017. Deformation of mantle pyroxenites provides clues to geodynamic processes in subduction zones: case study of the Cabo Ortegal Complex, Spain. Earth and Planetary Science Letters, 472: 174–185

Hobbs, B.E., 1968. Recrystallization of single crystals of quartz: Tectonophysics, 6: 353–401.

Hollister, L. S., & Crawford, M. L., 1986. Melt-enhanced deformation: a major tectonic process. Geology, 14: 558–561.

Holness, M. B., & Watt, G. R., 2001. Quartz recrystallization and fluid flow during contact metamorphism: a cathodoluminescence study. Geofluids, 1(3): 215–228

Holtz, F., Johannes, W., Tamic, N., Behrens, H., 2001. Maximum and minimum water contents of granitic melts generated in the crust: a reevaluation and implications. Lithos, 56(1): 1–14.

Howlett, D., Hand, M., Raimondo, T., Bendall, B., 2014. Episodic mid-crustal metamorphism during the Alice Springs Orogeny: the Strangways Range, central Australia. In: Fraser, G., Forster, M. & McClusky, S. (eds) SGTSG in the Snowies: Biennial Conference of the Specialist Group for Tectonics and Structural Geology, February 2014. Geological Society of Australia Abstracts, 109: 48.

Hulsbosch, N., Hertogen, J., Dewaele, S., André, L., Muchez, P., 2014. Alkali metal and rare earth element evolution of rock-forming minerals from the Gatumba area pegmatites (Rwanda): Quantitative assessment of crystal-melt fractionation in the regional zonation of pegmatite groups. Geochimica et Cosmochimica Acta, 132: 349–374.

Hutton, D. H., 1988. Granite emplacement mechanisms and tectonic controls: Inferences from deformation studies. Earth and Environmental Science Transactions of the Royal Society of Edinburgh, 79(2-3): 245–255.

Iyer, S.S.,1974. Granulites and associated schists from the northern Strangways Range, central Australia: Geochemical and isotopic studies. Unpublished PhD thesis, University of Queensland

Jamieson, R.A., Unsworth, M.J., Harris, N.B., Rosenberg, C.L. Schulmann, K., 2011. Crustal melting and the flow of mountains. Elements, 7: 253–260.

Jarosewich, E., Nelen, J. A., Norberg, J. A., 1980. Reference samples for electron microprobe analysis. Geostandards Newsletter, 4(1): 43–47.

Karato, S. I., 1986. Does partial melting reduce the creep strength of the upper mantle? Nature, 319(6051): 309.

Kelemen, P. B., Shimizu, N. Salters, V. J. M., 1995. Extraction of mid-ocean-ridge basalt from the upwelling mantle by focused flow of melt in dunite channels. Nature, 375: 747–753

Kriegsman, L. M., 2001. Partial melting, partial melt extraction and partial back reaction in anatectic migmatites. Lithos, 56(1): 75–96.

Kronenberg, A. K., Segall, P., Wolf, G. H., 1990. Hydrolytic weakening and penetrative deformation within a natural shear zone. Geophysical Monograph, 56: 21–36.

Laul, J. C., Lepel, E. A., 1987. Rare earth element patterns in biotite muscovite and tourmaline minerals. Journal of Radioanalytical and Nuclear Chemistry, 112(2): 461–471.

Le Breton, N., & Thompson, A. B., 1988. Fluid-absent (dehydration) melting of biotite in metapelites in the early stages of crustal anatexis. Contributions to Mineralogy and Petrology, 99(2): 226:237.

Le Pichon, X. L., Henry, P., Lallemant, S., 1993. Accretion and erosion in subduction zones: The role of fluids. Annual Review of Earth and Planetary Sciences, 21(1): 307–331.

Lee, A. L., Torvela, T., Lloyd, G. E., Walker, A. M., 2018. Melt organisation and strain partitioning in the lower crust. Journal of Structural Geology, 113: 188–199.

Lin, L., & Sawyer, E. W., 2019. Microstructure and compositional changes across biotiterich reaction selvedges around mafic schollen in a semipelitic diatexite migmatite. Journal of Metamorphic Geology.

Lloyd, G. E., & Freeman, B., 1994. Dynamic recrystallization of quartz under greenschist conditions. Journal of Structural Geology, 16(6): 867–881.

Lloyd, G. E., 2004. Microstructural evolution in a mylonitic quartz simple shear zone: the significant roles of dauphine twinning and misorientation. Flow Processes in Faults and Shear Zones. Geological Society, London, Special Publications, 224: 39–61.

Lloyd, G.E., & Knipe, R.J., 1992. Deformation mechanisms accommodating faulting of quartzite under upper crustal conditions. Journal of Structural Geology, 14(2): 127–143.

Maidment, D. W., 2005. Palaeozoic high-grade metamorphism within the Centralian Superbasin, Harts Range region, central Australia. (Doctoral dissertation). Australian National University, Canberra, Australia.

Maidment, D. W., Hand, M., Williams, I. S., 2005. Tectonic cycles in the Strangways Metamorphic Complex, Arunta Inlier, central Australia: geochronological evidence for exhumation and basin formation between two high-grade metamorphic events. Australian Journal of Earth Sciences, 52: 205–215.

Mancktelow, N. S., & Pennacchioni, G., 2004. The influence of grain boundary fluids on the microstructure of quartz-feldspar mylonites. Journal of Structural Geology, 26(1): 47–69.

Massonne, H. J., & Schreyer, W., 1987. Phengite geobarometry based on the limiting assemblage with K-feldspar, phlogopite, and quartz. Contributions to Mineralogy and Petrology, 96(2): 212–224

Mawby, J., Hand, M., Foden, J., 1999. Sm–Nd evidence for high–grade ordovician metamorphism in the Arunta block, central Australia. Journal of Metamorphic Geology, 17: 653–668.

McCaig, A. M., & Knipe, R. J., 1990. Mass-transport mechanisms in deforming rocks: Recognition, using microstructural and microchemical criteria. Geology, 18(9): 824–827.

McDonough, W. F., & Sun, S. S., 1995. The composition of the Earth. Chemical geology, 120(3–4): 223–253.

Meek, U., Piazolo, S., Daczko, N. R., 2019 The field and microstructural signatures of deformation-assisted melt transfer: Insights from magmatic arc lower crust, New Zealand. Journal of Metamorphic Geology.

Menegon, L., Fusseis, F., Stünitz, H., Xiao, X., 2015. Creep cavitation bands control porosity and fluid flow in lower crustal shear zones. Geology, 43(3): 227–230.

Menegon, L., Pennacchioni, G., Spiess, R., 2008. Dissolution-precipitation creep of K-feldspar in mid-crustal granite mylonites. Journal of Structural Geology, 30(5): 565–579.

Menegon, L., Piazolo, S., Pennacchioni, G., 2011. The effect of Dauphiné twinning on plastic strain in quartz. Contributions to Mineralogy and Petrology, 161(4): 635–652.

Menzies, M., & Murthy, V. R., 1980. Nd and Sr isotope geochemistry of hydrous mantle nodules and their host alkali basalts: Implications for local heterogeneities in metasomatically veined mantle. Earth and Planetary Science Letters, 46(3): 323–334.

Milord, I., & Sawyer, E. W., 2003. Schlieren formation in diatexite migmatite: Examples from the St Malo migmatite terrane, France. Journal of Metamorphic Geology, 21(4): 347–362.

Möller, A., Williams, I. S., Jackson, S., Hensen, B. J., 1999. Palaeozoic deformation and mineral growth in the Strangways Metamorphic Complex: in-situ dating of zircon and monazite in a staurolite-corundum bearing shear zone. Geological Society of Australia Abstracts, 54: 71–72.

Molnar, P., & Dayem, K. E., 2010. Major intracontinental strike-slip faults and contrasts in lithospheric strength. Geosphere, 6(4): 444–467.

Morris, J. D., Leeman, W. P., Tera, F., 1990. The subducted component in island arc lavas: Constraints from Be isotopes and B–Be systematics. Nature, 344(6261): 31.

Nachit, H., 1985. Composition chemique des biotites et typologie magmatique des granitoids. Comtes Rendus Hebdomadaires de l'Academie des Sciences, 301(11): 813–818.

Nachit, H., Ibhi, A., Abia, E. H., Ohoud, M. B., 2005. Discrimination between primary magmatic biotites, reequilibrated biotites and neoformed biotites. Comptes Rendus Geoscience, 337(16): 1415–1420.

Nash, W. P., & Crecraft, H. R., 1985. Partition coefficients for trace elements in silicic magmas. Geochimica et Cosmochimica Acta, 49(11): 2309–2322.

Neiva, A. M. R., Silva, M. M. V. G., Gomes, M. E. P., Campos, T. F. C., 2002. Geochemistry of coexisting biotite and muscovite of Portuguese peraluminous granitic differentiation series. Chemie der Erde-Geochemistry, 62(3): 197–215.

Norman, A.R., 1991. The structural and metamorphic evolution of the central Arunta Block: evidence from the Strangways Metamorphic Complex and the Harts Range Group, central Australia. (Doctoral dissertation). Macquarie University, Sydney, Australia.

O'Connor, P.J., Gallagher, V., Kennan, P.S., 1991. Genesis of lithium pegmatites from the Leinster Granite Margin, south-eastern Ireland: Geochemical constraints. Geological Journal, 26: 295–305.

Oliver, N. H. S., Valenta, R. K., Wall, V. J., 1990. The effect of heterogeneous stress and strain on metamorphic fluid flow, Mary Kathleen, Australia, and a model for large-scale fluid circulation. Journal of Metamorphic Geology, 8(3): 311–331.

Paterson, D., De Jonge, M. D., Howard, D. L., Lewis, W., McKinlay, J., Starritt, A., ... Siddons, D. P. (2011, September). The X-ray fluorescence microscopy beamline at the Australian synchrotron. In AIP Conference Proceedings (Vol. 1365, No. 1, pp. 219-222). AIP.

Patiño-Douce, A. E., & Beard, J. S., 1995. Dehydration-melting of biotite gneiss and quartz amphibolite from 3 to 15 kbar. Journal of Petrology, 36(3): 707-738.

Paton, C., Hellstrom, J., Paul, B., Woodhead, J., Hergt, J., 2011. Iolite: Freeware for the visualisation and processing of mass spectrometric data. Journal of Analytical Atomic Spectrometry, 26(12): 2508–2518.

Payne, J.L., Hand, M., Barovich, K.M., Wade, B.P., 2008. Temporal constraints on the timing of high-grade metamorphism in the northern Gawler Craton: implications for assembly of the Australian Proterozoic. Australian Journal of Earth Sciences, 55: 623–640.

Piazolo, S., Bestmann, M., Prior, D. J., Spiers, C. J., 2006. Temperature dependent grain boundary migration in deformed-then-annealed material: observations from experimentally deformed synthetic rocksalt. Tectonophysics, 427(1–4): 55–71.

Piazolo, S., Bons, P. D., Jessell, M. W., Evans, L., Passchier, C. W., 2002. Dominance of microstructural processes and their effect on microstructural development: Insights from numerical modelling of dynamic recrystallization. Geological Society, London, Special Publications, 200(1): 149–170.

Piazolo, S., Jessell, M. W., Bons, P. D., Evans, L., Becker, J. K., 2010. Numerical simulations of microstructures using the Elle platform: a modern research and teaching tool. Journal of the Geological Society of India, 75(1): 110–127.

Pichon, X. L., Henry, P., Lallemant, S., 1993. Accretion and erosion in subduction zones: the role of fluids. Annual Review of Earth and Planetary Sciences, 21(1), 307–331.

Prakash, A., Piazolo, S., Saha, L., Bhattacharya, A., Pal, D. K., Sarkar, S., 2018. Deformation behavior of migmatites: Insights from microstructural analysis of a garnet–sillimanite–mullite–quartz–feldspar-bearing anatectic migmatite at Rampura–Agucha, Aravalli–Delhi Fold Belt, NW India. International Journal of Earth Sciences, 107(6): 2265–2292.

Putnis, A., & Austrheim, H., 2010. Fluid-induced processes: Metasomatism and metamorphism. Geofluids, 10(1–2): 254–269.

Putnis, A., & Putnis, C. V., 2007. The mechanism of reequilibration of solids in the presence of a fluid phase. Journal of Solid State Chemistry, 180(5): 1783–1786.

Putnis, A., 2009. Mineral replacement reactions. Reviews in mineralogy and geochemistry, 70(1): 87–124.

Raimondo, T., Clark, C., Hand, M., Faure, K., 2011. Assessing the geochemical and tectonic impacts of fluid-rock interaction in mid-crustal shear zones: a case study from the intracontinental Alice Springs orogen, central Australia. Journal of Metamorphic Geology, 29(8): 821–850.

Raimondo, T., Hand, M., Collins, W. J., 2014. Compressional intracontinental orogens: Ancient and modern perspectives. Earth–Science Reviews, 130: 128–153.

Rajesh, V. J., Arima, M., Santosh, M., 2004. Dunite, glimmerite and spinellite in Achankovil Shear Zone, South India: implications for highly potassic CO2-rich melt influx along an intra-continental shear zone. Gondwana Research, 7(4): 961-974.

Rakotondrazafy, R., Pierdzig, S., Raith, M. M., Hoernes, S., 1997. Phlogopite-mineralisations in the Beraketa belt of southern Madagascar: a spectacular example of channelised fluid flow and fluid-rock interaction. Gondwana Research Group Miscellaneous Publication 5, 81–82.

Rasband, W.S., 1997–2015. ImageJ, U. S. National Institutes of Health. Bethesda, MD, USA. http://imagej.nih.gov/ij/.

Roberts, E. A., & Houseman, G. A., 2001. Geodynamics of central Australia during the intraplate Alice Springs Orogeny: thin viscous sheet models. Geological Society, London, Special Publications, 184(1): 139–164.

Rosenberg, C. L., & Handy, M. R., 2005. Experimental deformation of partially melted granite revisited: implications for the continental crust. Journal of metamorphic Geology, 23(1): 19–28.

Rosenberg, C. L., 2004. Shear zones and magma ascent: a model based on a review of the Tertiary magmatism in the Alps. Tectonics, 23(3).

Ryan, C. G., Cousens, D. R., Sie, S. H., Griffin, W. L., 1990. Quantitative analysis of PIXE spectra in geoscience applications. Nuclear Instruments and Methods in Physics Research Section B: Beam Interactions with Materials and Atoms, 49(1–4): 271–276.

Ryan, C. G., Jamieson, D. N., Churms, C. L., Pilcher, J. V., 1995. A new method for on-line true-elemental imaging using PIXE and the proton microprobe. Nuclear Instruments and Methods in Physics Research Section B: Beam Interactions with Materials and Atoms, 104(1–4): 157–165.

Ryan, C. G., Kirkham, R., Hough, R. M., Moorhead, G., Siddons, D. P., De Jonge, M. D., ... Cleverley, J. S., 2010. Elemental X-ray imaging using the Maia detector array: The benefits and challenges of large solid-angle. Nuclear Instruments and Methods in Physics Research Section A: Accelerators, Spectrometers, Detectors and Associated Equipment, 619(1–3): 37–43.

Ryan, C. G., Laird, J. S., Fisher, L. A., Kirkham, R., Moorhead, G. F., 2015. Improved Dynamic Analysis method for quantitative PIXE and SXRF element imaging of complex materials. Nuclear Instruments and Methods in Physics Research Section B: Beam Interactions with Materials and Atoms, 363: 42–47.

Sawyer, E. W., 2008. Atlas of migmatites. The Canadian Mineralogist, Special publication 9. NRC Research press, Ottawa, Canada.

Sawyer, E.W., 1999. Criteria for the recognition of partial melting. Physics and Chemistry of the Earth, Part A: Solid Earth and Geodesy, 24: 269–279.

Sawyer, E.W., Cesare, B., Brown, M., 2011. When the continental crust melts. Elements, 7: 229–234.

Schmidt, M. W., & Poli, S., 1998. Experimentally based water budgets for dehydrating slabs and consequences for arc magma generation. Earth and Planetary Science Letters, 163(1–4): 361–379.

Schulmann, K., Martelat, J. E., Ulrich, S., Lexa, O., Štípská, P., & Becker, J. K., 2008. Evolution of microstructure and melt topology in partially molten granitic mylonite: Implications for rheology of felsic middle crust. Journal of Geophysical Research: Solid Earth, 113: B10406.

Scrimgeour, I. R., 2013. Aileron Province, in Ahmad M. and Munson T. J., Geology and mineral resources of the Northern Territory. Northern Territory Geological Survey, Special Publication, 5.

Selverstone, J., Morteani, G. Staude, J. M., 1991. Fluid channelling during ductile shearing: transformation of gran- odiorite into aluminous schist in the Tauern Window, eastern Alps. Journal of Metamorphic Geology, 9: 419–431.

Seydoux-Guillaume, A. M., Montel, J. M., Bingen, B., Bosse, V., De Parseval, P., Paquette, J. L., ... & Wirth, R., 2012. Low-temperature alteration of monazite: Fluid mediated coupled dissolution–precipitation, irradiation damage, and disturbance of the U–Pb and Th–Pb chronometers. Chemical Geology, 330: 140–158.

Shaw, R. D., Stewart, A. T., Black, L. P., 1984. The Arunta Inlier: a complex ensialic mobile belt in central Australia. Part 2: tectonic history. Australian Journal of Earth Sciences, 31(4): 457-484.

Sibson, R. H., 1994. Crustal stress, faulting and fluid flow. Geological Society, London, Special Publications, 78(1): 69–84.

Silva, D., Piazolo, S., Daczko, N. R., Houseman, G., Raimondo, T., Evans, L., 2018. Intracontinental Orogeny Enhanced by Far-Field Extension and Local Weak Crust. Tectonics, 37(12): 4421–4443.

Skemer, P., Katayama, I., Jiang, Z., Karato, S. I., 2005. The misorientation index: Development of a new method for calculating the strength of lattice-preferred orientation. Tectonophysics, 411(1–4): 157–167.

Smart, K. A., Tappe, S., Ishikawa, A., Pfänder, J. A., Stracke, A., 2019. K-rich hydrous mantle lithosphere beneath the Ontong Java Plateau: Significance for the genesis of oceanic basalts and Archean continents. Geochimica et Cosmochimica Acta, 248: 311–342.

Smith, J. R., Piazolo, S., Daczko, N. R., Evans, L., 2015. The effect of pre-tectonic reaction and annealing extent on behaviour during subsequent deformation: insights from paired shear zones in the lower crust of Fiordland, New Zealand. Journal of Metamorphic Geology, 33(6): 557–577.

Sobolev, A. V., & Chaussidon, M., 1996. H2O concentrations in primary melts from supra-subduction zones and mid-ocean ridges: Implications for H2O storage and recycling in the mantle. Earth and Planetary Science Letters, 137(1–4): 45–55.

Spruzeniece, L., & Piazolo, S., 2015. Strain localization in brittle-ductile shear zones: fluid-abundant vs. fluid-limited conditions (an example from Wyangala area, Australia). Solid Earth, 6: 881–901,

Stepanov, A. S., & & Hermann, J., 2013. Fractionation of Nb and Ta by biotite and phengite: Implications for the “missing Nb paradox”. Geology, 41(3): 303–306.

Stern, R. J., 2002. Subduction zones. Reviews of geophysics, 40(4).

Stipp, M., Stunitz, H., Heilbronner, R., Schmid, S. M., 2002b. The eastern Tonale fault zone: a ‘natural laboratory’ for crystal plastic deformation of quartz over a temperature range from 250 to 700°C. Journal of Structural Geology, 24(12): 1861–1884.

Stipp, M., Stunitz, H., Heilbronner, R., Schmid, S.M., 2002a. Dynamic recrystallization of quartz: correlation between natural and experimental conditions. In: De Meer, S., Drury, M.R., De Bresser, J.H.P., Pennock, G.M. (Eds.), Deformation Mechanisms, Rheology, and Tectonics: Current Status and Future Perspectives: 171–190.

Stipp, M., Tullis, J., Scherwath, M., Behrmann, J.H., 2010. A new perspective on paleopiezometry: Dynamically recrystallized grain size distributions indicate mechanism changes. Geology, 38(8): 759–762.

Stuart, C. A., Daczko, N. R., Piazolo, S., 2017. Local partial melting of the lower crust triggered by hydration through melt–rock interaction: an example from Fiordland, New Zealand. Journal of Metamorphic Geology, 35(2): 213–230.

Stuart, C. A., Meek, U., Daczko, N. R., Piazolo, S., Huang, J. X., 2018a. Chemical signatures of melt–rock interaction in the root of a magmatic arc. Journal of Petrology, 59(2): 321–340.

Stuart, C. A., Piazolo, S., Daczko, N. R., 2016. Mass transfer in the lower crust: Evidence for incipient melt assisted flow along grain boundaries in the deep arc granulites of Fiordland, New Zealand. Geochemistry, Geophysics, Geosystems, 17(9): 3733–3753.

Stuart, C. A., Piazolo, S., Daczko, N. R., 2018b. The recognition of former melt flux through high-strain zones. Journal of Metamorphic Geology, 36(8): 1049–1069.

Stussi, J. M., & Cuney, M., 1996. Nature of biotites from alkaline, calc-alkaline and peraluminous magmas by Abdel-Fattah M. Abdel-Rahman: a comment. Journal of Petrology, 37(5): 1025–1029.

Tetley, M. G., & Daczko, N. R., 2014. Virtual Petrographic Microscope: a multi-platform education and research software tool to analyse rock thin-sections. Australian Journal of Earth Sciences, 61(4): 631–637.

Teyssier, C., 1985. A crustal thrust system in an intracratonic tectonic environment. Journal of Structural Geology, 7(6): 689–700.

Thompson A. B., & Connolly J. A. D., 1992. Migration of metamorphic fluid – some aspects of mass and heat transfer. Earth Science Reviews, 32: 107–21.

Thompson, A.B., 1982. Dehydration melting of pelitic rocks and the generation of H2O-undersaturated granitic liquids. American Journal of Science, 282: 1567–1595.

Tucker, N. M., Hand, M., Payne, J. L., 2015. A rift–related origin for regional medium–pressure, high–temperature metamorphism. Earth and Planetary Science Letters, 421: 75–88.

Urai, J. L., Means, W. D., Lister, G. S., 1986. Dynamic recrystallization of minerals. Mineral and rock deformation: 161–199.

Vernon, R. H., 2011. Microstructures of melt-bearing regional metamorphic rocks. Geological Society of America Memoirs, 207: 1–11.

Vigneresse, J.L., 1995. Crustal regime of deformation and ascent of granitic magma. Tectonophysics, 249: 187–202.

Waters, F. G., 1987. A geochemical study of metasomised peridotite and MARID nodules from the Kimberley pipes, South Africa. (Doctoral dissertation). University of Cape Town, South Africa.

Watson, E. B., & Baxter, E. F., 2007. Diffusion in solid-Earth systems. Earth and Planetary Science Letters, 253(3–4): 307–327.

Weinberg, R. F., & Hasalová, P., 2015. Water-fluxed melting of the continental crust: A review. Lithos, 212: 158–188.

Weinberg, R. F., Sial, A. N., Pessoa, R. R., 2001. Magma flow within the Tavares pluton, northeastern Brazil: Compositional and thermal convection. Geological Society of America Bulletin, 113(4): 508–520.

Wheeler, J., 2014. Dramatic effects of stress on metamorphic reactions. Geology, 42(8): 647–650.

White, S. T., & Knipe, R. J., 1978. Transformation-and reaction-enhanced ductility in rocks. Journal of the Geological Society, 135(5): 513–516.

Whitney, D. L., & Evans, B. W., 2010. Abbreviations for names of rock-forming minerals. American Mineralogist, 95(1): 185–187.

Winter, J. D., 2013. Principles of igneous and metamorphic petrology. Pearson education, London, U.K.

Wintsch, R. P., Christoffersen, R., Kronenberg, A. K., 1995. Fluid-rock reaction weakening of fault zones. Journal of Geophysical Research: Solid Earth, 100(B7): 13021–13032.

Wyllie, P. J., & Sekine, T., 1982. The formation of mantle phlogopite in subduction zone hybridization. Contributions to Mineralogy and Petrology, 79(4): 375–380.

Yardley, B. W., 2009. The role of water in the evolution of the continental crust. Journal of the Geological Society, 166(4): 585–600.

Žák, J., Verner, K., Týcová, P., 2008. Grain-scale processes in actively deforming magma mushes: New insights from electron backscatter diffraction (EBSD) analysis of biotite schlieren in the Jizera granite, Bohemian Massif. Lithos, 106(3–4): 309–322.

Závada, P., Schulmann, K., Racek, M., Hasalová, P., Jeřábek, P., Weinberg, R. F., ... Roberts, A., 2018. Role of strain localization and melt flow on exhumation of deeply subducted continental crust. Lithosphere, 10(2): 217–238.

Chapter 5. K-feldspar phenocrysts trapped during syn-tectonic melt expulsion from a melt fluxed high-strain zone

David Silva[1*], Sandra Piazolo[1,2], Nathan R. Daczko[1]

[1]ARC Centre of Excellence for Core to Crust Fluid Systems and GEMOC, Department of Earth and Planetary Sciences, Macquarie University, NSW 2109, Australia

[2]School of Earth and Environment, Institute of Geophysics and Tectonics, University of Leeds, Leeds, UK

*E-mail address: david.barbosa-da-silva@hdr.mq.edu.au

Keywords: Glimmerite; melt flux; collapse structures; phenocryst entrapment; melt extraction

Abstract

The migration of melt through the crust is fundamental to many geological processes including high-strain zones which may act as important melt migration pathways. The recognition of former melt-present deformation in high-strain zones is usually attained at the outcrop-scale by identification of felsic bodies or leucosome, with components inferred to have crystalized from melt. The melt may be sourced from local anatexis or may be externally derived and have migrated through sub-solidus rocks. Difficulty in inferring melt-present high-strain deformation arises in cases where time-integrated melt flux was low or if the melt volume was largely extracted at the end of a melt migration event. In these latter scenarios, the macro-scale evidence commonly used to recognize where melt once resided in migration pathways is lacking. Therefore, microscale studies of the deformed high-strain zone are needed to identify microstructures indicative of former melt. In this contribution, we investigate undeformed and partially faceted K-feldspar grains in the Gough Dam Shear Zone (Central Australia), a 2–4 km wide high-strain zone active during the Alice Springs Orogeny (c. 450–300 Ma). At some locations in the shear zone, weakly deformed granite layers (dykes) and lenses are observed and are used to infer former melt-present deformation. In other locations in the shear zone, coarse K-feldspar is observed in biotite-rich (>50 vol.%) schist (glimmerite) as individual grains or in aggregates with subordinate quartz forming lenses and bead structures. Our detailed characterisation of the isolated K-feldspar grains in glimmerite and their associated textures shows: (i) partially preserved crystal faces;

(ii) lack of internal grain deformation; (iii) reaction textures preferentially formed along a, b and c crystallographic axes showing dissolution of K-feldspar and precipitation of dominantly biotite; (iv) low-strain domains between multiple K-feldspar grains inferred to contain crystallised melt pockets, with some apparently isolated grains showing connectivity in three dimensions; and (v) weak quartz and K-feldspar crystallographic preferred orientation (CPO). These observations suggest a phenocrystic origin for the K-feldspar grains which is consistent with REE-depleted concentration patterns with a positive Eu anomaly that resemble igneous K-feldspar. We propose that the K-feldspar phenocrysts are early-formed crystals that were transported into the glimmerite rocks during high-strain melt-present deformation and melt flux. Some K-feldspar phenocrysts became trapped during collapse of the high-strain zone wall rocks constituting the melt pathway, when melt flux-related fluid pressure waned. We suggest that trapped phenocrysts are a viable indicator of former melt-present deformation in high-strain zones.

5-1. Introduction

High-strain zones are regarded by geologists as important crustal-scale conduits for melt transfer from regions of melt production (lower- to middle-crust) to shallower crustal depths, significantly contributing to the observed segregation of highly silicic melt towards the upper crust (Hollister & Crawford, 1986; Hutton, 1988; D'Lemos et al., 1992; Brown, 1994; Vigneresse, 1995; Weinberg et al, 2004; Brown & Rushmer, 2006). Although recognized to act as important crustal melt pathways, the inference of melt-present deformation in high-strain zones is non-trivial below a certain crystallised melt volume, usually <10%, resulting in limited macroscopic crystallised igneous seams, pockets or dykes in the deformed rock (Rosenberg & Handy, 2005; Brown & Solar, 1998; Collins & Sawyer, 1996; Weinberg et al, 2013; Stuart et al, 2017, 2018). Below this approximate crystallised melt threshold, an indication of the former presence of melt in high-strain zones is relegated to microstructures such as small mono- or multiphase pockets at triple points and/or elongated interstitial grains (Beere, 1975; von Bargen & Waff, 1986; Závada et al., 2007; Stuart et al., 2017, 2018; Lee et al., 2018).

Inferring the former presence of melt in highly strained rocks can provide important information for strain analysis due to the relative weakness of the melt fraction, and by consequence favourability in strain accumulation, when compared to the surrounding consolidated rock (Rosenberg & Handy, 2005; Levine et al., 2013; Searle, 2013; Lee et al., 2018). Whilst many shear zones preserve >10% crystallised melt, others show that at mid to lower crustal levels, melt expulsion (e.g. collapse structures) can result in high strain rocks that are difficult to interpret in terms of inferring the former presence of melt. This leads to erroneous quantification of the former melt volume fraction and can

lead to inaccurate interpretations of the strain history or even of the rock type (Bons, 1999; Kriegsman, 2001; Brown, 2005; Bons et al., 2008, Bons et al., 2009). Thus, the proper recognition of the former presence of melt in high-strain rocks is crucial to interpret and understand the correct tectonic history and possible fluid-rock interaction in melt transfer zones.

In this contribution, we present a detailed microstructural study of a highly strained, biotite dominated schist (glimmerite) comprising common individual or clustered, mm-scale facetted K-feldspar grains. The study site is located in the Gough Dam Shear Zone, Arunta Region, central Australia. Two localities within the 2–4 km-wide high strain zone are used to discriminate if the most recent tectonic event in this region (Alice Springs Orogeny) involved melt-present deformation. We use EBSD and SEM techniques to characterize quartz and K-feldspar microstructures that are uncommon in high strain rocks deformed by solid state deformation dominated by dislocation creep. We propose that the presence of large undeformed K-feldspar grains in the biotite dominated glimmerite schist may be used as a new indicator for the recognition of former melt flux in high-strain zones. We interpret their presence in highly metasomatized rocks as a consequence of early feldspar crystallization in a syn-tectonic melt, succeeded by structural collapse of the adjacent rocks during melt escape, resulting in K-feldspar entrapment in the biotite dominated schist.

5-2. General geological background

The study area is located in central Australia, in the Arunta region, which was most recently deformed in the Alice Springs Orogeny (ASO), a ~700 km longitude by ~80 km width intracontinental orogeny that spanned the period of 450 to 300 Ma (Collins & Teyssier, 1989; Hand & Sandiford, 1999; Mawby et al., 1999; Scrimgeour, 2013; Figure 1). An extensive regional system of anastomosing high-strain zones and localized deep crustal thrust faults are present and these cut most of the high-grade metamorphic complexes in the region; i.e. Harts, Reynolds-Anmatjira and Strangways ranges (Cartwright et al., 1999; Ballèvre et al., 2000; Raimondo et al., 2011, 2014; Figure 1). Crustal thickening with an estimated ~100 km of horizontal shortening involved exhumation of granulitic basement rocks and occurred by N–S compression (Shaw et al., 1984; Teyssier, 1985; Collins & Teyssier, 1989). The compression was enhanced during periods of extension in the Tasmanides Orogeny, adjacent to the Eastern Australian plate boundary (Raimondo et al., 2014; Silva et al., 2018). The focus area for this study lies in the Strangways Metamorphic Complex (SMC) which formed during the Strangways Orogeny at c. 1730 Ma (Figure 1). The SMC is cut by steeply dipping, km-wide, hydrous and multi-reactivated high-strain zones that formed during the ASO (Figure 1). These comprise upper amphibolite- to greenschist-facies schist belts that include layers of K-feldspar–biotite–quartz schist (hereafter named glimmerite schist in the text) and glimmerite (>75% mica with very low proportions of quartz).

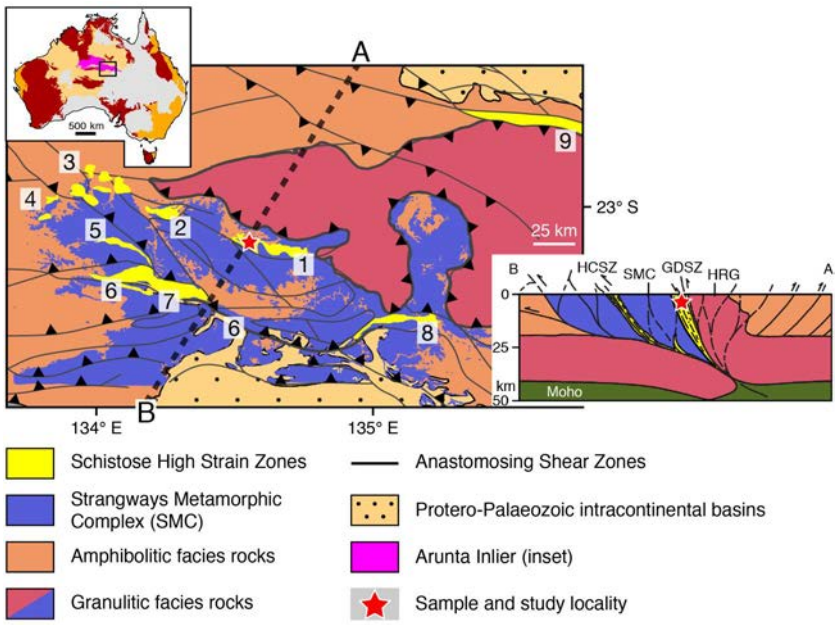

Figure 1. Geological map of the SE Arunta region showing study and sample locality (red star). The map emphasizes the distribution of regional high strain zones of hydrous schistose composition (e.g. Gough Dam shear zone, #1; yellow structures and respective number in map) in the mostly granulite and amphibolite facies rocks incorporating the Arunta region. Represented are the regional anastomosing shear zones and thrust faults relative to the Strangways Metamorphic Complex and the Hart Range Group (HRG). Simplified structural cross-sections (modified after Raimondo et al., 2014) display the principal crustal discontinuities and shear zones of the main geological domains in the Arunta region associated with the Alice Springs Orogeny (Collins & Teyssier, 1989; Ballèvre et al., 2000; Maidment, 2005; Raimondo et al, 2011; Scrimgeour, 2013).). #1 Gough Dam Shear Zone (GDSZ); #2 West Bore Shear Zone; #3 Wallaby Knob Shear Zone; #4 Yambah Shear Zone; #5 Southern Cross Shear Zone; #6 Harry Creek Shear Zone (HCSZ); #7 Erontonga/Two Mile Bore Shear Zone; #8 Illogwa Shear Zone; #9 Delny Shear Zone.

Glimmerite schist and glimmerite from this study are located in the Gough Dam Shear Zone (GDSZ), an E-W to NNW-SSE trending, 2–4 km-wide, steeply dipping (60–90° to N) shear zone that juxtaposed the northern SMC with the Harts Range Metamorphic Complex (HRMC) (Figure 1). This particular shear zone is characterized by metasomatic hydration and retrogression of the bi-modal interlayered anhydrous mafic-felsic granulites, quartzofeldspathic gneisses, minor calcsilicate and amphibolite rocks constituting the Paleoproterozoic SMC basement of the Arunta region. The GDSZ represents a S-directed reverse shear zone based on shear band orientations and sigma clast kinematic indicators (Collins & Shaw, 1995; Bendall, 2000; Figure 1).

5-2.1. Field relationships

The main rock types present in the GDSZ schist belt are phyllonitic quartzo-feldspathic gneiss, felsic and mafic granulite pods, and quartz rods, with sparse cm-wide garnet-bearing granulites, with biotite and sillimanite, occasionally kyanite, delineating the steep north-plunging lineation (Ballèvre et al., 1997). The study site is dominated by metre-scale layers of glimmerite schist composed of a matrix of dominantly biotite ±quartz, muscovite and sillimanite, with isolated or clustered, coarse (up to 2–3 cm across), near-euhedral K-feldspar (~30vol.%). These form discontinuous trails along

the foliation (Figure 2a–d). Continuous cm- to dm-scale banding parallel to the GDSZ foliation is observed in the study area and these span compositions ranging from granitic (i.e. near-euhedral Kfs ±qz and subordinate biotite (<5vol.%)) to glimmerite bands of high biotite content (~80vol.%). Small lenses of variably deformed granite display mm-width biotite-rich selvedges (Figure 2e–f). Common trains of granite resembling pinch-and-swell structures are observed, creating isolated lenses of granite elongate along the foliation (Figure 2e–f). Other layers in the GDSZ include quartz mylonite, felsic granulite and granitic gneiss forming bodies of more than 10 m in length and up to 50 cm in width (Figure 2g–h). Some kyanite and staurolite was observed in the GDSZ schists near the study area. The glimmerite component is observed to partially replace the quartzite mylonite, felsic granulite and granitic gneiss in some areas, with "invasions" into the layers, either into fractures or as embayments, dividing in the surficial planes into small, rounded, isolated blocks (Figure 2g–h).

5-3. Method of analysis

5-3.1. Petrography and quantitative orientation analysis

Sample mineral observations were made on polished thin sections cut in the structural XZ plane using a petrographic microscope, the Virtual Petrographic Microscope (Tetley and Daczko, 2014) and ImageJ 1.47v (Rasband, 1997-2018).

Microstructural/crystallographic characterisation of thin sections was performed using a FEI Quanta 650 FEG-ESEM with AZtec software and an Oxford/HKL Nordlys S EBSD system at the University of Leeds, UK. EBSD mapping was performed covering a large area of the thin section and small individual maps in specific regions of the sample, recording the mineral EDS spectra along with the EBSD data. Working conditions were: 20 kV accelerating voltage, 20–26 mm working distance, 70° specimen tilt and step size between 6 and 12 µm depending on the area covered and grain size. Automatic indexation was performed using AZtec software (Oxford Instruments). HKL software was used to execute standard noise reduction and to extrapolate missing data using at least and in succession 8, 7, 6 and finally 5 identical neighbours with similar orientation. Grain orientation maps using Euler angles and an inverse pole figure (IPF) were generated using MTex software and HKL (Bachmann et al., 2010; Henry et al., 2017; Henry 2018); these include grain boundaries, defined as a boundary with a misorientation above 10°, and dauphine twin boundaries for quartz, defined as a 60° misorientation around the c-axis. Crystallographic preferred orientation (CPO) of quartz and K-feldspar was assessed using pole figures plotted on the lower hemisphere with one point per grain. To quantify the intensity of the CPO, the J-index (i.e. second moment distribution of discrete crystal orientation data in Euler angle space (Bunge, 2013)) and M-index (i.e. distribution of uncorrelated misorientation angles (Skemer et al., 2005))

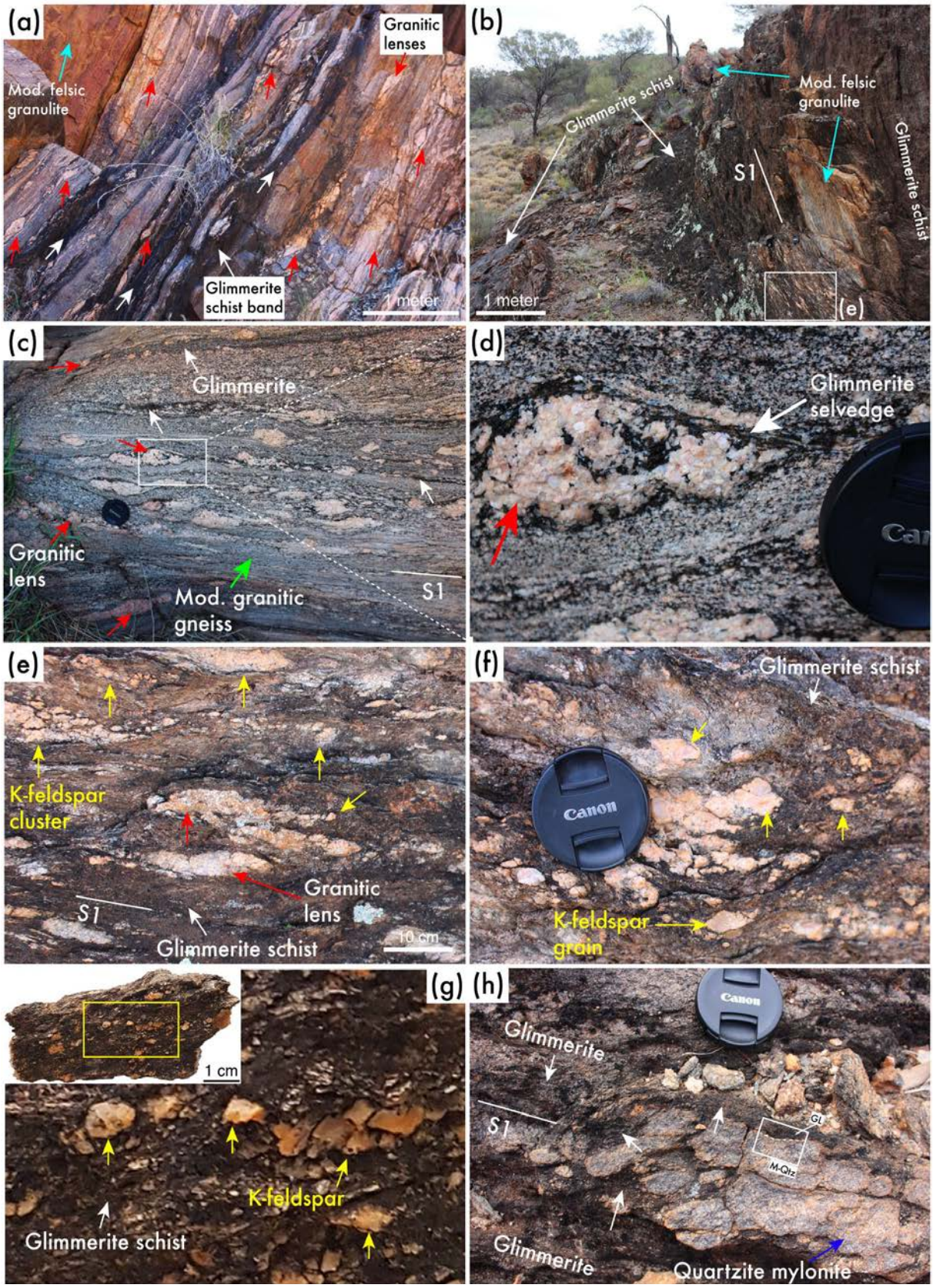

Figure 2. Field relationships of the Gough Dam Shear zone including sample localities; (a): Outcrop presenting biotite-rich glimmerite schist bands (white arrows) and trails of granite lenses along the foliation (red arrows), both cutting a host of modified felsic granulite; (b): Outcrop of meter-scale glimmerite schist with a well-developed foliation (S1) that contains layers and lenses of partially modified relict felsic rock types. Field sense of shear is top to the North (S1: N78°/70°); (c–d): Outcrop-scale and detailed views of domains of the GDSZ containing a high abundance of variably deformed granite lenses and glimmerite bands cutting modified granitic gneiss along foliation. Granite lenses present asymmetric envelopes or selvedges of glimmerite composition; (e–f): Magnification of glimmerite schist outcrop containing granitic lenses, along with isolated and clustered facetted K-feldspar grains aligned along the foliation in the biotite dominated matrix of the glimmerite schist; (g): Hand sample and detailed view of the collected (cont.)

Figure 2. (cont.) glimmerite schist used for petrographic study containing isolated and clustered, facetted, mm- to cm-wide K-feldspar grains; (h): Quartzite mylonite layer hosted by glimmerite. Glimmerite shows a reaction replacement relationship with, warps around and “invades” the quartzite mylonite, isolating individual quartz mylonite rounded blocks.

are presented. Grain internal deformation was estimated using an orientation point sample for the targeted grain in HKL software and highlighting misorientation data up to a 15° threshold from the selected source point. The majority of the non-indexed sectors in EBSD maps (black regions) are dominated by non-indexed biotite and lesser muscovite, as informed by petrographic microscopy.

5-3.2. Imaging and geochemical analysis

Micro X-ray Fluorescence (μ-XRF) analysis of the polished thin sections was used for mineral identification and spatial distribution mapping and quantification of modal proportions. μ-XRF analyses were performed using the Bruker M4 Tornado spectrometer at Macquarie University Geoanalytical (MQGA), Sydney, Australia. The μ-XRF analyses were run with a tube voltage of 50 kV, a beam current of 200 μA, a chamber pressure of 20 mbar, an acquisition time of 15 ms/pixel and using a step size of 25 μm. AMICS (Advanced Mineral Identification and Characterization System) was used to convert the X-ray fluorescence spectra to produce detailed mineral maps.

Backscatter Electron (BSE) images and associated *EDS point analyses* were used for both mineral identification and imaging of microstructures. Polished thin sections were carbon coated and imaged in a Hitachi Desktop Scanning Electron Microscope (SEM) at the OptoFab node of the Australian National Fabrication Facility, Macquarie University, Sydney, Australia. The operating conditions of the SEM were low vacuum and 15 kV accelerating voltage. A large BSE scan of the thin section was performed using the FEI 650 ESEM at the University of Tasmania, Australia, at low vacuum and 20 kV accelerating voltage.

Electron microprobe analyses acquired compositional data of silicates using a JEOL JXA 8530F Plus field emission electron microprobe at the Central Science Laboratory, University of Tasmania. The instrument is equipped with a field emission source, running an accelerating voltage of 15 kV, a beam current of 15 nA and a beam size of 10 μm. The instrument has 5 wavelength dispersive spectrometers and is operated using the Probe Software Inc. “Probe For EPMA” software package. Plagioclase Lake County, Hornblende Kakanui, Augite Kakanui, Pyrope Kakanui, Olivine Springwater, Garnet Roberts Victor Mine (all Smithsonian; Jarosewich et al., 1980) and Orthoclase from P&H Developments UK were analysed as secondary standards to confirm the quality of the analysis of the unknown material. A time dependent intensity correction was applied on Na and K if applicable. Oxygen was calculated by cation stoichiometry and included in the matrix correction. Hydrogen was calculated based on the mineral formula and included in the matrix correction as well. The matrix correction algorithm utilized was Armstrong/Love Scott (Armstrong, 1988) and the mass absorption coefficients dataset was LINEMU <10 keV (Henke, 1985) and

CITZMU >10 keV (Heinrich, 1966).

Laser Ablation Inductively Coupled Plasma Mass Spectrometry (LA-ICP-MS) was used to collect data for concentration of rare earth elements in K-feldspar in thin section using a Teledyne Analyte Excite 193 nm excimer laser coupled to an 7700x ICP-MS housed at Macquarie University Geoanalytical (MQGA), Sydney, Australia. Data was collected from thin sections using 60 seconds ablation at 10 Hz, 5 J/cm2 fluence and spot size of 150 µm. Silicon (measured by EMP) was used as internal standard for all minerals, and NIST 610 and 612, and basalt from the Columbia River (BCR-2) were used as external standards. The raw data signal was reduced using the GLITTER software (Griffin et al., 2008).

5-.3.2.1. *Biotite thermometer*

The P–T conditions for each sample are estimated using the titanium-in-biotite thermometer of Henry et al. (2005). The geothermometer is based on the titanium (Ti a.p.f.u.) composition of biotite in a peraluminous metapelite with Ti–bearing minerals (ilmenite or rutile) and graphite in the mineral assemblage, equilibrated at 4–6 kbar. Temperature estimates are made by using the concentration of Ti, Fe and Mg atoms per formula unit (a.p.f.u.) in biotite present in quartzite mylonite, glimmerite schist and glimmerite samples (Table 1). Compared to the Henry et al. (2005) experimental conditions for the geothermometer, the expected accuracy of the temperature estimates is going to be low, at around ± 50 °C. This high error is due (as described in Henry et al. (2005)) to the absence of graphite and accessory Ti-bearing minerals in the samples from this study (c.f. Figure 6b). Henry et al. (2005) describes the Ti-in-biotite temperature estimate calculations in the absence of Ti-saturating phases as being minimum temperatures estimates.

5-4. Results

5-4.1. Sample description

Representative samples of granite lenses, with and without glimmerite selvedges, hosted in modified granitic gneiss (Figure 2c,d; coordinates 23.14523°S, 134.56708°E, WGS84) and the main glimmerite containing coarse K–feldspar grains (glimmerite schist; Figure 2b,e–g); coordinates 23.14694°S, 134.56517°E, WGS84) were collected in the Gough Dam Shear Zone study area.

Two representative samples of granite lenses hosted in modified granitic gneiss (sample GD1617 [granite bead (segmented igneous sheets) with glimmerite selvedge] and sample GD1620A [granite lens (continuous igneous sheets) without glimmerite selvedge]; Figure 3) are used to describe the characteristics of granitic felsic bodies in the GDSZ. Both samples present the contact between granite lenses and the modified

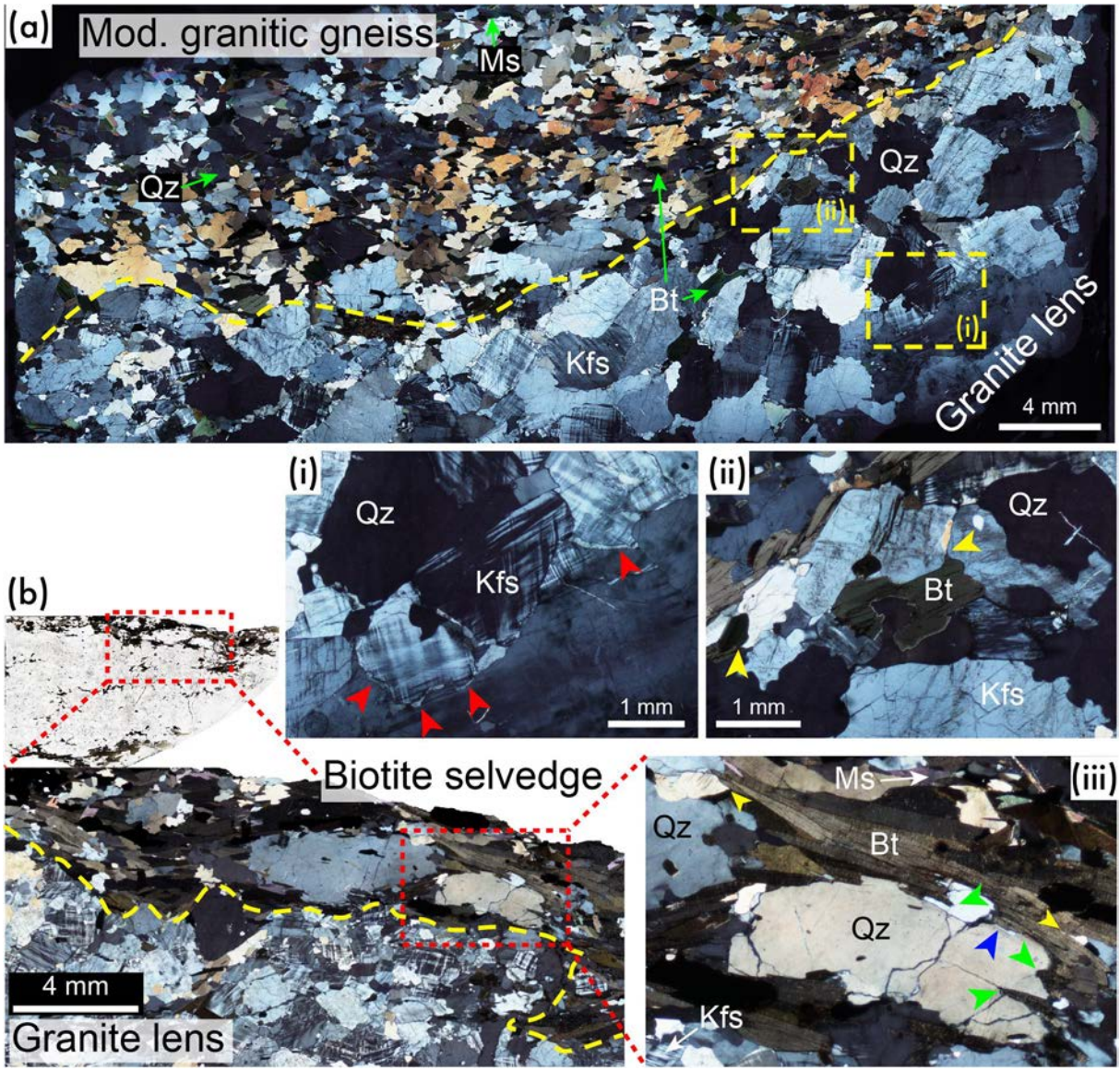

Figure 3. Characteristics typical of frozen melt. (a): Contact between granite lens and modified granitic gneiss. Elongated interstitial quartz highlighted by red arrows (i) and low dihedral angles by yellow arrows (ii), sample GD1620A (c.f. Fig. 2a for field relationship); (b): Extremity of granite lens bead featuring a glimmerite selvedge in modified granitic gneiss. Quartz grain from modified granitic gneiss in glimmerite selvedge shows biotite grain re-entrants (green arrows in (iii) detailed view). Quartz low apparent dihedral angles between two biotite grains (yellow arrow in detailed view) and interstitial quartz highlighted by blue arrow, sample GD1617 (c.f. Fig. 2c,d for field relationship). Mineral abbreviations follow Whitney & Evans (2010).

granitic gneiss. Both samples feature high vol.% of interlocked K-feldspar grains (>75%) in the granite lens, with interstitial quartz grains of varied dimensions (Figure 3). The granite lens present K-feldspar grains with apparent subhedral shape and dimensions of 3–4 mm and 1–3 mm for sample GD1620A and GD1617, respectively (Figure 3). Thin interstitial grain boundary films of quartz and plagioclase are observed between large K-feldspar grains in sample GD1620A (red arrows; Figure 3a)). The minor development of sub-grains in quartz and microcline with cross-hatched crystal twinning in K-feldspar is observed in both samples (Figure 3). Two types of contacts between granite lens and host rock are presented in Figure 3: with and without a glimmerite selvedge. Sample GD1617 (i.e. granite lens bead) shows a mm-scale glimmerite selvedge enriched in biotite compared to the modified granitic gneiss involving the granite lens. Biotite

presents a strong preferred orientation in the selvedge. Biotite grains lack typical solid-state internal deformation microstructures (e.g. kinking or folding; Figure 3b, magnified region). Biotite grains are observed to intrude fractures of relict quartz grains from the adjacent granitic gneiss (Figure 3b, magnified region). Quartz grains form low apparent dihedral angles between two biotite grains and appear as thin interstitial bands in both samples (Figure 3b, magnified region). Biotite grains in the modified granitic gneiss show a gradual increase in orientation parallel to the contact between granite lens–modified granitic gneiss, towards the aforementioned contact (Figure 3a).

The representative glimmerite schist sample (sample GD1606) is used to describe the main rock type containing large K-feldspar grains. The glimmerite schist

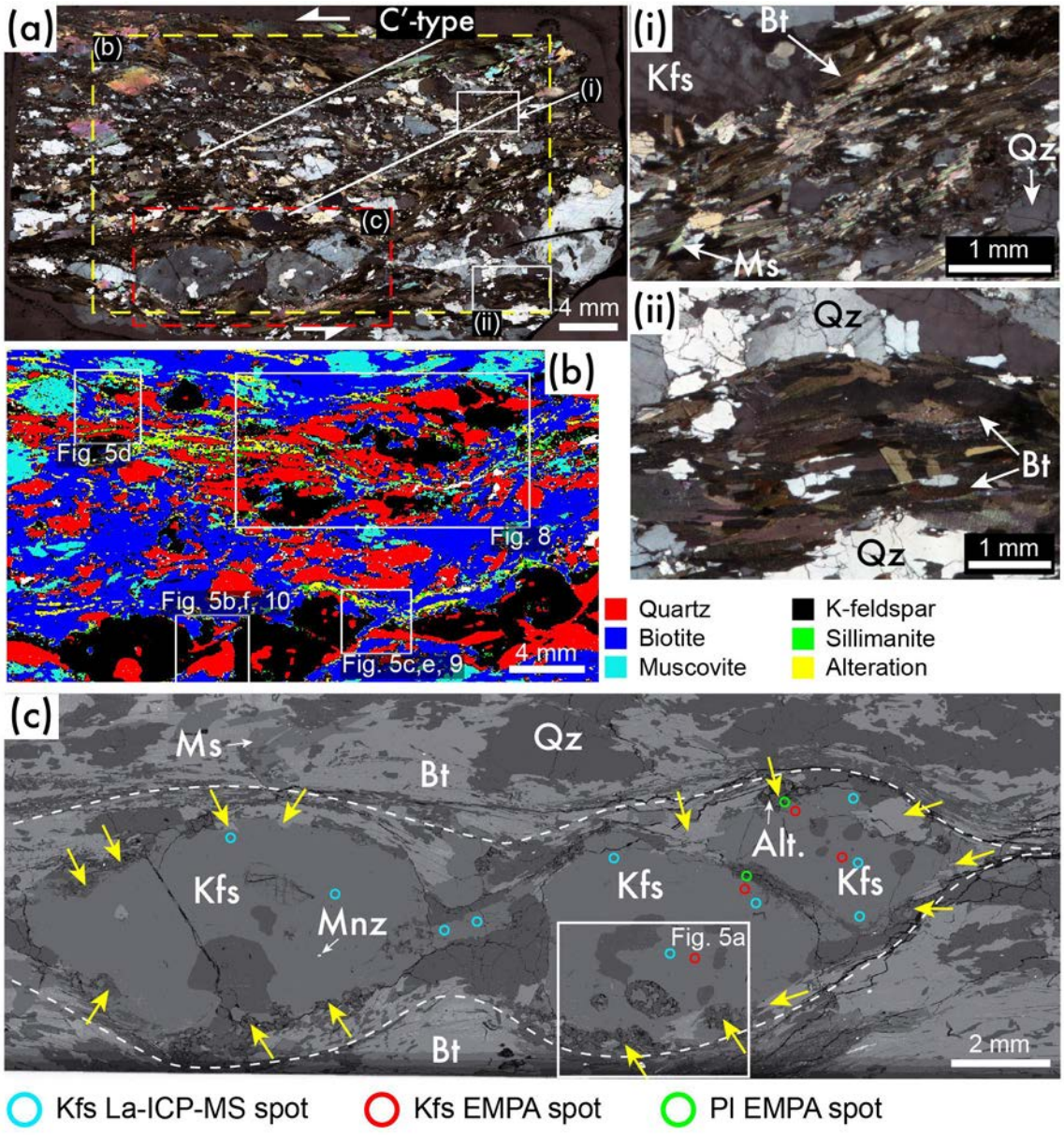

Figure 4. Characteristics of the glimmerite schist, sample GD1606; (a): Crossed-polarised light thin section photomicrograph of glimmerite schist sample showing top to the left (reverse) shear-sense informed by sigmoidal shapes formed by biotite, muscovite, quartz and sillimanite grains around K-feldspar and muscovite grains. Biotite-rich C'-type shear bands are observed. Photomicrographs for region (i) and (ii) display dominant biotite glimmerite matrix showing preferred orientation following C'-type shear band and S-plane, respectively; (b): Thin section μ-XRF mineral assemblage map; (c): SEM-BSE image of agglomeration of K-feldspar grains along the foliation. Dashed lines highlight biotite, muscovite, quartz and sillimanite grains warping around K-feldspar grains. Re-entrants of biotite and muscovite in K-feldspar are highlighted by yellow arrows. Mineral abbreviations follow Whitney & Evans (2010).

presents a bimodal grain size, with the matrix dominated by fine biotite (Bt; ~50vol.%) and containing coarse K-feldspar grains (Kfs; ~30vol.%) (Figure 4a, b). The remaining glimmerite schist matrix is constituted by quartz (Qz; ~30vol.%), muscovite (Ms; ~10vol.%), sillimanite (Sil; ~1vol.%) and ~9vol.% of a very fine-grained Al–Si-rich alteration product after plagioclase and sillimanite, inferred to be kaolinite or pyrophyllite (labelled on figures as Alt.), that fills grain micro-fractures (Figure 4a–c). Thus, the mode of sillimanite may have been higher, and plagioclase may have comprised a significant proportion of the assemblage. The mineral assemblage exhibits a strong shape preferred orientation, where large K-feldspar grains, biotite grains and bands of quartz grains are aligned parallel to the main lineation and lie in the foliation (S-plane;

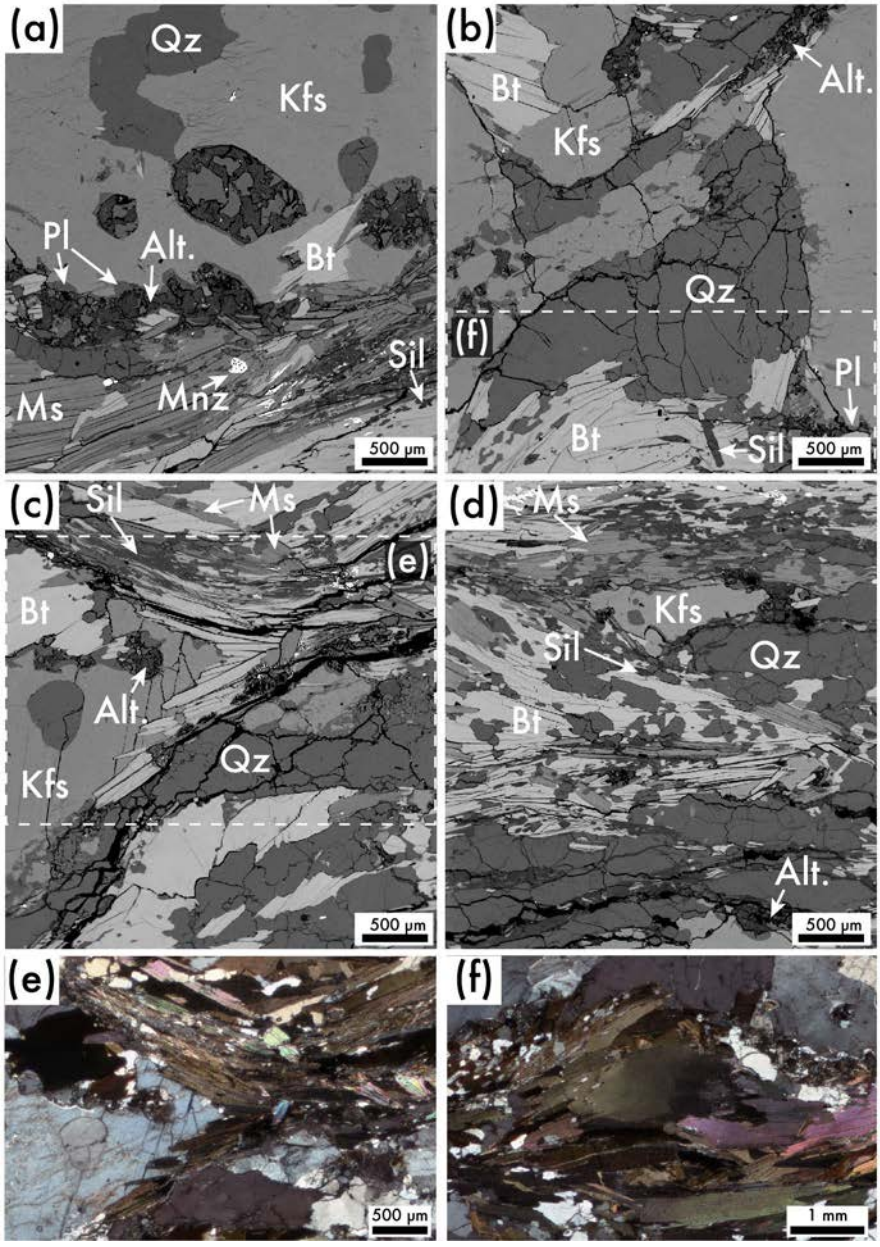

Figure 5. (a–d): SEM-BSE images of selected areas of the glimmerite schist presenting reaction replacement of (1) K-feldspar by biotite, muscovite and plagioclase “invasions” [panel a–c]; (2) low-pressure area between trail of large K-feldspar grains presenting wrapping biotite band and interstitial quartz and trail of small K-feldspar grains [panel b]; and (3) large muscovite grain featuring a pressure shadow tail comprising biotite, quartz and minor K-feldspar grains [panel d]; (e¬–f): Crossed-polarised light photomicrographs of featured region in panel (b) and (c) displaying the orientation and microstructures of the dominant biotite, quartz and muscovite present in the bands that warp around K-feldspar and located along the S-plane, respectively. Mineral abbreviations follow Whitney & Evans (2010).

Berthé et al., 1979) of the rock (Figure 4a). Bands of quartz grains and biotite are not only seen parallel to the glimmerite schist foliation but may also form bands oriented at 45° relative to the foliation (C'-type shear bands; Berthé et al., 1979) (Figure 4a). Similar to the biotite grains in the selvedges from sample GD1617, biotite grains lack kinking or folding microstructures (Figure 4i–ii, 5e–f). The coarse K-feldspar grains show (i) little evidence of crystal-plastic deformation (i.e. lack undulose extinction; Figure 4a), (ii) apparent subhedral shape (i.e. semi-straight crystal faces; Figure 4c), (iii) lack recrystallization around the grain edges (i.e. lack core-mantle microstructure common in high-strain mylonite; Figure 4), and (iv) display grain fractures filled by fine-grained reaction products (Figure 4). Most coarse K-feldspar grains exhibit inclusions of quartz and plagioclase and one grain contains a monazite inclusion. Biotite, sillimanite and small quartz grains are observed to warp around and form tails of matrix minerals at the extremities of the coarse K-feldspar and muscovite grains (Figure 4 and 5). Agglomerates of smaller quartz and feldspar grains together with minor biotite are visible in areas between the aligned coarse K-feldspar grains (i.e. in the strain shadows; Figure 4, 5b). The agglomerates of quartz are irregular-shaped being interstitial to the large K-feldspar and the finer grained agglomerates of K-feldspar filling the space between large K-feldspar grains and the K-feldspar agglomerates (Figure 4c, 5b). These small K-feldspar and quartz grains lack evidence for significant crystal-plastic deformation; i.e. they lack undulose extinction, subgrains and recrystallized grains (Figure 4c, 5b). Small and minor plagioclase grains show preferential spatial arrangement near to and/or in contact with K-feldspar grains (Figure 5a,b). Plagioclase grains are present in thin re-entrants into K-feldspar grain boundaries or are adjacent to K-feldspar (Figure 5a,b). Minor proportions (i.e. <1vol.%) of magnetite (~0.04vol.%), apatite (~0.017vol.%), monazite (~0.015vol.%) and zircon (~0.014vol.%) are observed in the matrix which is otherwise dominated by biotite and quartz.

5-4.2. Mineral chemistry

Recalculated formulae for biotite and feldspar were made on the basis of 22 and 16 oxygens, respectively, from EMP elemental spot analyses (Table 1). A feldspar ternary solid solution plot of components anorthite (An), albite (Ab) and orthoclase (Or) is presented in Figure 6a. In the feldspar ternary plot, the large K-feldspar grains present in the sample of glimmerite schist show a slightly variable composition presenting a solid solution of >80–90mol% of orthoclase. Analyses performed at the rim of the K-feldspar grains show an increase in orthoclase component relative to the bulk of analyses representing location of the core of K-feldspar grains (Figure 6a). In the same sample, plagioclase in K-feldspar re-entrants and forming films along K-feldspar grains boundary have almost pure albite composition.

Titanium-in-biotite thermometry for biotite in glimmerite bands adjacent to quartzite mylonite (sample GL; Figure 2h), and the main glimmerite schist (sample

Sample	GL	Glimmerite schist		
Mineral	Bt	Bt	Kfs	Pl
SiO_2 wt%	35.64	35.73	63.75	67.10
TiO_2	1.97	2.55	b.d.l.	b.d.l.
Al2O3	18.36	17.78	18.78	20.36
V_2O_3	0.04	0.04	b.d.l.	b.d.l.
Cr_2O_3	0.04	b.d.l.	b.d.l.	b.d.l.
FeO_{total}	15.20	17.69	0.04	b.d.l.
NiO	0.06	b.d.l.	b.d.l.	b.d.l.
MnO	0.05	0.10	b.d.l.	b.d.l.
MgO	12.66	11.58	b.d.l.	b.d.l.
CaO	b.d.l.	b.d.l.	b.d.l.	0.62
Na_2O	0.23	0.20	1.46	11.43
K_2O	9.79	9.71	14.18	0.11
P_2O_5	b.d.l.	b.d.l.	0.14	0.13
SO_3	b.d.l.	b.d.l.	b.d.l.	b.d.l.
Cl	0.19	0.41	0.04	b.d.l.
F	0.71	0.59	b.d.l.	b.d.l.
O	-0.34	-0.34	0.01	0.00
H_2O	3.98	3.93	0.00	0.00
Total	98.57	99.97	98.41	99.73

Mineral abbreviation following Whitney and Evans (2010). b.d.l.: Bellow detection limit. The complete dataset is available in Supplementary Data.

Table 1. Selected electron microprobe data on multiple minerals for the glimmerite seams and glimmerite schist present in GDSZ.

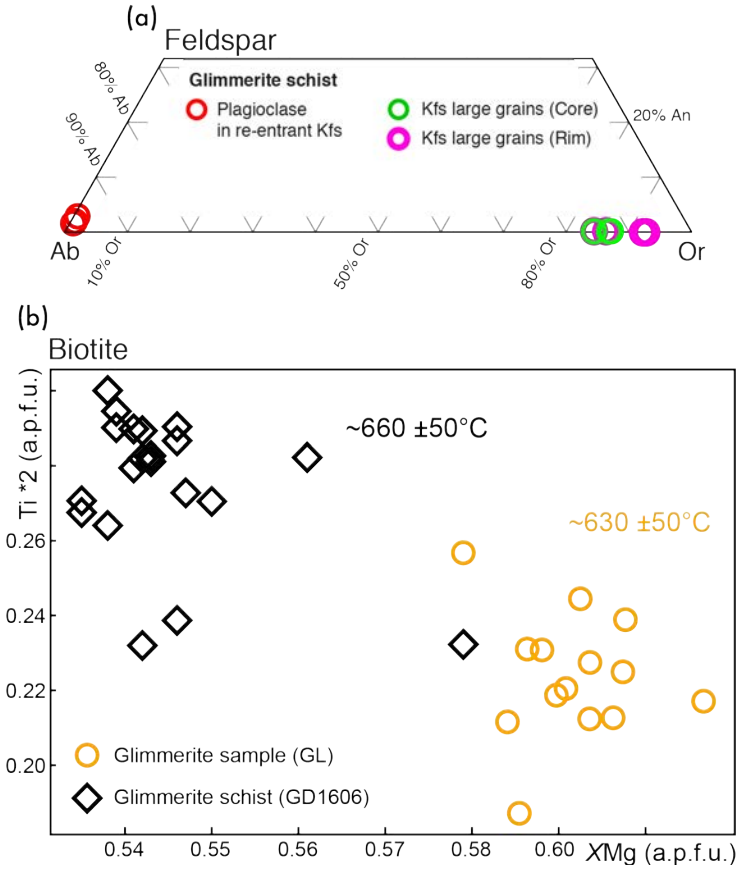

Figure 6. Mineral chemistry of feldspar and biotite. (a): An–Ab–Or ternary diagram for feldspar classification; (b): Biotite composition graph for GDSZ samples showing Ti in biotite thermometry results (Henry et al., 2005).

GD1606; Figure 2e, f) uses the Henry et al. (2005) thermometer. On the Ti a.p.f.u. vs XMg [=Mg/(Mg+Fe)] diagram, an increasing trend in Ti concentration in biotite is observed from the biotite present in the glimmerite band to the biotite constituting the glimmerite schist (Figure 6b). This increase in Ti concentration reflects an apparent increase of a minimum of 30°C from sample GL (630 ±50°C) to the glimmerite schist (660 ±50°C).

Large and interstitial K-feldspar of this study have a depleted REE concentration relative to chondrite values and show a progressive REE depletion from La to Lu, disrupted by a positive Eu anomaly that is more intense in some grains than others (Figure 7). Interstitial and large K-feldspar grains present similar values of REE concentration. Within the large K-feldspar grains, a slight increase in Eu is observed in spot analyses located close to the rim of the grains (Figure 7). All the compiled published values for K-feldspar present REE values fluctuating between enriched and depleted values, when compared to chondrite REE values, with values showing a progressive depletion from La to Lu and positive Eu anomaly (Figure 7). This fluctuation trend is most intense in the K-feldspar in granodiorite gneiss (Bingen et al., 1990), followed by the K-feldspar-rich leucosome of Carvalho et al (2016).

Sample/ Mineral	Gough Dam Shear Zone		Compilation of published Kfs composition			
	Glimmerite schist		Gneiss[(1)]	Pegmatite[(2)]	Migmatite[(3)(4)]	
	Large grains	Interstitial				
La	0.031	0.020	60.759	6.013	10.684	4.869
Ce	0.016	0.014	25.775	3.002	6.982	1.558
Pr	0.011	0.010	n.a.	1.638	5.065	0.472
Nd	0.008	0.008	b.d.l.	0.910	2.276	0.821
Sm	0.005	0.004	1.142	0.696	1.554	3.027
Eu	0.066	0.008	24.156	6.767	32.682	34.547
Gd	0.003	0.004	n.a.	0.538	0.905	0.061
Dy	0.003	0.003	n.a.	0.585	0.569	0.043
Er	0.002	0.003	n.a.	0.731	0.625	0.029
Yb	0.003	0.004	0.068	0.944	0.621	0.036
Lu	0.005	0.004	n.a.	1.098	0.407	0.041

REE values were normalised using McDonough & Sun (1995) chondritic values. (1) Granodiorite gneiss porphyroblasts (Bingen et al., 1990); (2) Pegmatite (Larsen, 2002); (3) Peraluminous migmatite leucosome (Bea et al., 1994); (4) Kfs-rich evolved leucosome (Carvalho et al., 2016). n.a.: Non available; b.d.l.: Bellow detection limit. Mineral abbreviation following Whitney and Evans (2010). The complete dataset is available in Supplementary

Table 2. Representative REE composition of feldspar grains from GDSZ and published data from multiple locations.

5-4.3. EBSD microstructures

An EBSD-indexed mineral phase map for K-feldspar and quartz from the glimmerite schist (Figure 8a) presents several mineralogically distinct bands at ~45° to the stretching lineation (C' plane in Figure 4a). These are constituted mainly by K-feldspar or quartz grains within an aggregate of K-feldspar, quartz and biotite of sigmoidal shape located in sample glimmerite schist, specifically in between two C' planes

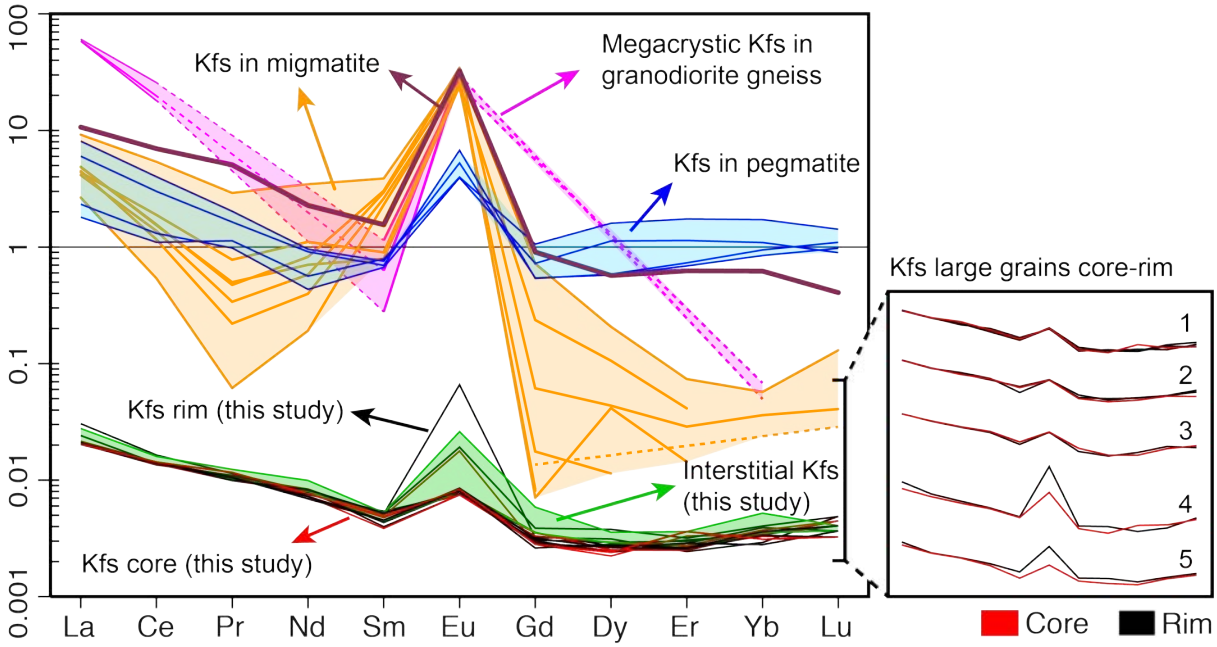

Figure 7. Chondrite-normalized REE patterns for a diverse set of K-feldspar (isolated coarse grains and interstitial grains) in the glimmerite schist compared to examples from literature of K-feldspar present in pegmatite (Larsen, 2002; blue lines), K-feldspar from leucocratic segregation in migmatites (Beat et al., 1994; Carvalho et al., 2016; dark purple and orange lines, respectively) and K-feldspar from the matrix of a granodiorite gneiss at granulite facies (Bingen et al., 1990; light purple lines). Rims of K-feldspar (this study; black lines) and interstitial grains (this study; green filled range) may be enriched in Eu compared to cores (this study; red lines).

forming a biotite shear band in thin section (Figure 4a). The elongation of quartz grains is observed to follow the sigmoidal shapes of the mica fabric (in Fig. 8a black areas) and individual quartz grains apparently bend around K-feldspar grains, yet show little internal deformation (Figure 8b). Pole figures show a weak crystallographic preferred orientation (CPO) for quartz grains with the majority of the grains c-axes oriented perpendicular, in the X-axis, to the stretching lineation of the sample (Figure 8c). The quartz [c]–axis maximum presents a main low cluster (max. 2.6 MAD) parallel to the Y-axis and <a> axes scattered along a pole figure great circle (Figure 8c). Both J-index and M-index are low with 1.27 and 0.02 respectively. Pole figures for K-feldspar are presented in two groups divided by grains size area. The threshold for the division in large K-feldspar and interpreted interstitial grains was set at 0.5% of map area. The group of identified large K-feldspar grains moderately clustered a-axes around the Y-axis and c-axes are clustered in the SW sector close to the great circle, similar in orientation to the C'-type shear bands displayed in Figure 8a. Interstitial K-feldspar grains show some alignment with a J- and M-index of 2.44 and 0.03, respectively (Figure 8c). K-feldspar shows [c]–axis orientations dispersed 45° top and bottom from X-axis pole figure. The distribution of misorientation between pairs of quartz and K-feldspar shows nearly perfect random distribution for quartz grains and weak correlation misorientation distribution for K-feldspar grains below 60° (Figure 8b).

There is no internal changes to crystal orientation within the large K-feldspar grains, nor is there sub-grain boundary formation at the rims of the grains (Figure 9). K-feldspar grains still preserve relatively straight grains boundaries (crystal facets)

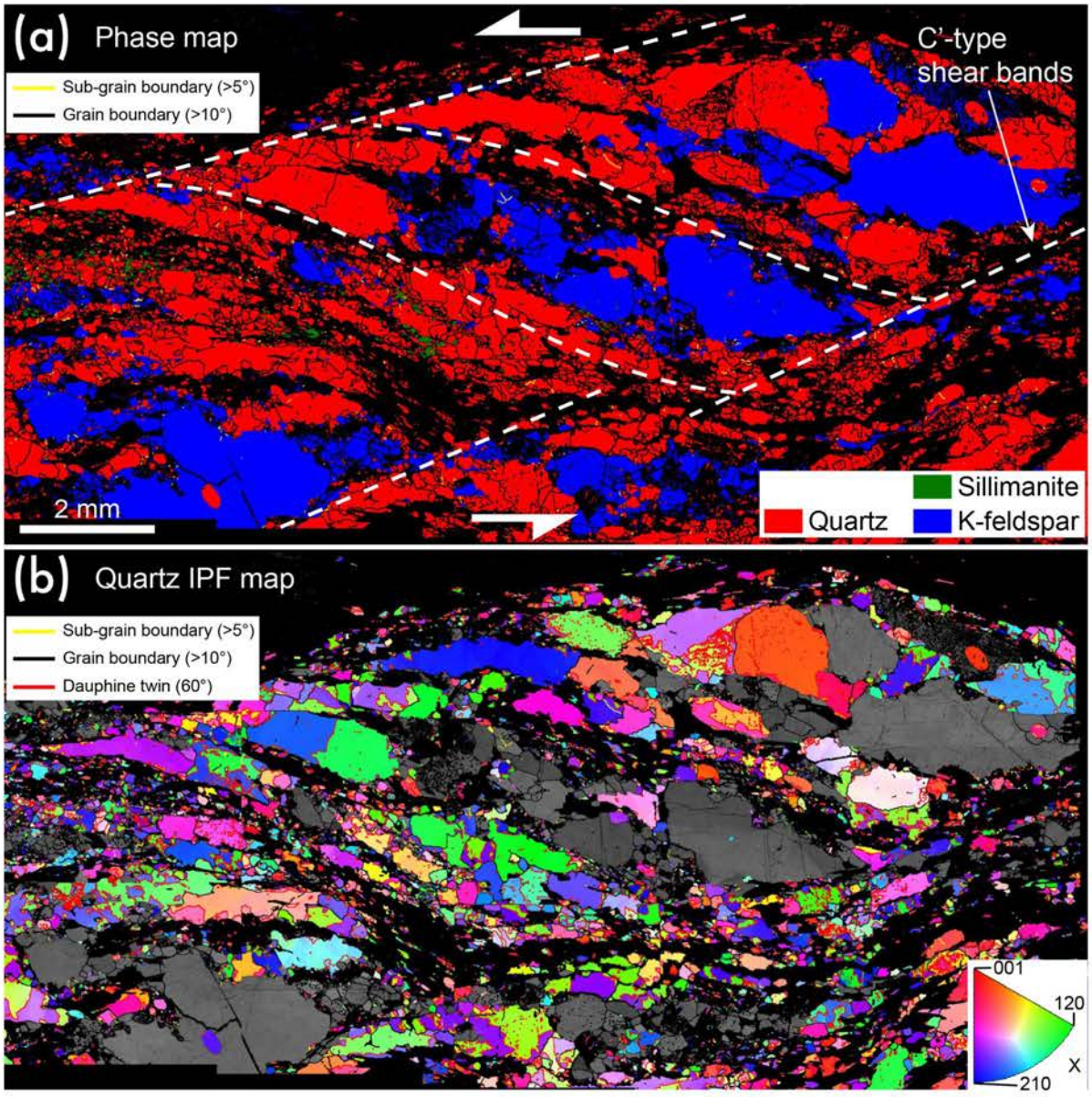
(a) Phase map
Sub-grain boundary (>5°)
Grain boundary (>10°)
C'-type shear bands
2 mm
Sillimanite
Quartz
K-feldspar
(b) Quartz IPF map
Sub-grain boundary (>5°)
Grain boundary (>10°)
Dauphine twin (60°)
001
120
210
X
(c)
Quartz
N: 4907
a [100]
c [001]
Z
X
J-Index: 1.27
M-index: 0.02
2.6
2.2
1.8
1.4
1
0.6
K-feldspar
Large grains
N: 6
a [100]
b [010]
c [001]
Quartz
K-feldspar
Quartz-Quartz
Quartz-Quartz
Theoretical random
Frequency (%)
Misorientation angle (°)
Orthoclase-Orthoclase
Orthoclase-Orthoclase
Theoretical random
Frequency (%)
Misorientation angle (°)
Interstitial grains
N: 1194
M-index: 0.03
J-Index: 2.42
3
2.5
2
1.5
1
0.5

when comparing the inferred boundaries to a 3-dimensional representation of the grain orientation and crystallographic system (white bars; Figure 9). Re-entrants into K-feldspar grains containing biotite and muscovite are common in the glimmerite schist (Figure 4c and 5). These “invasions” of mica are observed to preferentially follow the direction of the crystal axes i.e. perpendicular to the crystal planes, of the K-feldspar grains (white arrows; Figure 9).

In the low-strain areas between the aligned K-feldspar grains, quartz grains exhibit extensive formation of Dauphine twin boundaries (Figure 10a), while the K-feldspar grains in both the small grained agglomerates and large K-feldspar grains, do not present any significant misorientation within individual grains (Figure 10b). Similar to the K-feldspar in Figure 9, no sub-grain boundaries are observed. Two large interstitial quartz grains, separated in 2-dimensions by the clustered small K-feldspar grains, present a misorientation between them inferior to 15° (Figure 10a). Most of the clustered small K-feldspar grains exhibit similar characteristics to the large K-feldspar grains (c.f. Fig. 9) with limited crystal lattice bending, relatively straight grain boundaries and biotite “invasions” along the K-feldspar a, b and c axes, informed by the pole figure presented for each grain (Figure 10b). There are two small K-feldspar grains which exhibit similar orientation, inferior to 15° (pink grains on Figure 10b). Both these grains share grain boundaries with other small K-feldspar grains. The array of small K-felspar grains in the strain shadow of the large K-feldspar grains share similar orientations (green colours on Figure 10a inset), while the surrounding large K-feldspar grains also share similar orientation to each other (pink colours on Figure 10a inset), but different to the small interstitial grains.

5-5. Discussion

5-5.1. Melt-present high-strain deformation: petrographic and microstructural evidence

At the macro-scale, both biotite-rich and biotite-poor rocks constituting the GDSZ present features typical of high-strain zones: (i) preferential mineral alignment forming a distinct and well-developed foliation and lineation defined mainly by biotite and K-feldspar grains; (ii) lenses with granitic composition and coarse grains aligned along the foliation resemble pinch and swell patterns; (iii) elongated grains of quartz and feldspar in granitic gneisses, with some K-feldspar grains exhibiting sigmoidal shapes

Figure 8. Quantitative orientation analysis of K-feldspar and quartz; (a) EBSD mineral phase map for quartz (red) and K-feldspar grains (blue) in glimmerite schist. Polymineralic sigmoidal shape and C’-type shear bands are indicated by the dashed white lines. (b): IPF-derived map for quartz grains relative to the X-plane; (c): Pole figures for all quartz grains and two groups of K-feldspar divided by grain size area, with a threshold at 0.5 percent of map area, to distinguish large grains from interstitial grains. J- and M-index are displayed for all quartz grains and for interstitial K-feldspar grains. Uncorrelated misorientation angles distribution is featured for all grains from each mineral.

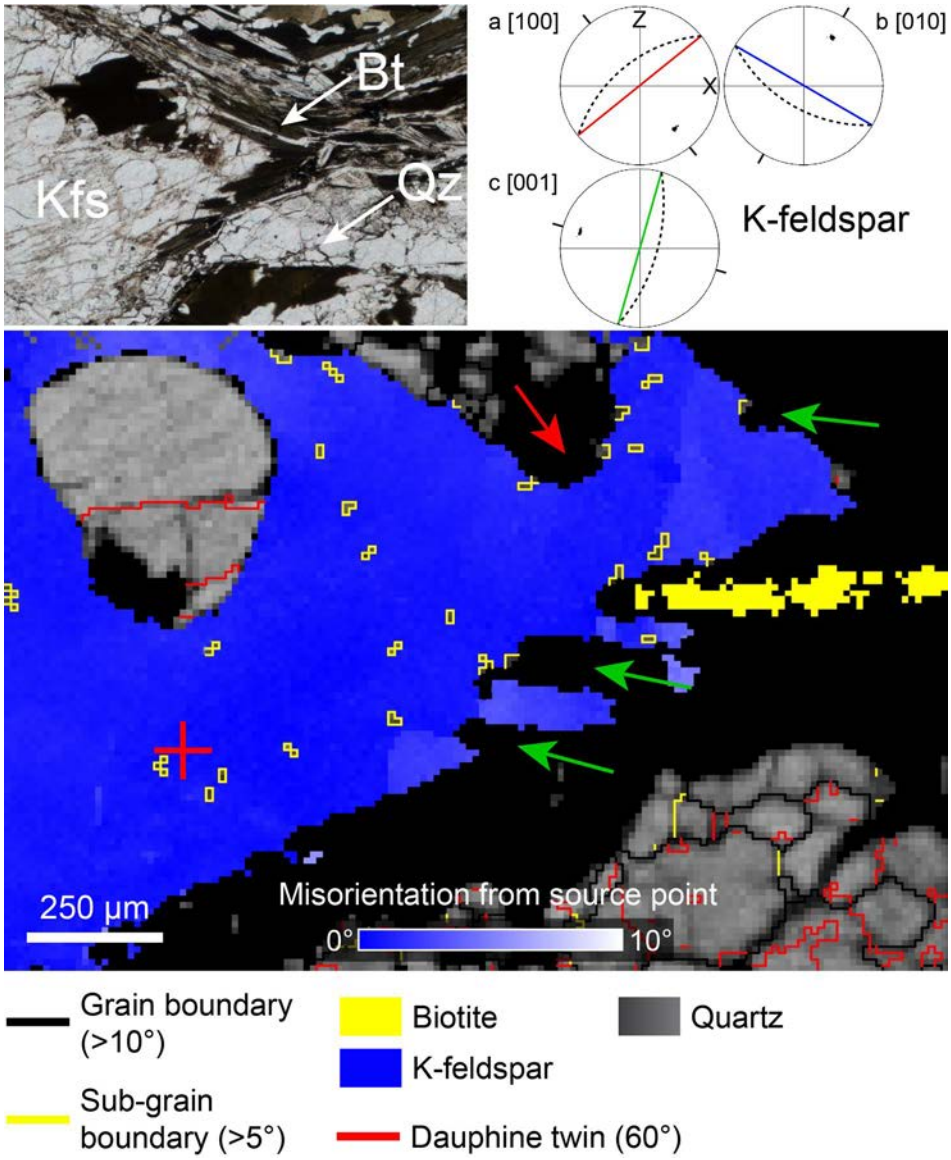

Figure 9. Crystallographic characteristics of a large K-feldspar grain. EBSD map showing the change in orientation within one large grain colour coded by crystallographic orientation divergence up to 15° relative to a reference orientation (red cross). White arrows highlight dissolution reaction sites on the K-feldspar grain and replacement by non-indexed minerals, i.e. mainly biotite and muscovite (top plane-polarized light photomicrographs), penetrating along the crystallographic axes of the K-feldspar grain. Quartz grains represented by variably grey EBSD band contrast, with rare sub-grain boundaries in yellow and common Dauphine twins in light blue.

(Figure 2; Vernon, 1987; Lister & Snoke 1984; Passchier & Trouw, 2005). Although commonly formed during solid state deformation, the alignment of biotite or K-feldspar grains can also be derived from magmatic flow (Paterson et al., 1998; Vernon, 2000; Zak et al., 2008; Zibra et al., 2014). Close examination of the granite lenses (Figure 2c,d and 3) show that these present igneous characteristics including interlocking, faceted feldspar grains of unimodal grain size and interstitial quartz. Even though the trains of granite lenses resemble pinch and swell structures, the minerals constituting the lenses show little evidence for solid-state deformation (e.g. bimodal grains size or mantled porphyroclast observed by, for example, Vernon et al. (1983) and Tullis & Yund (1991)). The lack of evidence for internal deformation in the granite lenses points toward a differential stress regime synchronous with melt injection to form the

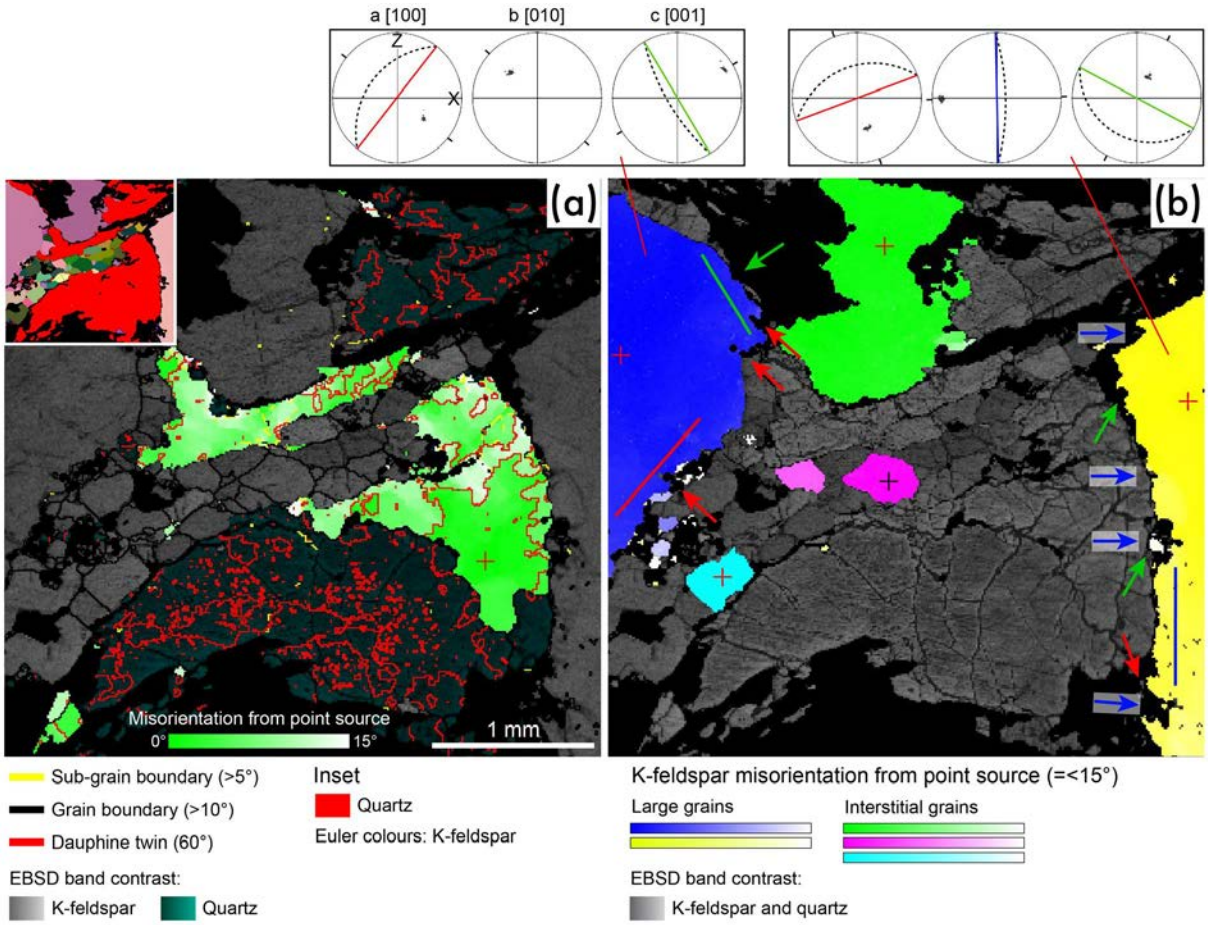

Figure 10. (a) Interstitial low-strain area between two large K-feldspar grains presenting isolated quartz grains at a maximum misorientation of 15° relative to a source point (red cross). Inset displays Euler colours of K-feldspar grains showing two main orientation groups (pink versus green colours); quartz grains are coloured red. (b) Each colour represents a different grain analysis for misorientation from a source point up to 15°, represented by the respective red and black crosses. Re-entrants and their orientation are highlighted by the direction of the yellow arrows. Pole figures for the two large grains at left and right of the image present a, b and c crystallographic planes in an equal area, lower hemisphere projection. The orientation of crystal faces is transferred to the EBSD map image. Coloured lines highlight the orientation of relict K-feldspar grain facets.

lenses. These lenses closely resemble the pseudo-boudinage of Bons et al (2004), in which they describe similar patterns resembling pinch and swell structures in partially crystallized pegmatites.

In the glimmerite schist, all minerals exhibit a preferential grain alignment, i.e. biotite, K-feldspar, quartz, muscovite and sillimanite (Figure 4). Apart from the inferred differential stress-assisted preferential mineral alignment, other microstructures are observed within the glimmerite schist that must be associated with non-coaxial strain accumulation; for example, polymineralic sigmoidal shaped structures comprising a combination of muscovite, K-feldspar and quartz (Figure 4b), and biotite shear bands (C'-type) at ~45° to the foliation (Figure 4a)(Berthé et al., 1979) are common. Close analysis of the minerals highlights very limited internal grain deformation and a distinct lack of features commonly observed in high-strain zones that deform in the solid-state (e.g. kinking and folding of biotite and/or undulose extinction in K-feldspar and quartz grains (Figure 4a) (e.g. Wilson 1980; Lister & Snoke 1984). Mica fish development, grain size reduction producing core-mantle structures and internal deformation

structures such as subgrain boundaries and continuous crystal lattice bending are commonly attributed to solid-state crystal-plastic deformation; yet these are missing from the glimmerite schist (Figure 4)(e.g. Ten Grotenhuis et al. 2003; Passchier & Trouw, 2005; Mancktelow & Pennacchioni, 2005). These microstructures are also absent in the K-feldspar and quartz grains in the granite lenses (Figure 3). We suggest that the absence of a strain record in the individual grains comprising the glimmerite schist and granite lenses is consistent with the presence of a weak medium, in this case interstitial melt, that accommodated a large part of the applied stresses via grain boundary sliding. This is similar to the experimental aggregate strength reduction with increase of melt fraction in mylonites from Rosenberg & Handy (2005). Our model of melt-present deformation is supported by the following microstructures in the different samples described. In the glimmerite schist melt-K-feldspar reaction can account for the presence of re-entrants containing plagioclase, biotite and muscovite at the edge of large K-feldspar grains (Figure 4c, 5a,c, 9 and 10b). These re-entrant reactions resemble a “back reaction” of the vapour absent melting reaction: Ms + Qz + Pl = Kfs + Sil (or Ky) + Melt (Patino Douce & Johnston, 1991). At the edge of the granite lenses, the described highly elongate grains of plagioclase and quartz (Figure 4b) are interpreted as minerals that pseudomorphed grain boundary melt films. The quartz and K-feldspar aggregates in the low-strain shadows between the large K-feldspar grains closely resemble interstitial textures, consistent with melt-present deformation (Figure 4 and 10). The fact that the CPO of quartz and K-feldspar is week even though there is a strong foliation and lineation contradicts the fact that in solid-state crystal plastic deformation high CPO intensity is expected at high strain (e.g. Lister & Hobbs, 1980; Law, 1990, 2010; Menegon et al., 2008). However, this conundrum can be explained by the presence of melt during deformation accommodating most of the strain. In the low-pressure or strain shadow regions between large K-feldspar grains, a trail of smaller K-feldspar grains resembling a deformation tail is observed (Figure 4c, 5 and 10). This type of microstructure is commonly featured in deformed porphyroclasts present in mylonite. However, in this scenario, the tails comprise recrystallized material from the porphyroclast or the strain shadows comprise minerals formed from solution precipitation (Yardley, 1977; Vernon, 1987; Passchier & Trouw, 2005). Although resembling a direct deformation trail by recrystallization, the smaller K-feldspar trail does not present microstructures indicative of such a process. This interpretation is informed by the lack of internal deformation and sub-grain formation close to K-feldspar grain boundary (Figure 10) (Tullis & Yund, 1985; Ree et al., 2005; Menegon et al., 2008, 2013). Some of the smaller isolated K-feldspar grains in the low-pressure regions are connected in three dimensions, informed by sharing the same orientation, indicating crystallisation from grain boundary melt connected in 3D (Figure 10b).

In addition, the microstructure of the re-entrants into the large K-feldspar grains is unusual for a high strain rock deformed by solid-state deformation (Figure 9 and 10b; Passchier & Trouw, 2005). In the latter case, one would expect interlocking microstructure between these minerals. Instead, a reactive nature of that contact,

where K-feldspar is dissolved, and plagioclase-biotite-muscovite grow is more likely. The fact that this texture is undeformed but still aligned with the general foliation of the sample suggests formation at a time the rock was under differential stress. We suggest that this microstructure formed when melt-K-feldspar interaction triggered dissolution of K-feldspar and precipitation of plagioclase-biotite-muscovite. This disequilibrium indicates that the melt involved in the reaction was different to that from which the K-feldspar grew, consistent with melt flux through the high strain zone.

The low quartz mode in the granite lenses and in the glimmerite schist suggests that the interstitial melt was physically removed from the system towards the end of the melt-present deformation. The expulsion of the melt fraction from the high-strain zone would exponentially increase the strength of the rock, as reviewed by Rosenberg & Handy (2005), hardening the previously rheologically soft high-strain zone. This now rheologically hard high-strain zone stopped to accommodate the differential stress and is consistent with the lack of deformation overprint of the granite component present in the high-strain zone.

In summary, the microstructures observed in the rocks of the Gough Dam Shear are consistent with high-strain melt-present deformation and these microstructures highlight the important role that melt played in the high-strain zone activity.

5-5.2. Origin of the large K-feldspar grains

The large K-feldspar grains observed as dominantly individual grains in the glimmerite schist are interpreted to have formed by early crystallization of granite melt (Figure 2e-g and 4). Other examples of concentration of K-feldspar are described in the literature (e.g. in granitoids [e.g.; Vernon, 1986; Vernon & Paterson, 2008], in schlieren suggesting phenocryst flow-sorting [e.g. Bateman and Chappell, 1979; Vernon, 1986], and in enclaves in megacrystic granitoids [e.g. Didier, 1973]).

The observed matrix foliation warping around the K-feldspar grains indicates pre- to syn-tectonic mineral growth (Figure 4c and 5). Porphyroblasts in shear zones share this characteristic and may also exhibit inclusion trails or sigmoidal shape commonly showing grain rotation relative to the matrix foliation (Passchier et al., 1992; Johnson, 1999). We use (1) the foliation warping around the K-feldspar grains in addition to (2) preservation of crystal faces, (3) lack of internal deformation and (4) lack of core-mantle microstructure, features indicating recrystallization by grain area reduction (Figure 4c, 5, 9 and 10)(see review of these microstructures in Passchier & Trouw (2005) and Blenkinsop (2007)) to interpret the K-feldspar grains as early crystallising minerals from the migrating melt. The shape of the K-feldspar has been modified by the re-entrant reaction replacement by plagioclase, biotite and muscovite that we interpret as due to subsequent K-feldspar-melt reaction (Figure 9 and 10b). It is apparent that reaction dissolution was enhanced along the crystallographic b and c axes of the K-feldspar phenocrysts, similar in concept to the observed forsterite

anisotropic dissolution favouring crystallographic axes (Grandstaff, 1978; Awad et al., 2000, Godinho et al. 2013, 2014) or preferential partial melting along subgrain boundaries in quartz and plagioclase of Levine et al. (2016).

The K-feldspar grains present no evident chemical zonation, except for some rim domains showing a localized stronger positive Eu anomaly and a slight increase in orthoclase component (Figure 6a and 7). This limited chemical zonation suggests that the crystallization of the K-feldspar grain was fast, and that the crystallization of melt was of short duration. This model of K-feldspar crystallization is informed by the tendency of feldspar grains to form chemical zonation due to the strength of the Si–O and Al–O bonds (Winter, 2013) and/or by an open system allowing the chemical or physical disruption of the boundary layer around the K-feldspar grain which is usually depleted in elements with mineral/melt partition coefficient >1, allowing maximum crystal growth (Green & Watson, 1982; Bacon, 1989). The fast growth of the K-feldspar phenocrysts can be explained by reduced nucleation in highly hydrous silicate melts. Once the mineral nucleates, fast mineral growth occurs at undercooled conditions (Nabelek et al., 2010). The fast growth surrounded by melt allied to delayed nucleation possibly explains the rarity of small inclusions in the K-feldspar phenocrysts (Figure 3, 5, 9 and 10). In experimental conditions, K-feldspar crystallization begins with at least 60–70% of liquid in the crystal mush which may suggest that the phenocrysts grew in pockets of the fluxing melt with a high fraction of liquid (Clemens & Wall, 1981; Winkler & Schultes, 1982). The crystallization of K-feldspar first is in accordance with the observed sequence of mineral crystallization in granite, as extensively discussed by Vernon & Paterson (2008) for K-feldspar megacrysts in granite, and zoned pegmatites that tends to form monomineralic segregations of K-feldspar or quartz, starting far from the liquidus, with an initial assemblage of K-feldspar + quartz ± biotite (Cameron et al., 1949; London, 2005). This may suggest that the melt migrating through the GDSZ may have had a chemical composition close to the aforementioned zoned pegmatites due to the similarities in the observed sequence of mineral crystallisation.

Some K-feldspar grains exhibit an increase in Eu and modal component of orthoclase at the rim of the grain (Figure 6a and 7). This increase in Eu concentration and orthoclase component occurs close to the re-entrants into the K-feldspar grains, suggesting that the contact with a subsequent melt triggers localised “back reaction” discussed previously. This may locally modify the Eu concentration in the K-feldspar due to the high Kfs/melt Eu partition coefficient; the higher orthoclase component may be due to coupled exchange of Na and K at the reaction interface during formation of albite (Labotka et al., 2004; Hövelmann et al., 2010). The REE concentrations normalized to chondrite of the K-feldspar in the glimmerite schist show highly depleted values, i.e. a maximum of 0.1 times chondrite values (Table 2 and Figure 7). The depleted REE concentration values observed in the K-feldspar contrasts with the mainly enriched REE concentration of magmatic K-feldspar in pegmatite and porphyroblastic K-feldspar in granodiorite gneiss (Larsen, 2002; Bingen et al., 1990). The progressively decreasing

REE pattern of the K-feldspar from La to Lu in the glimmerite schist resembles the patterns observed for some of the pegmatite K-feldspar and migmatite leucosome data (Figure 7). K-feldspar in leucosomes (Carvalho et al., 2016) show depleted HREE compared to our K-feldspar phenocrysts. This is explained by melt flow entrainment of accessory minerals with high HREE affinity from the adjacent rock. The contrast in REE patterns suggests that this physical process is unlikely to have taken place in the melt flow forming our K-feldspar phenocrysts. The similarity in REE concentration pattern with pegmatites and migmatite leucosomes is consistent with a magmatic origin for the glimmerite schist K-feldspar and our phenocryst interpretation. The highly depleted REE concentration observed in glimmerite schist K-feldspar may indicate crystallisation from a REE-depleted melt. These have been interpreted to form by disequilibrium melting of a paleosome armouring monazite and/or extensive fractional crystallization of monazite (Yurimoto et al., 1990; Nabelek & Glascock, 1995). A high proportion of monazite in glimmerite samples of the GDSZ supports the latter.

5-5.3. Trapped K-feldspar: A signature for melt extraction and physical collapse

Following our previous interpretation of melt-present deformation in the GDSZ, and that the K-feldspar has an igneous origin, one question remains: how did relatively undeformed K-feldspar grains end up in a high-strain zone? We interpret that the K-feldspar phenocrysts crystallized in the migrating melt and were trapped in the glimmerite schist during collapse of the melt pathways. We infer that a decrease in the melt supply (i.e. draining of the source), implying a decrease in the melt pressure, meant that the melt pressure could no longer maintain an open channel, leading to structural collapse of the system (Figure 11).

In our model, we interpret the melt filling of tensional fractures along strike, possibly formed due to an anisotropic tensile strength of the photolith (Wickham, 1987), as the most probable mechanism for the initiation of the melt pathways observed in the study area. Additionally, the physical size of the K-feldspar grains also argues against a more pervasive grain boundary melt flow process that would have formed interconnected melt flow bands (Figure 2a,c,d)(Brown, 1994; Weinberg, 1999; Bons et al., 2004). Other indications of fracture propagation are observed in the orthogonal mode 1 extensional fractures in the quartzite mylonite layers surrounded by the glimmerite schist (Figure 2h). The same development of pathways is believed to have happened early in the formation of the glimmerite schist. These pathways are presently not as visible in this rock type due to the higher amount of melt-rock interaction producing glimmerite at the expense of adjacent rocks by dissolution-precipitation (Figure 2b,h). Furthermore, the grain shape and preferred orientation of the micas possibly facilitated the extraction of melt during the collapse of the high-strain zone (Weinberg et al., 2001; Zak et al., 2008). The presence of a melt fraction in the glimmerite schist during the period of deformation would have decreased the strength

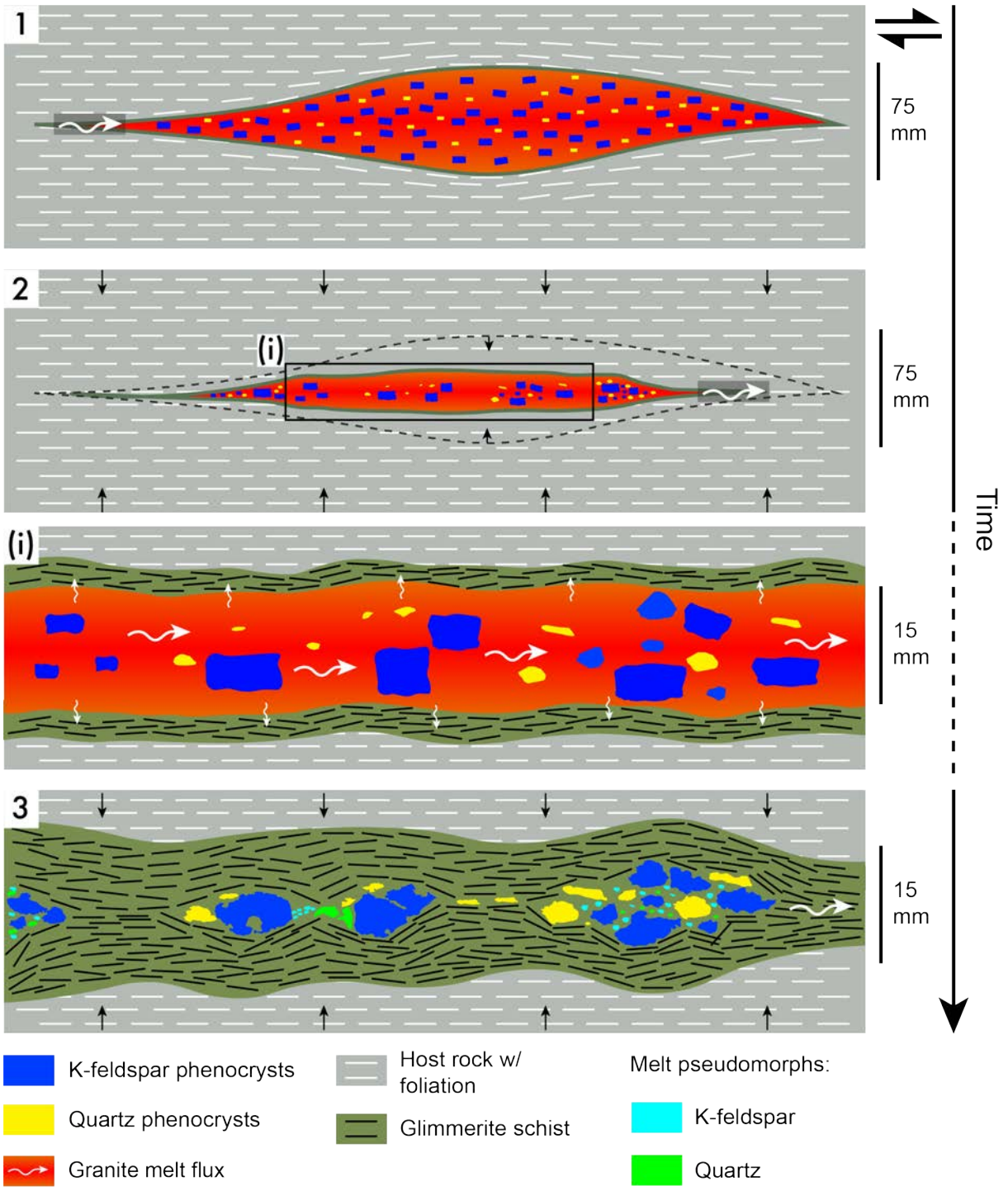

Figure 11. Cartoon depicting the proposed high-strain zone collapse and consequent entrapment of crystallized fraction from the externally derived fluxing melt.

of the rock by several orders of magnitude and increased the temperature of biotite formation compared to the glimmerite bands adjacent to the modified granulite rocks (Figure 6b). Extreme weakening increases non-linearly up to 10vol.% of melt fraction (Melt connectivity transition of Rosenberg & Handy, 2005), with the melt lubricating 90% of crystal boundaries at the 10vol.% melt fraction threshold described by van der Molen & Paterson (1979).

The final melt extraction and crystal entrapment occurred during collapse of the high-strain zone. The trains of granite lenses observed in the felsic bands (Figure 2a,c,d) follow closely the model of Bons et al (2004) for inflation and collapse of pegmatite

dykes in Cap de Creus, Spain. In Bons et al., (2004), one of the main features used to recognize collapse structures is the formation of thinning beads (Figure 9a in Bons et al., 2004) in partially crystallized pegmatite dykes. These can easily be interpreted as boudinage, in lieu of formation of collapse beads, due to the morphological similarities at outcrop scale (Bons et al., 2004, 2008). During the process of collapse, most of the strain and foliation deflection is localized at the corner of the beads, decreasing away from the beads. These observations are at odds to the observed strain spanning the entire area in between boudins. Furthermore, no evidence of dyke-parallel stretching within the beads or in the thin seams connecting the beads are observed when pegmatite beads form by local inflation and collapse, usually observed in boudin formation (Bons et al., 2004).

The overall main characteristics of the beads formation model fits the observed lack of extensional deformation of the granitic lenses in our study area and the diminute amount of strain observed in between them (Figure 2d and 3). The presence of large vol.% of melt during the period of deformation of the granitic lenses most possibly allowed the strain to concentrate into the melt instead of the crystallized mineral grains (Vigneresse & Tikoff, 1999), resulting in little internal evidence of the synchronous high-strain in the remaining beads. A similar process of melt filled fractures followed by collapse is proposed for the formation of the glimmerite schist. The sequence of melt inflation and latter collapse would explain the presence and entrapment of K-feldspar phenocrysts in the glimmerite matrix and the entrapment and crystallisation of melt in low-strain regions of the glimmerite schist (Figure 2e–f, 3c and 10). This collapse process would also explain the inferred melt extraction that mitigated the formation of granitic bodies within the glimmerite schist. It is also consistent with the diminute number of igneous microstructures in the glimmerite matrix and the lack of deformation of solid grains. Following the Bons et al. (2004) collapse model, we suggest that the contrast between the granite lenses and the isolated K-feldspar crystals was due to differential concentration of crystals locally present during collapse, leading to a decrease of crystal entrapment with an increase of melt fraction.

5-6. Conclusions

The presence of undeformed and faceted K-feldspar phenocrysts, as individual grains or clusters of grains in a high-strain zone, i.e. the Gough Dam Shear Zone, central Australia, occurred via the entrapment of early crystallised minerals due to the collapse of wall rocks constituting the melt pathway. Opening of melt pathways probably occurred by tensional fractures along rock anisotropies. This syn-deformational creation of melt migration pathways in a high-strain zone allowed melt flux and extensive melt-rock interaction. The reaction produced glimmerite schist and glimmerite and involved dissolution of the adjacent felsic wall rocks. Early, fast growing K-feldspar grains crystallized from the fluxing melt due to delayed mineral nucleation in an undercooled

and hydrous melt. Posterior collapse of the melt pathway, comprising glimmerite enriched walls, was achieved as a consequence of decreased melt supply. This ultimately led to the entrapment of the crystallized minerals (phenocrysts) in the melt and synchronous extraction of the remaining liquid fraction from the high-strain zone. This physical entrapment process allowed the formation of granite lenses in less reacted melt pathways (granitic gneiss) and an increase in the efficiency of entrapment of phenocrysts in the more reacted glimmerite schist bands. We suggest the presence of undeformed K-feldspar in high-strain zones is a new indicator of former melt flux in rock types with limited igneous features.

5-7. Acknowledgments

M. Bebbington and T. Murphy (Macquarie University) assisted with making thin sections and geochemical analysis. Sandrin Feig (Univ. of Tasmania) assisted with electron microprobe analysis. Duncan Hedges and Richard Walshaw (University of Leeds) assisted with EBSD data collection. This study used instrumentation funded by ARC LIEF and DEST Systemic Infrastructure Grants, Macquarie University and Industry. This is contribution 1381 from the ARC Centre of Excellence for Core to Crust Fluid Systems (http://www.CCFS.mq.edu.au) and GEMOC Key Centre (http://www.GEMOC.mq.edu.au). This work was carried out as part of a PhD study at Macquarie University and was supported by ARC Discovery grant DP160103449 to Putnis, TR and ND. We thank S. Cruden (Monash University) and A. Tommasi (University of Montpellier) for constructive comments on an earlier version of this manuscript. We thank the land owners for permission to visit and sample localities in the Gough Dam shear zone.

5-8. References

Acosta-Vigil, A., Buick, I., Hermann, J., Cesare, B., Rubatto, D., London, D., Morgan, G. B., 2010. Mechanisms of crustal anatexis: a geochemical study of partially melted metapelitic enclaves and host dacite, SE Spain. Journal of Petrology, 51(4): 785–821.

Awad A., vanGroos A. F. K., Guggenheim S., 2000. Forsteritic olivine: effect of crystallographic direction on dissolution kinetics. Geochimica et Cosmochimica Acta, 64: 1765–1772.

Bachmann, F., Hielscher, R., Schaeben, H., 2010. Texture analysis with MTEX–free and open source software toolbox. Solid State Phenomena, 160: 63–68.

Bacon, C. R., 1989. Crystallization of accessory phases in magmas by local saturation adjacent to phenocrysts. Geochimica et Cosmochimica Acta, 53(5): 1055–1066.

Ballèvre, M., Möller, A., Hensen, B. J., 2000. Exhumation of the lower crust during crustal shortening: an Alice Springs (380 Ma) age for a prograde amphibolite facies

shear zone in the Strangways Metamorphic Complex (central Australia). Journal of Metamorphic Geology, 18(6): 737–747.

Bateman, P. C. & Chappell, B, W., 1979. Crystallization, fractionation, and solidification of the Tuolumne Intrusive Series, Yosemite National Park, California. Bulletin of the Geological Society of America, 90: 465–482.

Bea, F., Pereira, M. D., Stroh, A., 1994. Mineral/leucosome trace-element partitioning in a peraluminous migmatite (a laser ablation-ICP-MS study). Chemical Geology, 117(1–4): 291–312.

Beere, W., 1975. A unifying theory of the stability of penetrating liquid phases and sintering pores. Acta Metallurgica, 23(1): 131–138.

Bendall, B., 2000. Mid-Palaeozoic shear zones in the Strangways Range: a record of intracratonic tectonism in the Arunta Inlier, Central Australia (Doctoral dissertation). University of Adelaide, Adelaide, Australia.

Bercovici, D., 1998. Generation of plate tectonics from lithosphere–mantle flow and void–volatile self-lubrication. Earth and Planetary Science Letters, 154(1-4): 139–151.

Berthé, D., Choukroune, P., Jégouzo, P., 1979. Orthogneiss, mylonite and non coaxial deformation of granites: the example of the South Armorican Shear Zone. Journal of Structural Geology, 1(1): 31–42.

Bingen, B., Demaiffe, D., Hertogen, J., 1990. Evolution of feldspars at the amphibolite-granulite-facies transition in augen gneisses (SW Norway): geochemistry and Sr isotopes. Contributions to Mineralogy and Petrology, 105(3): 275–288.

Blenkinsop, T. G., 2007. Deformation microstructures and mechanisms in minerals and rocks. Springer Science & Business Media, Germany.

Bons, P. D., Becker, J. K., Elburg, M. A., Urtson, K., 2009. Granite formation: stepwise accumulation of melt or connected networks? Earth and Environmental Science Transactions of the Royal Society of Edinburgh, 100(1–2): 105–115.

Bons, P. D., Druguet, E., Castaño, L. M., Elburg, M. A., 2008. Finding what is now not there anymore: Recognizing missing fluid and magma volumes. Geology, 36(11): 851–854.

Bons, P. D., Druguet, E., Hamann, I., Carreras, J., Passchier, C. W., 2004. Apparent boudinage in dykes. Journal of Structural Geology, 26(4): 625–636.

Bons, P.D., 1999. Apparent extensional structures due to volume loss. Estonian Academy of Sci- ences Proceedings: Geology, 48: 3–14.

Brodie, K. H., & Rutter, E. H., 1985. On the relationship between deformation and metamorphism, with special reference to the behavior of basic rocks. Metamorphic reactions: 138–179.

Brown, M. & Rushmer, T., 2006. Evolution and Differentiation of the Continental Crust. Cambridge University Press, Cambridge.

Brown, M. & Solar, G. S., 1998. Shear-zone systems and melts: feedback relations and self-organization in orogenic belts. Journal of Structural Geology, 20: 211–227.

Brown, M., 1994. The generation, segregation, ascent and emplacement of granite magma: the migmatite-to-crustally-derived granite connection in thickened orogens. Earth-Science Reviews, 36(1-2): 83–130.

Bunge, H. J., 2013. Texture analysis in materials science: Mathematical methods. Elsevier, Amsterdam, Netherlands.

Cameron, E. N., 1949. Internal structure of granitic pegmatites. Economic Geology Monograph, 2: 115.

Cartwright, I., Buick, I. S., Foster, D. A., Lambert, D. D., 1999. Alice Springs age shear zones from the southeastern Reynolds Range, central Australia. Australian Journal of Earth Sciences, 46(3): 355–363.

Carvalho, B. B., Sawyer, E. W., Janasi, V. A., 2016. Crustal reworking in a shear zone: transformation of metagranite to migmatite. Journal of Metamorphic Geology, 34(3): 237–264.

Cesare, B., Mariani, E. S., Venturelli, G., 1997. Crustal anatexis and melt extraction during deformation in the restitic xenoliths at El Joyazo (SE Spain). Mineralogical Magazine, 61(1): 15-27.

Clemens, J. D., & Wall, V. J., 1981. Origin and crystallization of some peraluminous (S-type) granitic magmas. The Canadian Mineralogist, 19(1): 111-131.

Coblentz, D. D., Zhou, S., Hillis, R. R., Richardson, R. M., Sandiford, M., 1998. Topography, boundary forces, and the Indo-Australian intraplate stress field. Journal of Geophysical Research: Solid Earth, 103(B1): 919–931.

Collins, W. J., & Sawyer, E. W., 1996. Pervasive granitoid magma transfer through the lower–middle crust during non-coaxial compressional deformation. Journal of Metamorphic Geology, 14(5): 565–579.

Collins, W., & Shaw, R., 1995. Geochronological constraints on orogenic events in the Arunta inlier: A review. Precambrian Research, 71(1): 315–346.

Collins, W., & Teyssier, C., 1989. Crustal scale ductile fault systems in the Arunta inlier, central Australia. Tectonophysics, 158(1): 49–66.

Cunningham, D., 2005. Active intracontinental transpressional mountain building in the mongolian Altai: Defining a new class of orogen. Earth and Planetary Science Letters 240(2): 436–444.

D'lemos, R. S., Brown, M., Strachan, R. A., 1992. Granite magma generation, ascent and emplacement within a transpressional orogen. Journal of the Geological Society,

149(4): 487–490.

Daczko, N.R., Piazolo, S., Meek, U., Stuart, C. A., Elliot, V., 2016. Hornblendite delineates zones of mass transfer through the lower crust. Scientific Reports, 6: 31369.

Didier, J., 1973. Granites and their Enclaves. Elsevier, Amsterdam.

Donovan, J.J., Snyder, D.A., Rivers, M.L., 1993. An improved interference correction for trace element analysis. Microbeam Analysis, 2: 2.

Girard, J., Chen, J., Raterron, P., Holyoke III, C. W., 2013. Hydrolytic weakening of olivine at mantle pressure: Evidence of [1 0 0] (0 1 0) slip system softening from single-crystal deformation experiments. Physics of the Earth and Planetary Interiors, 216: 12–20.

Godinho, J. R., Piazolo, S., Evans, L., 2014. Simulation of surface dynamics during dissolution as a function of the surface orientation: Implications for non-constant dissolution rates. Earth and Planetary Science Letters, 408: 163–170.

Godinho, J. R., Putnis, C. V., Piazolo, S., 2013. Direct observations of the dissolution of fluorite surfaces with different orientations. Crystal Growth & Design, 14(1): 69–77.

Grandstaff, D. E., 1978. Changes in surface area and morphology and the mechanism of forsterite dissolution. Geochimica et Cosmochimica Acta, 42(12): 1899–1901.

Green, T. H., & Watson, E. B., 1982. Crystallization of apatite in natural magmas under high pressure, hydrous conditions, with particular reference to ‘orogenic’ rock series. Contributions to Mineralogy and Petrology, 79(1): 96–105.

Griffin, W. L., 2008. GLITTER: data reduction software for laser ablation ICP-MS. Laser Ablation ICP-MS in the Earth Sciences: Current practices and outstanding issues: 308–311.

Hand, M., & Sandiford, M., 1999. Intraplate deformation in central Australia, the link between subsidence and fault reactivation. Tectonophysics, 305(1): 121–140.

Hasalova, P., Stipska, P., Powell, R., Schulmann, K., Janousek, V., Lexa, O., 1998. Transforming mylonitic metagranite by open-system interactions during melt flow. Journal of metamorphic Geology, 26(1): 55–80.

Heidbach, O., Tingay, M., Barth, A., Reinecker, J., Kurfeß, D., Müller, B., 2010. Global crustal stress pattern based on the World Stress Map database release 2008. Tectonophysics, 482(1–4): 3–15.

Heinrich, K.F.J., 1966. X-ray absorption uncertainty. The electron microprobe: 296.

Henke, B.L., 1985. Lawrence Berkeley Laboratories, unpublished.

Henry, D. J., Guidotti, C. V., Thomson, J. A., 2005. The Ti-saturation surface for low-to-medium pressure metapelitic biotites: Implications for geothermometry and Ti-substitution mechanisms. American Mineralogist, 90(2-3): 316–328.

Henry, H., 2018 Mantle Pyroxenites: Deformation and Seismic Properties. (Doctoral dissertation). Macquarie University, Sydney, Australia.

Henry, H., Tilhac, R., Griffin, W. L., O'Reilly, S. Y., Satsukawa, T., Kaczmarek, M. A., Ceuleneer, G., 2017. Deformation of mantle pyroxenites provides clues to geodynamic processes in subduction zones: case study of the Cabo Ortegal Complex, Spain. Earth and Planetary Science Letters, 472: 174–185

Hollister, L. S. & Crawford, M. L., 1986. Melt-enhanced deformation: A major tectonic process. Geology, 14: 558–561.

Holtz, F., Johannes, W., Tamic, N., Behrens, H., 2001. Maximum and minimum water contents of granitic melts generated in the crust: a reevaluation and implications. Lithos, 56(1): 1–14.

Hövelmann, J., Putnis, A., Geisler, T., Schmidt, B. C., Golla-Schindler, U., 2010. The replacement of plagioclase feldspars by albite: observations from hydrothermal experiments. Contributions to Mineralogy and Petrology, 159(1): 43–59.

Hulsbosch, N., Hertogen, J., Dewaele, S., André, L., Muchez, P., 2014. Alkali metal and rare earth element evolution of rock-forming minerals from the Gatumba area pegmatites (Rwanda): Quantitative assessment of crystal-melt fractionation in the regional zonation of pegmatite groups. Geochimica et Cosmochimica Acta, 132: 349–374.

Hutton, D. H., 1988. Granite emplacement mechanisms and tectonic controls: Inferences from deformation studies. Earth and Environmental Science Transactions of the Royal Society of Edinburgh, 79(2-3): 245–255.

Jamieson, R.A., Unsworth, M.J., Harris, N.B., Rosenberg, C.L. Schulmann, K., 2011. Crustal melting and the flow of mountains. Elements, 7: 253–260.

Jarosewich, E., Nelen, J. A., Norberg, J. A., 1980. Reference samples for electron microprobe analysis. Geostandards Newsletter, 4(1): 43–47.

Johnson, S. E., 1999. Porphyroblast microstructures: A review of current and future trends. American Mineralogist, 84(11–12): 1711–1726.

Kriegsman, L. M., 2001. Partial melting, partial melt extraction and partial back reaction in anatectic migmatites. Lithos, 56(1): 75–96.

Kronenberg, A. K., Segall, P., Wolf, G. H., 1990. Hydrolytic weakening and penetrative deformation within a natural shear zone. Geophysical Monograph, 56: 21–36.

Labotka, T. C., Cole, D. R., Fayek, M., Riciputi, L. R., Stadermann, F. J., 2004. Coupled cation and oxygen-isotope exchange between alkali feldspar and aqueous chloride solution. American Mineralogist, 89(11–12): 1822–1825.

Larsen, R. B., 2002. The distribution of rare-earth elements in K-feldspar as an indicator of petrogenetic processes in granitic pegmatites: examples from two pegmatite fields in southern Norway. The Canadian Mineralogist, 40(1): 137¬–152.

Laul, J. C., & Lepel, E. A., 1987. Rare earth element patterns in biotite muscovite and tourmaline minerals. Journal of Radioanalytical and Nuclear Chemistry, 112(2): 461¬–471.

Law, R. D., 1990. Crystallographic fabrics: a selective review of their applications to research in structural geology. Geological Society, London, Special Publications, 54(1): 335–352.

Law, R. D., Mainprice, D., Casey, M., Lloyd, G. E., Knipe, R. J., Cook, B., Thigpen, J. R., 2010. Moine thrust zone mylonites at the Stack of Glencoul: I–microstructures, strain and influence of recrystallization on quartz crystal fabric development. Geological Society, London, Special Publications, 335(1): 543–577.

Lee, A. L., Torvela, T., Lloyd, G. E., Walker, A. M., 2018. Melt organisation and strain partitioning in the lower crust. Journal of Structural Geology, 113: 188–199.

Levine, J. S., Mosher, S., Rahl, J. M., 2016. The role of subgrain boundaries in partial melting. Journal of Structural Geology, 89: 181–196.

Levine, J.S.F., Mosher, S., Siddoway, C.S., 2013. Relationship between syndeformational partial melting and crustal-scale magmatism and tectonism across the Wet Mountains, central Colorado. Lithosphere 5 (5): 456–476.

Lister, G. S., & Hobbs, B. E., 1980. The simulation of fabric development during plastic deformation and its application to quartzite: the influence of deformation history. Journal of Structural Geology, 2(3): 355–370.

Lister, G. S., & Snoke, A. W., 1984. SC mylonites. Journal of Structural Geology, 6(6): 617–638.

London, D., 2005. Granitic pegmatites: an assessment of current concepts and directions for the future. Lithos, 80(1–4): 281–303.

Maidment, D., Hand, M., Williams, I., 2005. Tectonic cycles in the Strangways metamorphic complex, Arunta inlier, central Australia: Geochronological evidence for exhumation and basin formation between two high–grade metamorphic events. Australian Journal of Earth Sciences, 52(2): 205–215.

Mancktelow, N. S., & Pennacchioni, G., 2005. The control of precursor brittle fracture and fluid–rock interaction on the development of single and paired ductile shear zones. Journal of Structural Geology, 27(4): 645–661.

Massonne, H. J., & Schreyer, W., 1987. Phengite geobarometry based on the limiting assemblage with K-feldspar, phlogopite, and quartz. Contributions to Mineralogy and Petrology, 96(2): 212–224.

Mawby, J., Hand, M., Foden, J., 1999. Sm–Nd evidence for high–grade ordovician metamorphism in the Arunta block, central Australia. Journal of Metamorphic Geology, 17: 653–668.

McDonough, W. F., & Sun, S. S., 1995. The composition of the Earth. Chemical geology, 120(3–4): 223–253.

Menegon, L., Pennacchioni, G., Heilbronner, R., Pittarello, L., 2008. Evolution of quartz microstructure and c-axis crystallographic preferred orientation within ductilely deformed granitoids (Arolla unit, Western Alps). Journal of Structural Geology, 30(11): 1332–1347.

Menegon, L., Stünitz, H., Nasipuri, P., Heilbronner, R., Svahnberg, H., 2013. Transition from fracturing to viscous flow in granulite facies perthitic feldspar (Lofoten, Norway). Journal of Structural Geology, 48: 95–112.

Morris, J. D., Leeman, W. P., Tera, F., 1990. The subducted component in island arc lavas: constraints from Be isotopes and B–Be systematics. Nature, 344(6261): 31.

Nabelek, P. I., & Glascock, M. D., 1995. REE-depleted leucogranites, Black Hills, South Dakota: a consequence of disequilibrium melting of monazite-bearing schists. Journal of Petrology, 36(4): 1055–1071.

Nabelek, P. I., Whittington, A. G., Sirbescu, M. L. C., 2010. The role of H 2 O in rapid emplacement and crystallization of granite pegmatites: resolving the paradox of large crystals in highly undercooled melts. Contributions to Mineralogy and Petrology, 160(3): 313–325.

Nash, W. P., & Crecraft, H. R., 1985. Partition coefficients for trace elements in silicic magmas. Geochimica et Cosmochimica Acta, 49(11): 2309–2322.

Passchier, C. W., & Trouw, R. A., 2005. Microtectonics. Springer Science & Business Media, Germany.

Passchier, C. W., Trouw, R. A. J., Zwart, H. J., Vissers, R. L. M., 1992. Porphyroblast rotation: eppur si muove*?. Journal of Metamorphic Geology, 10(3): 283–294.

Paterson, S.R., Fowler Jr., T.K., Schmidt, K.L., Yoshinobu, A.S., Yuan, E.S., Miller, R.B., 1998. Interpreting magmatic fabric patterns in plutons. Lithos 44(1–2): 53–82.

Patiño Douce, A. E., & Johnston, A. D., 1991. Phase equilibria and melt productivity in the pelitic system: implications for the origin of peraluminous granitoids and aluminous granulites. Contributions to Mineralogy and Petrology, 107(2): 202–218

Patiño-Douce, A. E., & Beard, J. S., 1995. Dehydration-melting of biotite gneiss and quartz amphibolite from 3 to 15 kbar. Journal of Petrology, 36(3): 707–738.

Piazolo, S., Bons, P. D., Jessell, M. W., Evans, L., Passchier, C. W., 2002. Dominance of microstructural processes and their effect on microstructural development: insights from numerical modelling of dynamic recrystallization. Geological Society, London, Special Publications, 200(1): 149–170.

Pichon, X. L., Henry, P., Lallemant, S., 1993. Accretion and erosion in subduction zones: The role of fluids. Annual Review of Earth and Planetary Sciences, 21(1): 307–331.

Raimondo, T., Clark, C., Hand, M., Faure, K., 2011. Assessing the geochemical and tectonic impacts of fluid-rock interaction in mid-crustal shear zones: A case study from the intracontinental Alice Springs orogen, central Australia. Journal of Metamorphic Geology, 29(8): 821–850.

Raimondo, T., Hand, M., Collins, W. J., 2014. Compressional intracontinental orogens: Ancient and modern perspectives. Earth–Science Reviews, 130: 128–153.

Rasband, W.S., 1997–2015. ImageJ, U. S. National Institutes of Health. Bethesda, MD, USA. Available at: http://imagej.nih.gov/ij/.

Ree, J. H., Kim, H. S., Han, R., Jung, H., 2005. Grain-size reduction of feldspars by fracturing and neocrystallization in a low-grade granitic mylonite and its rheological effect. Tectonophysics, 407(3-4): 227–237.

Rosenberg, C. L., & Handy, M. R., 2005. Experimental deformation of partially melted granite revisited: implications for the continental crust. Journal of Metamorphic Geology, 23(1): 19–28.

Sawyer, E.W., Cesare, B., Brown, M., 2011. When the continental crust melts. Elements, 7: 229–234.

Schmidt, M. W., & Poli, S., 1998. Experimentally based water budgets for dehydrating slabs and consequences for arc magma generation. Earth and Planetary Science Letters, 163(1–4): 361–379.

Scrimgeour, I. R., 2013. Aileron Province, in Ahmad M. and Munson T. J., Geology and mineral resources of the Northern Territory. Northern Territory Geological Survey, Special Publication, 5.

Searle, M., 2013. Crustal melting, ductile flow, and deformation in mountain belts: cause and effect relationships. Lithosphere 5(6): 547–554.

Shaw, R. D., Stewart, A. T., & Black, L. P., 1984. The Arunta Inlier: a complex ensialic mobile belt in central Australia. Part 2: tectonic history. Australian Journal of Earth Sciences, 31(4): 457–484.

Sibson, R. H., 1994. Crustal stress, faulting and fluid flow. Geological Society, London, Special Publications, 78(1): 69–84.

Silva, D., Piazolo, S., Daczko, N. R., Houseman, G., Raimondo, T., Evans, L., 2018. Intracontinental Orogeny Enhanced by Far-Field Extension and Local Weak Crust. Tectonics, 37(12): 4421–4443.

Skemer, P., Katayama, I., Jiang, Z., Karato, S. I., 2005. The misorientation index: Development of a new method for calculating the strength of lattice-preferred orientation. Tectonophysics, 411(1–4): 157–167.

Sobolev, A. V., & Chaussidon, M., 1996. H2O concentrations in primary melts from supra-subduction zones and mid-ocean ridges: implications for H2O storage and recycling in the mantle. Earth and Planetary Science Letters, 137(1–4): 45–55.

Spence, D. A., & Turcotte, D. L., 1985. Magma-driven propagation of cracks. Journal of Geophysical Research: Solid Earth, 90(B1): 575-580.

Stern, R. J., 2002. Subduction zones. Reviews of geophysics, 40(4): 1012.

Stipp, M., Stunitz, H., Heilbronner, R., Schmid, S.M., 2002. Dynamic recrystallization of quartz: correlation between natural and experimental conditions. In: De Meer, S., Drury, M.R., De Bresser, J.H.P., Pennock, G.M. (Eds.), Deformation Mechanisms, Rheology, and Tectonics: Current Status and Future Perspectives: 171–190.

Stuart, C. A., Daczko, N. R., Piazolo, S., 2017. Local partial melting of the lower crust triggered by hydration through melt–rock interaction: an example from Fiordland, New Zealand. Journal of Metamorphic Geology, 35(2): 213–230.

Stuart, C. A., Piazolo, S., Daczko, N. R., 2018. The recognition of former melt flux through high-strain zones. Journal of Metamorphic Geology, 36(8): 1049–1069.

Ten Grotenhuis, S. M., Trouw, R. A. J., Passchier, C. W., 2003. Evolution of mica fish in mylonitic rocks. Tectonophysics, 372(1-2): 1–21.

Tetley, M. G., & Daczko, N. R., 2014. Virtual Petrographic Microscope: a multi-platform education and research software tool to analyse rock thin-sections. Australian Journal of Earth Sciences, 61(4): 631–637.

Teyssier, C., 1985. A crustal thrust system in an intracratonic tectonic environment. Journal of Structural Geology, 7(6): 689–700.

Thompson, A.B., 1982. Dehydration melting of pelitic rocks and the generation of H2O-undersaturated granitic liquids. American Journal of Science, 282: 1567–1595.

Tucker, N. M., Hand, M., Payne, J. L., 2015. A rift–related origin for regional medium–pressure, high–temperature metamorphism. Earth and Planetary Science Letters, 421: 75–88.

Tullis, J., & Yund, R. A., 1985. Dynamic recrystallization of feldspar: a mechanism for ductile shear zone formation. Geology, 13(4): 238–241.

Tullis, J., & Yund, R. A., 1991. Diffusion creep in feldspar aggregates: experimental evidence. Journal of Structural Geology, 13(9): 987–1000.

Urai, J. L., Means, W. D., Lister, G. S., 1986. Dynamic recrystallization of minerals. Mineral and rock deformation: 161–199.

Van der Molen, I., & Paterson, M. S., 1979. Experimental deformation of partially-melted granite. Contributions to Mineralogy and Petrology, 70(3): 299–318.

Vernon, R. H., & Paterson, S. R., 2008. How late are K-feldspar megacrysts in granites? Lithos, 104(1–4): 327–336.

Vernon, R. H., 1986. K-feldspar megacrysts in granites—phenocrysts, not porphyroblasts. Earth-Science Reviews, 23(1): 1–63.

Vernon, R. H., 1987. Growth and concentration of fibrous sillimanite related to heterogeneous deformation in K-feldspar-sillimanite metapelites. Journal of Metamorphic Geology, 5(1): 51–68.

Vernon, R. H., 2000. Review of microstructural evidence of magmatic and solid-state flow. Visual Geosciences, 5(2): 1–23.

Vernon, R. H., Williams, V. A., D'arcy, W. F., 1983. Grain-size reduction and foliation development in a deformed granitoid batholith. Tectonophysics, 92(1–3): 123–145.

Vigneresse, J. L., & Tikoff, B., 1999. Strain partitioning during partial melting and crystallizing felsic magmas. Tectonophysics, 312(2-4): 117–132.

Vigneresse, J.L., 1995. Crustal regime of deformation and ascent of granitic magma. Tectonophysics, 249: 187–202.

von Bargen, N., & Waff, H. S., 1986. Permeabilities, interfacial areas and curvatures of partially molten systems: results of numerical computations of equilibrium microstructures. Journal of Geophysical Research: Solid Earth, 91(B9): 9261–9276.

Weinberg, R. F., 1999. Mesoscale pervasive felsic magma migration: alternatives to dyking. Lithos 46: 393–410.

Weinberg, R. F., Hasalová, P., Ward, L., Fanning, C. M., 2013. Interaction between deformation and magma extraction in migmatites: Examples from Kangaroo Island. South Australia Bulletin, 125(7-8): 1282–1300.

Weinberg, R. F., Sial, A. N., Mariano, G., 2004. Close spatial relationship between plutons and shear zones. Geology, 32(5): 377–380.

Weinberg, R. F., Sial, A. N., Pessoa, R. R., 2001. Magma flow within the Tavares pluton, northeastern Brazil: Compositional and thermal convection. Geological Society of America Bulletin, 113(4): 508–520.

Whitney, D. L., & Evans, B. W., 2010. Abbreviations for names of rock-forming minerals. American Mineralogist, 95(1): 185–187.

Wickham, S. M., 1987. The segregation and emplacement of granitic magmas. Journal of the Geological Society, 144(2): 281–297.

Wilson, C. J. L., 1980. Shear zones in a pegmatite: a study of albite-mica-quartz deformation. Journal of Structural Geology, 2(1–2): 203–209.

Winkler, H. G. F., & Schultes, H., 1982. On the problem of alkali feldspar phenocrysts in granitic-rocks. Neues Jahrbuch fur Mineralogie. Monatshefte, 12: 558–564.

Winter, J. D., 2013. Principles of igneous and metamorphic petrology. Pearson education, UK.

Wintsch, R. P., Christoffersen, R., Kronenberg, A. K., 1995. Fluid-rock reaction weakening of fault zones. Journal of Geophysical Research: Solid Earth, 100(B7): 13021–13032.

Yardley, B. W., 1977. The nature and significance of the mechanism of sillimanite growth in the Connemara Schists, Ireland. Contributions to Mineralogy and Petrology, 65(1): 53–58.

Yurimoto, H., Duke, E. F., Papike, J. J., Shearer, C. K., 1990. Are discontinuous chondrite-normalized REE patterns in pegmatitic granite systems the results of monazite fractionation? Geochimica et Cosmochimica Acta, 54(7): 2141–2145.

Žák, J., Verner, K., Týcová, P., 2008. Grain-scale processes in actively deforming magma mushes: New insights from electron backscatter diffraction (EBSD) analysis of biotite schlieren in the Jizera granite, Bohemian Massif. Lithos, 106(3–4): 309–322.

Závada, P., Schulmann, K., Konopásek, J., Ulrich, S., Lexa, O., 2007. Extreme ductility of feldspar aggregates—Melt-enhanced grain boundary sliding and creep failure: Rheological implications for felsic lower crust. Journal of Geophysical Research: Solid Earth, 112(B10).

Zibra, I., Gessner, K., Smithies, H. R., Peternell, M., 2014. On shearing, magmatism and regional deformation in Neoarchean granite-greenstone systems: Insights from the Yilgarn Craton. Journal of Structural Geology, 67: 253–267.

Chapter 6. Synthesis and Conclusions

In this thesis, high strain-zones in the intracontinental Alice Springs Orogeny were investigated to provide a better understanding of the role that these crustal structures played in melt migration and ascent that lead to melt-rock interaction and reaction softening at mid-crustal levels. The subsequent effect that these rheologically weak structures had in the initiation and development of orogenesis and the ultimate exhumation of lower crustal rocks was explored.

6-1. Achievement of the thesis aims

6-1.1. Assess the continental-scale geodynamic effect of lithospheric weak zones in central Australia, coupled with changing far-field stresses, on the observed spatial strain intensity, localization and kinematics of deformation in an intracontinental setting, i.e. the Alice Springs Orogeny.

One of the keystones in understanding the formation of orogenic belts is to assume that stress accommodation is focused at the margin of lithospheric plates during convergence, as predicted by the plate tectonic model. In Chapter 3, a thin viscous sheet deformation numerical model was used to investigate the role of pre-existing weak regions, located in the Arunta region of central Australia, in the accommodation of transmitted intraplate stresses. The Alice Springs Orogeny presents a complex temporal and structural deformation pattern, linked to stresses originating at plate margins by tectonic activity at both the northern and eastern boundaries of the Australian plate. These periods of compressional or extensional stresses used in the thin viscous sheet numerical model are informed by a compilation of tectonic events that occurred in the Australian plate, i.e., the Canning basin extensional periods and the Tasmanides Orogeny compressional and extensional periods (see Chapter 2 and 3).

The thin viscous sheet deformation numerical model, representing the Australian plate (Chapter 3), demonstrated that the pattern of temporal and structural deformation observed in the Alice Spring Orogeny is best matched when the external stresses located at the plate margins are transmitted by strong lithospheric blocks into weak zones, such as the failed Larapinta rift in central Australia. The strong lithospheric blocks are present in the Australian plate as cratonic blocks to the north and south of the Arunta region. The presence of a failed rift and an extremely deep (>30km) sedimentary basin (Harts Range Group) in the Arunta region created a weak zone that accommodated stresses when a plate tectonic reconfiguration inverted the rift, thus beginning the Alice Springs Orogeny. Extreme weakening of some of the shear zones

present in the Strangways Metamorphic Complex was achieved by the combination of extreme melt-rock interaction forming weak glimmerite (i.e. reaction softening) and syn-tectonic melt flux through the high-strain zones (see Chapter 2, 4 and 5). The principal N–S-directed compressional stress ongoing during most of the Alice Spring Orogeny, and transmitted through the cratonic blocks to the weak regions of the failed rift in central Australia, are influenced by synchronous stresses propagated from the Tasmanides Orogen of eastern Australia. The models show that these additional stresses from the eastern boundary either reduce (i.e. during periods of E–W convergence) or increase (i.e. during periods of E–W extension) the N–S maximum compressional stress in central Australia and hence influence the tectonic activity. This model behavior explains the episodic and long-lived nature of the Alice Spring Orogeny; i.e., episodes of activity were dampened during periods of compression at the eastern Australia boundary (see Chapter 2 and 3).

The geometry of the various primary crustal features present in the Arunta region exert an important control on the accommodation and concentration of the differential far-field stresses propagated to the plate interiors (Chapter 3). The orientation of orogenic systems such as the Alice Spring Orogeny are controlled by pre-existing crustal structures in the form of failed rifts, deep basins or crustal-scale shear zones if these are oriented at a low angle to the principal transmitted stresses. In the numerical model of Chapter 3, where these weak crustal structures or terrains were oriented at low angle to the principal stress, a higher magnitude of crustal thickening was modelled. Enhanced thrusting was also observed in sectors of the model at the boundaries between terrains of contrasting rheological properties or proximal to rheologically weak crustal structures such as shear zones or the failed rift. It is therefore advocated that the coupled crustal thickening and increased trusting of rheologically weak regions and crustal structures oriented at a low angle to the principal stress favors the interpretation that both these geological factors have a profound effect in the accommodation of far-field transmitted stresses and exhumation of deep crust in intracontinental settings.

6-1.2. Identify the changes resulting from high-strain melt flux on the chemical, mineralogical and rheological evolution of a mid-crustal high strain zone, i.e. the Gough Dam shear zone.

Melt migration through lower to middle crust exerts an important control on crustal processes as it changes the physical conditions, such as the rheology and P–T-x conditions, and also it influences chemical processes, through melt-rock interaction driving dissolution-precipitation mineral reactions. Open system channels of melt migration facilitate the modification of crustal and melt P-T-x conditions; these systems commonly result in disequilibrium when melt comes into contact with the host rock, resulting in enhanced melt-rock interaction. Migration and ascent of hydrous melt through anhydrous, metastable, high-metamorphic rocks has the potential to trigger

extreme chemical exchange between melt and host rock, driving metasomatism.

Chapter 4 characterizes the increasing mode of biotite to form glimmerite in the Gough Dam shear zone which resulted from intense melt-rock interaction, hydration and metasomatism at mid-crustal depths. Flux of an externally-derived peraluminous melt through the deforming high-strain zone involved deformation-assisted diffuse porous flow and was accompanied by dyking along shear fractures parallel to the foliation, and subordinate, small-scale, fractures orthogonal to the foliation. Dyking and fracturing increased the melt-rock surface area, thus facilitating the process of intergranular melt infiltration, dissolution reaction of precursor rock and crystallization of biotite ±muscovite and sillimanite to form glimmerite. At the macro-scale, rare igneous bodies of felsic composition are observed within the high-strain zone and support the interpretation of melt-induced reaction (see Chapter 2 and 5). Glimmerite bands indicate pathways of high time-integrated melt flux, and these bands develop invasive, crosscutting hydration reaction-replacement textures that cut various types of host rocks of felsic composition. Some glimmerite domains of the Gough Dam shear zone contain individual or multigrain pockets of large K-feldspar grains that were shown to have crystalized from the migrating melt and were trapped when melt pathways collapsed within the glimmerite bands (see Chapter 5).

The change in biotite mode from modified quartzite mylonite to glimmerite (from 8 to 17 vol.%) permitted the calculation minimum time-integrated melt flux volumes in the high-strain zone. The calculations ranged from a minimum of 0.03 m3 per m3 of rock to a maximum of 0.23 m3 per m3 of rock. The modal increase in biotite was also reflected in an increase in the apparent temperature of biotite formation (570 to 660 ±50°C), coupled with increased trace element concentrations in biotite (Zr, Hf, Ti, Li, Sc, Nb, Ba and Eu) (Chapter 4). The extensive resetting of Proterozoic-aged monazite grains, present in the high-strain zone, to Paleozoic ages near the inception of the Alice Springs Orogeny is inferred to involve melt-assisted coupled dissolution-precipitation of monazite (Chapter 4). The extensive melt-rock dissolution-precipitation reactions forming the rheologically weak glimmerite bands is suggested to greatly decrease the rheological competence of the previously competent anhydrous granulitic protolith by the formation of weak hydrous mineral assemblage.

6-1.3. Identify macroscopic and microstructural attributes of former melt ascent through sub-solidus rocks during melt-present deformation in a high-strain zone and assess the role that melt-present deformation plays in enabling intracontinental orogenesis.

In high strain zones lacking macroscopic proportions of crystallized melt, the recognition of melt-present deformation and the role that melt may have played in metasomatic reactions can easily be overlooked and misrepresented as aqueous metasomatism. One of the aims of both Chapters 4 and 5 was to present a set of preserved microstructures indicative of the former presence of melt in the Gough Dam shear zone. These formed the basis to understand the syn-tectonic timing of melt flux and therefore the likely importance of melt-present high-strain deformation in the initiation and evolution of the Alice Springs Orogeny.

In Chapters 4 and 5, careful microscale study of glimmerite bands, glimmerite schist and granite lenses recognized microstructures indicative of the former melt presence and hydration reaction products characterized by: (1) small dihedral angles of interstitial minerals inferred to have crystallized from and pseudomorphed melt; (2) mm-scale melt pockets of granitic composition; (3) elongated interstitial grains inferred to be melt pseudomorphs of grain boundary films; (4) small interstitial grains connected in three dimensions but appearing as isolated grains with similar orientation in the two dimensions thin section; (5) localized static grain growth and recovery; (6) crystallographically controlled re-entrant dissolution-precipitation reaction sites in K-feldspar. Chemical data on biotite indicates an increase in Ti and Fe concentration with proximity to the melt pathway or higher degrees of time-integrated melt flux (Chapter 4 and 5). Additionally, an increase in Eu and orthoclase component in K-feldspar grains near to the rims or close to re-entrant reactions was identified (Chapter 5).

Melt-present high-strain deformation during open system melt flux through the Gough Dam shear zone was recognized using microstructures lacking much evidence of crystal-plastic deformation. At the macro-scale, granite lenses comprising euhedral K-feldspar and quartz grains, exhibit a pseudo-boudinage field pattern along the foliation, with no evidence of internal deformation of the lenses of granite (Chapter 2 and 5). Large faceted K-feldspar grains in glimmerite schist form trains in the glimmerite matrix (Chapter 5). These features indicate melt migration along the shear zone foliation and subsequent entrapment of melt to form (1) granite lenses in modified granitic gneiss and (2) granite melt with K-feldpsar phenocrysts to form the isolated K-feldspar grains in glimmerite schist following expulsion of the liquid during collapse of the melt pathway. On the basis of the lack of deformation in both the granite lenses and K-feldspar phenocrysts in glimmerite schist, it is implied that there was a large liquid fraction during the collapse and entrapment of the fluxing melt.

Microstructures confirmed the macro-scale interpretation of high-strain melt-present deformation, with the shear zone displaying features such as: (1) random orientation and interlocking texture of phenocrystic grains (Chapter 4 and 5); (2) activation of multiple slip systems in quartz melt pseudomorphs (Chapter 4); (3) lack of internal deformation in K-feldspar phenocrysts (Chapter 5); and (4) preservation of K-feldspar phenocryst facets (Chapter 5). These microstructures are present in glimmerite and/or glimmerite schist presenting typical non-coaxial deformation features, e.g. S- planes and C'-type shear bands, large grains with apparent sigmoidal shaped solution-precipitation tails, and/or grains oriented with elongation along both the foliation (S-planes) and C'-type shear bands (Chapter 4 and 5). It is believed that the presence of melt during periods of active deformation in the Gough Dam shear zone played an important role in the exhumation of lower crustal granulite facies rocks in the region, exponentially decreasing the competence of the high-strain zone, thus more efficiently accommodating the low N–S far-field stresses during the Alice Springs Orogeny.

6-2. Implications for hydrous melt-rock metasomatism in the middle continental crust

This thesis identified extensive melt-rock interaction forming glimmerite in the Gough Dam shear zone, showing that melt metasomatism, sensu lato, involving granitic melt is a viable process to occur in high-strain zones located in the middle continental crust. If the intense melt-rock interaction recognised in the Gough Dam shear zone is prototypical for the mid-crust, this research highlights the possibility of syn-tectonic melt migration as a major agent in the weakening of crustal high-strain zones. The rheological consequences of melt-assisted deformation, i.e. extreme weakening, are due to the melt accommodating the applied stresses instead of the relatively stronger solid framework of the rock. This phenomenon decreases the viscosity of the high-strain zone, making it very weak and able to be active under low differential stresses typical of continental interiors. The combination of developing a weak hydrous mineral assemblage and the inherent decrease of rock strength due to the physical presence of melt may prove to be a critical factor for the activation and/or re-activation of crustal structural heterogeneities. The key outcomes of this thesis emphasize the possibility of overlooking such weakening mechanisms if low volumes of melt crystallize in the high-strain zone and the hydration reactions observed in this study may easily be misinterpreted as hydrothermal metasomatism. In the future, the mechanism of melt-rock interaction forming abundant hydrous minerals and the weakening effect of melt migration in high-strain zones should be considered when interpreting mid-crustal high-strain zones.

6-3. Additional research suggestions

The formation of glimmerite by high-strain melt-ascent and high time-integrated melt flux through anhydrous host rocks has been demonstrated in this thesis. Additionally, it is interpreted that this had a rheological effect of creating weak zones that allowed the accommodation of far-field stresses and enhanced intracontinental orogeny in the SE Arunta region. This mechanism of melt-enhanced hydration and weakening in high-strain zones should be explored in other tectonic settings and rock types. Suggested further research areas include:

- The role of melt-rock interaction in high-strain zones elsewhere in central Australia, such as in the Harts Range Group (eastern most ASO) and the Petermann Ranges (south of the ASO and formed during the early Palaeozoic Petermann Orogeny), or in other high-grade metamorphic terrains in different intracontinental orogens, such as the Tien Shan and Altai orogens in Asia, Borborema province in Brazil, or the North American Sevier-Laramide orogen.
- In the thin viscous numerical model developed in this thesis, the orientation of the weak zone (at low angle to the far-field stresses) played an important role in strain development. What is the effect of different weak zone orientations on the strain partitioning in the continental crust? Additionally, preexisting weak structures, such as regional shear zones or faults, could be further explored in the numerical model.
- What are the relative roles of the hydrous mineral assemblage versus the physical presence of melt in the weakening of high-strain zones in high-grade metamorphic rocks? Does the combination of both of these weakening mechanisms enhance weakening in a special way or does the presence of melt completely dominate weakening? These questions can be explored using experimental or numerical rheological models.
- The geochemical evolution of the melt during melt-rock interaction that forms hydrous minerals (i.e. biotite and muscovite in this study) is crucial to understand the development of granitic melts in such high-strain melt-ascent systems. Does the extreme melt-rock interaction have a considerable effect in the composition of the fluxing melt? How prolonged does the melt-rock interaction have to be to result in a measurable effect in the composition of the fluxing melt? The study of natural outcrops or high pressure-temperature experimental techniques can be applied to understand the geochemical evolution of the melt in such scenarios.
- In the Gough Dam shear zone, the production of extensive glimmerite obliterated the original protolithic rock. Further geochemical and microstructural investigation is recommended to understand the progression from unaltered protolithic rock to glimmerite schist. What exact chemical parameters can be quantified in the

melt-metasomatic system?

- The recognition of high-strain fluid-flux of aqueous fluid (current paradigm) vs melt (this study) is currently fraught. Comparative studies using microstructure, whole rock geochemistry and isotopes can be applied in order to develop criteria to distinguish these two metasomatic systems in high-strain zones.
- Hydration crystallization reactions in felsic systems are still not fully understood, especially in the context of high-strain melt ascent. What is the main driver for the reaction? It is P, T or chemical gradient between melt and host rock? At what P-T-x conditions is the reaction expected to fully develop? High pressure-temperature experiments are in need to answer these questions.

Appendix A. Supplementary data for chapter two and three

SUPPORTING INFORMATION

Melt-present high-strain zones enhance intracontinental orogeny

S. Piazolo, N. R. Daczko, D. Silva, T. Raimondo

Table S1. Compilation of Palaeozoic geochronological data from the Arunta Region.

Intracontinental orogeny enhanced by far-field extension and local weak crust

D. Silva, S. Piazolo, N. R. Daczko, G. Houseman, T. Raimondo, L. Evans

Table S1. Compilation of Palaeozoic geochronological data from the Arunta Region.

Figure S1. Simulations presenting the models full area for vertical crustal variation.

Figure S2. Simulations presenting the models full area for the relative vorticity.

Figure S3. Simulations presenting the models full area for the near-surface faulting.

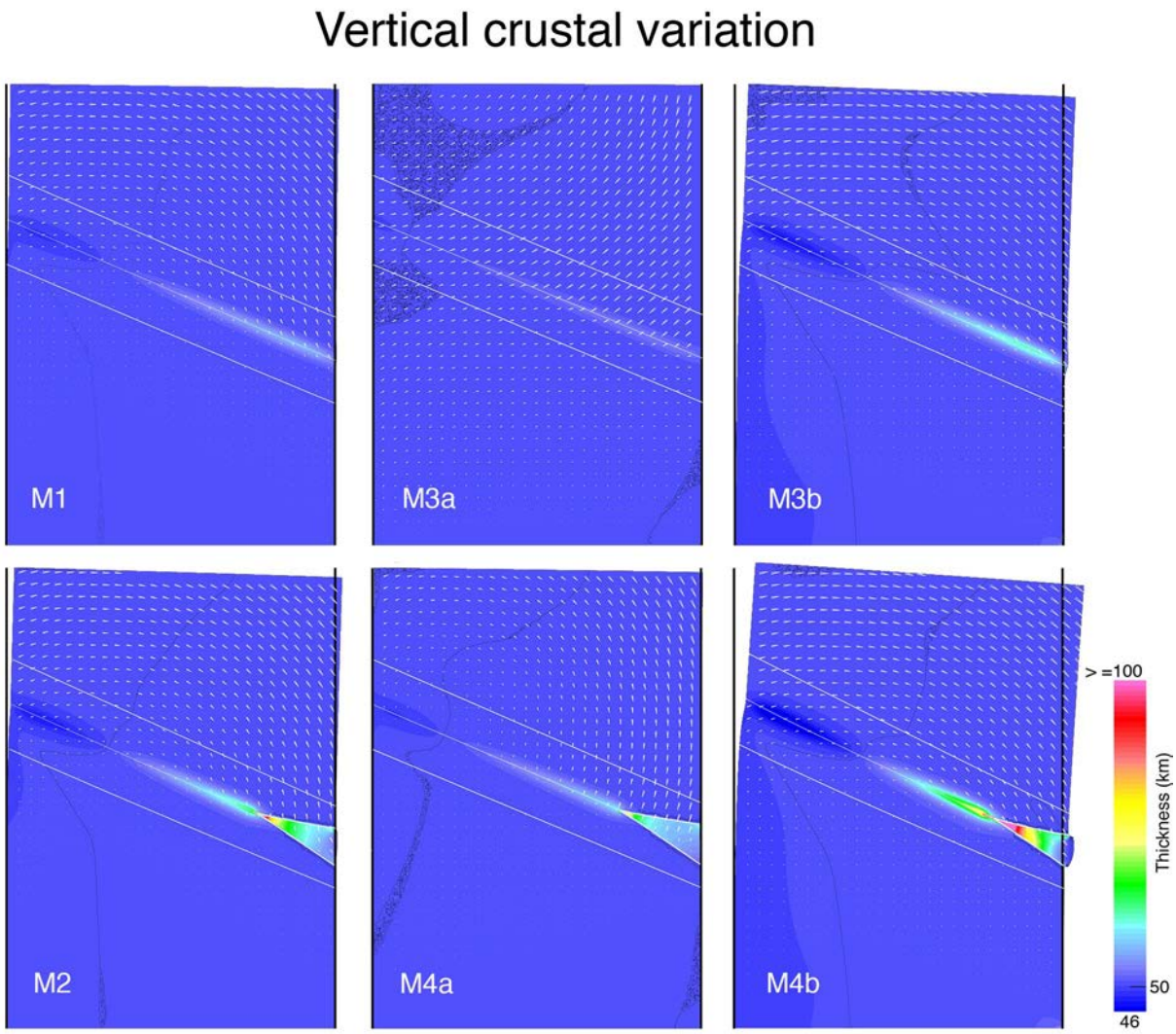

Figure S1. Simulations presenting the models full area for vertical crustal variation.

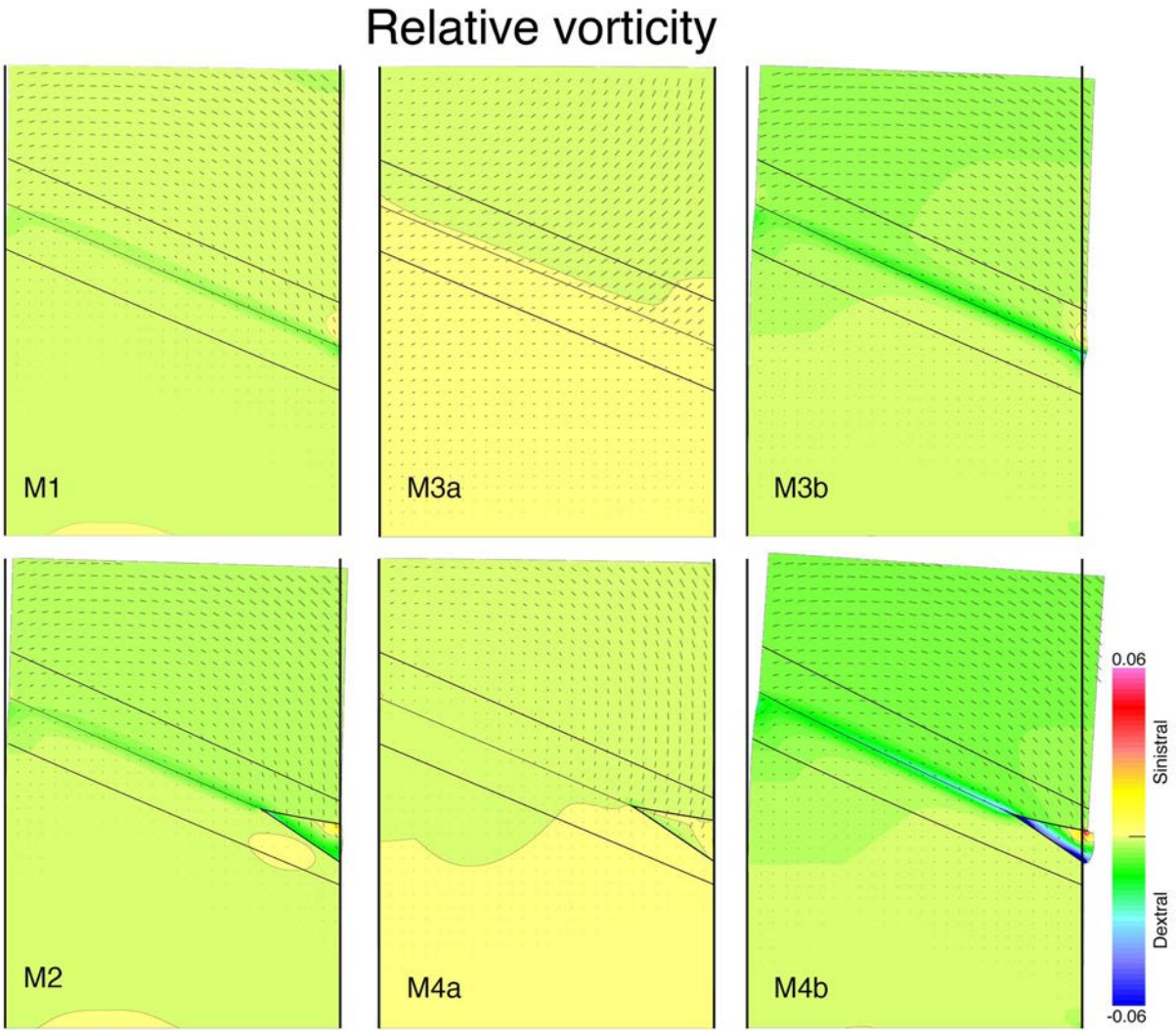

Figure S2. Simulations presenting the models full area for the relative vorticity.

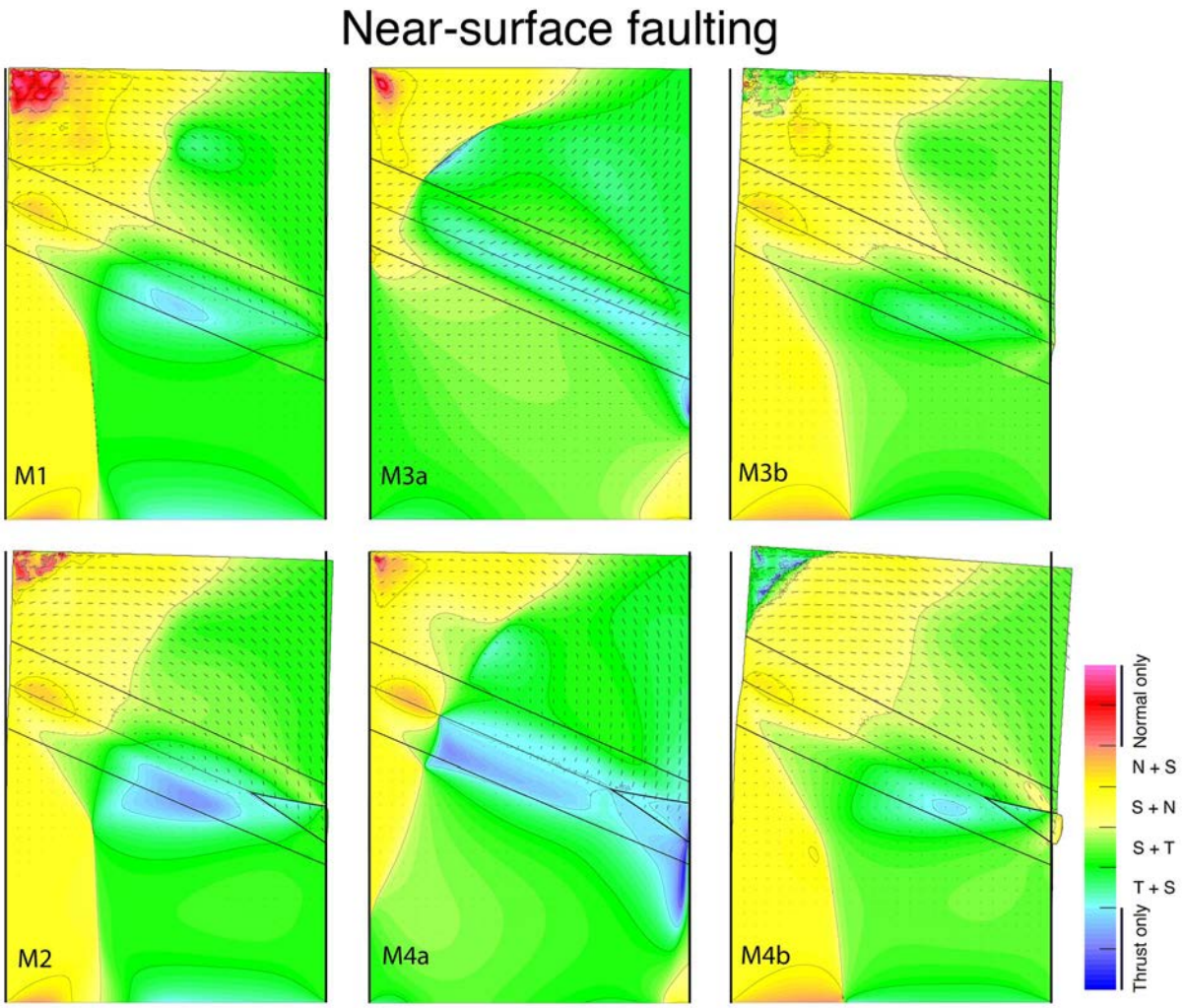

Figure S3. Simulations presenting the models full area for the near-surface faulting.

Location	Age (Ma)	Error (Ma)	Geochronology method	Reference	Type of process	Type of rock
West Bore Shear Zone, Strangways Range	381	7	Sm-Nd Grt core-Grt rim-leucocratic halo isochron	Ballèvre et al., 2000	Metamorphic	Amphibolite
Winnecke region, S Strangways Range	312	18	Sm-Nd Grt-St-Bt-WR isochron	Bendall et al., 1998; Bendall, 2000	Metamorphic	Amphibolite
Winnecke region, S Strangways Range	322	7	Sm-Nd Grt-St-Bt-WR isochron	Bendall et al., 1998; Bendall, 2000	Metamorphic	Micaschist
Mallee Bore, N Harts Range	384	7	SHRIMP U-Pb Ttn	Buick et al., 2001	Metamorphic	Granulite metabasite migmatite
Mallee Bore, N Harts Range	457	5	SHRIMP U-Pb Mnz	Buick et al., 2001	Metamorphic	Granulite metapelite migmatite
Mallee Bore, N Harts Range	387	4	SHRIMP U-Pb Zrc overgrowths	Buick et al., 2001	Igneous	Weakly deformed granite
Brett Creek, N Harts Range	327	3	SHRIMP U-Pb Mnz	Buick et al., 2008	Igneous	Deformed leucogneiss
Brett Creek, N Harts Range	455	4	SHRIMP U-Pb Zrc	Buick et al., 2008	Igneous	Deformed leucogneiss
Brett Creek, N Harts Range	454	5	SHRIMP U-Pb Zrc	Buick et al., 2008	Igneous	Deformed leucogneiss
Brett Creek, N Harts Range	454	9	SHRIMP U-Pb Mnz	Buick et al., 2008	Igneous	Deformed leucogneiss
Brett Creek, N Harts Range	364	8	SHRIMP U-Pb Mnz	Buick et al., 2008	Igneous	Deformed leucogneiss
Brett Creek, N Harts Range	392	16	SHRIMP U-Pb Mnz	Buick et al., 2008	Igneous	Deformed leucogneiss
Brett Creek, N Harts Range	376	16	SHRIMP U-Pb Mnz	Buick et al., 2008	Igneous	Deformed leucogneiss
Brett Creek, N Harts Range	386	6	SHRIMP U-Pb Mnz	Buick et al., 2008	Igneous	Deformed leucogneiss
Brett Creek, N Harts Range	399	18	SHRIMP U-Pb Mnz	Buick et al., 2008	Igneous	Deformed leucogneiss
Brett Creek, N Harts Range	383	15	SHRIMP U-Pb Mnz	Buick et al., 2008	Igneous	Deformed leucogneiss
Brett Creek, N Harts Range	380	16	SHRIMP U-Pb Mnz	Buick et al., 2008	Igneous	Deformed leucogneiss
Brett Creek, N Harts Range	389	14	SHRIMP U-Pb Mnz	Buick et al., 2008	Igneous	Deformed leucogneiss
Brett Creek, N Harts Range	348	10	SHRIMP U-Pb Zrc	Buick et al., 2008	Igneous	Undeformed pegmatite
Brett Creek, N Harts Range	341	4	SHRIMP U-Pb Mnz	Buick et al., 2008	Igneous	Undeformed pegmatite
Brett Creek, N Harts Range	324	5	SHRIMP U-Pb Mnz	Buick et al., 2008	Igneous	Undeformed pegmatite
Brett Creek, N Harts Range	320	4	SHRIMP U-Pb Mnz	Buick et al., 2008	Igneous	Undeformed pegmatite
Brett Creek, N Harts Range	313	5	SHRIMP U-Pb Mnz	Buick et al., 2008	Igneous	Undeformed pegmatite
Harts Range	361	2	SHRIMP U-Pb Mnz	Buick et al., 2008	Igneous	Undeformed pegmatite
Harts Range	454	8	SHRIMP U-Pb Zrc	Buick et al., 2008	Igneous	Deformed pegmatite
Harts Range	439	14	SHRIMP U-Pb Zrc	Buick et al., 2008	Igneous	Deformed pegmatite
Harts Range	438	6	SHRIMP U-Pb Mnz	Buick et al., 2008	Igneous	Undeformed pegmatite
Harts Range	415	6	SHRIMP U-Pb Mnz	Buick et al., 2008	Igneous	Undeformed pegmatite
Harts Range	448	7	SHRIMP U-Pb Mnz	Buick et al., 2008	Igneous	Deformed pegmatite
Harts Range	320	6	SHRIMP U-Pb Mnz	Buick et al., 2008	Igneous	Undeformed pegmatite
Harts Range	420	8	SHRIMP U-Pb Mnz	Buick et al., 2008	Igneous	Weakly deformed pegmatite
Harts Range	425	11	SHRIMP U-Pb Mnz	Buick et al., 2008	Igneous	Undeformed pegmatite
Entia Gneiss Complex	334	15	SHRIMP U-Pb Zrc	Buick et al., 2008	Igneous	Undeformed pegmatite
Harts Range	335	9	SHRIMP U-Pb Zrc	Buick et al., 2008	Igneous	Undeformed pegmatite
Sandy Creek granites	334.1	2.6	Ar-Ar Ms	Cartwright et al., 1999	Metamorphic	Sheared granites
Sandy Creek granites	333.4	2	Ar-Ar Ms	Cartwright et al., 1999	Metamorphic	Sheared granites
Sandy Creek granites	333.9	2	Ar-Ar Ms	Cartwright et al., 1999	Metamorphic	Sheared granites
Sandy Creek granites	334.5	3.5	Ar-Ar Ms	Cartwright et al., 1999	Metamorphic	Sheared granites
E Entia Dome	360	5	U–Pb Mnz	Cooper et al., 1988	Igneous	Injected Leucogneiss
Ruby Gap	340.1	3.5	K-Ar Phg	Dunlap et al., 1991	Metamorphic	Granitic gneiss
Ruby Gap	413.5	4.3	K-Ar Phg	Dunlap et al., 1991	Metamorphic	Granitic gneiss
Ruby Gap	311.5	0.4	Ar-Ar Phg	Dunlap et al., 1991	Metamorphic	Quartzite mylonites
Ruby Gap	318.1	0.6	Ar-Ar Phg	Dunlap et al., 1991	Metamorphic	Quartzite mylonites
Ruby Gap	321.7	0.5	Ar-Ar Phg	Dunlap et al., 1991	Metamorphic	Quartzite mylonites
Ruby Gap	328.2	0.5	Ar-Ar Phg	Dunlap et al., 1991	Metamorphic	Quartzite mylonites
Ruby Gap	317.8	5	K-Ar Phg	Dunlap et al., 1991	Metamorphic	Quartzite mylonites
Ruby Gap	375.85	3.9	K-Ar Phg	Dunlap et al., 1991	Metamorphic	Quartzite mylonites
Mallee Bore, N Harts Range	353	14	Sm-Nd Grt-Hbl isochron	Hand and Mawby, unpublished data	Metamorphic	Schists and Metamorphosed mafic rocks
Mallee Bore, N Harts Range	357	17	Sm-Nd Grt-Hbl isochron	Hand and Mawby, unpublished data	Metamorphic	Schists and Metamorphosed mafic rocks
E Entia Gneiss Complex	415	4	Sm-Nd Grt-WR isochron	Hand and Mawby, unpublished data	Metamorphic	Schists and Metamorphosed mafic rocks
E Entia Gneiss Complex	442	9	Sm-Nd Grt-WR isochron	Hand and Mawby, unpublished data	Metamorphic	Schists and Metamorphosed mafic rocks
E Entia Gneiss Complex	444	4	Sm-Nd Grt-WR isochron	Hand and Mawby, unpublished data	Metamorphic	Schists and Metamorphosed mafic rocks
Oonagalabi, Harts Range	372	5	Sm-Nd Grt-Hbl-WR isochron	Hand and Mawby, unpublished data	Metamorphic	Schists and Metamorphosed mafic rocks
Oonagalabi, Harts Range	376	6	Sm-Nd Grt-Hbl-WR isochron	Hand and Mawby, unpublished data	Metamorphic	Schists and Metamorphosed mafic rocks
Yamba Shear Zone, Strangways Range	384	5	Sm-Nd Grt-Hbl-St isochron	Hand and Mawby, unpublished data	Metamorphic	Schists and Metamorphosed mafic rocks
Oonagalabi, Harts Range	444	4	Sm-Nd Grt-Bt-WR isochron	Hand and Mawby, unpublished data	Metamorphic	Schists and Metamorphosed mafic rocks
SE Entia Gneiss Complex	343	8	SHRIMP U-Pb Mnz	Hand et al., 1999	Metamorphic	Metapelite
SE Entia Gneiss Complex	330	6	SHRIMP U-Pb Zrc overgrowths	Hand et al., 1999	Igneous	Deformed pegmatite
Yambah Shear Zone, Strangways Range	448	5	LA-ICP-MS U-Pb Mnz	Howlett et al., 2015	Metamorphic	Grt-St-Ky schist
Yambah Shear Zone, Strangways Range	374	3	LA-ICP-MS U-Pb Mnz	Howlett et al., 2015	Metamorphic	Grt-St-Ky schist
Yambah Shear Zone, Strangways Range	363	3	LA-ICP-MS U-Pb Mnz	Howlett et al., 2015	Metamorphic	Grt-St-Ky schist
Yambah Shear Zone, Strangways Range	355	3	LA-ICP-MS U-Pb Mnz	Howlett et al., 2015	Metamorphic	Grt-St-Ky schist
Yambah Shear Zone, Strangways Range	384	5	Sm-Nd Grt isochron	Howlett et al., 2015	Metamorphic	Grt-St-Ky schist
Gough Dam Shear Zone, Strangways Range	441	6	LA-ICP-MS U-Pb Mnz	Howlett et al., 2015	Metamorphic	Amphibolite
Gough Dam Shear Zone, Strangways Range	350	5	LA-ICP-MS U-Pb Mnz	Howlett et al., 2015	Metamorphic	Grt-Bt-Ms schist
Cattlewater Pass, Strangways Range	454	3	LA-ICP-MS U-Pb Mnz	Howlett et al., 2015	Metamorphic	Grt-Sil schist
Oonagalabi, Strangways Range	448	4	LA-ICP-MS U-Pb Mnz	Howlett et al., 2015	Metamorphic	Grt-Bt ± Sil and Grt-Hbl annealed mylonitic gneiss
Oonagalabi, Strangways Range	449	3	LA-ICP-MS U-Pb Mnz	Howlett et al., 2015	Metamorphic	Grt-Bt ± Sil and Grt-Hbl annealed mylonitic gneiss
Oonagalabi, Strangways Range	376	4	Sm-Nd Grt isochron	Howlett et al., 2015	Metamorphic	Grt-Bt ± Sil and Grt-Hbl annealed mylonitic gneiss
Oonagalabi, Strangways Range	372	5	Sm-Nd Grt isochron	Howlett et al., 2015	Metamorphic	Grt-Bt ± Sil and Grt-Hbl annealed mylonitic gneiss
Oonagalabi, Strangways Range	379	20	Sm-Nd Grt isochron	Howlett et al., 2015	Metamorphic	Grt-Bt ± Sil and Grt-Hbl annealed mylonitic gneiss
Oonagalabi, Strangways Range	444	4	Sm-Nd Grt isochron	Howlett et al., 2015	Metamorphic	Grt-Bt ± Sil and Grt-Hbl annealed mylonitic gneiss
Oonagalabi, Strangways Range	440	15	Sm-Nd Grt isochron	Howlett et al., 2015	Metamorphic	Grt-Bt ± Sil and Grt-Hbl annealed mylonitic gneiss
Pinnacles Bore Shear Zone, Strangways Range	350	3	LA-ICP-MS U-Pb Mnz	Howlett et al., 2015	Metamorphic	Grt-St-Ky schist
Pinnacles Bore Shear Zone, Strangways Range	359	2	LA-ICP-MS U-Pb Mnz	Howlett et al., 2015	Metamorphic	Grt-St-Ky schist
Pinnacles Bore Shear Zone, Strangways Range	326	13	Sm-Nd Grt isochron	Howlett et al., 2015	Metamorphic	Grt-St-Ky schist
Erontonga Shear Zone, Strangways Range	334	5	Sm-Nd Grt isochron	Howlett et al., 2015	Metamorphic	Grt-Bt-Ms schist
Ongeva region, Strangways Range	445	11	LA-ICP-MS U-Pb Mnz	Howlett et al., 2015	Metamorphic	Grt bearing pelitic ultramylonite
Nolans Bore	345.3	0.8	Ar-Ar Ms	Huston et al., 2016	Metamorphic	Mylonitic gneiss band
Nolans Bore	367.2	0.75	Ar-Ar Bt	Huston et al., 2016	Metamorphic	Mylonitic gneiss band
Nolans Bore	375.9	0.8	Ar-Ar Bt	Huston et al., 2016	Metamorphic	Granitic gneiss
Coggan Bore, Harts Range	364	6	ID-TIMS U-Pb Ttn	Lavery, 2003	Metamorphic	Calcsilicate
Harts Range Detachment Zone	365	1	MC-ICP-MS U-Pb Ttn	Lavery, 2003	Metamorphic	Calcsilicate
Brady Gneiss, Harts Range	412	1	ID-TIMS U-Pb Ttn	Lavery, 2003	Metamorphic	Calcsilicate
Kong Bore, Harts Range	416	1	ID-TIMS U-Pb Ttn	Lavery, 2003	Metamorphic	Calcsilicate
Brady Gneiss, Harts Range	417	1	ID-TIMS U-Pb Ttn	Lavery, 2003	Metamorphic	Calcsilicate
Strangways Range	332	3	SHRIMP U-Pb Zrc overgrowths	Maidment et al., 2005	Igneous	Granodiorite
Lower Stanovos Gneiss, Harts Range	453	4	SHRIMP U-Pb Zrc overgrowths	Maidment et al., 2013	Metamorphic	Quartzite
Lower Irinda Gneiss, Harts Range	365	10	SHRIMP U-Pb Zrc	Maidment et al., 2013	Metamorphic	Grt-Sil metapelite migmatite
Upper Brady Gneiss, Harts Range	359	6	SHRIMP U-Pb Zrc overgrowths	Maidment et al., 2013	Metamorphic	Calcsilicate
Upper Brady Gneiss, Harts Range	361	5	SHRIMP U-Pb Zrc overgrowths	Maidment et al., 2013	Metamorphic	Calcsilicate
Upper Brady Gneiss, Harts Range	379	5	SHRIMP U-Pb Zrc overgrowths	Maidment et al., 2013	Metamorphic	Calcsilicate
InkaMsIla Bore, Entia Dome	336	4	SHRIMP U-Pb Mnz	Maidment, 2005	Metamorphic	Ky-Bt-Ms-Grt metapelite
Huckitta Gorge, Entia Gneiss Complex	357	4	SHRIMP U-Pb Zrc	Maidment, 2005	Igneous	Pegmatite
Mt Mary, Entia Dome	361	3	SHRIMP U-Pb Zrc	Maidment, 2005	Igneous	Granite
Atitjere, Brady Gneiss	361	3	SHRIMP U-Pb Zrc	Maidment, 2005	Igneous	Granite
Painted Canyon	375	4	SHRIMP U-Pb Zrc	Maidment, 2005	Igneous	Pegmatite
Detachment Zone, Entia Gneiss Complex	449	10	Sm-Nd Hbl-Grt-WR isochron	Mawby et al., 1999	Metamorphic	Gneiss
Mount Liebig	401	1	Ar-Ar Ms	McLaren et al., 2009	Metamorphic	Grt-Ms-Chl schist
Heavitree Qz (S Mount Liebig)	376	1	Ar-Ar Ms	McLaren et al., 2009	Metamorphic	Quartzite
Edwards Creek Prospect, Strangways Range	385	20	LA-ICP-MS Mnz	Moller at al., 1999a,b	Metamorphic	Metasediments, Calc-silicate, Mafic granulites and Bt-gneiss
Edwards Creek Prospect, Strangways Range	443	6	SHRIMP U-Pb Zrc rims	Moller et al., 1999a,b	Metamorphic	Metasediments, Calc-silicate, Mafic granulites and Bt-gneiss
Hart Range Irinda	343	3	Rb-Sr total rock Ms isochron	Mortimer et al., 1987	Igneous	Pegmatite
Peaked Hill Shear Zone, Reynolds Range	354	3	LA-ICP-MS U-Pb Mnz	Raimondo et al., 2012	Metamorphic	Granitic gneiss
Peaked Hill Shear Zone, Reynolds Range	360	3	LA-ICP-MS U-Pb Mnz	Raimondo et al., 2012	Metamorphic	Granitic gneiss
Peaked Hill Shear Zone, Reynolds Range	333	20	Sm-Nd Grt-Ms-Bt isochron	Raimondo et al., 2012	Metamorphic	Granitic gneiss
Nolans Bore	351.1	4.6	U–Pb Mnz	Schoneveld et al., 2015	Metamorphic	Breccia
Nolans Bore	344	10	U–Pb Mnz	Schoneveld et al., 2015	Metamorphic	Breccia
Nolans Bore	403	15	Sm–Nd allanite, apatite	Schoneveld et al., 2015	Metamorphic	Breccia
Entire Point Shear Zone	434	6	Sm-Nd Grt-Hbl-WR isochron	Scrimgeour and Raith, 2001	Metamorphic	Recrystallized mafic rocks
Entire Point Shear Zone	445	5	SHRIMP U-Pb Mnz	Scrimgeour and Raith, 2001	Metamorphic	Recrystallized mafic rocks
Huckitta Creek, SE Entia Gneiss Complex	325	8	LA-ICP-MS U-Pb Mnz lower intercept	Wade et al., 2008	Metamorphic	Grt-Hbl-two mica metapelite
W Entia Gneiss Complex	341	5	LA-ICP-MS U-Pb Mnz lower intercept	Wade et al., 2008	Metamorphic	Grt-Hbl-two mica metapelite

Bt, biotite; Chl, chlorite; Grt, garnet; Hbl, hornblende; Ky, kyanite; Mnz, monazite; Ms, muscovite; Phg, phengite; Sil, sillimanite; St, staurolite; Ttn, titanite; WR, whole rock; Zrc, zircon

Table S1. Compilation of Palaeozoic geochronological data from the Arunta Region. Table S1 compiles U-Pb, Sm-Nd, 40Ar-39Ar and K-Ar geochronological data from the Arunta region for the Palaeozoic period. The compilation used the following criteria: (1) ages must lie within the Alice Springs Orogeny timeframe (300–450/460 Ma; Buick et al., 2008), (2) ages must have error less than or equal to 20 Ma, and (3) ages were excluded when interpreted by the author(s) to reflect a cooling age.

References Below Represent the Sources for Table S1

Ballèvre, M., Möller, A. and Hensen, B.J., 2000. Exhumation of the lower crust during crustal shortening: an Alice Springs (380 Ma) age for a prograde amphibolite facies shear zone in the Strangways Metamorphic Complex (central Australia). Journal of Metamorphic Geology, 18(6): 737-747.

Bendall, B., 2000. Mid-Palaeozoic shear zones in the Strangways Range: a record of intracratonic tectonism in the Arunta Inlier, central Australia. University of Adelaide, PhD thesis.

Bendall, B., Hand, M. and Foden, J., 1998. Sm-Nd evidence for mid-Palaeozoic regional amphibolite facies metamorphism in the Strangways Range, central Australia. Geological Society of Australia Abstracts, 49: 27.

Buick, I.S., Miller, J.A., Williams, I.S. and Cartwright, I., 2001. Ordovician high-grade metamorphism of a newly recognised late Neoproterozoic terrane in the northern Harts Range, central Australia. Journal of Metamorphic Geology, 19(4): 373-394.

Buick, I.S., Storkey, A. and Williams, I.S., 2008. Timing relationships between pegmatite emplacement, metamorphism and deformation during the intra-plate Alice Springs Orogeny, central Australia. Journal of Metamorphic Geology, 26(9): 915-936.

Cartwright, I., Buick, I. S., Foster, D. A., & Lambert, D. D. 1999. Alice Springs age shear zones from the southeastern Reynolds Range, central Australia. Australian Journal of Earth Sciences, 46(3): 355-363.

Cooper, J.A., Mortimer, G.E. and James, P.R., 1988. Rate of Arunta Inlier evolution at the eastern margin of the Entia Dome, central Australia. Precambrian Research, 40–41(0): 217-231.

Dunlap, W. J., Teyssier, C., McDougall, I., & Baldwin, S. 1991. Ages of deformation from K/Ar and 40Ar/39Ar dating of white micas. Geology, 19(12): 1213-1216.

Hand, M., Mawby, J., Kinny, P.D. and Foden, J., 1999. U-Pb ages from the Harts Range, central Australia: evidence for early Ordovician extension and constraints on Carboniferous metamorphism. Journal of the Geological Society, 156(4): 715-730.

Howlett, D., Hand, M., Raimondo, T., 2015. 120 Myr of episodic mid-crustal metamorphism and fluid-rock interaction during the Alice Springs Orogeny: the Strangways Range, central Australia. Poster session at the TIGeR conference, Curtin University, Perth, Western Australia.

Huston, D. L., Maas, R., Cross, A., Hussey, K. J., Mernagh, T. P., Fraser, G., & Champion, D. C. 2016. The Nolans Bore rare-earth element-phosphorus-uranium mineral system: geology, origin and post-depositional modifications. Mineralium Deposita, 51(6): 797-822.

Lavery, P., 2003. Petrological, stable isotope and geochronological constraints on the metamorphic fluid flow history of the Harts Ranges, central Australia. La Trobe University, PhD thesis.

Maidment, D.W., 2005. Palaeozoic high-grade metamorphism within the Centralian Superbasin, Harts Range region, central Australia. Australian National University, PhD thesis.

Maidment, D.W., Hand, M. and Williams, I.S., 2005. Tectonic cycles in the Strangways Metamorphic Complex, Arunta Inlier, central Australia: geochronological evidence for exhumation and basin formation between two high-grade metamorphic events. Australian Journal of Earth Sciences, 52(2): 205-215.

Maidment, D.W., Hand, M. and Williams, I.S., 2013. High grade metamorphism of sedimentary rocks during Palaeozoic rift basin formation in central Australia. Gondwana Research, 24(3–4): 865-885.

Mawby, J., Hand, M. and Foden, J., 1999. Sm–Nd evidence for high-grade Ordovician metamorphism in the Arunta Block, central Australia. Journal of Metamorphic Geology, 17(6): 653-668.

McLaren, S., Sandiford, M., Dunlap, W. J., Scrimgeour, I., Close, D., & Edgoose, C. 2009. Distribution of Palaeozoic reworking in the Western Arunta Region and northwestern Amadeus Basin from 40Ar/39Ar thermochronology: implications for the evolution of intracratonic basins. Basin Research, 21(3): 315-334.

Möller, A., Armstrong, R., Hensen, B. and Williams, I., 1999a. Dating metamorphic events & deformation: Shrimp U–Pb zircon examples from the Strangways Metamorphic Complex, Arunta Inlier, Australia. European Union of Geosciences 10, Strasbourg, Journal of Conference Abstracts, 4:

711.

Möller, A., Williams, I.S., Jackson, S., and Hensen, B.J., 1999b. Palaeozoic deformation and mineral growth in the Strangways Metamorphic Complex: in-situ dating of zircon and monazite in a staurolite–corundum bearing shear zone. Geological Society of Australia Abstracts, 54: 71-72.

Mortimer, G. E., Cooper, J. A., & James, P. R. 1987. U/Pb and Rb/Sr geochronology and geological evolution of the Harts Range ruby mine area of the Arunta Inlier, central Australia. Lithos, 20(6): 445-467.

Raimondo, T., Clark, C., Hand, M., Cliff, J. and Harris, C., 2012. High-resolution geochemical record of fluid–rock interaction in a mid-crustal shear zone: a comparative study of major element and oxygen isotope transport in garnet. Journal of Metamorphic Geology, 30(3): 255-280.

Schoneveld, L., Spandler, C., & Hussey, K. 2015. Genesis of the central zone of the Nolans Bore rare earth element deposit, Northern Territory, Australia. Contributions to Mineralogy and Petrology, 170(2): 1-22.

Scrimgeour, I. and Raith, J.G., 2001. High-grade reworking of Proterozoic granulites during Ordovician intraplate transpression, eastern Arunta Inlier, central Australia. Geological Society, London, Special Publications, 184(1): 261-287.

Wade, B.P., Hand, M., Maidment, D.W., Close, D.F. and Scrimgeour, I.R., 2008. Origin of metasedimentary and igneous rocks from the Entia Dome, eastern Arunta region, central Australia: a U–Pb LA–ICPMS, SHRIMP and Sm–Nd isotope study. Australian Journal of Earth Sciences, 55(5): 703-719.

Appendix B. Supplementary data for chapter four

SUPPORTING INFORMATION

Glimmerite: a product of melt-rock interaction within a crustal scale high-strain zone

D. Silva, N. R. Daczko, S. Piazolo, T. Raimondo

Table S1. Description of biotites samples from literature for comparison with GDSZ biotites.

Table S2. La-ICP-MS monazite U–Pb data.

Figure S1. Map of monazite age spatial distribution in M–Qtz/GL sample.

Reference	Rock type	Mineralogy	Texture and fabric	Comments
Bea et a., 1994a	Two-mica granite	Quartz, K-feldspar, plagioclase, biotite, muscovite ± apatite ± zircon ± monazite ± ilmenite ± pyrite	Hypidiomorphic, porphyritic granular textures, with K-feldspar phenocrysts defining a subhorizonal planar fabric	Pedrobernardo pluton, Spain (2 Layered, sheet-like granite boc vertical zoning, anatectically g intruded almost free of restite, a closed system by in situ crys
Bea et a., 1994b	Diatexite migmatite	Mesosome: Quartz, plagioclase, cordierite, biotite, K-feldspar ± sillimanite ± garnet. Melanosome: Sillimanite, biotite, ilmenite, cordierite ± quartz ± plagioclase. Leucosome: Quartz, K-feldspar, plagioclase, cordierite ± biotite ± sillimanite.	Mesosome: Porphyritic texture with mega-porphyroblasts of idiomorphic/subidiomorphic grt. Melanosome: Alternate schistose (sil, bt, ilm ± crd) and granoblastic (crd ± qz ± pl) layers. Leucosome: Porphyritic texture with porphyroblasts of idiomorphic/subidiomorphic crd.	Low-pressure peraluminous m the Peña Negra Complex, Spa Melanosome: Small enclaves v mesosome, or as mafic selvag leucosome veins and the mes Leucosome: In-situ melt. Small melanosome fragments compo and ilm.
Cesare et al., 1997; Acosta-Vigil et al., 2010	Metapelite xenoliths	Matrix: biotite, plagioclase, pyroxene, amphibole, cordierite, groundmass. Xenoliths: Biotite, fibrous sillimanite, garnet, plagioclase, graphite, apatite, glass ± ilmenite± cordierite ± spinel ± quartz.	Xenoliths: Medium to coarse grain-size matrix and grt porphyroblasts. Weak stretching lineation and faint schistosity marked by bi and sill alternation.	Erupted anatectic El Hoyazo d 0.15 Ma), Spain. El Hoyazo da the contaminated granitoid mel metamorphic xenoliths the Al-r portion of a semipelitic rock un P–T conditions of 5–7 kbar an
Hulsbosch et al., 2014	Pegmatite	Biotite pegmatite: Quartz, plagioclase, microcline, schorl, biotite ± garnet. Two-mica pegmatite: Quartz, plagioclase, microcline, albite, schorl, biotite ± monazite	Biotite pegmatite: coarse grain, allotriomorphic Qz-Kfs matrix with subhedral schorl. Two-mica pegmatite: coarse grain allotriomorphic Qz-Kfs matrix with cm-sized sheets of muscovite macroscopically intergrown with biotite.	Gatumba pegmatite field, Rwa fractionation zonation sequenc proximal granite in the sequen mica, muscovite and rare-elem pegmatites.
Laul & Lepel, 1987	Mica schist	Quartz, plagioclase, biotite, muscovite, tourmaline, apatite		Mica schist is part of the count Black Hills pegmatite field, USA
Nash & Crecraft, 1985	Rhyolite/Rhyodacite	Quartz, K-feldspar, Plagioclase, biotite, pyroxene, oxides, groundmass		Rhyodacite and rhyolite lavas Peaks volcanic complex (2.7–
Stepanov & Hermann, 2013	Experimental	Garnet, clinopyroxene, coesite, glass ± Mg-calcite ± kyanite ± rutile		Experiment C-1505 used the s material as reported in Hermar (2009), with 6.2 wt% of H_2O ar 9% of a carbonate mix consist calcite and 80% dolomite

Mineral abbreviation following Whitney & Evans (2010).

Table S1. Description of biotites samples from literature for comparison with GDSZ biotites.

Spot	^{206}Pb (cts/sec)	^{207}Pb (cts/sec	^{238}U (cts/sec)	$^{206}Pb/^{238}U$ age	±	$^{207}Pb/^{206}Pb$ age	±	$^{207}Pb/^{235}U$ age	±	% Disc.	Total $^{207}Pb/^{206}Pb$	±%	Total $^{207}Pb/^{235}U$	±%	Total $^{206}Pb/^{238}U$	±%
GD1606 - 01	34900	1987	607000	450.1	5.3	433	40	448.0	7.0	-0	0.0558	2	0.5550	2	0.0723	1
GD1606 - 02	28200	1580	473000	476.2	6.4	408	53	464.1	9.1	-3	0.0549	2	0.5810	2	0.0767	1
GD1606 - 03	27500	1600	480000	434.9	5.7	487	50	445.6	9.0	+2	0.0572	2	0.5520	3	0.0698	1
GD1606 - 04	23660	1456	308000	566	11	595	98	575.0	19.0	+2	0.0606	4	0.7640	4	0.0917	2
GD1606 - 05	37500	2130	643000	459.6	5	428	49	457.0	7.4	-1	0.0558	2	0.5670	2	0.0739	1
GD1606 - 06	40800	2330	714000	447.1	4.5	432	48	446.5	7.7	-0	0.0559	2	0.5530	2	0.0718	1
GD1606 - 07	26800	1546	511000	419.3	5.7	454	63	424.6	9.9	+1	0.0566	3	0.5200	3	0.0672	1
GD1606 - 08	13600	780	230000	480.4	7.1	424	76	475.0	13.0	-1	0.0561	4	0.5940	3	0.0774	2
GD1606 - 09	8380	502	149000	460	11	500	140	472.0	22.0	+3	0.0591	7	0.5970	6	0.0740	3
GD1606 - 10	22400	1351	288000	603.6	6.8	534	68	592.0	13.0	-2	0.0589	3	0.7950	3	0.0982	1
GD1606 - 11	26300	1481	502000	405.6	6.6	411	63	410.0	10.0	+1	0.0555	3	0.4970	3	0.0649	2
GD1606 - 12	27800	1600	482000	461.2	5.8	465	59	461.3	9.7	+0	0.0566	3	0.5770	3	0.0742	1
GD1606 - 13	38600	2187	622000	462.9	6.3	420	68	458.0	12.0	-1	0.0556	3	0.5710	3	0.0745	1
GD1606 - 14	38240	2185	667000	444.1	4.3	438	44	444.4	7.6	+0	0.0560	2	0.5500	2	0.0713	1
GD1606 - 15	36400	2080	626000	456.5	5.1	440	52	455.5	8.5	-0	0.0562	2	0.5670	2	0.0734	1
GD1606 - 16	39300	2240	675000	458.5	6.5	430	45	455.2	8.7	-1	0.0558	2	0.5670	2	0.0737	1
GD1606 - 17	39500	2250	696000	444.5	4.3	436	51	444.1	8.2	-0	0.0560	2	0.5500	2	0.0714	1
GD1606 - 18	38430	2214	636000	468.5	5.3	455	49	466.2	6.9	-0	0.0565	2	0.5830	2	0.0754	1
GD1606 - 19	48300	2760	855000	442.7	3.5	435	39	441.9	5.8	-0	0.0558	2	0.5458	2	0.0711	1
GD1606 - 20	34880	2108	574000	479.1	6.2	558	60	496.4	9.7	+3	0.0593	3	0.6320	3	0.0772	1
GD1607_1 - 01	9.37E+04	5.63E+03	1.39E+06	553.5	6.5	531	43	555.0	10.0	+0	0.0582	2	0.7290	2	0.0897	1
GD1607_1 - 02	1.14E+05	6.71E+03	1.95E+06	510.8	6.1	505	41	511.7	9.1	+0	0.0572	2	0.6520	2	0.0825	1
GD1607_1 - 03	1.57E+05	9.50E+03	2.27E+06	593.9	4.3	563	26	579.8	5.8	-2	0.0590	1	0.7710	1	0.0965	1
GD1607_1 - 04	9.81E+04	5.63E+03	1.83E+06	458.4	2.9	446	34	450.2	5.5	-2	0.0560	2	0.5584	2	0.0737	1
GD1607_1 - 05	1.12E+05	6.92E+03	1.60E+06	598.6	5.5	614	26	592.2	5.9	-1	0.0604	1	0.7920	1	0.0973	1
GD1607_1 - 06	1.09E+05	6.21E+03	2.06E+06	460.3	3.9	419	30	446.9	4.9	-3	0.0553	1	0.5532	1	0.0740	1
GD1607_1 - 07	1.73E+05	9.93E+03	3.34E+06	459.2	5.4	448	36	451.2	4.3	-2	0.0560	2	0.5597	1	0.0738	1
GD1607_1 - 08	8.53E+04	4.65E+03	1.97E+06	394.9	7.1	332	58	378.6	7.8	-4	0.0533	2	0.4520	2	0.0632	2
GD1607_1 - 09	7.62E+04	4.39E+03	1.43E+06	463.3	3.4	457	32	452.8	5.6	-2	0.0563	1	0.5625	2	0.0745	1
GD1607_1 - 10	6.72E+04	3.83E+03	1.26E+06	465.8	3.7	435	35	450.4	5.4	-3	0.0555	1	0.5587	2	0.0749	1
GD1607_1 - 11	1.08E+05	6.61E+03	1.83E+06	513.3	4.3	582	30	515.0	5.6	+0	0.0596	1	0.6612	1	0.0829	1
GD1607_1 - 12	5.65E+04	3.36E+03	9.92E+05	488.7	4.8	523	35	484.7	7.1	-1	0.0580	2	0.6130	2	0.0788	1
GD1607_1 - 13	6.41E+04	3.63E+03	1.22E+06	467.5	4.7	416	42	450.6	6.7	-4	0.0553	2	0.5590	2	0.0752	1
GD1607_1 - 14	9.13E+04	5.17E+03	1.78E+06	445.5	4.5	423	25	432.2	5.1	-3	0.0554	1	0.5311	1	0.0716	1
GD1607_1 - 15	5.58E+04	3.15E+03	1.04E+06	464.5	3.9	405	40	446.4	6.8	-4	0.0551	2	0.5510	2	0.0747	1
GD1607_1 - 16	9.60E+04	5.64E+03	1.70E+06	487.9	4.8	498	34	480.6	5.7	-2	0.0570	2	0.6039	2	0.0786	1
GD1607_1 - 17	1.39E+05	1.11E+04	1.74E+06	689.2	9.4	1151	28	796.0	12.0	+13	0.0779	2	1.1900	2	0.1128	1
GD1607_1 - 18	5.32E+04	3.01E+03	9.79E+05	469	3.7	409	51	452.5	8.3	-4	0.0549	2	0.5630	2	0.0755	1
GD1607_1 - 19	5.91E+04	3.86E+03	7.93E+05	635.4	8.2	714	36	644.0	12.0	+1	0.0635	2	0.8880	3	0.1036	1
GD1607_1 - 20	7.95E+04	4.59E+03	1.40E+06	489	3.9	459	30	476.5	5.5	-3	0.0564	1	0.5994	1	0.0788	1
GD1607_1 - 21	5.37E+04	3.29E+03	7.57E+05	603.4	4.8	585	33	591.1	6.1	-2	0.0596	1	0.7910	1	0.0981	1
GD1607_1 - 22	5.57E+04	3.20E+03	1.04E+06	461.8	3.9	442	42	453.8	6.5	-2	0.0560	2	0.5640	2	0.0743	1
GD1607_1 - 23	56660	3230	1048000	459.8	4.2	442	35	452.8	6.0	-2	0.0560	2	0.5625	2	0.0739	1
GD1607_1 - 24	1.03E+05	5.91E+03	2.03E+06	444.2	4.6	437	38	440.8	5.3	-1	0.0558	2	0.5440	1	0.0714	1
GD1607_1 - 25	5.15E+04	3.02E+03	9.51E+05	452.6	3.6	492	40	466.7	6.8	+3	0.0573	2	0.5840	2	0.0727	1
GD1607_1 - 26	6.57E+04	3.82E+03	1.34E+06	414.8	4	478	36	430.7	5.7	+4	0.0569	2	0.5289	2	0.0665	1
GD1607_1 - 27	4.64E+04	2.70E+03	8.87E+05	436.6	4.2	471	41	450.9	7.1	+3	0.0568	2	0.5600	2	0.0701	1
GD1607_1 - 28	2.22E+05	2.33E+04	1.30E+06	1405	18	1670	22	1527.0	12.0	+8	0.1026	1	3.5020	1	0.2435	1
GD1607_1 - 29	9.30E+04	5.52E+03	1.48E+06	517.4	4.3	525	27	529.0	6.0	+2	0.0580	1	0.6808	1	0.0836	1
GD1607_1 - 30	7.70E+04	4.47E+03	1.43E+06	445.3	3.5	468	36	458.9	5.1	+3	0.0567	2	0.5718	1	0.0715	1
GD1607_1 - 31	5.31E+04	3.09E+03	9.98E+05	439.1	3.9	478	38	455.9	6.3	+4	0.0569	2	0.5673	2	0.0705	1
GD1607_1 - 32	7.33E+04	4.68E+03	1.22E+06	494.5	4.6	680	38	541.3	6.8	+9	0.0623	2	0.7050	2	0.0797	1
GD1607_1 - 33	6.79E+04	4.33E+03	8.99E+05	606.2	4.6	677	36	635.3	7.9	+5	0.0623	2	0.8700	2	0.0986	1
GD1607_1 - 34	1.21E+05	7.00E+03	2.22E+06	449.9	3	458	27	461.9	4.6	+3	0.0563	1	0.5764	1	0.0723	1
GD1607_1 - 35	44460	2617	823000	447.2	4.3	497	43	467.5	6.5	+4	0.0575	2	0.5850	2	0.0718	1
GD1607_1 - 36	7.18E+04	4.05E+03	1.50E+06	407.9	6.3	431	55	422.5	8.5	+3	0.0557	3	0.5170	3	0.0653	2
GD1607_1 - 37	1.25E+05	7.26E+03	2.35E+06	442.6	3.4	476	28	458.3	5.0	+3	0.0567	1	0.5708	1	0.0711	1
GD1607_1 - 38	6.74E+04	3.85E+03	1.27E+06	438.2	3.9	426	40	445.7	6.1	+2	0.0556	2	0.5516	2	0.0703	1
GD1607_1 - 39	6.45E+04	3.65E+03	1.39E+06	374.8	4.4	414	46	389.0	6.9	+4	0.0553	2	0.4674	2	0.0599	1
GD1607_1 - 40	7.07E+04	3.92E+03	1.53E+06	383.3	2.5	362	36	389.4	5.5	+2	0.0540	2	0.4678	2	0.0613	1
GD1607_1 - 41	1.26E+05	7.53E+03	1.86E+06	560.1	5.4	549	30	568.7	7.6	+2	0.0585	1	0.7520	2	0.0908	1
GD1607_1 - 45	73430	5160	1310000	470.3	4.9	869	38	551.1	6.7	+15	0.0683	2	0.7220	2	0.0757	1
GD1607_1 - 46	6.97E+04	4.05E+03	1.31E+06	448.5	3.7	464	33	455.7	5.5	+2	0.0565	1	0.5669	1	0.0721	1
GD1607_1 - 47	7.57E+04	4.34E+03	1.41E+06	452.3	3.4	434	32	452.6	5.4	+0	0.0557	1	0.5621	1	0.0727	1
GD1609C - 01	1.05E+05	6.09E+03	2.11E+06	442.6	3.4	465	32	444.1	5.2	+0	0.0565	1	0.5489	1	0.0711	1
GD1609C - 02	4.65E+05	4.97E+04	2.11E+06	1666	12	1696	13	1669.5	7.7	+0	0.1040	1	4.1790	1	0.2950	1
GD1609C - 03	1.32E+05	7.56E+03	2.55E+06	444	3.4	445	25	440.4	4.0	-1	0.0559	1	0.5433	1	0.0713	1
GD1609C - 04	1.64E+05	9.79E+03	2.49E+06	560.4	3.6	532	23	550.4	4.8	-2	0.0582	1	0.7199	1	0.0908	1
GD1609C - 05	1.48E+05	9.34E+03	2.02E+06	596	10	646	53	598.0	16.0	+0	0.0614	2	0.8040	3	0.0968	2
GD1609C - 06	9.09E+04	5.24E+03	1.68E+06	467.8	3.1	447	34	459.8	6.4	-2	0.0560	2	0.5735	2	0.0753	1
GD1609C - 07	3.75E+05	4.00E+04	1.74E+06	1639	17	1687	15	1648.7	9.3	+1	0.1036	1	4.0750	1	0.2895	1
GD1609C - 08	3.50E+05	3.21E+04	3.41E+06	898	14	1399	23	1048.0	14.0	+14	0.0889	1	1.8100	2	0.1494	2
GD1609C - 09	3.65E+05	3.91E+04	1.62E+06	1696	18	1691	22	1679.0	11.0	-1	0.1038	1	4.2280	1	0.3010	1
GD1609C - 10	1.36E+05	7.70E+03	2.78E+06	438.7	4.7	414	30	431.9	5.3	-2	0.0550	1	0.5304	2	0.0704	1
GD1609C - 11	6.95E+04	4.29E+03	1.21E+06	507.4	6	602	35	521.1	8.2	+3	0.0601	2	0.6720	2	0.0819	1
GD1609C - 12	9.07E+04	5.23E+03	1.74E+06	448.6	3.8	441	29	444.7	5.5	-1	0.0559	1	0.5500	2	0.0721	1
GD1609C - 13	32190	3050	194300	1368	15	1450	46	1399.0	21.0	+2	0.0916	2	2.9770	3	0.2364	1
GD1609C - 14	6.08E+05	6.51E+04	2.71E+06	1726	11	1684.8	9.5	1702.8	6.7	-1	0.1034	1	4.3520	1	0.3071	1
GD1609C - 15	2.85E+05	2.59E+04	2.56E+06	965	12	1382	30	1100.0	13.0	+12	0.0881	2	1.9550	2	0.1616	1
GD1609C - 16	1.23E+05	7.47E+03	1.90E+06	544	3.7	526	27	550.5	5.6	+1	0.0579	1	0.7201	1	0.0881	1
GD1609C - 17	9.60E+04	5.49E+03	1.88E+06	434.2	2.8	403	29	437.2	4.7	+1	0.0548	1	0.5384	1	0.0697	1
GD1609C - 18	3.00E+05	3.05E+04	1.71E+06	1332	16	1573	27	1442.0	15.0	+8	0.0974	1	3.1400	2	0.2295	1
GD1609C - 19	3.83E+05	3.77E+04	2.69E+06	1120	16	1510	24	1282.0	13.0	+13	0.0942	1	2.5360	2	0.1898	2
GD1609C - 20	1.48E+06	1.58E+05	6.63E+06	1656	14	1664	12	1677.5	8.8	+1	0.1022	1	4.2210	1	0.2930	1
GD1609C - 21	2.77E+05	1.64E+04	4.53E+06	513.6	3.6	464	20	514.9	3.8	+0	0.0564	1	0.6608	1	0.0829	1
GD1609C - 22	7.26E+05	7.82E+04	3.20E+06	1673	16	1677	13	1690.4	8.5	+1	0.1030	1	4.2870	1	0.2964	1
GD1609C - 23	9.58E+04	5.91E+03	1.36E+06	599.8	6.1	561	38	605.1	8.6	+1	0.0590	2	0.8160	2	0.0975	1
GD1609C - 24	9.90E+04	5.54E+03	2.33E+06	370.9	3.6	346	40	376.2	5.6	+1	0.0536	2	0.4488	2	0.0592	1
GD1609C - 25	8.97E+04	5.36E+03	1.44E+06	518.9	4.4	491	34	523.7	6.4	+1	0.0572	2	0.6760	2	0.0838	1

Table S2. La-ICP-MS monazite U–Pb data.

Table S2. (continued)

GD1609C - 26	9.22E+04	5.48E+03	1.46E+06	536.1	4.6	477	34	535.7	6.8	-0	0.0568	2	0.6960	2	0.0867	1
GD1609C - 27	6.02E+04	3.52E+03	1.16E+06	432.6	3.9	441	40	442.2	6.0	+2	0.0560	2	0.5462	2	0.0694	1
GD1609C - 28	1.68E+05	9.72E+03	3.15E+06	455.7	3.5	417	26	457.8	4.9	+0	0.0552	1	0.5700	1	0.0733	1
GD1609C - 29	1.29E+05	7.56E+03	2.35E+06	471.1	5.2	451	27	475.0	6.5	+1	0.0561	1	0.5970	2	0.0758	1
GD1609C - 30	1.32E+05	8.01E+03	2.30E+06	498	5.7	542	37	514.7	9.7	+3	0.0586	2	0.6620	2	0.0803	1
GD1609C - 31	5.43E+04	3.35E+03	7.70E+05	606.1	5.8	557	43	597.9	7.5	-1	0.0590	2	0.8030	2	0.0986	1
GD1609C - 32	1.81E+05	1.04E+04	3.33E+06	473.4	3.7	418	23	466.0	4.3	-2	0.0553	1	0.5826	1	0.0762	1
GD1609C - 33	9.33E+04	5.51E+03	1.74E+06	458.6	3.6	469	28	460.2	5.0	+0	0.0563	1	0.5737	1	0.0737	1
GD1609C - 34	8.45E+05	8.95E+04	3.84E+06	1665	11	1647	12	1653.8	7.6	-1	0.1013	1	4.0990	1	0.2947	1
GD1609C - 35	1.08E+06	1.15E+05	4.95E+06	1740	16	1664	11	1708.8	9.4	-2	0.1022	1	4.3840	1	0.3098	1
GD1609C - 36	1.71E+06	1.80E+05	8.60E+06	1630	19	1636	14	1635.0	11.0	+0	0.1007	1	4.0060	1	0.2878	1
GD1609C - 38	2.25E+04	1.36E+03	4.30E+05	482	13	530	100	490.0	24.0	+2	0.0578	5	0.6250	6	0.0777	3
GD1609C - 39	6.02E+05	6.00E+04	3.87E+06	1259	18	1531	30	1372.0	18.0	+8	0.0952	2	2.8640	2	0.2157	2
GD1609C - 40	2.55E+05	2.62E+04	1.51E+06	1316	16	1594	25	1428.4	9.3	+8	0.0985	1	3.0830	1	0.2265	1
GD1609C - 41	6.04E+05	6.46E+04	2.89E+06	1672	16	1687	13	1688.0	10.0	+1	0.1035	1	4.2660	1	0.2961	1
GD1609C - 42	2.58E+05	2.37E+04	2.09E+06	976	13	1399	25	1124.0	15.0	+13	0.0889	1	2.0260	2	0.1636	1
GD1609C - 43	3.94E+05	4.21E+04	1.72E+06	1689	18	1687	17	1693.0	10.0	+0	0.1036	1	4.3010	1	0.2997	1
GD1609C - 44	1.71E+06	1.87E+05	7.58E+06	1728	12	1719	10	1733.8	5.9	+0	0.1053	1	4.5170	1	0.3074	1
GD1609C - 45	1.65E+05	1.42E+04	1.69E+06	778.1	6.9	1272	36	929.1	9.2	+16	0.0833	2	1.4910	2	0.1283	1
GD1609C - 46	1.11E+05	6.52E+03	1.83E+06	500.5	3.4	487	29	504.7	5.5	+1	0.0570	1	0.6443	1	0.0807	1
GD1609C - 48	9.76E+04	5.72E+03	1.68E+06	482.9	6.1	474	27	488.4	6.7	+1	0.0567	1	0.6180	2	0.0778	1
GD1609C - 49	9.85E+04	5.91E+03	1.54E+06	559.6	4.9	564	52	568.9	9.2	+2	0.0591	2	0.7520	2	0.0907	1
GD1609C - 50	9.58E+04	5.99E+03	1.55E+06	501	4.5	617	55	530.0	12.0	+5	0.0608	3	0.6870	3	0.0808	1
GD1609C - 51	8.12E+04	5.19E+03	1.45E+06	464	4	703	58	516.0	12.0	+10	0.0636	3	0.6650	3	0.0746	1
GD1609C - 52	8.31E+04	4.76E+03	1.54E+06	453.4	3.4	431	30	455.8	5.8	+1	0.0557	1	0.5672	2	0.0729	1
GD1609C - 53	7.23E+04	4.21E+03	1.35E+06	446	3.6	468	31	456.8	5.5	+2	0.0566	1	0.5686	1	0.0716	1
GD1609C - 54	1.46E+05	8.42E+03	2.77E+06	450.2	4.3	459	31	458.9	5.2	+2	0.0563	1	0.5716	1	0.0723	1
GD1609C - 55	8.32E+04	5.07E+03	1.17E+06	580	4.5	571	36	586.7	7.3	+1	0.0593	2	0.7830	2	0.0942	1
GD1609C - 56	1.64E+05	9.64E+03	2.75E+06	481	4.6	493	29	487.2	5.1	+1	0.0571	1	0.6160	1	0.0775	1
GD1609C - 57	70400	3919	1430000	412.6	3.8	375	38	410.8	5.9	-0	0.0543	2	0.4993	2	0.0661	1
GD1609C - 58	1.22E+05	6.99E+03	2.20E+06	464.9	4.1	455	25	466.7	4.9	+0	0.0561	1	0.5839	1	0.0748	1
GD1609C_3 - 01	53900	3380	800000	509	11	639	99	536.0	20.0	+5	0.0614	4	0.6960	5	0.0822	2
GD1609C_3 - 02	56800	3250	991000	444.7	4.6	452	41	447.3	7.0	+1	0.0561	2	0.5540	2	0.0714	1
GD1609C_3 - 03	29000	1633	504000	453	5.1	408	58	447.6	8.3	-1	0.0554	3	0.5550	2	0.0728	1
GD1609C_3 - 04	49200	3100	761000	553	15	657	89	575.0	23.0	+4	0.0619	4	0.7630	5	0.0895	3
GD1609C_3 - 05	46700	2683	808000	445	4	450	39	447.7	6.8	+1	0.0562	2	0.5550	2	0.0715	1
GD1609C_3 - 06	47700	2900	665000	568.4	6.8	584	48	572.2	9.1	+1	0.0598	2	0.7580	2	0.0922	1
GD1609C_3 - 07	33730	1931	577000	447.5	7	457	60	451.0	11.0	+1	0.0565	3	0.5600	3	0.0719	2
GD1609C_3 - 08	26500	1537	463000	446.6	5.7	488	53	453.4	9.4	+1	0.0571	3	0.5620	2	0.0717	1
GD1609C_3 - 09	40100	2221	732000	419.5	6.5	370	50	413.8	8.9	-1	0.0543	2	0.5040	3	0.0672	2
GD1609C_3 - 10	57300	3270	971000	463.5	4.9	439	45	462.8	7.4	-0	0.0560	2	0.5780	2	0.0746	1
GD1609C_3 - 11	40000	2440	521000	589.6	5.9	588	41	589.8	9.0	+0	0.0597	2	0.7890	2	0.0958	1
GD1609C_3 - 12	43500	2760	736000	480.3	7	667	65	516.0	12.0	+7	0.0622	3	0.6630	3	0.0774	2
GD1609C_3 - 13	38900	2344	503000	593.3	6.6	555	45	587.7	9.7	-1	0.0589	2	0.7860	2	0.0964	1
GD1609C_3 - 14	35660	2087	621900	450.9	5.3	503	54	461.1	8.0	+2	0.0574	3	0.5750	2	0.0725	1
GD1609C_3 - 15	43500	2680	563000	594	6.6	597	45	596.9	9.2	+0	0.0602	2	0.8020	2	0.0965	1
GD1609C_3 - 16	39000	2249	699000	433.4	3.7	465	45	440.2	7.5	+2	0.0567	2	0.5440	2	0.0696	1
GD1609C_3 - 17	63200	3760	984000	520	6.2	535	47	523.0	11.0	+1	0.0584	2	0.6750	3	0.0840	1
GD1609C_3 - 18	60500	3540	962000	498.7	5.1	489	41	497.6	6.8	-0	0.0571	2	0.6330	2	0.0804	1
GD1609C_3 - 19	46600	2810	664000	518.8	6.8	567	50	527.9	9.6	+2	0.0590	3	0.6830	2	0.0838	1
GD1609C_3 - 20	83000	7290	648000	937	16	1339	42	1068.0	20.0	+12	0.0858	2	1.8520	3	0.1564	2
GD1609C_3 - 21	65100	4730	758000	655.6	9.3	956	53	730.0	14.0	+10	0.0713	3	1.0530	3	0.1071	1
GD1609C_3 - 22	70400	4120	1146000	523	15	489	80	517.0	16.0	-1	0.0571	4	0.6650	4	0.0846	3
GD1609C_3 - 23	48900	2840	827000	460.4	5.4	469	36	463.1	6.0	+1	0.0567	2	0.5785	2	0.0740	1
GD1609C_3 - 24	43900	2540	728000	451	5.7	464	54	455.6	9.7	+1	0.0566	2	0.5670	3	0.0725	1
GD1609C_3 - 25	448000	48200	1845000	1650	16	1720	15	1683.2	9.8	+2	0.1055	1	4.2510	1	0.2917	1
GD1609C_3 - 26	122500	10940	1176000	833	20	1366	43	994.0	23.0	+16	0.0874	2	1.6650	4	0.1380	3
GD1609C_3 - 29	146500	11810	1415000	836	12	1169	35	934.0	13.0	+10	0.0790	2	1.5100	2	0.1386	2
GD1609C_3 - 30	89200	5530	1221000	588.8	8.5	643	48	601.0	11.0	+2	0.0613	2	0.8090	2	0.0956	1
GD1609C_3 - 31	277200	29050	1462000	1435	21	1672	24	1534.0	14.0	+6	0.1027	1	3.5320	2	0.2493	2
GD1609C_3 - 32	50900	2960	868000	460.8	5.6	479	47	465.8	7.9	+1	0.0570	2	0.5830	2	0.0741	1
GD1609C_3 - 33	66500	3810	1103000	468.1	5.5	452	37	465.7	6.8	-1	0.0561	2	0.5830	2	0.0753	1
GD1609C_3 - 34	60400	3690	931000	478.6	8.7	575	54	498.0	13.0	+4	0.0595	3	0.6350	3	0.0771	2
GD1609C_3 - 35	34900	2130	526000	498.6	7.7	549	57	511.0	13.0	+2	0.0587	3	0.6480	3	0.0804	2
GD1609C_3 - 36	239700	24500	1301000	1363	22	1619	25	1467.0	17.0	+7	0.0998	1	3.2440	2	0.2354	2
GD1609C_3 - 37	51600	3060	834000	463.7	5.9	522	51	475.7	9.5	+3	0.0581	2	0.5960	2	0.0746	1
GD1609C_3 - 38	41200	2540	536000	594.4	6	609	40	598.6	8.4	+1	0.0605	2	0.8040	2	0.0966	1
GD1609C_3 - 39	60900	3600	1005000	485.6	6.1	519	53	494.3	9.9	+2	0.0580	2	0.6280	3	0.0782	1
GD1609C_3 - 40	326000	34800	1302000	1680	17	1707	19	1694.0	9.8	+1	0.1047	1	4.3060	1	0.2978	1
GD1609C_3 - 41	62400	3627	1108000	444.5	6.5	484	43	452.0	7.5	+2	0.0570	2	0.5610	2	0.0714	2
GD1609C_3 - 42	318000	34000	1273000	1786	25	1702	17	1751.0	11.0	-2	0.1045	1	4.6170	1	0.3194	2
GD1609C_3 - 43	62700	4590	827000	598	15	957	46	680.0	20.0	+12	0.0714	2	0.9590	4	0.0972	3
GD1609C_3 - 44	31100	1800	542000	452.8	5.4	455	51	455.4	8.9	+1	0.0565	2	0.5670	2	0.0728	1
GD1609C_3 - 45	32400	1808	584000	436.2	5.1	387	50	429.7	7.3	-2	0.0548	2	0.5280	2	0.0700	1
GD1609C_3 - 46	28700	1606	489000	459.5	4.9	389	57	448.2	8.6	-3	0.0547	2	0.5560	2	0.0739	1
GD1609C_3 - 47	30530	1823	432000	561.8	9.6	542	52	559.0	12.0	-1	0.0586	2	0.7360	3	0.0911	2
GD1609C_3 - 48	39700	2303	651000	492.1	9.1	474	77	491.0	14.0	-0	0.0571	4	0.6230	4	0.0793	2
GD1609C_3 - 49	45280	2678	730000	495.5	7.8	528	46	500.0	11.0	+1	0.0580	2	0.6380	3	0.0799	2
GD1609C_3 - 50	34100	2000	590000	461	6	495	54	467.1	9.7	+1	0.0574	2	0.5830	2	0.0741	1
GD1609C_3 - 51	37400	2220	542000	540.1	6.5	523	52	539.0	11.0	-0	0.0581	2	0.7020	3	0.0874	1
GD1609C_3 - 52	33860	1952	581000	451.7	5.2	456	51	454.4	8.2	+1	0.0565	2	0.5650	2	0.0726	1
GD1609C_3 - 53	12740	737	216000	463.8	6.6	429	85	462.0	13.0	-0	0.0566	4	0.5790	3	0.0746	1
GD1609C_3 - 54	15630	884	270700	461.9	9.1	449	84	461.0	14.0	-0	0.0566	4	0.5770	4	0.0743	2
GD1609C_3 - 55	47400	2710	819000	451.1	4.4	450	36	451.5	6.7	+0	0.0562	2	0.5610	2	0.0725	1
GD1609C_3 - 56	55800	3150	973000	446.6	4.4	417	36	441.3	6.2	-1	0.0551	2	0.5449	2	0.0717	1
GD1609C_3 - 57	67700	4360	949000	555	10	687	69	582.0	15.0	+5	0.0627	3	0.7750	3	0.0899	2
GD1609C_3 - 58	36800	2220	471000	610.1	7.1	573	52	602.4	9.4	-1	0.0597	2	0.8110	2	0.0993	1
GD1609C_3 - 59	19900	1213	259000	600.1	9.5	571	69	596.0	14.0	-1	0.0599	3	0.7980	3	0.0976	2
GD1609C_3 - 60	33100	2000	421000	605.2	5.9	573	44	599.1	9.1	-1	0.0595	2	0.8060	2	0.0984	1
GD1609C_3 - 61	28700	1760	365000	603.9	6.6	595	48	602.6	8.8	-0	0.0602	2	0.8120	2	0.0982	1
GD1609C_3 - 62	35800	2170	445000	599.1	6.8	574	52	595.0	12.0	-1	0.0592	2	0.7980	3	0.0974	1

Table S2. (continued)

GD1609C_3 - 63	43300	2440	801000	422.2	3.8	414	41	422.0	6.9	-0	0.0553	2	0.5160	2	0.0677	1
GD1610 - 01	38300	2220	616000	469.7	6.3	477	45	473.2	9.2	+1	0.0569	2	0.5950	2	0.0756	1
GD1610 - 02	34400	2187	578000	469	4.7	722	77	521.0	16.0	+10	0.0647	4	0.6750	4	0.0755	1
GD1610 - 03	35150	1979	645000	431.4	4.9	405	54	429.1	8.9	-1	0.0552	2	0.5270	2	0.0692	1
GD1610 - 04	34970	1984	626000	435.5	5.1	427	50	436.0	8.1	+0	0.0558	2	0.5370	2	0.0699	1
GD1610 - 05	24300	1400	472000	438	13	450	130	441.0	16.0	+1	0.0565	5	0.5450	4	0.0703	3
GD1610 - 06	37000	2068	823000	375.2	8.3	390	98	378.0	13.0	+1	0.0549	4	0.4520	4	0.0599	2
GD1610 - 07	32710	1881	598000	454.8	9.9	448	99	455.0	16.0	+0	0.0564	5	0.5670	4	0.0731	2
GD1610 - 08	32180	1864	567000	443.9	6	473	54	450.5	8.4	+1	0.0570	2	0.5590	2	0.0713	1
GD1610 - 09	32890	1907	579000	448.5	5.7	465	57	453.4	9.6	+1	0.0568	3	0.5640	3	0.0721	1
GD1610 - 10	27790	1643	468000	467.4	5.2	503	54	475.4	8.3	+2	0.0575	2	0.5980	2	0.0752	1
GD1610 - 11	27320	1562	490000	436.3	4.6	431	54	437.7	8.7	+0	0.0560	3	0.5400	2	0.0700	1
GD1610 - 12	53100	3011	954000	435.2	4.5	426	40	435.1	6.8	-0	0.0556	2	0.5360	2	0.0698	1
GD1610 - 13	27900	1605	486000	446.2	5	454	58	449.8	9.3	+1	0.0563	2	0.5590	3	0.0717	1
GD1610 - 14	27600	1587	484000	443.2	4.7	446	55	446.6	9.0	+1	0.0564	2	0.5540	3	0.0712	1
GD1610 - 15	19010	1171	311000	475.6	6.3	587	81	500.0	14.0	+5	0.0607	4	0.6360	3	0.0766	1
GD1610 - 16	23300	1371	392000	470.8	5.8	523	82	476.0	13.0	+1	0.0576	3	0.5950	3	0.0758	1
GD1610 - 17	16400	2460	285000	438	11	2210	110	869.0	43.0	+50	0.1408	7	1.3700	7	0.0703	3
GD1610 - 18	12630	754	206000	478.7	7.1	500	77	486.0	13.0	+2	0.0582	4	0.6160	3	0.0771	2
GD1610 - 19	28400	1668	497000	449.4	4.8	485	57	455.7	8.7	+1	0.0571	2	0.5680	2	0.0722	1
GD1610 - 20	13530	797	229000	467.3	6.4	472	79	472.0	13.0	+1	0.0571	4	0.5910	3	0.0752	1
GD1610 - 21	21700	1223	362000	470.7	5.7	409	59	462.1	9.0	-2	0.0555	3	0.5780	2	0.0758	1
GD1610 - 22	22200	1277	375000	463.9	5.3	457	58	465.2	9.1	+0	0.0567	3	0.5830	2	0.0746	1
GD1610 - 23	63800	3660	1170000	430.1	4.4	457	39	433.7	6.5	+1	0.0564	2	0.5334	2	0.0690	1
GD1610 - 24	51100	2980	971000	420.4	5.7	513	63	437.0	11.0	+4	0.0580	3	0.5380	3	0.0674	1
GD1610 - 25	30100	1710	520000	455.3	5.3	426	46	450.4	7.3	-1	0.0555	2	0.5590	2	0.0732	1
GD1610 - 26	30500	1752	540000	443.5	5.1	451	49	447.0	7.0	+1	0.0564	2	0.5520	2	0.0712	1
GD1610 - 27	29520	1710	525000	443.8	4.3	460	55	449.0	8.6	+1	0.0567	2	0.5530	2	0.0713	1
GD1610 - 28	61800	3480	1221000	402.6	5.7	412	62	407.0	11.0	+1	0.0554	3	0.4920	3	0.0645	1
GD1610 - 29	36340	2083	670000	442.3	5.9	438	69	444.0	11.0	+0	0.0560	3	0.5490	3	0.0710	1
GD1610 - 30	23720	1391	412000	447.4	4.8	507	55	458.8	8.6	+2	0.0580	2	0.5730	2	0.0719	1
GD1610 - 31	29340	1699	525000	437.8	4.5	466	46	443.7	8.0	+1	0.0567	2	0.5470	2	0.0703	1
GD1610 - 32	28000	1640	487000	452.3	4.9	479	59	459.0	10.0	+1	0.0573	3	0.5730	3	0.0727	1
GD1610 - 33	20020	1270	330000	475.3	6.3	646	98	515.0	21.0	+8	0.0632	5	0.6680	6	0.0765	1
GD1610 - 34	31100	1837	537000	459.1	5.7	514	62	471.0	11.0	+3	0.0582	3	0.5920	3	0.0738	1
GD1610 - 35	32600	1891	569000	447	4.8	479	52	453.7	7.8	+1	0.0572	2	0.5640	2	0.0718	1
GD1610 - 36	50900	2980	947000	420.5	4	503	50	435.0	8.1	+3	0.0578	2	0.5360	2	0.0674	1
GD1610 - 37	28000	1940	652000	368.8	9.1	858	73	444.0	13.0	+17	0.0679	3	0.5490	4	0.0589	3
GD1610 - 38	39600	2219	827000	376	4.6	388	49	378.7	6.9	+1	0.0548	2	0.4530	2	0.0601	1
GD1610 - 39	41300	2270	880000	369.4	3.9	353	43	368.0	5.9	-0	0.0539	2	0.4373	2	0.0590	1
GD1610 - 40	13750	821	227400	470.5	6.5	516	69	481.0	12.0	+2	0.0585	3	0.6090	3	0.0757	1
GD1610 - 41	24200	1377	419000	445.3	5.8	432	71	446.0	12.0	+0	0.0562	3	0.5530	3	0.0715	1
GD1610 - 42	84800	4820	1543000	435	4.4	438	37	435.8	6.0	+0	0.0557	2	0.5365	2	0.0698	1
GD1610 - 43	30100	1687	622000	390.7	4.8	396	51	390.5	6.9	-0	0.0547	2	0.4690	2	0.0625	1

Errors are 2 sigma. Disc: discordance.
GD1607_1: Glimmerite schist; GD1609C_3: Quartz mylonite with glimmerite reaction band; GD1610: K-feldspar rich granite lens.

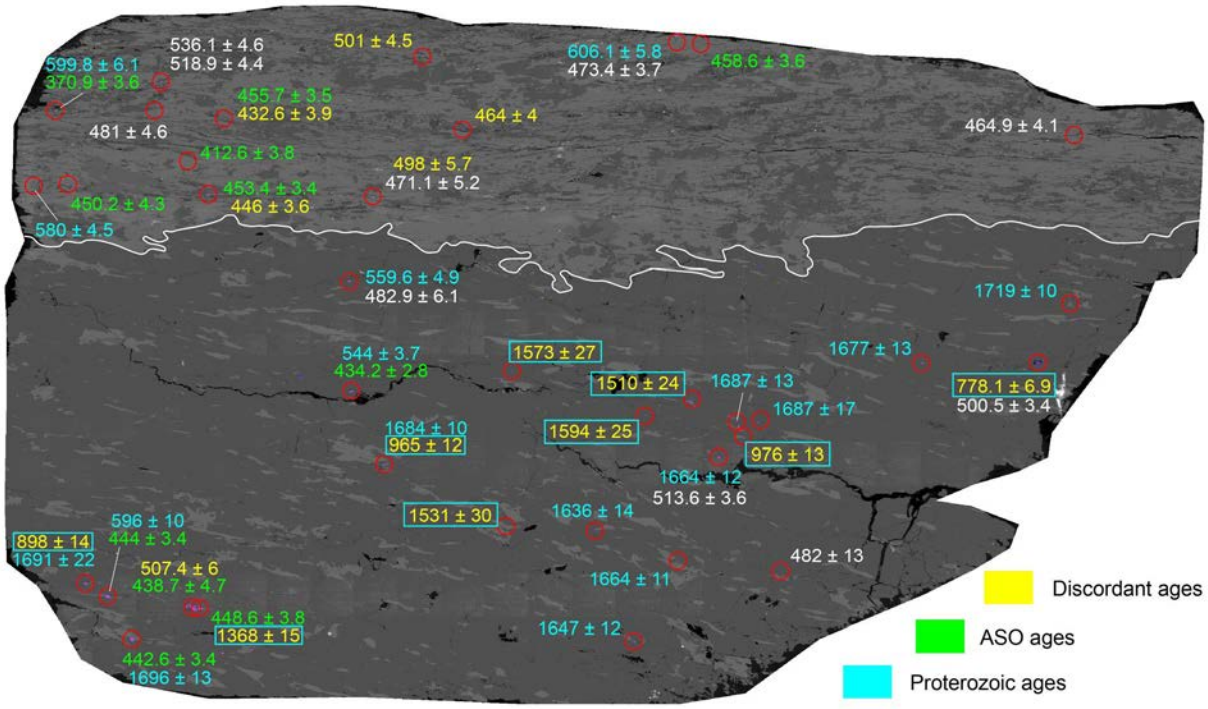

Figure S1. Map of monazite age spatial distribution in M–Qtz/GL sample.

Electronic Appendices. Supplementary data for chapter four and five

SUPPORTING INFORMATION

Glimmerite: a product of melt-rock interaction within a crustal scale high-strain zone

D. Silva, N. R. Daczko, S. Piazolo, T. Raimondo

K-feldspar phenocrysts trapped during syn-tectonic melt expulsion from a melt fluxed high-strain zone

D. Silva, S. Piazolo, N. R. Daczko

Table ES1. Mineral major and trace oxide composition for L–Qtz to glimmerite schist samples. (Microprobe data)

Table ES2. Mineral major and trace element composition for L–Qtz to glimmerite schist samples. (La–ICP–MS data)

Table ES3. Mineral major and trace element composition for M–Qtz/GL and glimmerite schist samples. (micro-XRF data)